Highly sensitive quantum magnetometry using Nitrogen-Vacancy centers in diamond

Poulsen, Andreas Feldt Lomholt

Publication date:
2021

Document Version
Publisher's PDF, also known as Version of record

Citation (APA):
Poulsen, A. F. L. (2021). *Highly sensitive quantum magnetometry using Nitrogen-Vacancy centers in diamond*. Department of Physics, Technical University of Denmark.

PH.D. THESIS

Highly sensitive quantum magnetometry using Nitrogen-Vacancy centers in diamond

Department of Physics
Technical University of Denmark

by
Andreas Feldt Lomholt Poulsen, M. Sc.
(anflp@fysik.dtu.dk)

Supervisor: Alexander Huck
Co-supervisor: Kirstine Berg-Sørensen
Co-supervisor: Ulrik Lund Andersen

31. October 2021

Acknowledgments

I would like to thank my supervisors Alexander Huck and Kirstine Berg-Sørensen for their support and guidance during the course of my PhD. I would also like to thank both them and professor Ulrik Lund Andersen for helping me adjust my project to better suit my skillset and for providing inspiration for my research.

I would further like to thank Joshua Clement and James Webb for their contributions to our collaborations. James aka Jim also provided a lot of useful input on my work.

Lastly, I would like to thank Joshua and Luca Troise, with whom I shared an office for most of my PhD, for many engaging and entertaining conversations.

Abstract

The work presented in this thesis deals with magnetic field sensing using the nitrogen-vacancy (NV) defect center in diamond. The NV center is a solid-state defect in diamond with a level structure and properties that render its electron spin state sensitive to many environmental factors including magnetic fields. The NV center can be used for sensing even under ambient conditions, and the diamond substrate is both mechanically stable and chemically inert. These properties would represent significant advantages compared to existing quantum magnetometers if the sensitivity of NV magnetometers were higher. The ultimate goal of the presented work was thus to explore and investigate various different ways to improve the sensitivity of NV magnetometry.

Ensembles of NV centers yield higher sensitivity than single NV centers, but controlling an ensemble is complicated by inhomogeneous broadening of the transition frequencies and drive field inhomogeneities. Smooth optimal control theory was used to design shaped control pulses that are robust against inhomogeneous broadening and drive amplitude variations. Furthermore, the theory was expanded to explicitly include the hyperfine splitting of the NV center electron spin states. The resulting optimal control pulses were found theoretically and shown experimentally to yield significant improvements in the sensitivity compared to the best equivalent standard control pulses.

The typical sensing approach based on measuring changes in the red fluorescence is limited by the need to measure a low contrast on a bright background. These limitations can be avoided by utilizing the green absorption to perform laser threshold magnetometry. A setup where the drive-dependent change in green absorption is used to push an external laser cavity across the lasing threshold was proposed and theoretically investigated. The predicted sensitivity was found to reach the $\mathrm{pT}/\sqrt{\mathrm{Hz}}$ range for realistic optimal parameters. However, it was also shown that the effect of amplified spontaneous emission near lasing threshold can significantly reduce the achievable sensitivity.

Different sensing schemes are affected differently by inhomogeneous broadening (IHB) and drive amplitude variations (DAV), which makes it challenging to select the optimal scheme for a given situation. The maximum achievable sensitivity of the three most commonly used low-frequency sensing schemes was simulated and compared for different levels of IHB and DAV. The three schemes were continuous-wave (CW) optically detected magnetic resonance (ODMR), π-pulse ODMR and Ramsey interferometry. It was found that Ramsey interferometry only yields the best sensitivity for low inhomogeneous broadening, while CW ODMR yields the best sensitivity for large drive amplitude variations. π-pulse ODMR was found to yield the best sensitivity when the inhomogeneous broadening is not low and the drive amplitude variations are not large.

Dansk resume

Det arbejde, der præsenteres i denne afhandling, omhandler måling af magnetfelter ved hjælp af nitrogen-vacancy (NV) defekten i diamant. NV centeret er en solid defekt i diamant med egenskaber og en struktur af dens energiniveauer, der bevirker, at dens spin-tilstand er følsom over for adskillige faktorer i omgivelserne heriblandt magnetfelter. NV centeret kan anvendes til måling selv under normale omstændigheder, og diamantsubstratet er mekanisk stabilt og kemisk inaktivt. Disse egenskaber ville repræsentere betydelige fordele sammenlignet med eksisterende kvante-magnetometre, hvis sensitiviteten af NV magnetometre var højere. Det ultimative mål med det præsenterede arbejde er således at udforske og undersøge forskellige måder, hvorpå sensitiviteten af NV magnetometri kan forbedres.

Ensembler af NV centre har højere sensitivitet end enkelte NV centre, men kontrollen af et ensemble kompliceres af inhomogen spredning af overgangsfrekvenserne og inhomogeniteter i kontrolfeltet. Smooth optimal control teori blev anvendt til at designe formede kontrolpulser, der er robuste overfor inhomogen spredning og variationer i amplituden af kontrolfeltet. Derudover blev teorien udvidet til eksplicit at inkludere den hyperfine splittelse af NV center spin-tilstandene. De resulterende optimal control pulser blev teoretisk og eksperimentelt vist at medføre betydelige forbedringer af sensitiviteten sammenlignet med de bedste ækvivalente standard kontrol-pulser.

Den typiske tilgang til målinger med NV centre, som er baseret på at måle ændringer i den røde fluorescens, begrænses af behovet for at måle en lille kontrast på en betydelig baggrund. Disse begrænsninger kan undgås ved at udnytte den grønne absorption til at udføre laser threshold magnetometri. Et setup, hvor den kontrol-afhængige ændring i grøn absorption anvendes til at skubbe en external laser cavity over laser thresholdet, blev præsenteret og teoretisk undersøgt. Det blev konstateret, at den forventede sensitivitet kunne nå $\mathrm{pT}/\sqrt{\mathrm{Hz}}$-niveauet for realistiske optimale parametre. Det blev dog også vist, at forstærket spontan emission nær laser thresholdet kan betydeligt reducere den opnåelige sensitivitet.

Forskellige målingsmetoder påvirkes forskelligt af inhomogen spredning og variationer i amplituden af kontrolfeltet, hvilket gør det vanskeligt at vælge den optimale metode for en given situation. Den maksimalt opnåelige sensitivitet af de tre hyppigst anvendte lavfrekvens målingsmetoder blev simuleret og sammenlignet for forskellige niveauer af inhomogen spredning og variationer i amplituden af kontrolfeltet. De tre metoder var continuous-wave (CW) optically detected magnetic resonance (ODMR), π-puls ODMR og Ramsey interferometri. Det blev vist, at Ramsey interferomtri kun opnår den bedste sensitivitet for lave niveauer af inhomogen spredning, mens CW ODMR opnår den bedste sensitivitet for store variationer i amplituden af kontrolfeltet. π-puls ODMR opnåede den bedste sensi-

tivitet, når den inhomogene spredning ikke var lav, og der ikke var store variationer i amplituden af kontrolfeltet.

Contents

1 Introduction

The ability to measure extremely weak magnetic fields with high spatial resolution is incredibly valuable for the study and understanding of biology [1–5]. The weak electrical signals involved in neural activity produce miniscule magnetic fields that can be measured in order to make inferences about the neural activity. This is the basis of magnetoencephalography (MEG), which is used to study the brain, [6, 7] and magnetogastrography (MGG), which is used to study the stomach [8, 9]. The neural activity in muscles and other parts of the body, such as the heart, can similarly be studied by measuring the associated magnetic fields [3, 10–12]. These techniques can all be carried out noninvasively and are an important part of modern medicine.

MEGs and MGGs are normally carried out using a superconducting quantum interference device (SQUID), which is perhaps the most well-known high-sensitivity quantum magnetometer [13–15]. These devices can reach sensitivities on the order of $\mathrm{fT}/\sqrt{\mathrm{Hz}}$ and have been in use for several decades. However, SQUIDs are not without their limitations. They require cryogenic temperatures in order to operate, which limits how close the sensor can be brought to the object to be sensed, and makes it highly impractical to perform sensing inside living subjects. Another well-researched high-sensitivity quantum magnetometer that can function at ambient temperatures is the atomic-vapor magnetometer [16–18]. These devices boast potentially higher sensitivity than SQUIDs, but the sensor size is significantly larger, and they can only operate in near-zero magnetic fields, which can necessitate the use of magnetic shielding.

The desire to obtain a high-sensitivity quantum magnetometer without the limitations of SQUID or atomic-vapor magnetometers is part of the motivation behind the research of alternative magnetometers, such as atomic defects in diamond. In particular, the nitrogen-vacancy (NV) defect in diamond has been the focus of a lot of research due to its many advantageous properties. An NV magnetometer can operate at ambient temperatures, does not require a near-zero magnetic field, and the spatial resolution is only limited by the size of a single defect or the diamond dimensions when an ensemble of defects is used [19–23]. Furthermore, the electron spin state of the NV center, which is utilized for sensing, has a long coherence time and allows for all-optical readout and initialization [24, 25]. These attributes make the NV center a very attractive quantum magnetometer. However, while NV magnetometers have demonstrated high sensitivity on the order of sub-$\mathrm{pT}/\sqrt{\mathrm{Hz}}$ [26], their sensitivity has yet to reach the level of SQUID and atomic-vapor magnetometers. As a result, a significant portion of NV magnetometry research is currently focused on boosting the sensitivity of NV magnetometers [23, 26, 27]. The aim of this project is likewise to explore and investigate various different avenues for increasing the sensitivity of NV magnetometry, primarily through numerical simulations.

This thesis is structured in the following way. The first part, chapter 2, introduces the properties of the NV center, common sensing schemes and ensemble-specific effects, followed by a description of the relevant theory for optimal control, measurement simulations and laser threshold magnetometry. The main part of the thesis consists of chapters 3, 4 and 5, which present the three covered projects. Each chapter begins with a brief introduction and motivation, followed by the research article that resulted from the study. Each paper further motivates and provides context for the study, followed by an overview of the relevant theory, the main approach and findings and ending with a discussion and conclusion.
Chapter 6 contains a final conclusion and outlook.

2 Theory

It is of vital importance to understand the behavior of quantum systems and their responses to external stimuli in order to properly utilize the quantum properties. Without a thorough understanding of the underlying theory of quantum systems, it would be extremely challenging to predict and explain the results of experiments or the operation of quantum devices.

For this reason, the present chapter will attempt to provide a detailed description of the properties of the NV center that are relevant for the three covered projects along with the rest of the theory that was utilized in the projects. Some of said theory has already been explained in the resulting publications, but this chapter aims to provide more detail, such as a full derivation of the relations used for smooth optimal control and the simulation of CW ODMR. The chapter begins with a description of the NV properties, common sensing schemes and ensemble-specific effects, which provide a foundation for the remaining theory, before moving on to a description of optimal control theory. The optimal control theory is followed by a description of the methodology used to simulate measurements, which utilizes the same Hamiltonians as the optimal control theory. Finally, the relevant laser threshold magnetometry theory is explained.

2.1 The NV center

The NV center is an atomic defect in diamond consisting of a substitutional nitrogen atom and an adjacent vacancy [22, 24, 25, 27–29]. Due to the crystal structure of diamond, four different orientations of the NV center are possible. The orientation is typically denoted by the NV axis, which is the axis connecting the nitrogen atom and the vacancy. For the purposes of sensing, one almost always utilizes the negatively charged NV$^-$ center with the extra electron typically being donated by a nitrogen defect elsewhere in the diamond. This work also focuses on the NV$^-$ center. Throughout the remainder of this thesis, the negatively charged NV$^-$ center will be referred to as an NV or the NV center for the sake of brevity. The NV center is a spin-1 system with a level structure located inside the 5.47 eV band gap of diamond [1, 29–31]. This level structure is illustrated in simplified form in Fig. 2.1.

The level structure consists of spin triplet excited and ground states and metastable intermediate singlet states. The zero-field splitting between the $m_S = 0$ and the degenerate $m_S = \pm 1$ spin states is $D_{gs} = 2.87\,\text{GHz}$ [32] for the ground state and $D_{es} = 1.42\,\text{GHz}$ [33] for the excited state. The NV center can be off-resonantly excited from the triplet ground state ^3A to the triplet excited state ^3E by illuminating it with green laser light ($\lambda = 532\,\text{nm}$) [34, 35]. This transition is spin-conserving. The excited state decays back to the ground state via either

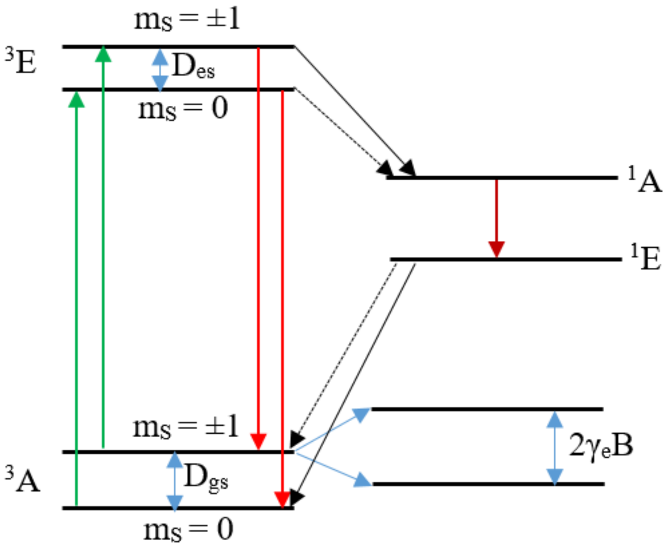

Figure 2.1: Simplified sketch of the level structure of the NV center. The triplet ground state ^{3}A and the triplet excited state ^{3}E both consist of $m_S = 0$ and degenerate $m_S = \pm 1$ spin states. The zero-field splitting is $D_{gs} = 2.87\,\mathrm{GHz}$ for the ground state and $D_{es} = 1.42\,\mathrm{GHz}$ for the excited state. The colored arrows indicate the spin-conserving excitation via green ($\lambda = 532\,\mathrm{nm}$) laser light illumination, the spin-conserving (red, $\lambda \approx 637\,\mathrm{nm}$) fluorescing decay paths from the triplet excited states to the triplet ground states and the (infrared, $\lambda = 1046\,\mathrm{nm}$) fluorescing decay from the singlet excited state to the singlet ground state. The black arrows indicate non-spin-conserving non-fluorescing decay paths with relatively weaker decays indicated by dashed arrows. The degeneracy of the $m_S = \pm 1$ states can be lifted by applying a magnetic field B parallel to the NV axis, which leads to a splitting of $2\gamma_e B$ with the electron gyromagnetic ratio $\gamma_e = 28\,\mathrm{MHz/mT}$.

a direct spin-conserving transition that involves the emission of red fluorescence ($\lambda \approx 637\,\mathrm{nm}$) or via an indirect non-spin-conserving path over the singlet states that involves the emission of infrared fluorescence ($\lambda = 1046\,\mathrm{nm}$) [36–38]. The singlet ground state ^{1}E has a significantly longer lifetime ($\approx 300\,\mathrm{ns}$) than the excited states [38]. The excited $m_S = \pm 1$ states have a greater probability of decaying via the singlet states than the excited $m_S = 0$ state. Additionally, the singlet ground state has a greater probability of decaying to the ground $m_S = 0$ state than the ground $m_S = \pm 1$ states. As a result, it is possible to initialize the NV center in the $m_S = 0$ spin state by continuously illuminating it with green laser light for a sufficient length of time. The spin state-dependence of the decay probabilities also makes it possible to determine the electron spin state of an NV by measuring the red fluorescence. Due to the greater probability of decaying via the indirect path that does not involve emission of red fluorescence, an NV in one of the $m_S = \pm 1$ spin states will emit up to 30% less fluorescence than an NV in the $m_S = 0$ spin state [36,37,39]. These properties enable the all-optical initialization and read-out of the NV center electron spin state.

The degeneracy of the $m_S = \pm 1$ states can be lifted by applying an external magnetic field B parallel to the NV axis via the Zeeman effect [23, 32, 40, 41]. If the field is applied at an angle to the NV axis, only the component that is parallel to the NV axis will contribute to lifting the degeneracy. Each state is then shifted in frequency by $m_S \gamma_e B$ resulting in a splitting of $2\gamma_e B$, as indicated in Fig. 2.1, with the electron gyromagnetic ratio $\gamma_e = 28\,\mathrm{MHz/mT}$. The $m_S = \pm 1$ spin states are also shifted in frequency by the hyperfine interaction between the NV electron spin and the nitrogen nuclear spin, which is not depicted in Fig. 2.1. The magnitude of this shift depends on the nitrogen isotope and nuclear spin state m_I. The shift is $m_I \delta_I$ with $\delta_I = 2.16\,\mathrm{MHz}$ for $^{14}\mathrm{N}$ with $I = 1$, which is the most naturally abundant, and $\delta_I = 3.03\,\mathrm{MHz}$ for $^{15}\mathrm{N}$ with $I = 1/2$. The nitrogen nuclear spin state can be $m_I = -1, 0, 1$ for $^{14}\mathrm{N}$ and $m_I = -1/2, 1/2$ for $^{15}\mathrm{N}$. The lifetime of the nitrogen nuclear spin state is very long compared to the lifetime of the NV electron spin state. The hyperfine interaction will thus shift the frequency of the $m_S = \pm 1$ spin states of a single NV center by a few MHz, which is a small shift compared to the zero-field splitting.

The transitions between electron spin states can be driven directly by applying microwaves (MW) resonant with the transition frequency [22]. Most commonly, either the $m_S = 0 \iff m_S = 1$ or the $m_S = 0 \iff m_S = -1$ transition will be chosen and treated as an effective two-level system [39]. The $m_S = 0$ spin state then serves as state $|0\rangle = (1, 0)$, and the $m_S = 1$ or $m_S = -1$ spin state serves as state $|1\rangle = (0, 1)$. This is the basis of most NV magnetometry schemes, which typically involve applying a static external magnetic field, also called a bias field, parallel to the NV axis in order to lift the degeneracy and then utilizing the effective two-level system to measure any additional external magnetic fields. The state of the effective two-level system can be visualized on the Bloch sphere as illustrated in Fig. 2.2.

The driving can be performed either continuously with constant application of fixed amplitude microwaves and green laser power, or in a pulsed manner with finite pulses of microwaves and green laser light. The most commonly used MW pulses are so-called flat pulses that have a constant amplitude and a duration chosen so that they accomplish a desired operation. Two frequently used MW pulses are π-pulses and $\pi/2$-pulses. A π-pulse causes a π-rotation around an axis in the xy-plane of the Bloch sphere, typically the x- or y-axis, and can be used to invert the electron spin state population from $|0\rangle$ to $|1\rangle$ or vice-versa. A $\pi/2$-pulse similarly causes a $\pi/2$-rotation around an axis in the xy-plane of the Bloch sphere and can be used to transfer the electron spin state population from $|0\rangle$ to a superposition of $|0\rangle$ and $|1\rangle$. In order to determine the pulse duration that is required to achieve a flat π- or $\pi/2$-pulse, it is necessary to perform a Rabi measurement. Such a measurement involves initializing the NV spin in state $|0\rangle$, applying constant amplitude resonant microwaves for a duration τ and then measuring the NV

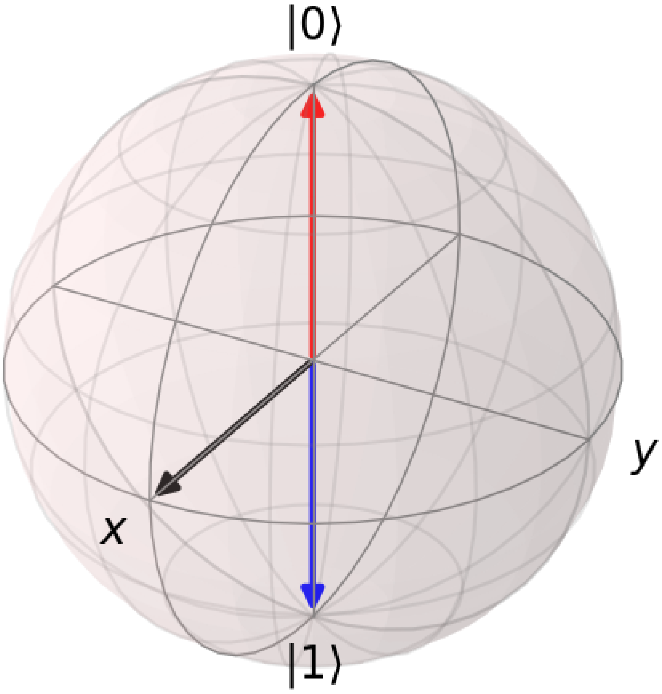

Figure 2.2: Bloch sphere representation of three possible states of the NV two-level system. The state $|0\rangle$ (red arrow) can be achieved via optical initialization. The state $|1\rangle$ (blue arrow) can be achieved by applying a π-pulse to state $|0\rangle$. The state $\frac{1}{\sqrt{2}}(|0\rangle + |1\rangle)$ (black arrow) can be achieved by applying a $\pi/2$-pulse to state $|0\rangle$.

fluorescence. This sequence is repeated for varying values of τ, which yields an oscillation in the measured fluorescence as a function of τ. The frequency of this oscillation is referred to as the Rabi frequency Ω_R and is indicative of how strongly the $|0\rangle \iff |1\rangle$ transition is being driven. Increasing the applied MW power will also increase the Rabi frequency. The duration of a $\pi-$ or $\pi/2$-pulse can then be determined as the time it takes to complete half or a quarter of a full Rabi oscillation, respectively. For instance, if the Rabi frequency is $\Omega_R = 2\pi \cdot 1\,\text{MHz}$, the duration of a π-pulse will be $0.5\,\mu\text{s}$, and the duration of a $\pi/2$-pulse will be $0.25\,\mu\text{s}$.

2.2 Common sensing schemes

Three of the most commonly used sensing schemes for NV magnetometry are continuous-wave (CW) optically detected magnetic resonance (ODMR) [27,42–44], π-pulse ODMR [26,27,44–46] and Ramsey interferometry [23,27]. The sequences of laser power and MW application that make up each of these schemes are illustrated in Fig. 2.3. CW ODMR is the simplest of these three schemes and involves the constant application of MW and laser power while scanning the MW driving

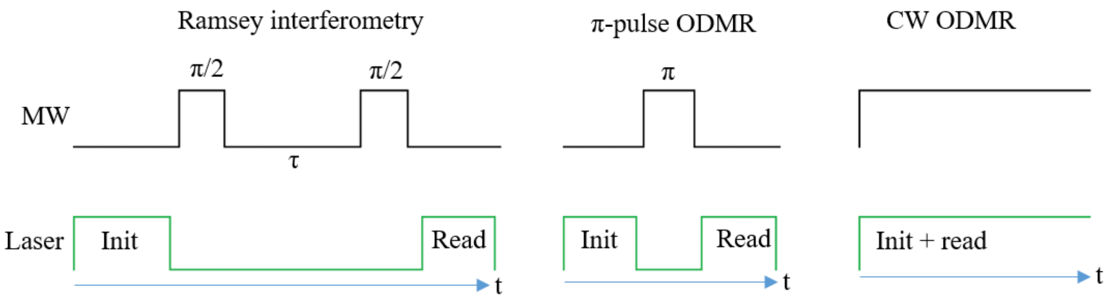

Figure 2.3: Simple sketch illustrating the application of laser light and MW for CW ODMR, π-pulse ODMR and Ramsey interferometry. CW ODMR is a continuous sensing scheme with constant application of MW and laser power, while the other two are pulsed schemes.

frequency. The constant laser illumination will continuously excite the NV center, leading to continuous emission of red fluorescence. The microwaves will drive the $|0\rangle \iff |1\rangle$ transition when they are resonant with the transition frequency. By plotting the measured fluorescence as a function of MW driving frequency, one will thus observe a drop in the fluorescence at the transition frequency. An example of a simulated CW ODMR spectrum where the transition frequency was 2.83 GHz is shown in Fig. 2.4.

In this way, the scheme can be used to determine the transition frequency for an arbitrary magnetic field. In both CW ODMR and the two other mentioned schemes, it is also common to consider the contrast between the fluorescence obtained from a given measurement and the fluorescence obtained when the MW drive is far off-resonance. This is due to the fact that the true quantity of interest is the relative change in fluorescence caused by the driving, rather than the absolute value of the fluorescence. A contrast plot will behave as the inverse of the corresponding fluorescence plot, peaking where the fluorescence drops, but the same measurement principles still apply. When using the CW ODMR scheme to perform magnetometry, the MW driving frequency is fixed at the position of the largest slope in fluorescence/contrast. Any additional external magnetic field will then shift the transition frequency by $m_S \gamma_e B$, which effectively shifts the entire ODMR feature up or down in frequency, leading to a measurable change in the fluorescence/contrast. The larger the slope in fluorescence/contrast at the fixed frequency, the greater the change in fluorescence/contrast caused by the addition of a particular external magnetic field. For a CW ODMR scheme, the maximum slope in fluorescence/contrast as a function of MW driving frequency is thus directly linked to the maximum achievable sensitivity.

The π-pulse ODMR scheme is the pulsed counterpart to the CW ODMR scheme. As illustrated in Fig. 2.3, it involves applying a laser pulse to initialize the NV center in state $|0\rangle$, followed by the application of a MW π-pulse at a certain driving

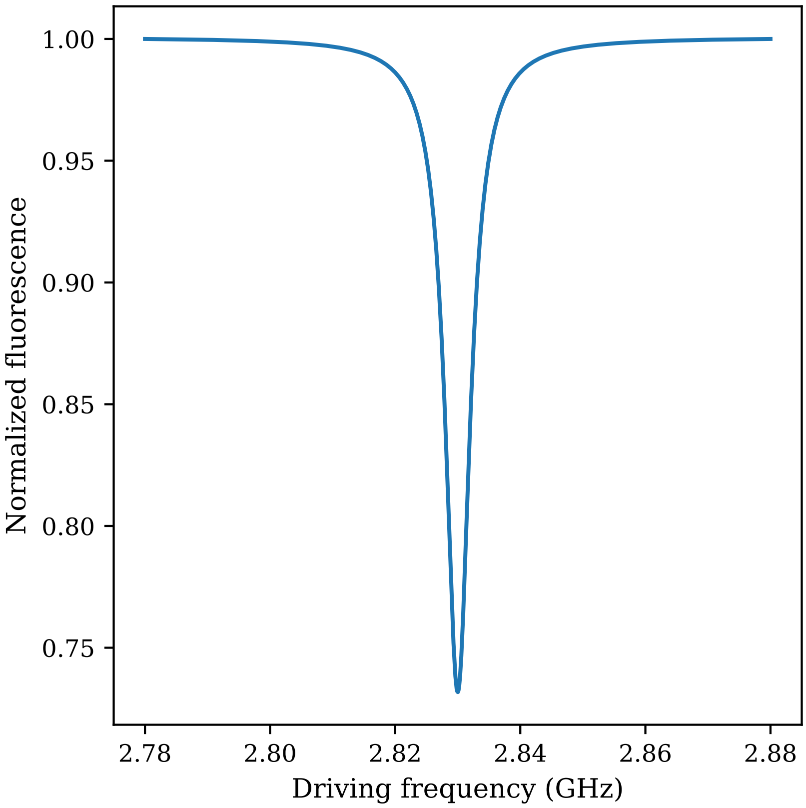

Figure 2.4: An example of a simulated CW ODMR spectrum where the transition frequency is 2.83 GHz. The fluorescence has been normalized to be 1 in the off-resonant case.

frequency, before using a second laser pulse to measure the resulting spin state-dependent fluorescence. This is repeated while varying the MW driving frequency. The π-pulse will only properly invert the electron spin state population to $|1\rangle$ if it is applied on-resonance. When plotting the measured fluorescence as a function of the driving frequency, one will thus observe a drop in the fluorescence at the transition frequency, as was the case for CW ODMR. Conversely, the contrast will be observed to peak at the transition frequency. The principles of magnetometry with π-pulse ODMR are the same as those for CW ODMR.

Ramsey interferometry utilizes somewhat different principles than the ODMR schemes. As is illustrated in Fig. 2.3, the scheme involves applying a laser pulse to initialize the NV center in state $|0\rangle$, followed by the application of a slightly off-resonant MW $\pi/2$-pulse then turning off both MW and laser for a time τ, before applying another MW $\pi/2$-pulse and finally using a second laser pulse to measure the resulting fluorescence/contrast. This is repeated while varying the time τ, which is called the free precession time in this context. The first $\pi/2$-pulse transfers the initialized spin state to the superposition $\frac{1}{\sqrt{2}}(|0\rangle + |1\rangle)$. The spin state will then undergo precession around the z-axis of the Bloch sphere at a frequency equal to the transition frequency for the duration of the free precession time τ, hence the name. The precession leads to the acquisition of a phase $\phi(\tau)$, transforming the spin state into $\frac{1}{\sqrt{2}}(|0\rangle + \mathrm{e}^{i\phi(\tau)}\,|1\rangle)$. The acquired phase is converted into a change in spin state population by the second $\pi/2$-pulse. For instance, if $\phi(\tau) = \pi$, the final spin state will be $|0\rangle$, whereas if $\phi(\tau) = 2\pi n$ with integer n, the final spin state will be $|1\rangle$. The resulting spin state-dependent fluorescence is measured using the second laser pulse. When plotting the measured fluorescence/contrast as a function of the free precession time τ, one will thus observe an oscillation in the fluorescence/contrast as a function of τ. It is common to consider these Ramsey fringes in a rotating frame rotating at the MW driving frequency, such that the Ramsey oscillation frequency becomes equal to the detuning between the transition frequency and the MW driving frequency. The degree of detuning used is a compromise between the desire for multiple clear fringes, and the fact that the performance of the $\pi/2$-pulses is degraded the further off-resonance they are.

If the total magnetic field affecting the NV center contains random noise fluctuations, the phase acquisition during τ will also contain random noise fluctuations, given that the magnetic field affects the transition frequency. This effect leads to a dephasing of the spin precession and ultimately a loss of coherence, which causes the Ramsey signal to decay $\propto \exp\left(-\left(\tau/T_2^*\right)^2\right)$ on a time-scale T_2^* referred to as the free dephasing time [28]. Dephasing also affects Rabi and ODMR measurements, though it is more readily apparent in Ramsey interferometry measurements.

Performing magnetometry with Ramsey interferometry involves repeated measurements with a fixed value of τ. The presence of an additional external magnetic field will change the transition frequency and hence the detuning between transition frequency and MW driving frequency by $m_S\gamma_e B$, which changes the Ramsey oscillation frequency. An additional external magnetic field B will thus cause the Ramsey fringes to become compressed or stretched in time, which leads to a measurable oscillation in the fluorescence/contrast at a fixed $\tau \neq 0$ as a function of B. It is the maximum slope in this oscillation that is linked to the maximum achievable sensitivity of Ramsey interferometry. The change in the Ramsey fringes caused by an additional external magnetic field B is illustrated in Fig. 2.5(a), and the Ramsey contrast oscillation as a function of B for fixed τ is illustrated in Fig. 2.5(b).

The choice of the optimal τ for such a magnetometry scheme is a compromise between two competing effects. The effect of dephasing causes the Ramsey signal to decay with increasing τ, thereby causing the maximum slope as a function of B to decrease with increasing τ. On the other hand, the change in total acquired phase caused by an additional external magnetic field $B(t)$ is given by

$$\Delta\phi(\tau) = 2\pi\gamma_e \int_0^\tau B(t)\,\mathrm{d}t. \tag{2.1}$$

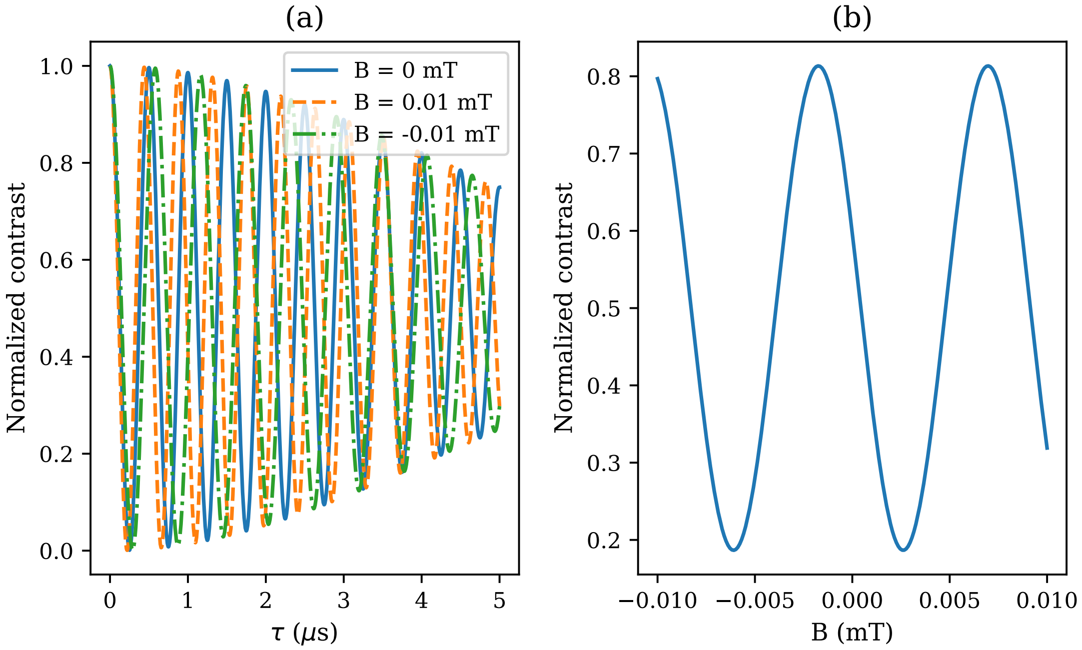

Figure 2.5: (a) Examples of simulated Ramsey interferometry contrast values as a function of τ for three different values of the additional external magnetic field B. The measurements represent a situation where $T_2^* = 6\,\mu\text{s}$ and the detuning between the transition frequency and the MW driving frequency is $\Delta = 2\pi \cdot 2\,\text{MHz}$ for $B = 0$. The contrast has been normalized to lie between 0 and 1. (b) Ramsey interferometry contrast values as a function of B for fixed $\tau = 4.1\,\mu\text{s}$ for the same situation as in (a).

A given static external magnetic field B will thus cause a greater change in the acquired phase for greater τ-values, thereby causing the maximum slope as a function of B to increase with increasing τ.

2.3 Ensemble considerations

So far, we've only considered the use of a single NV center for magnetometry. In many cases, however, it is advantageous to work with a large ensemble of NV centers because the sensitivity scales as $1/\sqrt{N}$ with the number of NV centers N in the ultimately shot-noise limited regime [28]. Using an NV ensemble does yield lower spatial resolution than a single NV center, but when this is not a concern, ensembles are preferable. All of the previously described theory and methods still apply when working with an NV ensemble, but several additional complications arise due to ensemble effects.

For one, all four possible crystallographic orientations of the NV center are equally likely, meaning that an NV ensemble will consist of an equal mixture of NVs with each of the possible axes. As such, it is only possible to align an external magnetic field along the axis of 1/4 of the NVs in an ensemble, which reduces the effective ensemble size. Given that the four possible NV axes exhibit $mathrmC_{3v}$ symmetry due to the crystal structure of diamond, the 3 axes that are not parallel to the field will all experience the same magnitude of the magnetic field projection along their axis. The ODMR spectrum for an NV ensemble where the bias field has been aligned along one NV axis will thus contain four features; two for $m_S = 1$ and $m_S = -1$ of the NVs with the chosen axis, and two for $m_S = 1$ and $m_S = -1$ of the NVs with the remaining three axes. However, the symmetric behavior is lost if the field is not perfectly aligned with one axis, and the magnetic field projection along the other three axes is only a fraction of the full magnetic field. Furthermore, the presence of a significant static magnetic field component perpendicular to their axes will introduce state mixing for the NVs with the other three axes, which is generally undesirable [23, 40, 41]. As a result, it is common to only work with the single NV axis that the bias field has been aligned with, such that the effective ensemble size indeed becomes 1/4 of the total ensemble size.

Furthermore, the previously mentioned hyperfine interaction has greater significance for NV ensembles. If the nuclear spins are in a thermal state, all of the possible nuclear spin states m_I will be equally represented in the ensemble. Given that the frequency shift caused by the hyperfine interaction is $m_I\delta_I$, the hyperfine interaction will thus effectively divide the NV ensemble into three (two for ^{15}N) groups with their $m_S = 1$ or $m_S = -1$ states split in frequency by $\delta_I = 2.16\,\text{MHz}$ ($\delta_I = 3.03\,\text{MHz}$ for ^{15}N). The $m_S = 0 \iff m_S = 1$ and $m_S = 0 \iff m_S = -1$ transitions are thereby each split into multiple hyperfine transitions also separated by δ_I. These transitions are reflected in ODMR spectra and can complicate the dynamics of NV magnetometry schemes. The accompanying issues can be avoided by polarizing the nitrogen nuclear spins in order to suppress the hyperfine splitting [47] or by using a multi-frequency MW driving scheme to drive all of the hyperfine transitions simultaneously.

The transition frequencies of NVs in an ensemble are also affected by differences in their local environment caused by e.g. strain variations or gradients in the bias field [24]. If the z-axis is chosen to lie along the NV axis, the effects of strain on the evolution of an NV center can be described by the Hamiltonian

$$\mathcal{H}_{strain} = E_x(S_x^2 - S_y^2) + E_y(S_xS_y + S_yS_x), \tag{2.2}$$

where E_x (E_y) is the strain along the x (y) direction, and the spin matrices are given by

$$S_x = \frac{\hbar}{\sqrt{2}}\begin{pmatrix} 0 & 1 & 0 \\ 1 & 0 & 1 \\ 0 & 1 & 0 \end{pmatrix},\; S_y = \frac{i\hbar}{\sqrt{2}}\begin{pmatrix} 0 & -1 & 0 \\ 1 & 0 & -1 \\ 0 & 1 & 0 \end{pmatrix},\; S_z = \hbar\begin{pmatrix} 1 & 0 & 0 \\ 0 & 0 & 0 \\ 0 & 0 & -1 \end{pmatrix}. \tag{2.3}$$

This formalism necessarily considers the NV center spin as a three-level system with $m_S = 0, -1, 1$ all included. Gradients in the bias field affect the transition

frequencies via the Zeeman effect. The differences in transition frequency across an ensemble caused by these effects are collectively referred to as inhomogeneous broadening. The consequence of such inhomogeneous broadening is that it becomes challenging for a single-frequency MW drive to be on-resonance with all of the NV centers in an ensemble. Given that the performance of flat MW pulses degrades the further off-resonance the pulses are applied, this effectively makes it difficult to properly control an inhomogeneously broadened ensemble, which negatively affects the various measurement schemes and reduces the achievable sensitivity.
In addition to the issues caused by inhomogeneous broadening, the amplitude of the MW driving field can vary across the ensemble if the antenna used to deliver the microwaves is not capable of providing a perfectly uniform MW field. This effectively causes the Rabi frequency to vary between different NV centers in the ensemble, meaning that the correct pulse duration for e.g. a $\pi/2$-pulse will differ between different NV centers in the ensemble. Seeing as the applied pulse must have a single duration, such drive amplitude variations will thus cause some NV centers to undergo more or less than the desired rotation, which further degrades the possible control over the ensemble and reduces the achievable sensitivity.

Ideally, one would simply use high-quality diamonds with low or zero inhomogeneous broadening and MW antennas capable of delivering uniform MW fields, but this is not always practical. While it is possible to fabricate diamonds with near-zero inhomogeneous broadening [43], such diamonds are complicated and expensive to fabricate and are not broadly available. The design and manufacture of MW antennas capable of delivering uniform MW fields is also a focus of active research, but the existing designs are only able to ensure field uniformity over areas significantly smaller than a typical diamond [48, 49]. As an alternative to eliminating the sources of inhomogeneous broadening and drive amplitude variations, various methods can be used to compensate for their effects. One such method that I explored is the use of optimal control theory [50–56] to design shaped MW pulses that are robust against the effects of inhomogeneous broadening and drive amplitude variations.

2.4 Optimal control theory

The general principle behind optimal control theory is relatively simple. It involves defining a performance functional $\mathcal{F}$ that describes how well a given set of control functions achieve the desired purpose, and then optimizing the control functions to maximize or minimize the performance functional subject to relevant restraints [50, 51, 53–55]. As a result, optimal control theory can be applied to many different types of problems both classical and quantum. Furthermore, while the derivations in this section are based on the NV center, they are, in fact, general and could be applied to any other defect center with a similar level structure by changing the defect-specific parameters. In the case of quantum optimal control of NV electron spin states, the control functions describe the shaped MW pulse, and two different performance functionals are commonly considered. Note that these functionals and all of the expressions to be derived only relate to a single NV, denoted i. The approach used to consider an ensemble and achieve robustness against inhomogeneous broadening and drive amplitude variations will be explained once the relevant single NV expressions have been derived.

The two most commonly considered performance functionals are the state transfer functional $\mathcal{F}_{st}$, which describes how well the shaped MW pulse transfers the NV electron spin state from a certain initial state $|\psi_{init}\rangle$ to a targeted final state $|\psi_f\rangle$, and the operator functional $\mathcal{F}_{op}$, which describes how well the shaped MW pulse implements a desired unitary operation $\hat{U}_f$ on the NV electron spin state [52–54]. The functionals are defined as

$$\mathcal{F}_{st} = \left| \langle \psi_f | \, \hat{U}(t_p) \, | \psi_{init} \rangle \right|^2 , \tag{2.4}$$

$$\mathcal{F}_{op} = \mathrm{Re} \left[\mathrm{Tr} \left(\hat{U}(t_p) \hat{U}_f^\dagger \right) \right] /2, \tag{2.5}$$

where $\hat{U}(t_p)$ is a unitary time evolution operator describing the influence of the shaped MW pulse, and t_p is the pulse duration. Note that the states used for the calculation of $\mathcal{F}_{st}$ should obey the standard normalization $\langle \psi | \psi \rangle = 1$. The value of these functionals is also referred to as the fidelity and will at most be 1 when the shaped MW pulse perfectly achieves its intended purpose. The closer the fidelity is to 1, the better the shaped MW pulse achieves the intended purpose. Shaped MW pulses obtained using $\mathcal{F}_{st}$ are typically called state transfer pulses, and pulses obtained using $\mathcal{F}_{op}$ are typically called unitary rotation pulses. The design and use of state transfer pulses will naturally only work as intended for situations where the initial state $|\psi_{init}\rangle$ is known, e.g. after initialization of the NV electron spin state. Unitary rotation pulses, on the other hand, are designed with the goal of implementing the desired rotation regardless of the initial state. However, when they are applicable, state transfer pulses generally perform better than equivalent unitary rotation pulses [53, 54]. I primarily consider state transfer pulses.

The goal of the optimization procedure is to find the MW pulse-shape, as described by the control functions, that maximizes the fidelity of the desired performance functional subject to relevant restraints, such as limits on the maximum or total MW power. However, even when subject to such restraints, the space of all possible functions is infinite and impractical to search through. As such, it is common to limit the MW pulse-shape to a certain basis in order to simplify the optimization. The choice of basis and exact method of optimization characterizes the many existing types of optimal control theory used for shaped pulse design. One of the more frequently used types of optimal control theory is gradient ascent pulse engineering (GRAPE) [50, 56–59], which involves the use of a basis consisting of piecewise constant functions of time. The control parameters to be optimized are then the amplitudes of these functions and possibly also the

total pulse duration. The optimization is performed by calculating the gradient of the used functional with respect to the control parameters and then updating the parameters by stepping along the gradient. This is repeated until convergence is achieved. The basis used for GRAPE allows for efficient calculation of the necessary gradients, which leads to fast and effective optimization procedures, but the resulting pulse-shapes often contain high-frequency components [52, 53].
In my work, I chose to focus on a different type of optimal control theory known as smooth optimal control [52–54, 56], which involves the use of a basis consisting of sine functions with a fundamental frequency given by the pulse duration. The resulting smooth MW pulses have the general form

$$S(t) = I(t)\cos(\omega_{MW}t) + Q(t)\sin(\omega_{MW}t), \tag{2.6}$$

where the in-phase and quadrature components are given by

$$I(t) = \sum_{j=1}^{N_f} 2a_{jx}\sin(j\Omega_f t),\ Q(t) = \sum_{j=1}^{N_f} 2a_{jy}\sin(j\Omega_f t), \tag{2.7}$$

ω_{MW} is the central driving frequency, N_f is the number of frequency components, and $\Omega_f = \frac{2\pi}{2t_p}$ is the fundamental frequency. It has been previously shown [53] that the performance of smooth MW pulses improves with increasing N_f until it saturates for $N_f \geq 7$. I chose to work with $N_f = 10$ for all of my pulses in order to ensure that they were in the saturated regime. The control parameters to be optimized are then the 20 amplitudes a_{jk} of the individual sine functions, which are given in units of radial frequency. As with GRAPE, the optimization is performed by calculating the gradient of the functional with respect to the control parameters and updating the parameters by stepping along the gradient. Given that there are 20 control parameters, the optimization thus involves stepping along the gradient in a 20-dimensional space, which can be hard to visualize. The main benefits to using smooth optimal control are that the resulting MW pulses are smooth, hence the name, and their bandwidth and frequency components are known in advance so long as the pulse duration is kept fixed as an input. The frequency components will be $f_j = j\Omega_f$ for $j = 1..N_f$, and the bandwidth will be $N_f\Omega_f$. These aspects ease the experimental implementation of smooth optimal control pulses.

In order to perform the optimization, it is thus necessary to obtain expressions for the unitary time evolution operator $\hat{U}(t_p)$ and the gradient of the functional with respect to the control parameters $\frac{\partial\mathcal{F}}{\partial a_{jk}}$. Given that $\hat{U}(t_p)$ is the only term in both of the mentioned functionals that depends on the control parameters a_{jk}, the calculation of the functional gradient mainly involves calculating $\frac{\partial\hat{U}(t_p)}{\partial a_{jk}}$. The functional gradients can be determined directly to be

$$\frac{\partial\mathcal{F}_{st}}{\partial a_{jk}} = 2\mathrm{Re}\left(\langle\psi_f|\frac{\partial\hat{U}(t_p)}{\partial a_{jk}}|\psi_{init}\rangle\langle\psi_{init}|\hat{U}^\dagger(t_p)|\psi_f\rangle\right) \tag{2.8}$$

and

$$\frac{\partial \mathcal{F}_{op}}{\partial a_{jk}} = \mathrm{Re}\left[\mathrm{Tr}\left(\frac{\partial \hat{U}(t_p)}{\partial a_{jk}}\hat{U}_f^\dagger\right)\right]/2 \tag{2.9}$$

via standard derivation methods.
In order to obtain an expression for the time evolution operator $\hat{U}(t_p)$, it is necessary to consider how the NV electron spin state evolves under the influence of the MW drive. The evolution of the NV spin state $|\psi\rangle$ can, in general, be described by the Schrödinger equation

$$i\frac{\partial}{\partial t}|\psi\rangle = \hat{\mathcal{H}}(t)|\psi\rangle, \tag{2.10}$$

where $\hbar$ has been set equal to one with the Hamiltonian

$$\hat{\mathcal{H}}(t) = \hat{\mathcal{H}}_0 + \hat{\mathcal{H}}_c(t) \tag{2.11}$$

consisting of a time-independent drift term $\hat{\mathcal{H}}_0$ that describes the drive-independent evolution of the spin state and a time-dependent control term $\hat{\mathcal{H}}_c(t)$ that describes the contribution of the MW drive to the spin state evolution. When considering the previously mentioned effective two-level system consisting of either the $m_S = 0 \Longleftrightarrow m_S = 1$ or the $m_S = 0 \Longleftrightarrow m_S = -1$ transition, the two Hamiltonian terms can be written as

$$\hat{\mathcal{H}}_0 = \frac{\omega_0}{2}\sigma_z,\ \hat{\mathcal{H}}_c(t) = \sigma_x S(t) \tag{2.12}$$

and

$$\hat{\mathcal{H}}(t) = \frac{\omega_0}{2}\sigma_z + \sigma_x\left(I(t)\cos(\omega_{MW}t) + Q(t)\sin(\omega_{MW}t)\right), \tag{2.13}$$

where $\hbar = 1$, ω_0 is the transition frequency, $S(t)$ is given in units of radial frequency, and σ_x, σ_z are the standard Pauli spin-matrices. This representation assumes that the z-direction is defined by the NV axis and that the MW field is linearly polarized in a direction perpendicular to the NV axis, here chosen to be the x-direction.
The later calculations can be simplified by moving to a rotating frame rotating at the driving frequency ω_{MW}. To this end, a unitary rotation operator $\hat{R}$ is introduced.

$$\hat{R} = \mathrm{e}^{i\omega_{MW}t\sigma_z/2} \tag{2.14}$$

The Schrödinger equation is rewritten in the frame defined by $\hat{R}$ in order to obtain

$$i\frac{\partial}{\partial t}|\psi'\rangle = \hat{\mathcal{H}}'(t)|\psi'\rangle, \tag{2.15}$$

where $|\psi'\rangle = \hat{R}|\psi\rangle$ and $\hat{\mathcal{H}}'(t) = \hat{R}\hat{\mathcal{H}}(t)\hat{R}^\dagger + i\frac{\partial\hat{R}}{\partial t}\hat{R}^\dagger$ with $i\frac{\partial\hat{R}}{\partial t}\hat{R}^\dagger = -\frac{\omega_{MW}}{2}\sigma_z$. The first term in $\hat{\mathcal{H}}'(t)$ can be expanded to get

$$\begin{aligned}\hat{R}\hat{\mathcal{H}}(t)\hat{R}^\dagger &= \hat{R}(\hat{\mathcal{H}}_0 + \hat{\mathcal{H}}_c(t))\hat{R}^\dagger = \hat{\mathcal{H}}_0 + \hat{R}\hat{\mathcal{H}}_c(t)\hat{R}^\dagger\\ &= \frac{\omega_0}{2}\sigma_z + \mathrm{e}^{i\omega_{MW}t\sigma_z/2}\sigma_x\left[I(t)\cos(\omega_{MW}t) + Q(t)\sin(\omega_{MW}t)\right]\mathrm{e}^{-i\omega_{MW}t\sigma_z/2}\end{aligned} \tag{2.16}$$

by noting that σ_z naturally commutes with itself. The expression can be simplified by utilizing the Baker-Campbell-Hausdorff lemma

$$\begin{aligned} \mathrm{e}^{i\omega_{MW}t\sigma_z/2}\sigma_x\mathrm{e}^{-i\omega_{MW}t\sigma_z/2} = \sigma_x + \frac{-i\omega_{MW}t}{2}\left[\sigma_z,\sigma_x\right] \\ + \left(\frac{-i\omega_{MW}t}{2}\right)^2 \frac{1}{2!}\left[\sigma_z,\left[\sigma_z,\sigma_x\right]\right] + ..., \end{aligned} \tag{2.17}$$

the commutators for Pauli spin matrices

$$[\sigma_z,\sigma_x] = 2i\sigma_y,\ [\sigma_z,\sigma_y] = -2i\sigma_x, \tag{2.18}$$

and the Taylor expansions of sine and cosine functions around $t = 0$.

$$\sin(ft) = ft - (ft)^3/3! + ...;\ \cos(ft) = 1 - (ft)^2/2! + ... \tag{2.19}$$

Combining these relations allows one to write

$$\mathrm{e}^{i\omega_{MW}t\sigma_z/2}\sigma_x\mathrm{e}^{-i\omega_{MW}t\sigma_z/2} = \sigma_x\cos(\omega_{MW}t) + \sigma_y\sin(\omega_{MW}t) \tag{2.20}$$

and thus

$$\begin{aligned} \hat{R}\hat{\mathcal{H}}(t)\hat{R}^\dagger = \frac{\omega_0}{2}\sigma_z + (\sigma_x\cos(\omega_{MW}t) + \sigma_y\sin(\omega_{MW}t)) \\ \cdot\left(I(t)\cos(\omega_{MW}t) + Q(t)\sin(\omega_{MW}t)\right), \end{aligned} \tag{2.21}$$

which can be expanded to

$$\begin{aligned} \hat{R}\hat{\mathcal{H}}(t)\hat{R}^\dagger = \frac{\omega_0}{2}\sigma_z + \frac{I(t)}{2}\sigma_x[1+\cos(2\omega_{MW}t)] + \frac{Q(t)}{2}\sigma_x\sin(2\omega_{MW}t) \\ + \frac{I(t)}{2}\sigma_y\sin(2\omega_{MW}t) + \frac{Q(t)}{2}\sigma_y[1-\cos(2\omega_{MW}t)] \end{aligned} \tag{2.22}$$

via the use of trigonometric identities. Utilizing the rotating wave approximation to get rid of the rapidly oscillating terms $\cos(2\omega_{MW}t)$, $\sin(2\omega_{MW}t)$ simplifies the expression to

$$\hat{R}\hat{\mathcal{H}}(t)\hat{R}^\dagger = \frac{\omega_0}{2}\sigma_z + \frac{I(t)}{2}\sigma_x + \frac{Q(t)}{2}\sigma_y, \tag{2.23}$$

which allows the full Hamiltonian in the rotating frame to be written as

$$\hat{\mathcal{H}}'(t) = \frac{\Delta_i}{2}\sigma_z + \frac{I(t)}{2}\sigma_x + \frac{Q(t)}{2}\sigma_y, \tag{2.24}$$

where $\Delta_i = \omega_0 - \omega_{MW}$ is the detuning between the transition frequency ω_0 and the driving frequency ω_{MW} for a single NV. Eq. 2.24 makes it clear that the in-phase $I(t)$ and quadrature $Q(t)$ components of the shaped MW pulse rotate the NV electron spin state around the x- and y-axis of the Bloch sphere, respectively. In the optimization algorithm, $I(t)$ and $Q(t)$ further represent the Rabi frequency of the rotation around their respective axis at a given time t, which is the reason for the radial frequency units. These observations further make it clear that a flat MW pulse is simply a special case of an optimal control pulse where $I(t) = \Omega_R$ and $Q(t) = 0$ for all t during the pulse duration.

As is also clear from Eq. 2.24 and the definitions in Eq. 2.7, the choice of basis for smooth optimal control has made the total Hamiltonian periodic with periodicity $T = 2t_p$, which allows us to use Floquet theory to solve the Schrödinger equation.

2.4.1 Floquet theory for smooth optimal control

According to Floquet's theorem [52, 53, 60], a time-periodic Hamiltonian will yield a complete set of solutions to the Schrödinger equation of the form

$$|\psi_k(t)\rangle = \mathrm{e}^{-i\epsilon_k t} |\Phi_k(t)\rangle \tag{2.25}$$

where $|\Phi_k(t)\rangle = |\Phi_k(t+T)\rangle$ is a time-periodic eigenstate of the Floquet eigenvalue problem

$$\mathcal{K} |\Phi_k(t)\rangle = \epsilon_k |\Phi_k(t)\rangle \,,\ \mathcal{K} = \hat{\mathcal{H}}(t) - i\frac{\partial}{\partial t} \tag{2.26}$$

with the corresponding quasi-energy ϵ_k. One uses the term quasi-energy to distinguish from the actual energies obtained as eigenvalues of the Hamiltonian. The actual energies have physical meaning, whereas the Floquet quasi-energies do not. We thus need to solve the Floquet eigenvalue problem in order to obtain solutions to the Schrödinger equation. This is easier to do in Fourier space. To this end, the Floquet eigenstates $|\Phi_k(t)\rangle$ are rewritten as a Fourier series

$$|\Phi_k(t)\rangle = \sum_{v=-\infty}^{\infty} \mathrm{e}^{iv\Omega_f t} |\phi_{kv}\rangle \tag{2.27}$$

and the Fourier coefficients of the Hamiltonian are defined as

$$\hat{\mathcal{H}}_n = \frac{1}{T}\int_0^T \mathrm{e}^{-in\Omega_f t}\hat{\mathcal{H}}(t)\,\mathrm{d}t. \tag{2.28}$$

Eq. 2.27 is inserted in Eq. 2.26, both sides are multiplied by $\mathrm{e}^{-iu\Omega_f t}$ and integrated from $t=0$ to $t=T$ in order to obtain

$$\frac{1}{T}\int_0^T \mathrm{d}t\mathrm{e}^{-iu\Omega_f t}\left(\hat{\mathcal{H}}(t) - i\frac{\partial}{\partial t}\right)\sum_{v=-\infty}^{\infty} \mathrm{e}^{iv\Omega_f t}|\phi_{kv}\rangle = \frac{\epsilon_k}{T}\int_0^T \mathrm{d}t\mathrm{e}^{-iu\Omega_f t}\sum_{v=-\infty}^{\infty}\mathrm{e}^{iv\Omega_f t}|\phi_{kv}\rangle\,. \tag{2.29}$$

By utilizing the exponential form of the Kronecker delta, $\delta_{n,m} = \frac{1}{2\pi}\int_0^{2\pi} \mathrm{e}^{i(n-m)\varphi}\mathrm{d}\varphi$, Eq. 2.29 reduces to

$$\sum_{v=-\infty}^{\infty}\frac{1}{T}\int_0^T \mathrm{d}t\left(\mathrm{e}^{-i(u-v)\Omega_f t}\hat{\mathcal{H}}(t) + v\Omega_f \mathrm{e}^{i(v-u)\Omega_f t}\right)|\phi_{kv}\rangle = \epsilon_k |\phi_{ku}\rangle\,, \tag{2.30}$$

which further reduces to

$$u\Omega_f |\phi_{ku}\rangle + \sum_{v=-\infty}^{\infty}\hat{\mathcal{H}}_{u-v}|\phi_{kv}\rangle = \epsilon_k|\phi_{ku}\rangle \tag{2.31}$$

by again utilizing the exponential form of the Kronecker delta and the expression for the Fourier coefficients of the Hamiltonian (Eq. 2.28). Finding solutions to Eq. 2.31 is equivalent to finding solutions to the eigenvalue problem

$$\tilde{\mathcal{K}}\left|\tilde{\phi}_k\right\rangle = \epsilon_k\left|\tilde{\phi}_k\right\rangle \tag{2.32}$$

where $\left|\tilde{\phi}_k\right\rangle = (..., \left|\phi_{k,-1}\right\rangle, \left|\phi_{k,0}\right\rangle, \left|\phi_{k,1}\right\rangle, ...)^T$, $\hat{I}$ is the identity operator and

$$\tilde{\mathcal{K}} = \begin{pmatrix} \ddots & \ddots & & & \\ \ddots & \hat{\mathcal{H}}_0 - \hat{I}\Omega_f & \hat{\mathcal{H}}_{-1} & \hat{\mathcal{H}}_{-2} & \\ ... & \hat{\mathcal{H}}_1 & \hat{\mathcal{H}}_0 & \hat{\mathcal{H}}_{-1} & ... \\ & \hat{\mathcal{H}}_2 & \hat{\mathcal{H}}_1 & \hat{\mathcal{H}}_0 + \hat{I}\Omega_f & \ddots \\ & & & \ddots & \ddots \end{pmatrix} \tag{2.33}$$

is the infinite-dimensional Floquet matrix. The main difference between Eq. 2.26 and Eq. 2.32 is that the shift to Fourier space has made the problem in Eq. 2.32 time-independent. The problem has thus been changed from solving the differential Schrödinger equation to diagonalizing the $\tilde{\mathcal{K}}$ matrix. Note that the individual Fourier coefficients $\hat{\mathcal{H}}_n$ are themselves $d \times d$ matrices where d is the dimension of the configuration space. For the effective two-level system with the Hamiltonian shown in Eq. 2.24, $d = 2$. The exact form of the Fourier coefficients can be determined by inserting Eq. 2.24 into Eq. 2.28. Doing so yields

$$\hat{\mathcal{H}}_n = \frac{1}{T}\int_0^T \mathrm{e}^{-in\Omega_f t}\left(\frac{\Delta_i}{2}\sigma_z + \frac{I(t)}{2}\sigma_x + \frac{Q(t)}{2}\sigma_y\right)\mathrm{d}t, \tag{2.34}$$

which can be expanded by using the definitions of $I(t)$ and $Q(t)$ in Eq. 2.7.

$$\hat{\mathcal{H}}_n = \frac{1}{T}\int_0^T \mathrm{e}^{-in\Omega_f t}\left(\frac{\Delta_i}{2}\sigma_z + \sum_{j=1}^{N_f}\left[a_{jx}\sigma_x + a_{jy}\sigma_y\right]\sin(j\Omega_f t)\right)\mathrm{d}t \tag{2.35}$$

Using the exponential form of a sine $\sin(ft) = 1/(2i)\left[\mathrm{e}^{ift} - \mathrm{e}^{-ift}\right]$ and the exponential form of the Kronecker delta, the expression can be rewritten as

$$\hat{\mathcal{H}}_n = \frac{\Delta_i}{2}\sigma_z\delta_{n,0} - \frac{i}{2}\sum_{j=1}^{N_f}\left[a_{jx}\sigma_x + a_{jy}\sigma_y\right](\delta_{n,j} - \delta_{n,-j}) \tag{2.36}$$

The effects of drive amplitude variations are included by multiplying the control amplitudes a_{jk} by the relative control amplitude α_i, which represents the ratio between the actual Rabi frequency experienced by the single NV and the intended Rabi frequency. The final expression for the Fourier coefficients of the Hamiltonian thus becomes

$$\hat{\mathcal{H}}_n = \frac{\Delta_i}{2}\sigma_z\delta_{n,0} - \frac{i}{2}\sum_{j=1}^{N_f}\alpha_i\left[a_{jx}\sigma_x + a_{jy}\sigma_y\right](\delta_{n,j} - \delta_{n,-j}), \tag{2.37}$$

which is used to obtain the 2×2 matrix elements of $\tilde{\mathcal{K}}$. As an example, $\hat{\mathcal{H}}_{-1}$, $\hat{\mathcal{H}}_0$, $\hat{\mathcal{H}}_1$ are given in Eq. 2.38 for a single NV with Δ_i and α_i.

$$\begin{gathered} \hat{\mathcal{H}}_{-1} = \begin{pmatrix} 0 & \frac{\alpha_i}{2}(ia_{1x} + a_{1y}) \\ \frac{\alpha_i}{2}(ia_{1x} - a_{1y}) & 0 \end{pmatrix}, \hat{\mathcal{H}}_0 = \begin{pmatrix} \frac{\Delta_i}{2} & 0 \\ 0 & -\frac{\Delta_i}{2} \end{pmatrix}, \\ \hat{\mathcal{H}}_1 = \begin{pmatrix} 0 & -\frac{\alpha_i}{2}(ia_{1x} + a_{1y}) \\ -\frac{\alpha_i}{2}(ia_{1x} - a_{1y}) & 0 \end{pmatrix} \end{gathered} \tag{2.38}$$

The $\tilde{\mathcal{K}}$ matrix is infinite, but in reality one can only use a finite number of frequencies to control the system. As a result, far-off diagonal elements will be negligible compared to the diagonal elements, i.e. $|\tilde{\mathcal{K}}_{ii} - \tilde{\mathcal{K}}_{jj}| \gg |\tilde{\mathcal{K}}_{ij}|$ for large $i - j$, and the eigenvectors and eigenvalues of $\tilde{\mathcal{K}}$ can be well-approximated by those of a finite truncated version $\tilde{\mathcal{K}}_{trunc}$. By utilizing symmetry principles, it is further possible to construct all of the eigenvectors and eigenvalues from a very limited set of eigenvalues and eigenvectors. The Floquet matrix $\tilde{\mathcal{K}}$ will satisfy the relation $\hat{S}\tilde{\mathcal{K}}\hat{S}^\dagger = \tilde{\mathcal{K}} + \hat{I}\Omega_f$, where $\hat{S}$ has the effect of shifting the elements of $\left|\tilde{\phi}_k\right\rangle$ by one. In other words, $(\hat{S}\left|\tilde{\phi}_k\right\rangle)_v = (\left|\tilde{\phi}_k\right\rangle)_{v+1}$. As such, the vector $\hat{S}^m\left|\tilde{\phi}_k\right\rangle$ will be an eigenvector of $\tilde{\mathcal{K}}$ for any integer m if $\left|\tilde{\phi}_k\right\rangle$ is itself an eigenvector. If $\left|\tilde{\phi}_k\right\rangle$ is an eigenvector to the eigenvalue ϵ_k then $\hat{S}^m\left|\tilde{\phi}_k\right\rangle$ will be an eigenvector to the eigenvalue $\epsilon_k - m\Omega_f$. In this way, it is possible to construct all of the eigenvalues and eigenvectors by translation, provided we know the right d eigenvalues that fulfil the condition $(\epsilon_k - \epsilon_j)/\Omega_f \notin \mathcal{Z}$, $k \neq j$. The interval where these eigenvalues are found is also called a Brillouin zone, as in Bloch theory.

Having determined a way to obtain the eigenvalues and eigenvectors of $\tilde{\mathcal{K}}$, it is now possible to determine the time evolution of any state by expanding the state in the basis of steady states, with the time evolution given by the quasi-energies and Floquet eigenstates $|\Phi_k(t)\rangle$. As such, the time evolution operator $\hat{U}(t)$ can be written as

$$\begin{aligned}\hat{U}(t) &= \sum_{k=1}^{d} |\psi_k(t)\rangle\langle\psi_k(0)| = \sum_{k=1}^{d} \mathrm{e}^{-i\epsilon_k t}|\Phi_k(t)\rangle\langle\Phi_k(0)| \\ &= \sum_{k=1}^{d}\sum_{v=-\infty}^{\infty} \mathrm{e}^{i(v\Omega_f - \epsilon_k)t}|\phi_{kv}\rangle\langle\Phi_k(0)|\,.\end{aligned} \tag{2.39}$$

The sum over v is written as being infinite, but in reality one will only use as many terms as are needed to ensure a negligible error in the unitarity of $\hat{U}(t)$. The sum is always kept symmetric around $v = 0$ and determines the size of the truncated Floquet matrix.

An expression for the time evolution operator $\hat{U}(t)$ has now been determined, which was one of the requirements for performing the optimization with optimal control theory. An expression for the gradient of $\hat{U}(t)$ with respect to a_{jk} was also required. To this end, perturbation theory is applied to determine the gradient.

2.4.2 Perturbation theory with the Floquet operator

The derivative of $\hat{U}(t)$ with respect to the control amplitudes a_{jk}, which will also be referred to as a_l to avoid confusion, can be directly obtained from the previously defined expression for $\hat{U}(t)$.

$$\begin{aligned}\frac{\partial \hat{U}(t)}{\partial a_l} &= \frac{\partial}{\partial a_l}\sum_{k=1}^{d}\sum_{v=-\infty}^{\infty} \mathrm{e}^{i(v\Omega_f-\epsilon_k)t}\left|\phi_{kv}\right\rangle\left\langle\Phi_k(0)\right| \\ &= \sum_{k=1}^{d}\sum_{v=-\infty}^{\infty}\Big(-it\mathrm{e}^{i(v\Omega_f-\epsilon_k)t}\frac{\partial\epsilon_k}{\partial a_l}\left|\phi_{kv}\right\rangle\left\langle\Phi_k(0)\right| \\ &\quad + \mathrm{e}^{i(v\Omega_f-\epsilon_k)t}\frac{\partial\left|\phi_{kv}\right\rangle}{\partial a_l}\left\langle\Phi_k(0)\right| + \mathrm{e}^{i(v\Omega_f-\epsilon_k)t}\left|\phi_{kv}\right\rangle\sum_{u=-\infty}^{\infty}\frac{\partial\left\langle\phi_{ku}\right|}{\partial a_l}\end{aligned} \tag{2.40}$$

In order to utilize Eq. 2.40, we need expressions for $\frac{\partial\epsilon_k}{\partial a_l}$ and $\frac{\partial|\phi_{kv}\rangle}{\partial a_l}$. These will be obtained via perturbation theory. In the considered case, the perturbation can be a change in the MW driving field, and the response is a change in the NV electron spin state dynamics. Note, however, that the perturbation $\delta\vec{a}$ is a change in the control amplitudes $\vec{a} = (a_{1x}, a_{2x}, ..., a_{Nx}, a_{1y}, a_{2y}, ..., a_{Ny})$ and is therefore a vector. The control Hamiltonian $H_c(t)$ is linear in the control amplitudes and thus so is the Floquet operator $\tilde{\mathcal{K}}$.

$$\tilde{\mathcal{K}}(\vec{a}+\delta\vec{a}) = \tilde{\mathcal{K}}(\vec{a}) + \delta\vec{a}\cdot\tilde{\mathcal{K}}_{int},\ \tilde{\mathcal{K}}_{int} = \nabla_a\tilde{\mathcal{K}}|_{\vec{a}=\vec{0}} \tag{2.41}$$

Adding a small perturbation to the Floquet eigenvalue problem in Eq. 2.32 yields

$$(\tilde{\mathcal{K}}(\vec{a}) + \delta\vec{a}\cdot\tilde{\mathcal{K}}_{int})\left|\tilde{\phi}_k\right\rangle = \epsilon_k(\vec{a})\left|\tilde{\phi}_k\right\rangle. \tag{2.42}$$

Furthermore, one can expand the eigenvalues $\epsilon_k(\vec{a})$ and eigenstates $\left|\tilde{\phi}_k\right\rangle$ in the perturbation parameter $\delta\vec{a}$ in order to obtain

$$\epsilon_k(\vec{a}) = \epsilon_k^{(0)}(\vec{a}) + \delta\vec{a}\cdot\epsilon_k^{(1)}(\vec{a}) + \delta\vec{a}^2\cdot\epsilon_k^{(2)}(\vec{a}) + ... = \sum_{\lambda=0}^{\infty}\delta\vec{a}^{\lambda}\cdot\epsilon_k^{(\lambda)}(\vec{a}) \tag{2.43}$$

$$\left|\tilde{\phi}_k\right\rangle = \left|\tilde{\phi}_k^{(0)}\right\rangle + \delta\vec{a}\cdot\left|\tilde{\phi}_k^{(1)}\right\rangle + \delta\vec{a}^2\cdot\left|\tilde{\phi}_k^{(2)}\right\rangle + ... = \sum_{\lambda=0}^{\infty}\delta\vec{a}^{\lambda}\cdot\left|\tilde{\phi}_k^{(\lambda)}\right\rangle \tag{2.44}$$

The expansions are well approximated by the sum of the zeroth and first order terms, and the first order eigenvalue perturbations are simply given by the first order derivative of the eigenvalue with respect to $\vec{a}$.

$$\epsilon_k(\vec{a}+\delta\vec{a}) \approx \epsilon_k^{(0)}(\vec{a}) + \delta\vec{a}\cdot\epsilon_k^{(1)}(\vec{a}) = \epsilon_k^{(0)}(\vec{a}) + \delta\vec{a}\cdot\nabla_a\epsilon_k(\vec{a}) \tag{2.45}$$

The same is true of the higher order eigenvalue perturbations. Inserting the expansions of $\epsilon_k(\vec{a})$ and $\left|\tilde{\phi}_k\right\rangle$ in the perturbed Floquet eigenvalue problem (Eq. 2.42) yields the expression

$$(\tilde{\mathcal{K}}(\vec{a}) + \delta\vec{a}\cdot\tilde{\mathcal{K}}_{int})\sum_{\lambda=0}^{\infty}\delta\vec{a}^{\lambda}\cdot\left|\tilde{\phi}_k^{(\lambda)}\right\rangle = \sum_{\lambda=0}^{\infty}\delta\vec{a}^{\lambda}\cdot\epsilon_k^{(\lambda)}(\vec{a})\sum_{\gamma=0}^{\infty}\delta\vec{a}^{\gamma}\cdot\left|\tilde{\phi}_k^{(\gamma)}\right\rangle \tag{2.46}$$

from which we collect the terms that go to first order in $\delta\vec{a}$.

$$\tilde{\mathcal{K}}(\vec{a})\left|\tilde{\phi}_k^{(1)}\right\rangle + \tilde{\mathcal{K}}_{int}\left|\tilde{\phi}_k^{(0)}\right\rangle = \epsilon_k^{(1)}(\vec{a})\left|\tilde{\phi}_k^{(0)}\right\rangle + \epsilon_k^{(0)}(\vec{a})\left|\tilde{\phi}_k^{(1)}\right\rangle \tag{2.47}$$

Multiplying from the left with $\left\langle \tilde{\phi}_k^{(0)} \right|$ and utilizing the standard perturbation theory normalization $\left\langle \tilde{\phi}_n^{(0)} | \tilde{\phi}_n^{(m)} \right\rangle = \delta_{0m}$, an expression for the first order correction to the eigenvalues is obtained. Noting that the first order correction is equivalent to the first order derivative, the individual derivatives can be obtained similarly.

$$\epsilon_k^{(1)}(\vec{a}) = \left\langle \tilde{\phi}_k^{(0)} \right| \tilde{\mathcal{K}}_{int} \left| \tilde{\phi}_k^{(0)} \right\rangle \Rightarrow \epsilon_k^{(1i)} = \frac{\partial \epsilon_k}{\partial a_l} = \left\langle \tilde{\phi}_k^{(0)} \right| \frac{\tilde{\mathcal{K}}}{\partial a_l} \left| \tilde{\phi}_k^{(0)} \right\rangle \tag{2.48}$$

So far, we have worked with the standard form of perturbation theory, which is also known as Rayleigh-Schrödinger perturbation theory. However, the corrections to the eigenstates are easier to determine and the calculations are faster when using Brillouin-Wigner perturbation theory. This approach involves rewriting the perturbed Floquet eigenvalue problem (Eq. 2.42) and setting the perturbation constant $\delta\vec{a}$ equal to unity.

$$(\epsilon_k(\vec{a}) - \tilde{\mathcal{K}}(\vec{a})) \left| \tilde{\phi}_k \right\rangle = \tilde{\mathcal{K}}_{int} \left| \tilde{\phi}_k \right\rangle \tag{2.49}$$

Next, the set of projection operators

$$\hat{Q}_n = \sum_{k \neq n} \left| \tilde{\phi}_k^{(0)} \right\rangle \left\langle \tilde{\phi}_k^{(0)} \right| = \hat{I} - \left| \tilde{\phi}_n^{(0)} \right\rangle \left\langle \tilde{\phi}_n^{(0)} \right|, \tag{2.50}$$

which project a state into the orthogonal space of the unperturbed state $\left| \tilde{\phi}_k^{(0)} \right\rangle$, is introduced. These operators will commute with the Floquet operator $\tilde{\mathcal{K}}(\vec{a}))$ because they have the same eigenvectors. Applying $\hat{Q}_n$ to Eq. 2.49 yields

$$\hat{Q}_n(\epsilon_k(\vec{a}) - \tilde{\mathcal{K}}(\vec{a})) \left| \tilde{\phi}_k \right\rangle = (\epsilon_k(\vec{a}) - \tilde{\mathcal{K}}(\vec{a}))\hat{Q}_n \left| \tilde{\phi}_k \right\rangle = \hat{Q}_n \tilde{\mathcal{K}}_{int} \left| \tilde{\phi}_k \right\rangle, \tag{2.51}$$

which can be rewritten as

$$\hat{Q}_n \left| \tilde{\phi}_k \right\rangle = (\epsilon_k(\vec{a}) - \tilde{\mathcal{K}}(\vec{a}))^{-1} \hat{Q}_n \tilde{\mathcal{K}}_{int} \left| \tilde{\phi}_k \right\rangle, \tag{2.52}$$

where the (pseudo-)inverse of a matrix has been used. The perturbed eigenstates must be normalized according to standard perturbation theory normalization, meaning that $\left\langle \tilde{\phi}_k^{(0)} | \tilde{\phi}_k \right\rangle = 1$, which allows the perturbed eigenstates to be rewritten as

$$\left| \tilde{\phi}_k \right\rangle = \left| \tilde{\phi}_k^{(0)} \right\rangle + \hat{Q}_n \left| \tilde{\phi}_k \right\rangle \tag{2.53}$$

Defining the operator $\hat{R}_n = (\epsilon_k(\vec{a}) - \tilde{\mathcal{K}}(\vec{a}))^{-1} \hat{Q}_n$ and inserting Eq. 2.52 into Eq. 2.53 yields

$$\left| \tilde{\phi}_k \right\rangle = \left| \tilde{\phi}_k^{(0)} \right\rangle + \hat{R}_n \tilde{\mathcal{K}}_{int} \left| \tilde{\phi}_k \right\rangle, \tag{2.54}$$

which can be solved via iteration under the reasonable assumption that the perturbation $\tilde{\mathcal{K}}_{int} = \nabla_a \tilde{\mathcal{K}}|_{\vec{a}=\vec{0}}$ is small. The first order correction to the eigenstates can then be calculated by using the zeroth order approximation to the eigenstates on the right. The individual derivatives can again be obtained similarly by noting that the first order correction is equivalent to the first order derivative.

$$\left| \tilde{\phi}_k^{(1)} \right\rangle = \hat{R}_n \tilde{\mathcal{K}}_{int} \left| \tilde{\phi}_k^{(0)} \right\rangle \Rightarrow \left| \tilde{\phi}_k^{(1i)} \right\rangle = \frac{\partial \left| \tilde{\phi}_k \right\rangle}{\partial a_l} = \hat{R}_n \frac{\partial \tilde{\mathcal{K}}}{\partial a_l} \left| \tilde{\phi}_k^{(0)} \right\rangle \tag{2.55}$$

Expressions for $\frac{\partial \epsilon_k}{\partial a_l}$ and $\frac{\partial |\phi_{kv}\rangle}{\partial a_l}$ have now been derived, which allows us to determine $\frac{\partial \hat{U}(t)}{\partial a_l}$, thereby fulfilling the second requirement for performing the optimization with optimal control theory.

2.4.3 Optimization details

So far, however, we have only considered single NV with some value of Δ_i and α_i. Robustness against inhomogeneous broadening and drive amplitude variations is then achieved by averaging across a representative sample of N_s different NV with varying Δ_i and α_i. The different NV electron spins are assumed to be independent and non-interacting. In other words, we seek to maximize the averaged fidelity

$$\mathcal{F}_{st,avg} = \sum_{i=1}^{N_s} w_i \mathcal{F}_{st}(\Delta_i, \alpha_i) \tag{2.56}$$

by stepping along the averaged fidelity gradient

$$\left(\frac{\partial \mathcal{F}_{st}}{\partial a_{jk}}\right)_{avg} = \sum_{i=1}^{N_s} w_i \frac{\partial \mathcal{F}_{st}}{\partial a_{jk}}(\Delta_i, \alpha_i), \tag{2.57}$$

where $\sum\limits_{i=1}^{N_s} w_i = 1$ are normalized weights representing the expected distribution of Δ_i and α_i, while the used values of Δ_i and α_i should represent the level of inhomogeneous broadening and drive amplitude variations that one wishes to achieve robustness against. The representative sample need not be anywhere near as large as the ensemble that the resulting pulse is meant to be used on, so long as the values of Δ_i, α_i and w_i represent the level of inhomogeneous broadening and drive amplitude variations sufficiently well.

A common approach that I also utilized is to use an equal number N_r of different Δ and α values to cover the considered ranges, and then average across all possible combinations of these values. The representative sample will thus have the size $N_s = N_r \times N_r$, and the lists of Δ_i and α_i will include N_r repetitions of each distinct value. The values of Δ_i are chosen to lie symmetrically around $\Delta = 0$, i.e. no detuning, and are assumed to follow a Gaussian distribution centered at zero with a full width at half maximum (FWHM) equal to the maximum value of Δ_i. A given optimization might thus, for instance, use values of Δ_i between $\pm 1\,\mathrm{MHz}$ assumed to follow a Gaussian distribution centered at zero with a FWHM equal to $1\,\mathrm{MHz}$. The values of α_i are chosen to lie symmetrically around $\alpha = 1$, i.e. no drive amplitude variation, and are assumed to follow a flat distribution. The weights w_i are thus purely determined by the values of Δ_i and can be calculated as

$$w_i = \frac{\frac{1}{\sigma\sqrt{2\pi}} \mathrm{e}^{-\frac{\Delta_i^2}{2\sigma^2}}}{\sum\limits_{i=1}^{N_s} \frac{1}{\sigma\sqrt{2\pi}} \mathrm{e}^{-\frac{\Delta_i^2}{2\sigma^2}}} \iff w_i = \frac{\mathrm{e}^{-\frac{\Delta_i^2}{2\sigma^2}}}{\sum\limits_{i=1}^{N_s} \mathrm{e}^{-\frac{\Delta_i^2}{2\sigma^2}}}, \tag{2.58}$$

where

$$\sigma = \frac{\mathrm{FWHM}}{2\sqrt{2\ln(2)}} \tag{2.59}$$

is given by the value of the FWHM.

In order to limit the maximum Rabi frequency (MW power) that is used during the application of the shaped MW pulse, it is common to include a penalty functional

$$\mathcal{F}_{penalty} = -c_{penalty} t_p \vec{a}^2, \tag{2.60}$$

$$\frac{\partial \mathcal{F}_{penalty}}{\partial a_{jk}} = -2c_{penalty} t_p a_{jk} \tag{2.61}$$

in the optimization, where $c_{penalty} \geq 0$ is a penalty constant that determines how harshly large Rabi frequencies are penalized. The final total functional value and functional gradient used for the optimization thereby becomes

$$\mathcal{F}_{st,tot} = -c_{penalty} t_p \vec{a}^2 + \sum_{i=1}^{N_s} w_i \mathcal{F}_{st}(\Delta_i, \alpha_i) \tag{2.62}$$

and

$$\left(\frac{\partial \mathcal{F}_{st}}{\partial a_{jk}}\right)_{tot} = -2c_{penalty} t_p a_{jk} + \sum_{i=1}^{N_s} w_i \frac{\partial \mathcal{F}_{st}}{\partial a_{jk}}(\Delta_i, \alpha_i). \tag{2.63}$$

The total functional is not referred to as the fidelity, but the goal is still to maximize the total functional value by stepping along the total functional gradient. Furthermore, the penalty constant $c_{penalty}$ is not kept fixed, but is updated after every optimization step. The optimization is started with some initial value of $c_{penalty}$ and after each optimization step, the maximum Rabi frequency that occurs during the resulting pulse is calculated and compared to the maximum allowed Rabi frequency R_{lim}, i.e. the upper limit chosen for the Rabi frequency. Values of R_{lim} will be given in regular frequency units. If the maximum Rabi frequency of the pulse exceeds the upper limit R_{lim}, the penalty constant is increased by a chosen step size. If the maximum Rabi frequency of the pulse does not exceed the upper limit R_{lim}, the penalty constant is decreased by that same step size. This approach serves to not only ensure that the final shaped MW pulse will not exceed the upper limit R_{lim}, but also helps to prevent the optimization algorithm from getting stuck in a local maxima. I used an initial penalty constant value of 1.0 and a penalty constant step size of 0.05 for all of the optimizations that will be referenced in this thesis, as these values were found to yield good results.

Finally, the step size along the gradient in the optimization is determined in two different ways depending on the number of previous optimization steps. For the first 51 optimization steps, the gradient step size is kept constant at $\beta = 0.007$, whereas for the later optimization steps, the optimal step size is determined via a line search. This is done in order to speed up the optimization without compromising the quality of the obtained optimal control pulses.

2.4.4 Including the effects of hyperfine splitting

All of the necessary components in the optimization have now been explained. However, the Hamiltonian and its related Fourier coefficients that were presented only relate to a single hyperfine transition, as is usual for the use of optimal control theory for NV sensing. As previously mentioned, it is possible to suppress the hyperfine splitting by polarizing the nitrogen nuclear spin, but doing so is not straightforward and adds to the complexity of the NV sensing scheme. As a result, it is also relevant to consider the option of expanding the optimal control approach to include all of the hyperfine transitions, such that shaped MW pulses capable of simultaneously driving all of the transitions might be achieved. Doing so involves expanding the considered Hamiltonian and thus also its Fourier coefficients to include all of the hyperfine transitions.

The different hyperfine transitions (two-level systems) are assumed to be independent, which follows naturally from the previous assumption that the NV electron spins do not interact. The total Hamiltonian describing the evolution of all of the hyperfine transitions can thus be written as a sum over separate versions of the single NV Hamiltonian in Eq. 2.13 with different transition frequencies ω_0.

$$\hat{\mathcal{H}}(t) = \sum_k \frac{\omega_{0,k}}{2}\sigma_{z,k} + \sigma_{x,k}\left(I(t)\cos(\omega_{MW}t) + Q(t)\sin(\omega_{MW}t)\right) \tag{2.64}$$

Here, $\sigma_{x,k}$, $\sigma_{y,k}$ and $\sigma_{z,k}$ are Pauli spin-matrices specific to transition k. The number of hyperfine transitions is 3 when considering ^{14}N nuclear spins and 2 when considering ^{15}N nuclear spins. The states of the considered two-level systems can thus be completely described by a single vector of length 6 for ^{14}N nuclear spins and a single vector of length 4 for ^{15}N nuclear spins. For instance, the states initialized in $m_S = 0$ can be described by $|\psi\rangle = 1/\sqrt{3}(1,0,1,0,1,0)$ for ^{14}N nuclear spins or $|\psi\rangle = 1/\sqrt{2}(1,0,1,0)$ for ^{15}N nuclear spins. Note that these vectors inherently describe the electron spin states of 3(2) NV centers, such that the fidelity obtained from Eq. 2.4 becomes the average fidelity across 3(2) NV centers. The transition-specific Pauli spin-matrices can likewise be represented by either 6×6 or 4×4 matrices. To avoid confusion, the matrices are denoted $1,2,3$ for ^{14}N and l, r for ^{15}N. For ^{14}N nuclear spins, the relevant 6×6 matrices are

$$\sigma_{z,1} = \begin{pmatrix} 1 & 0 & 0 & 0 & 0 & 0 \\ 0 & -1 & 0 & 0 & 0 & 0 \\ 0 & 0 & 0 & 0 & 0 & 0 \\ 0 & 0 & 0 & 0 & 0 & 0 \\ 0 & 0 & 0 & 0 & 0 & 0 \\ 0 & 0 & 0 & 0 & 0 & 0 \end{pmatrix},\ \sigma_{z,2} = \begin{pmatrix} 0 & 0 & 0 & 0 & 0 & 0 \\ 0 & 0 & 0 & 0 & 0 & 0 \\ 0 & 0 & 1 & 0 & 0 & 0 \\ 0 & 0 & 0 & -1 & 0 & 0 \\ 0 & 0 & 0 & 0 & 0 & 0 \\ 0 & 0 & 0 & 0 & 0 & 0 \end{pmatrix},\ \sigma_{z,3} = \begin{pmatrix} 0 & 0 & 0 & 0 & 0 & 0 \\ 0 & 0 & 0 & 0 & 0 & 0 \\ 0 & 0 & 0 & 0 & 0 & 0 \\ 0 & 0 & 0 & 0 & 0 & 0 \\ 0 & 0 & 0 & 0 & 1 & 0 \\ 0 & 0 & 0 & 0 & 0 & -1 \end{pmatrix}, \tag{2.65}$$

$$\sigma_{x,1} = \begin{pmatrix} 0 & 1 & 0 & 0 & 0 & 0 \\ 1 & 0 & 0 & 0 & 0 & 0 \\ 0 & 0 & 0 & 0 & 0 & 0 \\ 0 & 0 & 0 & 0 & 0 & 0 \\ 0 & 0 & 0 & 0 & 0 & 0 \\ 0 & 0 & 0 & 0 & 0 & 0 \end{pmatrix},\ \sigma_{x,2} = \begin{pmatrix} 0 & 0 & 0 & 0 & 0 & 0 \\ 0 & 0 & 0 & 0 & 0 & 0 \\ 0 & 0 & 0 & 1 & 0 & 0 \\ 0 & 0 & 1 & 0 & 0 & 0 \\ 0 & 0 & 0 & 0 & 0 & 0 \\ 0 & 0 & 0 & 0 & 0 & 0 \end{pmatrix},\ \sigma_{x,3} = \begin{pmatrix} 0 & 0 & 0 & 0 & 0 & 0 \\ 0 & 0 & 0 & 0 & 0 & 0 \\ 0 & 0 & 0 & 0 & 0 & 0 \\ 0 & 0 & 0 & 0 & 0 & 0 \\ 0 & 0 & 0 & 0 & 0 & 1 \\ 0 & 0 & 0 & 0 & 1 & 0 \end{pmatrix} \tag{2.66}$$

and

$$\sigma_{y,1} = \begin{pmatrix} 0 & -i & 0 & 0 & 0 & 0 \\ i & 0 & 0 & 0 & 0 & 0 \\ 0 & 0 & 0 & 0 & 0 & 0 \\ 0 & 0 & 0 & 0 & 0 & 0 \\ 0 & 0 & 0 & 0 & 0 & 0 \\ 0 & 0 & 0 & 0 & 0 & 0 \end{pmatrix},\ \sigma_{y,2} = \begin{pmatrix} 0 & 0 & 0 & 0 & 0 & 0 \\ 0 & 0 & 0 & 0 & 0 & 0 \\ 0 & 0 & 0 & -i & 0 & 0 \\ 0 & 0 & i & 0 & 0 & 0 \\ 0 & 0 & 0 & 0 & 0 & 0 \\ 0 & 0 & 0 & 0 & 0 & 0 \end{pmatrix},\ \sigma_{y,3} = \begin{pmatrix} 0 & 0 & 0 & 0 & 0 & 0 \\ 0 & 0 & 0 & 0 & 0 & 0 \\ 0 & 0 & 0 & 0 & 0 & 0 \\ 0 & 0 & 0 & 0 & 0 & 0 \\ 0 & 0 & 0 & 0 & 0 & -i \\ 0 & 0 & 0 & 0 & i & 0 \end{pmatrix}. \tag{2.67}$$

For ^{15}N nuclear spins, the relevant 4×4 matrices are

$$\sigma_{z,l} = \begin{pmatrix} 1 & 0 & 0 & 0 \\ 0 & -1 & 0 & 0 \\ 0 & 0 & 0 & 0 \\ 0 & 0 & 0 & 0 \end{pmatrix}, \ \sigma_{z,r} = \begin{pmatrix} 0 & 0 & 0 & 0 \\ 0 & 0 & 0 & 0 \\ 0 & 0 & 1 & 0 \\ 0 & 0 & 0 & -1 \end{pmatrix}, \tag{2.68}$$

$$\sigma_{x,l} = \begin{pmatrix} 0 & 1 & 0 & 0 \\ 1 & 0 & 0 & 0 \\ 0 & 0 & 0 & 0 \\ 0 & 0 & 0 & 0 \end{pmatrix}, \ \sigma_{x,r} = \begin{pmatrix} 0 & 0 & 0 & 0 \\ 0 & 0 & 0 & 0 \\ 0 & 0 & 0 & 1 \\ 0 & 0 & 1 & 0 \end{pmatrix} \tag{2.69}$$

and

$$\sigma_{y,l} = \begin{pmatrix} 0 & -i & 0 & 0 \\ i & 0 & 0 & 0 \\ 0 & 0 & 0 & 0 \\ 0 & 0 & 0 & 0 \end{pmatrix}, \ \sigma_{y,r} = \begin{pmatrix} 0 & 0 & 0 & 0 \\ 0 & 0 & 0 & 0 \\ 0 & 0 & 0 & -i \\ 0 & 0 & i & 0 \end{pmatrix}. \tag{2.70}$$

As before, the calculations can be simplified by moving to a rotating frame rotating at the driving frequency ω_{MW}. The unitary rotation operator when considering multiple transitions has the form

$$\hat{R} = \mathrm{e}^{\sum\limits_k i\omega_{MW} t \sigma_{z,k}/2}. \tag{2.71}$$

As before, the Schrödinger equation is rewritten in the frame defined by $\hat{R}$ in order to obtain $i\frac{\partial}{\partial t}|\psi'\rangle = \hat{\mathcal{H}}'(t)|\psi'\rangle$ where $|\psi'\rangle = \hat{R}|\psi\rangle$ and $\hat{\mathcal{H}}'(t) = \hat{R}\hat{\mathcal{H}}(t)\hat{R}^\dagger + i\frac{\partial \hat{R}}{\partial t}\hat{R}^\dagger$. Now, however, the last term in $\hat{\mathcal{H}}'(t)$ is $i\frac{\partial \hat{R}}{\partial t}\hat{R}^\dagger = -\sum\limits_k \frac{\omega_{MW}}{2}\sigma_{z,k}$. The first term in $\hat{\mathcal{H}}'(t)$ can be expanded to get

$$\begin{aligned} \hat{R}\hat{\mathcal{H}}(t)\hat{R}^\dagger = \sum_k \frac{\omega_{0,k}}{2}\sigma_{z,k} + \mathrm{e}^{\sum\limits_k i\omega_{MW} t \sigma_{z,k}/2} \sum_k \sigma_{x,k}\Big(I(t)\cos(\omega_{MW}t) \\ + Q(t)\sin(\omega_{MW}t)\Big)\mathrm{e}^{\sum\limits_k -i\omega_{MW} t \sigma_{z,k}/2} \end{aligned} \tag{2.72}$$

by noting that $[\sigma_{z,k}, \sigma_{z,k'}] = 0$ for all k, k'. This expression is equivalent to the one we obtained when considering a single transition except that it contains multiple terms. We note that the relevant commutation relations for the transition specific Pauli spin-matrices can easily be shown to be $[\sigma_{z,k}, \sigma_{x,k'}] = 2i\sigma_{y,k}\delta_{k,k'}$ and $[\sigma_{z,k}, \sigma_{y,k'}] = -2i\sigma_{x,k}\delta_{k,k'}$. Utilizing these commutation relations, the Baker-Campbell-Hausdorff lemma and the Taylor expansions of sine and cosine functions allows us to write

$$\mathrm{e}^{\sum\limits_k i\omega_{MW} t \sigma_{z,k}/2} \sum_k \sigma_{x,k} \mathrm{e}^{\sum\limits_k -i\omega_{MW} t \sigma_{z,k}/2} = \sum_k \Big(\sigma_{x,k}\cos(\omega_{MW}t) + \sigma_{y,k}\sin(\omega_{MW}t)\Big), \tag{2.73}$$

and thus

$$\begin{aligned} \hat{R}\hat{\mathcal{H}}(t)\hat{R}^\dagger = \sum_k \Big(\frac{\omega_{0,k}}{2}\sigma_{z,k} + (\sigma_{x,k}\cos(\omega_{MW}t) + \sigma_{y,k}\sin(\omega_{MW}t)) \\ \cdot (I(t)\cos(\omega_{MW}t) + Q(t)\sin(\omega_{MW}t))\Big), \end{aligned} \tag{2.74}$$

which can be expanded to

$$\hat{R}\hat{\mathcal{H}}(t)\hat{R}^\dagger = \sum_k \Big(\frac{\omega_{0,k}}{2}\sigma_{z,k} + \frac{I(t)}{2}\sigma_{x,k}[1+\cos(2\omega_{MW}t)] + \frac{Q(t)}{2}\sigma_{x,k}\sin(2\omega_{MW}t) + \frac{I(t)}{2}\sigma_{y,k}\sin(2\omega_{MW}t) + \frac{Q(t)}{2}\sigma_{y,k}[1-\cos(2\omega_{MW}t)]\Big) \tag{2.75}$$

via the use of trigonometric identities. Once more, the rotating wave approximation is utilized to get rid of the rapidly oscillating terms $\cos(2\omega_{MW}t)$, $\sin(2\omega_{MW}t)$ and simplify the expression to

$$\hat{R}\hat{\mathcal{H}}(t)\hat{R}^\dagger = \sum_k \Big(\frac{\omega_{0,k}}{2}\sigma_{z,k} + \frac{I(t)}{2}\sigma_{x,k} + \frac{Q(t)}{2}\sigma_{y,k}\Big). \tag{2.76}$$

Next, Δ_i is defined to be the detuning between the driving frequency ω_{MW} and the average transition frequency $\omega_{0,avg} = 1/N_t \sum_k \omega_{0,k}$, where N_t is 3 when considering ^{14}N nuclear spins and 2 when considering ^{15}N nuclear spins. For ^{14}N nuclear spins, the average transition frequency is simply the transition frequency of the central hyperfine transition due to the hyperfine splitting being symmetric. The total Hamiltonian which includes all of the hyperfine transitions in the rotating frame can then be written as

$$\hat{\mathcal{H}}'(t) = \sum_k \Big(\frac{\Delta_i + m_k\delta_I}{2}\sigma_{z,k} + \frac{I(t)}{2}\sigma_{x,k} + \frac{Q(t)}{2}\sigma_{y,k}\Big), \tag{2.77}$$

where $m_1 = -1$, $m_2 = 0$, $m_3 = 1$ and $\delta_I = 2\pi \cdot 2.16\,\text{MHz}$ for ^{14}N nuclear spins, while $m_l = -1/2$, $m_r = 1/2$ and $\delta_I = 2\pi \cdot 3.03\,\text{MHz}$ for ^{15}N nuclear spins. Inserting Eq. 2.77 into Eq. 2.28 yields

$$\hat{\mathcal{H}}_n = \sum_k \frac{1}{T}\int_0^T \mathrm{e}^{-in\Omega_f t}\left(\frac{\Delta_i + m_k\delta_I}{2}\sigma_{z,k} + \frac{I(t)}{2}\sigma_{x,k} + \frac{Q(t)}{2}\sigma_{y,k}\right)\mathrm{d}t, \tag{2.78}$$

which can be expanded by using the definitions of $I(t)$ and $Q(t)$ in Eq. 2.7.

$$\hat{\mathcal{H}}_n = \frac{1}{T}\sum_k \int_0^T \mathrm{e}^{-in\Omega_f t}\left(\frac{\Delta_i + m_k\delta_I}{2}\sigma_{z,k} + \sum_{j=1}^{N_f}[a_{jx}\sigma_{x,k} + a_{jy}\sigma_{y,k}]\sin(j\Omega_f t)\right)\mathrm{d}t \tag{2.79}$$

The final expression for the Fourier coefficients of the Hamiltonian when all of the hyperfine transitions are included is then obtained by utilizing the exponential form of a sine and the exponential form of the Kronecker delta, which yields

$$\hat{\mathcal{H}}_n = \sum_k \Big(\frac{\Delta_i + m_k\delta_I}{2}\sigma_{z,k}\delta_{n,0} - \frac{i}{2}\sum_{j=1}^{N_f}\alpha_i\,[a_{jx}\sigma_{x,k} + a_{jy}\sigma_{y,k}]\,(\delta_{n,j} - \delta_{n,-j})\Big), \tag{2.80}$$

where the control amplitudes have once again been multiplied by the relative control amplitude α_i in order to include the effects of drive amplitude variations. The optimization can thus be performed while considering either a single transition or all of the hyperfine transitions by using the relevant expression for $\hat{\mathcal{H}}_n$. When performing optimizations with the hyperfine splitting included, I exclusively consider ^{14}N nuclear spins, as this is the most naturally abundant isotope.

2.4.5 Smooth optimal pulse examples

As an example of the shaped MW pulses that might be designed by the smooth optimal control algorithm, Fig. 2.6 shows $I(t)$ and $Q(t)$ in regular frequency units for two smooth optimal pulses that were optimized to perform a state transfer π-flip with and without hyperfine splitting included for otherwise identical parameters. Both of the optimizations needed approximately 150 optimization steps to achieve convergence of the fidelity.

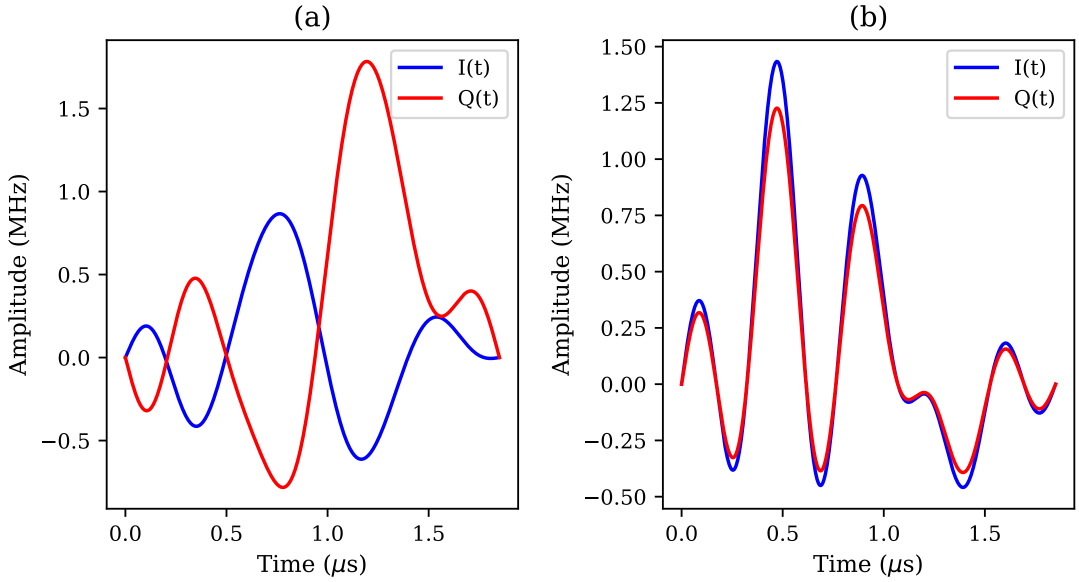

Figure 2.6: Plots of $I(t)$ and $Q(t)$ in regular frequency units for smooth optimal control pulses optimized to perform a state transfer π-flip for $\Delta_i/(2\pi)$ between ± 1 MHz, α_i between 1 ± 0.1 and $t_p = 1.85$ μs with an upper limit on the Rabi frequency of $R_{\text{lim}} = 1.9$ MHz. The optimizations were performed (a) without and (b) with hyperfine splitting included.

A common method for visualizing the performance of optimal control pulses is to calculate and plot the single NV fidelity as a function of Δ_1 and α_1 in a 2D plot called a fidelity map. Here, the subscript 1 is used to indicate that each fidelity value is obtained using a single value of Δ and α. Similarly, the performance when hyperfine splitting is included can be visualized by plotting the fidelity averaged across the hyperfine transitions as a function of Δ_1 and α_1. Note that the single NV fidelity is equivalent to the fidelity of the performance on a single transition.

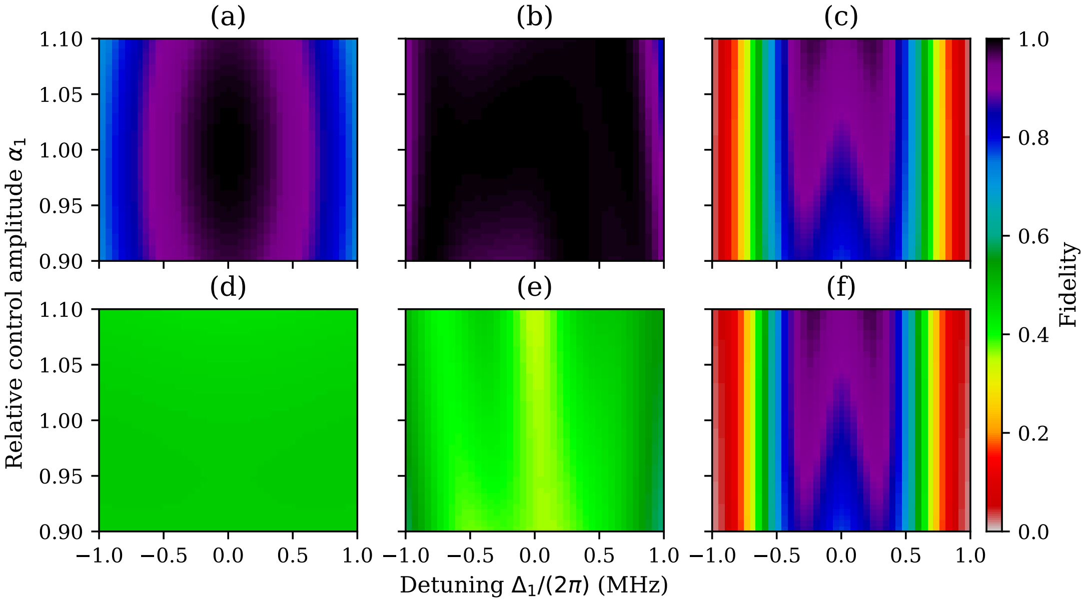

Figure 2.7: State transfer π-flip fidelity maps for three different pulses with and without hyperfine splitting included. The top row shows the single NV fidelity, and the bottom row shows the fidelity averaged across the hyperfine transitions as a function of Δ_1 and α_1 for (a, d) a flat π-pulse with $\Omega_R = 2\pi \cdot 1.9\,\text{MHz}$, (b, e) the smooth optimal pulse shown in Fig. 2.6(a) and (c, f) the smooth optimal pulse shown in Fig. 2.6(b).

As an illustration of both this method and the performance achievable with optimal control pulses, Fig. 2.7 shows six different fidelity maps based on the optimal control pulses shown in Fig. 2.6 and an equivalent flat pulse. The methods used to obtain the flat pulse fidelity are explained in section 2.5.1. The fidelity maps in Fig. 2.7(a, b, c) show the single NV fidelity as a function of Δ_1 and α_1, and the fidelity maps in Fig. 2.7(d, e, f) show the fidelity averaged across the hyperfine transitions as a function of Δ_1 and α_1. The pulse used for Fig. 2.7(a, d) was a flat π-pulse with $\Omega_R = 2\pi \cdot 1.9\,\text{MHz}$, the pulse used for Fig. 2.7(b, e) was the smooth optimal pulse shown in Fig. 2.6(a), and the pulse used for Fig. 2.7(c, f) was the smooth optimal pulse shown in Fig. 2.6(b).

Figure 2.7 illustrates how the optimal pulse optimized without hyperfine splitting (Fig. 2.6(a)) achieves high single NV fidelity for a much wider range of values of Δ_1 and α_1 than the flat pulse or the optimal pulse optimized with hyperfine splitting included (Fig. 2.6(b)). This is as expected, given that said pulse was optimized without hyperfine splitting and would thus be expected to outperform an equivalent flat pulse under those conditions. Conversely, the optimal pulse optimized with hyperfine splitting (Fig. 2.6(b)) performs worse in terms of single NV fidelity than either the flat pulse or the optimal pulse optimized without hyperfine splitting because it was not optimized for that situation. When considering the fidelity averaged across the hyperfine transitions, which is the situation that it was optimized for, the pulse in Fig. 2.6(b) achieves significantly larger fidelity than either of the two other considered pulses, at least in the central region of the fidelity map. One can also note that the fidelity maps in Fig. 2.7(c) and Fig. 2.7(f) have almost the exact same shape, which indicates that the pulse in Fig. 2.6(b) has almost the exact same effect on all of the hyperfine transitions.

2.5 Measurement simulations

2.5.1 Pulsed measurement simulations

In addition to using the previously derived expressions to calculate the fidelity via Eq. 2.4, it is also possible to simulate the effect of an optimal pulse by numerically solving the Schrödinger equation. The relevant Hamiltonians describing the evolution of the NV center electron spin state under influence of an optimal control pulse have already been derived in Eqs. 2.24 and 2.77. The differential equation to be solved thus becomes

$$\frac{d\left|\psi\right\rangle}{dt} = -i\left(\frac{\Delta_i}{2}\sigma_z + \alpha_i\left[\frac{I(t)}{2}\sigma_x + \frac{Q(t)}{2}\sigma_y\right]\right)\left|\psi\right\rangle \tag{2.81}$$

when considering a single hyperfine transition and

$$\frac{d\left|\psi\right\rangle}{dt} = -i\sum_k\Big(\frac{\Delta_i + m_k\delta_I}{2}\sigma_{z,k} + \alpha_i\left[\frac{I(t)}{2}\sigma_{x,k} + \frac{Q(t)}{2}\sigma_{y,k}\right]\Big)\left|\psi\right\rangle \tag{2.82}$$

when considering all of the hyperfine transitions. Note that Eq. 2.82 technically describes 2 or 3 separate NV centers depending on whether one is considering ^{15}N or ^{14}N. The simulation can thus be performed by numerically solving either Eq. 2.81 or Eq. 2.82 with the relevant $I(t)$ and $Q(t)$ for a duration equal to the pulse duration t_p using the intended initial state $\left|\psi_{init}\right\rangle$. The resulting state is then equal to the term $\hat{U}(t_p)\left|\psi_{init}\right\rangle$ in Eq. 2.4 for the state transfer fidelity and can be used to compute said fidelity. Furthermore, the normalized contrast between 0 and 1 expected after application of a given pulse can be calculated as the overlap of the resulting state with state $\left|1\right\rangle$. This is due to the fact that the contrast will be maximal when the NV center is completely in state $\left|1\right\rangle$, i.e. $m_S = 1$ or $m_S = -1$, and minimal when it is completely in state $\left|0\right\rangle$, i.e. $m_S = 0$. In the case of Eq. 2.82, where all of the hyperfine transitions are considered, one would use the average overlap across the hyperfine transitions. The response of an ensemble can also be simulated by performing a weighted average of the obtained fidelities or normalized contrast values across different values of Δ_i and α_i. The average can be performed according to Eq. 2.56, which was also used for the optimal control approach.

The same approach can be used to simulate the effect of a flat MW pulse by utilizing the earlier observation that a flat MW pulse is simply a special case of an optimal pulse where $I(t) = \Omega_R$ and $Q(t) = 0$ for all t during the pulse duration t_p.

The contrast expected from π-pulse ODMR can thus be simulated by using the initial state $|\psi_{init}\rangle = |0\rangle$, which corresponds to an NV center initialized in $m_S = 0$, and numerically solving Eq. 2.81 or Eq. 2.82 with the appropriate $I(t)$, $Q(t)$ and pulse duration t_p. The contrast is then obtained as the overlap of the resulting state with state $|1\rangle$. For an optimal control pulse, the pulse duration t_p will be whatever it was designed to be, whereas it will be $t_p = \frac{\pi}{\Omega_R}$ for a flat MW pulse. The effect of scanning the MW driving frequency can be included by adding a constant term, which corresponds to the difference between the MW driving frequency and the central transition frequency, to all of the considered Δ_i-values. Similarly, the effect of an additional external magnetic field B is to change the transition frequency and thus Δ_i by $\gamma_e B$ for the $m_S = 0 \Longleftrightarrow m_S = 1$ transition and $-\gamma_e B$ for the $m_S = 0 \Longleftrightarrow m_S = -1$ transition.

The contrast expected from Ramsey interferometry can be simulated in a similar manner, although the simulation requires three steps. First, the state resulting from applying a $\pi/2$-pulse to the initial state $|\psi_{init}\rangle = |0\rangle$ is simulated by numerically solving Eq. 2.81 or Eq. 2.82 with the appropriate $I(t)$, $Q(t)$ and pulse duration t_p. For a flat MW pulse, the pulse duration is $t_p = \frac{\pi/2}{\Omega_R}$. This simulates the effect of the initial $\pi/2$-pulse. The resulting output state from the first simulation is then used as the initial state for a second simulation where all $\alpha_i = 0$, which corresponds to no MW drive, and the duration is τ. This simulates the effect of the free precession. The resulting output state from the second simulation is then used as the initial state for a third simulation where $I(t)$, $Q(t)$ and pulse duration t_p are again chosen to match a $\pi/2$-pulse. This simulates the effect of the final $\pi/2$-pulse. The expected contrast can then be obtained as the overlap of the resulting state from the third simulation with state $|1\rangle$. The effect of changing the MW driving frequency or an additional external magnetic field can be included in the same manner as for π-pulse ODMR.

Apart from the previously mentioned simulations, it will also be relevant to simulate a three-frequency drive with flat MW pulses for comparison with optimal control pulses optimized while considering all of the hyperfine transitions. Using a multi-frequency drive is, after all, one of the typical ways of compensating for the effects of hyperfine splitting. To do so, it is necessary to change the considered Hamiltonian to reflect the three-frequency driving. This is done by replacing the $\cos(\omega_{MW} t)$ and $\sin(\omega_{MW} t)$ terms in Eq. 2.64 with sums of three such terms with the driving frequency split by δ_I.

$$\cos(\omega_{MW} t) \longrightarrow \cos(\omega_{MW} t) + \cos([\omega_{MW} + \delta_I]t) + \cos([\omega_{MW} - \delta_I]t) \tag{2.83}$$

$$\sin(\omega_{MW} t) \longrightarrow \sin(\omega_{MW} t) + \sin([\omega_{MW} + \delta_I]t) + \sin([\omega_{MW} - \delta_I]t) \tag{2.84}$$

The sums can be rewritten via the use of trigonometric relations.

$$\begin{aligned}\cos(\omega_{MW}t) &+ \cos([\omega_{MW}+\delta_I]t)\\ &+ \cos([\omega_{MW}-\delta_I]t) = \cos(\omega_{MW}t)(1+2\cos(\delta_I t))\end{aligned} \tag{2.85}$$

$$\begin{aligned}\sin(\omega_{MW}t) &+ \sin([\omega_{MW}+\delta_I]t)\\ &+ \sin([\omega_{MW}-\delta_I]t) = \sin(\omega_{MW}t)(1+2\cos(\delta_I t))\end{aligned} \tag{2.86}$$

We have thus effectively multiplied the $\cos(\omega_{MW}t)$ and $\sin(\omega_{MW}t)$ terms in Eq. 2.64 with a factor $1+2\cos(\delta_I t)$. This is equivalent to multiplying $I(t)$ and $Q(t)$ with the same factor. As before, we now wish to move to a rotating frame rotating at ω_{MW}. However, we know from our previous derivation of Eq. 2.77 that the shift to a rotating frame only changes the $\sigma_{x,k}$-factor and adds a term $-\sum_k \frac{\omega_{MW}}{2}\sigma_{z,k}$. The factor $1+2\cos(\delta_I t)$ will thus not be affected by the shift to a rotating frame. Similarly, the factor $1+2\cos(\delta_I t)$ does not change what terms are removed by utilizing the rotating wave approximation, as it only includes (relatively) slowly oscillating terms. As such, we can conclude that the inclusion of three-frequency driving simply adds a factor $1+2\cos(\delta_I t)$ to $I(t)$ and $Q(t)$ in the total Hamiltonian in the rotating frame. The situation with three-frequency driving of all the hyperfine transitions can thus be described by the Hamiltonian

$$\hat{\mathcal{H}}'(t) = \sum_k \Big(\frac{\Delta_i + m_k\delta_I}{2}\sigma_{z,k} + \left[\frac{I(t)}{2}\sigma_{x,k} + \frac{Q(t)}{2}\sigma_{y,k}\right][1+2\cos(\delta_I t)]\Big). \tag{2.87}$$

The simulations can also be altered to include the effects of pure dephasing by adopting a master equation approach [61], which involves replacing the Schrödinger equation with the quantum master equation

$$\frac{d\rho}{dt} = -i[\hat{\mathcal{H}}'(t),\rho] + \Gamma_{pure}\left(\frac{1}{4}\sigma_z\rho\sigma_z - \frac{1}{8}\sigma_z\sigma_z\rho - \frac{1}{8}\rho\sigma_z\sigma_z\right), \tag{2.88}$$

where $\rho = |\psi\rangle\langle\psi|$ for a pure state, and the rate of pure dephasing is $\Gamma_{pure} \approx 1/T_2^*$. The initial state of an NV center initialized in $m_S = 0$ is given as $\rho_{init} = \begin{bmatrix}1 & 0\\ 0 & 0\end{bmatrix}$ in density matrix notation when neglecting hyperfine splitting. The overlap with state $|1\rangle$ and hence the normalized contrast is obtained directly as the second diagonal element of the resulting density matrix obtained from the simulations. Aside from these differences, the simulations are performed using the same methods that were previously described.

2.5.2 CW measurement simulations

The approaches that have been described so far can be used to simulate both π-pulse ODMR and Ramsey interferometry. However, they are not suited to simulating CW ODMR, which involves continuous reinitialization of the NV center electron spin state rather than some fixed initial state. Instead, we utilize a simplified five-level model for the NV center as the basis for CW ODMR simulations [62]. The $m_S = \pm 1$ states are considered to be a single level and so are the singlet states. The model thus involves level 1 (ground state $m_S = 0$), level 2 (ground state $m_S = \pm 1$), level 3 (excited state $m_S = 0$), level 4 (excited state $m_S = \pm 1$) and level 5 (singlet state). The population in level n is denoted ρ_{nn}, and the decay rate from level n to level m is denoted k_{nm}. The laser illumination is constant with optical pumping rate Γ_p, and the MW drive is constant with intended Rabi frequency Ω_R and detuning Δ_i between the driving frequency and the transition frequency. The evolution of the normalized population $\sum_{n=1}^{5} \rho_{nn} = 1$ in the five considered levels can then be described by the rate equations

$$\begin{aligned}
\frac{d\rho_{11}}{dt} &= -\Gamma_p\rho_{11} + k_{31}\rho_{33} + k_{41}\rho_{44} + k_{51}\rho_{55} - \frac{k_{21}}{2}(\rho_{11} - \rho_{22}) - \frac{i}{2}\alpha_i\Omega_R(\rho_{12} - \rho_{21}),\\
\frac{d\rho_{22}}{dt} &= -\Gamma_p\rho_{22} + k_{32}\rho_{33} + k_{42}\rho_{44} + k_{52}\rho_{55} - \frac{k_{21}}{2}(\rho_{22} - \rho_{11}) + \frac{i}{2}\alpha_i\Omega_R(\rho_{12} - \rho_{21}),\\
\frac{d\rho_{33}}{dt} &= \Gamma_p\rho_{11} - (k_{35} + k_{31} + k_{32})\rho_{33},\\
\frac{d\rho_{44}}{dt} &= \Gamma_p\rho_{22} - (k_{45} + k_{41} + k_{42})\rho_{44},\\
\frac{d\rho_{55}}{dt} &= k_{45}\rho_{44} + k_{35}\rho_{33} - (k_{52} + k_{51})\rho_{55},\\
\frac{d\rho_{12}}{dt} &= -(\gamma_2' - i\Delta_i)\rho_{12} + \frac{i}{2}\alpha_i\Omega_R(\rho_{22} - \rho_{11}),\\
\frac{d\rho_{21}}{dt} &= -(\gamma_2' + i\Delta_i)\rho_{21} - \frac{i}{2}\alpha_i\Omega_R(\rho_{22} - \rho_{11}),
\end{aligned} \tag{2.89}$$

where $\gamma_2' = \gamma_2 + \Gamma_p/2$ is the optical dephasing rate, and $\gamma_2 = 2\pi/T_2^* + k_{21}/2$ is the spin dephasing rate. The effect of pure dephasing is thus included in the rate equations via the term $2\pi/T_2^*$ and can be neglected by setting this term to zero. In regular frequency units, the decay rates are $k_{21} = 1/6\,\text{ms}$, $k_{31} = 1/16\,\text{ns}$, $k_{32} = 0.01k_{31}$, $k_{41} = 0.01k_{42}$, $k_{42} = 1/15\,\text{ns}$, $k_{35} = 1/95\,\text{ns}$, $k_{45} = 1/13\,\text{ns}$, $k_{51} = 1/330\,\text{ns}$ and $k_{52} = 1/380\,\text{ns}$ [63]. We can simplify the rate equations by introducing the total decay rates

$$K_3 = k_{35} + k_{31} + k_{32},\ K_4 = k_{45} + k_{41} + k_{42},\ K_5 = k_{51} + k_{52}. \tag{2.90}$$

We assume that the system will rapidly reach a steady-state for any realistic set of operating conditions, such that we need only concern ourselves with the rate equations under steady-state conditions. Given that red fluorescence is only emitted as part of a decay from level 3 or 4 to level 2 or 1, the CW ODMR signal $\mathcal{I}_{CW}$ can then be calculated as a linear combination of the steady-state populations of levels 3 and 4

$$\mathcal{I}_{CW} = R_\alpha\rho_3^{ss} + R_\beta\rho_4^{ss}, \tag{2.91}$$

where R_α and R_β are the ratios of the relevant fluorescing decay rates to the total decay rate.

$$R_\alpha = \frac{k_{32}+k_{31}}{K_3},\; R_\beta = \frac{k_{42}+k_{41}}{K_4} \tag{2.92}$$

We thus need to solve the rate equations for the steady-state populations in order to obtain the CW ODMR signal. Under steady-state conditions ($d\rho/dt = 0$), we can rewrite the last 5 rate equations to obtain the expressions

$$\rho_{33}^{ss} = \frac{\Gamma_p}{K_3}\rho_{11}^{ss},\; \rho_{44}^{ss} = \frac{\Gamma_p}{K_4}\rho_{22}^{ss}, \tag{2.93}$$

$$\rho_{55}^{ss} = \frac{k_{45}\rho_{44}^{ss} + k_{35}\rho_{33}^{ss}}{K_5} = \frac{k_{45}\Gamma_p}{K_4K_5}\rho_{22}^{ss} + \frac{k_{35}\Gamma_p}{K_3K_5}\rho_{11}^{ss}, \tag{2.94}$$

$$\rho_{12}^{ss} = \frac{\frac{i}{2}\alpha_i\Omega_R(\rho_{22}^{ss}-\rho_{11}^{ss})}{\gamma_2' - i\Delta_i},\; \rho_{21}^{ss} = -\frac{\frac{i}{2}\alpha_i\Omega_R(\rho_{22}^{ss}-\rho_{11}^{ss})}{\gamma_2' + i\Delta_i}. \tag{2.95}$$

The expressions in Eq. 2.93 allow us to reformulate the expression for $\mathcal{I}_{CW}$ in terms of the steady-state populations of levels 1 and 2.

$$\mathcal{I}_{CW} = R_\alpha\frac{\Gamma_p}{K_3}\rho_{11}^{ss} + R_\beta\frac{\Gamma_p}{K_4}\rho_{22}^{ss} \tag{2.96}$$

The expressions in Eq. 2.95 can be combined to obtain

$$\rho_{12}^{ss} - \rho_{21}^{ss} = \frac{i\gamma_2'\alpha_i\Omega_R(\rho_{22}^{ss}-\rho_{11}^{ss})}{\gamma_2'^2 + \Delta_i^2}. \tag{2.97}$$

The expressions in Eqs. 2.93, 2.94 and 2.97 can be combined with the second rate equation under steady-state conditions to obtain

$$\begin{aligned}\Gamma_P\rho_{22}^{ss} = \frac{k_{32}\Gamma_p}{K_3}\rho_{11}^{ss} + \frac{k_{42}\Gamma_p}{K_4}\rho_{22}^{ss} + \frac{k_{45}k_{52}\Gamma_p}{K_4K_5}\rho_{22}^{ss} + \frac{k_{35}k_{52}\Gamma_p}{K_3K_5}\rho_{11}^{ss}\\ - \frac{k_{21}}{2}(\rho_{22}-\rho_{11}) - \frac{\gamma_2'(\alpha_i\Omega_R)^2(\rho_{22}^{ss}-\rho_{11}^{ss})}{2(\gamma_2'^2+\Delta_i^2)},\end{aligned} \tag{2.98}$$

which can be rewritten as

$$\begin{aligned}\rho_{22}^{ss}\left[\Gamma_P - \frac{k_{42}\Gamma_p}{K_4} - \frac{k_{45}k_{52}\Gamma_p}{K_4K_5} + \frac{k_{21}}{2} + \frac{\gamma_2'(\alpha_i\Omega_R)^2}{2(\gamma_2'^2+\Delta_i^2)}\right]\\ = \rho_{11}^{ss}\left[\frac{k_{32}\Gamma_p}{K_3} + \frac{k_{35}k_{52}\Gamma_p}{K_3K_5} + \frac{k_{21}}{2} + \frac{\gamma_2'(\alpha_i\Omega_R)^2}{2(\gamma_2'^2+\Delta_i^2)}\right].\end{aligned} \tag{2.99}$$

If we now define

$$\Xi = \frac{\left[\frac{k_{21}}{2} + \frac{\Gamma_p(k_{32}K_5+k_{52}k_{35})}{K_3K_5} + \frac{(\alpha_i\Omega_R)^2\gamma_2'}{2(\gamma_2'^2+\Delta_i^2)}\right]}{\left[\Gamma_p + \frac{k_{21}}{2} - \frac{\Gamma_p(k_{42}K_5+k_{52}k_{45})}{K_4K_5} + \frac{(\alpha_i\Omega_R)^2\gamma_2'}{2(\gamma_2'^2+\Delta_i^2)}\right]}, \tag{2.100}$$

we arrive at the relation

$$\rho_{22}^{ss} = \Xi \rho_{11}^{ss} \tag{2.101}$$

between the steady-state populations of levels 1 and 2. Finally, we utilize the normalization of the steady-state populations and Eqs. 2.93, 2.94 and 2.101 to obtain

$$\begin{aligned} 1 &= \rho_{11}^{ss} + \rho_{22}^{ss} + \rho_{33}^{ss} + \rho_{44}^{ss} + \rho_{55}^{ss} \\ &= \rho_{11}^{ss} \left[1 + \Xi + \frac{\Gamma_p}{K_3} + \frac{\Gamma_p \Xi}{K_4} + \frac{k_{45}\Gamma_p \Xi}{K_4 K_5} + \frac{k_{35}\Gamma_p}{K_3 K_5} \right], \end{aligned} \tag{2.102}$$

which gives us the final expression

$$\rho_{11}^{ss} = \left[1 + \Xi + \frac{\Gamma_p}{K_3} + \frac{\Gamma_p \Xi}{K_4} + \frac{k_{45}\Gamma_p \Xi}{K_4 K_5} + \frac{k_{35}\Gamma_p}{K_3 K_5} \right]^{-1} \tag{2.103}$$

for the steady-state population in level 1. Inserting Eq. 2.103 in Eq. 2.101 gives us the expression

$$\rho_{22}^{ss} = \left[1 + \frac{1}{\Xi} + \frac{\Gamma_p}{K_3 \Xi} + \frac{\Gamma_p}{K_4} + \frac{k_{45}\Gamma_p}{K_4 K_5} + \frac{k_{35}\Gamma_p}{K_3 K_5 \Xi} \right]^{-1} \tag{2.104}$$

for the steady-state population in level 2. We have now obtained analytical expressions that can be used to calculate the CW ODMR signal $\mathcal{I}_{CW}$ for a given set of parameters. As with both π-pulse ODMR and Ramsey interferometry, we can simulate an ensemble by performing an average across different values of α_i and Δ_i. The scanning of the MW driving frequency can be represented by adding a constant term to all of the Δ_i-values. The CW ODMR signal can be converted to contrast relative to the signal obtained when the MW drive is far off-resonance. The contrast values can then be divided by the maximum contrast obtained in the asymptotic limit where Ω_R is very large in order to obtain normalized contrast values.

2.6 Laser threshold magnetometry

As previously explained, the typical approach to NV diamond magnetometry involves measuring changes in the red fluorescence caused by the presence of an additional external magnetic field separate from the static bias field. This can be done in several different ways via several different sensing schemes, some of which were detailed in the previous sections. However, all of these schemes suffer from two significant limitations that are inherent to the approach based on measuring changes in the red fluorescence. The first of these limitations is the fact that the signal to be measured, i.e. the fluorescence contrast, is relatively small compared to the background, particularly when working with an ensemble of NV centers. For single NV centers or small ensembles, the contrast can be up to 30% [39], as was previously mentioned, but for large ensembles, the contrast will often be no more than a few % [64, 65]. Meanwhile, the background fluorescence and thus the shot noise will generally increase with increasing ensemble size, given that all of the excited NV centers will produce fluorescence, regardless of whether or not they are being driven on-resonance. These effects serve to limit the achievable signal-to-noise ratio (SNR) in an NV magnetometry scheme based on measuring changes in the red fluorescence. The second limitation is related to the high refractive index of diamond, which traps a significant portion of the fluorescence inside the diamond [66]. This reduces the achievable fluorescence signal.

An alternative measurement approach that circumvents these limitations is to use the absorption of green light ($\lambda = 532\,\mathrm{nm}$) by the NV centers to perform laser threshold magnetometry [67]. Due to the long lifetime of the singlet ground state, which cannot absorb green light, and the spin state-dependence of the decay paths, an NV center will absorb less green light when the electron spin state transition is being driven on-resonance than when the drive is off-resonance. Through proper selection of components and parameters, it should thus be possible to engineer a laser setup with an NV diamond where the switch from off-resonance to on-resonance driving will cause a crossing of the lasing threshold. The switch can be caused by the presence of an additional external magnetic field, which will shift the NV spin resonance frequency as previously explained. Such a setup could then be used for a measurement scheme similar to standard CW ODMR, with the difference that one measures the green output laser power instead of the red fluorescence from the diamond. The resulting ODMR spectrum would effectively have zero background and a contrast of 100% due to the output laser power being zero in the absence of on-resonance driving, at least under ideal circumstances. This can potentially be done in several different ways given the many existing laser devices. We chose to focus on a technically simple setup consisting of a standard external cavity laser formed by a current driven semiconductor laser diode and an external mirror, with the diamond included in the external cavity as an extra source of loss. The setup is illustrated in Fig. 2.8 along with relevant parameters such as the laser diode cavity length L_m and end-facet power reflectivities R_1 and R_2, the external cavity length L_r, the external mirror power reflectivity R_3, the diamond thickness d and the effective loss due to green light absorption by the diamond α_e. The laser emission is assumed to be through R_1.

The idea is then to fix the drive current for the laser diode at the threshold current I_{off} for the situation where the electron spin transitions of the NV centers in the diamond are being driven off-resonantly. As the MW driving frequency is shifted towards on-resonance driving, the green light absorption by the NV centers in the diamond will decrease, thereby decreasing the threshold current and causing the external cavity laser to cross the lasing threshold. The change $\Delta I_{th} = I_{off} - I_{on}$ in threshold current caused by the shift from the threshold current I_{off} under off-resonant driving to the threshold current I_{on} under on-resonant driving is then

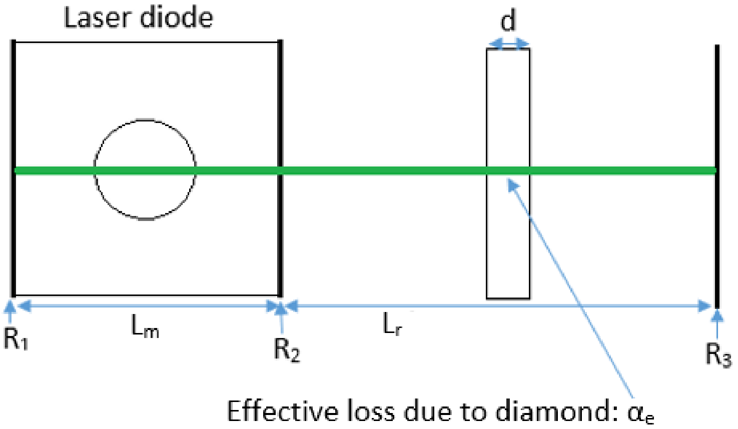

Figure 2.8: Sketch of the external cavity laser setup formed by a current driven semiconductor laser diode with cavity length L_m and end-facet power reflectivities R_1 and R_2 coupled to an external cavity of length L_r via an external mirror with power reflectivity R_3. Laser emission is through R_1. The diamond of thickness d is included in the external cavity as a source of additional effective loss α_e.

related to the external cavity laser output power under on-resonant driving and thus the sensitivity of such a setup. The two different threshold currents can be determined by considering the threshold condition that the gain G must be equal to the total cavity loss α_t, which is valid when spontaneous emission is neglected.

$$G = \alpha_t \tag{2.105}$$

The total loss can be determined as the sum of the intrinsic cavity loss α_c due to the gain medium, the loss α_m from the mirrors and end facets and the effective loss α_e due to the diamond.

$$\alpha_t = \alpha_c + \alpha_m + \alpha_e \tag{2.106}$$

The individual loss terms are more easily obtained by using the three-mirror model [68–71] to treat the entire external cavity structure as a single cavity of length $L = L_m + L_r$ with the power reflectivities R_2 and R_3 replaced by an effective reflectivity $R_e = |r_e|^2$. All of the losses are then contained within the single cavity. The effective reflectivity R_e is obtained via the expression

$$r_e = r_2 \frac{1 - R_2}{r_2} \sum_n \varepsilon_n (-r_2 r_3 \mathrm{e}^{2i\Theta})^n, \tag{2.107}$$

where ε_n are the individual coupling factors from the nth reflection in the cavity, $\Theta = 2\pi L_r/\lambda$ is the phase component resulting from the external cavity, and r_2, r_3 are the complex field reflectivities, $R_2 = |r_2|^2$, $R_3 = |r_3|^2$, which can be derived from the Fresnel equations [72]

$$r_s = \frac{n_1 \cos(\theta_i) - n_2 \cos(\theta_t)}{n_1 \cos(\theta_i) + n_2 \cos(\theta_t)} \tag{2.108}$$

and

$$r_p = \frac{n_2\cos(\theta_i) - n_1\cos(\theta_t)}{n_2\cos(\theta_i) + n_1\cos(\theta_t)}. \tag{2.109}$$

The Fresnel equations describe the complex field reflectivities of s- and p-polarized light incident on the plane of a transition from a medium with refractive index n_1 to a medium with refractive index n_2 at an angle θ_i to the normal of the plane, with the transmitted light travelling at an angle θ_t to the normal of the plane. The orthogonal linear s- and p-polarizations refer to light polarized with its electric field normal and parallel to the plane of incidence, respectively. Given that any polarization can be decomposed into a combination of two orthogonal linear polarizations, these equations are sufficient to describe any given polarization.

For the sake of simplicity, we assume that the green light contains a single optical mode at a single frequency. We further assume normal incidence of the green light on the diamond and that the reflection from the diamond facets is minimal, such that the transmission is high. The diamond is assumed not to be in contact with the laser diode or the external mirror, such that the interface is always to air. We thus have $\theta_i = \theta = t = 0$, which allows us to simplify the Fresnel equations as

$$r_s = \frac{n_1 - n_2}{n_1 + n_2},\ r_p = \frac{n_2 - n_1}{n_2 + n_1}. \tag{2.110}$$

We assume that the length of the external cavity can be adjusted so that the resulting phase term $\mathrm{e}^{2i\Theta} = 1$. No exact analytical expression for ε_n exists [73], but the values can be approximated by assuming that the near field emission spot of the laser diode is elliptical with width $2b$ and height $2a$. The Fresnel numbers

$$F_a(L) = \frac{a^2}{\lambda L},\ F_b(L) = \frac{b^2}{\lambda L} \tag{2.111}$$

can then be used to approximate the coupling factors as

$$\varepsilon_n \approx \left[1 - 0.3(F_a(nL_r))^{-3/2} - 0.3(F_b(nL_r))^{-3/2}\right]^{1/2} \text{ for } F_a, F_b \gg 1 \tag{2.112}$$

and

$$\varepsilon_n \approx 0.72\left[F_a(nL_r)\cdot F_b(nL_r)\right]^{1/2} \text{ for } F_a, F_b \ll 1. \tag{2.113}$$

Under the previously mentioned assumptions regarding the green light, the green intensity $I(z)$ as a function of path length z in the diamond can be described as

$$I(z) = I_0\mathrm{e}^{-\alpha_d z}, \tag{2.114}$$

where I_0 is the green intensity without the diamond, and α_d is the absorption coefficient in the diamond. The absorption coefficient can be measured experimentally or derived from a rate equation model that will be presented later. If we assume that the losses due to the diamond are spread evenly throughout the cavity, we can define the effective loss due to the diamond as

$$\alpha_e = \alpha_d\frac{d}{L}. \tag{2.115}$$

The loss from the mirrors and end facets can be defined as

$$\alpha_m = \frac{1}{L} \ln \left(\frac{1}{\sqrt{R_1 R_e}} \right) \tag{2.116}$$

for the single cavity in the three-mirror model. The gain G can be defined phenomenologically [74] as

$$G = \Gamma a (N - N_{tr})(1 - \epsilon S), \tag{2.117}$$

where Γ is the confinement factor, a is the differential gain coefficient, N is the carrier density, N_{tr} is the carrier density at transparency, S is the photon density, and ϵ is the gain compression factor, which serves to phenomenologically account for spectral hole burning at high optical power and similar effects. The expression is valid for heterostructure laser diodes and certain quantum well structures where the carrier density at threshold N_{th} is close to N_{tr}. The differential gain coefficient a is determined by the construction of the diode and defines how well the semiconductor can generate carriers.

The carrier density N and photon density S can be described by the standard laser diode rate equations

$$\frac{dN}{dt} = \frac{I}{qV} - \frac{N}{\tau_N} - GS \tag{2.118}$$

and

$$\frac{dS}{dt} = GS - \frac{S}{\tau_P} + \frac{\beta N}{\tau_N}, \tag{2.119}$$

where I is the drive current, q is the electron charge, V is the volume of the gain region, τ_N is the carrier lifetime in the diode, τ_P is the photon lifetime in the cavity, and β is the spontaneous emission factor. The term GS is related to stimulated emission in the laser diode gain medium, the term $\frac{\beta N}{\tau_N}$ describes spontaneous emission, and the term $\frac{S}{\tau_P}$ describes the cavity loss due to the mirrors, gain medium and diamond. The volume of the gain region can be calculated as $V = L \cdot w \cdot t_h$, where w is the width and t_h the thickness of the laser diode active region. Given that we are only interested in the steady-state operation of the laser diode, we need only solve the rate equations for steady-state conditions where $\frac{dN}{dt} = \frac{dS}{dt} = 0$. At the lasing threshold without spontaneous emission ($\beta = 0$), where $G = \alpha_t$ and $S = 0$, we can use Eq. 2.117 to derive an expression for N_{th} the threshold carrier density.

$$N_{th} = N_{tr} + \frac{\alpha_t}{\Gamma a} \tag{2.120}$$

Inserting Eq. 2.120 into Eq. 2.118 under steady-state and threshold conditions yields an expression for the threshold current I_{th} as

$$I_{th} = \frac{qV}{\eta_i \tau_N} N_{th} = \frac{qV}{\eta_i \tau_N} \left[N_{tr} + \frac{\alpha_t}{\Gamma a} \right], \tag{2.121}$$

where the quantum efficiency η_i of the carrier to photon conversion has been introduced. By adjusting α_t to reflect the situation with either on-resonance or off-resonance driving of the NV center electron spin transitions, we can thus use Eq. 2.121 to obtain the threshold current for these situations. Furthermore, we can define the output coupling efficiency η_0 as the ratio between the photon loss through R_1 and the total photon loss, i.e.

$$\eta_0 = \frac{\alpha_{m1}}{\alpha_t} = \frac{\ln\left(\frac{1}{\sqrt{R_1}}\right)}{\ln\left(\frac{1}{\sqrt{R_1 R_e}}\right) + L(\alpha_c + \alpha_e)}, \tag{2.122}$$

and use it to calculate the output laser power from R_1 for a given photon density S as

$$P_{out} = \eta_0 \frac{hc}{\lambda \tau_P} \frac{V}{\Gamma} S, \tag{2.123}$$

where h is Planck's constant, c is the speed of light, λ is the wavelength, and V/Γ is the effective mode volume of the cavity. The photon density S can be obtained by numerically solving Eqs. 2.118-2.119, which is a valid approach regardless of whether or not the spontaneous emission is being neglected.

Eq. 2.123 can thus be used to simulate the expected ODMR spectrum, from which the maximum ODMR slope can be extracted. The sensitivity can then be estimated by dividing the background noise level by the maximum ODMR slope in order to determine the smallest transition frequency shift that can be detected, which can be converted to magnetic sensitivity via the electron gyromagnetic ratio $\gamma_e = 28\,\mathrm{MHz/mT}$.

However, as was previously mentioned, we need to determine α_t and thus $\alpha_e = \alpha_d L/d$ for the situations with on- and off-resonance driving of the NV center electron spin transitions in order to utilize the expressions for I_{th} and also P_{out}. To this end, we need to model the absorption of green light by the NV centers.

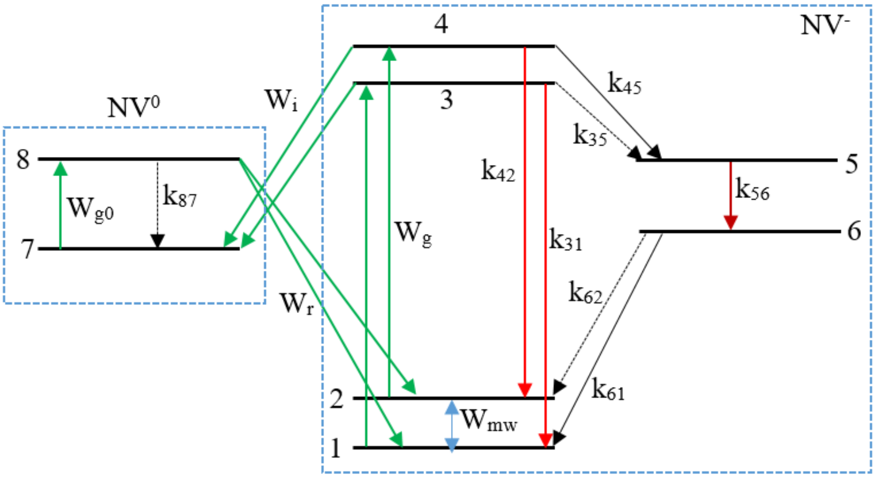

Figure 2.9: Sketch of the 8-level model used to describe the green absorption by the NV center. The model includes both the negatively charged NV$^-$ and the neutral NV^0. The rate of ionization of NV$^-$ to NV^0 is W_i, the rate of recombination of NV^0 to NV$^-$ is W_r, the rate of green excitation of NV$^-$ is W_g, the rate of green excitation of NV^0 is W_{g0}, and the rate of MW driving of the $1 \Longleftrightarrow 2$ transition is W_{MW}. The decay rate from state i to state j is k_{ij}.

2.6.1 Modelling the green absorption

The green absorption can be described via a model for the NV center similar to the one depicted in Fig. 2.1. However, when considering the green absorption, it is relevant to also include the ionization of NV$^-$ to NV^0 and the recombination of NV^0 to NV$^-$, both of which involve absorption of green light. The NV^0 center has a ground and excited state, and the ionization goes from the NV$^-$ triplet excited states to the NV^0 ground state with rate W_i. The NV^0 ground state is excited with rate W_{g0}, and the recombination goes from the NV^0 excited state to the NV$^-$ triplet ground states with rate W_r. The other possible transitions are the same as those depicted in Fig. 2.1. Both the excited $m_S = \pm 1$ states and the ground $m_S = \pm 1$ states are treated as single states because the $m_S = \pm 1$ states have the same properties regarding the absorption of green light. The excitation from the triplet ground states to the triplet excited states occurs with rate W_g. The transition between the ground $m_S = 0$ state and the ground $m_S = \pm 1$ state is driven with a rate W_{MW}. We then consider a system of 8 states with the normalized population densities $\sum_{i=1}^{8} n_i = 1$, where n_1 refers to the ground $m_S = 0$ state, n_2 refers to the ground $m_S = \pm 1$ state, n_3 refers to the excited $m_S = 0$ state, n_4 refers to the excited $m_S = \pm 1$ state, n_5 refers to the singlet excited state, n_6 refers to the singlet ground state, n_7 refers to the NV^0 ground state, and n_8 refers to the NV^0 excited state. The decay rate from state i to state j is written as k_{ij}. The model is illustrated in Fig. 2.9.

The evolution of the normalized population densities can then be described by the rate equations

$$\begin{aligned}
\frac{dn_1}{dt} &= -(W_g + W_{MW})n_1 + W_{MW}n_2 + k_{31}n_3 + k_{61}n_6 + \frac{W_r}{2}n_8 \\
\frac{dn_2}{dt} &= W_{MW}n_1 - (W_g + W_{MW})n_2 + k_{42}n_4 + k_{62}n_6 + \frac{W_r}{2}n_8 \\
\frac{dn_3}{dt} &= W_g n_1 - (k_{31} + k_{35} + W_i)n_3 \\
\frac{dn_4}{dt} &= W_g n_2 - (k_{42} + k_{45} + W_i)n_4 \\
\frac{dn_5}{dt} &= k_{35}n_3 + k_{45}n_4 - k_{56}n_5 \\
\frac{dn_6}{dt} &= k_{56}n_5 - (k_{61} + k_{62})n_6 \\
\frac{dn_7}{dt} &= W_i n_3 + W_i n_4 - W_{g0}n_7 + k_{87}n_8 \\
\frac{dn_8}{dt} &= W_{g0}n_7 - (k_{87} + W_r)n_8
\end{aligned} \tag{2.124}$$

with the rates given as $W_g = \sigma_g I_g \lambda/(hc)$, $W_{g0} = \sigma_{g0} I_g \lambda/(hc)$, $W_i = \sigma_i I_g \lambda/(hc)$, $W_r = \sigma_r I_g \lambda/(hc)$ and $W_{MW} = \Omega_R^2 T_2^*/2$, where I_g is the green intensity, and the σ_β-parameters are absorption cross-sections. The decay rates and cross-sections are $k_{31} = k_{42} = 66\ \mu\text{s}^{-1}$, $k_{35} = 7.9\ \mu\text{s}^{-1}$, $k_{45} = 53\ \mu\text{s}^{-1}$, $k_{61} = 1.0\ \mu\text{s}^{-1}$, $k_{62} = 0.7\ \mu\text{s}^{-1}$, $k_{56} = 1.0\,\text{ns}^{-1}$, $k_{87} = 53\ \mu\text{s}^{-1}$, $\sigma_g = 3.0 \times 10^{-21}\,\text{m}^2$, $\sigma_{g0} = 1.8\sigma_g$, $\sigma_i = 9.5 \times 10^{-21}\,\text{m}^2$ and $\sigma_r = 9.8 \times 10^{-21}\,\text{m}^2$ [75]. The rate equations can be solved under steady-state conditions ($\frac{dn_i}{dt} = 0$) to obtain the normalized population densities for a given set of parameters. The situation with off-resonance MW driving can be represented by $W_{MW} = 0$. In the case of off-resonance MW driving, all of the NV centers will be off-resonantly driven, and the number density N_i^{off} of NV centers in a given state can be obtained by multiplying the normalized population density of that state n_i^{off} with the total NV density N_{NV}.

$$N_i^{off} = N_{NV} n_i^{off} \tag{2.125}$$

In the case of on-resonance MW driving, however, we will only be able to drive 1/4 of the NV centers on-resonance due to the four different possible crystallographic axes, as was previously mentioned. The remaining NV centers will be driven off-resonance. The number density N_i^{off} of NV centers in a given state during on-resonance driving will thus be given by

$$N_i^{on} = 1/4 N_{NV} n_i^{on} + 3/4 N_{NV} n_i^{off}. \tag{2.126}$$

The absorption coefficient α_d for either on- or off-resonance driving can then be calculated by multiplying the number density of NV centers in the states that can absorb green light by the relevant absorption cross-sections.

$$\alpha_d^{on} = \sigma_g(N_1^{on} + N_2^{on}) + \sigma_{g0}N_7^{on} + \sigma_i(N_3^{on} + N_4^{on}) + \sigma_r N_8^{on} \tag{2.127}$$

$$\alpha_d^{off} = \sigma_g(N_1^{off} + N_2^{off}) + \sigma_{g0}N_7^{off} + \sigma_i(N_3^{off} + N_4^{off}) + \sigma_r N_8^{off} \tag{2.128}$$

We have now derived all of the necessary expressions to simulate the considered laser threshold magnetometry setup.

3 Optimal control of a nitrogen-vacancy spin ensemble in diamond for sensing in the pulsed domain

3.1 Introduction

It is desirable to work with a large ensemble of NV centers when seeking to maximize the sensitivity. However, the ability to control such an ensemble is negatively impacted by inhomogeneous broadening of the transition frequencies and drive field inhomogeneity. In order to address this issue, we considered the use of optimal control theory to design shaped MW pulses that are robust against inhomogeneous broadening and drive field amplitude variations. Furthermore, we expanded the approach to explicitly include the effects of hyperfine splitting. The expanded methodology could then be used to design robust pulses capable of simultaneously driving all of the hyperfine transitions.

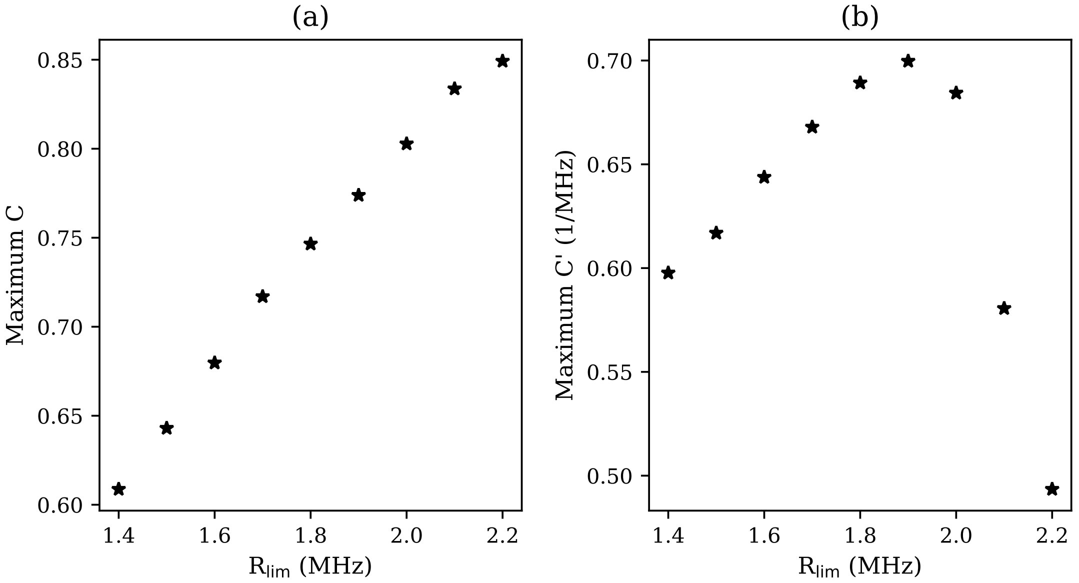

Figure 3.1: Results obtained from simulations of π-pulse ODMR on an ensemble with inhomogeneous broadening between $\pm 1\,\mathrm{MHz}$ and drive amplitude variations between $\pm 10\%$ around the intended value using optimal control π-pulses. The optimal control pulses were optimized for the same level of inhomogeneous broadening and drive amplitude variations as the ensemble with pulse duration $t_p = 1.85\,\mu\mathrm{s}$ and the listed values of the maximum allowed Rabi frequency R_{lim}. The plots indicate (a) the extracted maximum contrast C and (b) the extracted maximum slope in contrast C' as a function of R_{lim}.

We designed optimal control π-pulses optimized for reasonable inhomogeneous broadening between $\pm 1\,\mathrm{MHz}$, low drive amplitude variations between $\pm 10\%$ around the intended value and various values of the pulse duration t_p and the maximum allowed Rabi frequency R_{lim}. These pulses were then used for simulations of π-pulse ODMR on an ensemble with the same level of inhomogeneous broadening and drive amplitude variations. From these simulations, we extracted the maximum ODMR slope, which is directly linked to the maximum achievable sensitivity. It was found that pulses with durations of approximately 1.85 µs yielded the largest maximum ODMR slope. The dependence of the maximum contrast C and ODMR slope C' for these pulses on the maximum allowed Rabi frequency R_{lim} is illustrated in Fig. 3.1.

As expected, the maximum contrast is observed to increase with increasing values of R_{lim}. However, the maximum slope in contrast peaks at $R_{\text{lim}} = 1.9\,\text{MHz}$ and then decreases with increasing R_{lim}. This is due to the fact that the slope, naturally, represents the change in contrast, and thus the maximum slope will occur for the simulated ODMR spectrum that features the largest change in contrast rather than simply maximum contrast. In other words, the maximum slope in a simulated ODMR spectrum depends on both the maximum contrast, the adjacent minima in the contrast and the distance in frequency between them. Even if the maximum contrast is increased, the maximum slope might still decrease if the minimum contrast or the distance between minima and maxima is increased. The simulations thus indicate that the largest ODMR slope is achieved using the optimal control π-pulse with $R_{\text{lim}} = 1.9\,\text{MHz}$.

For comparison, the slope obtained from π-pulse ODMR simulations with flat π-pulses can similarly be investigated to determine the Rabi frequency $\leq R_{\text{lim}}$ that yields the maximum slope. It was found that a three-frequency drive with a Rabi frequency of the individual drives equal to $\Omega_R = 2\pi \cdot 0.6\,\text{MHz}$ yielded the largest slope in contrast for the considered ensemble. The simulated π-pulse ODMR spectra and associated contrast slopes for the optimal and flat drives that achieve the largest slope in contrast are shown together in Fig. 3.2.

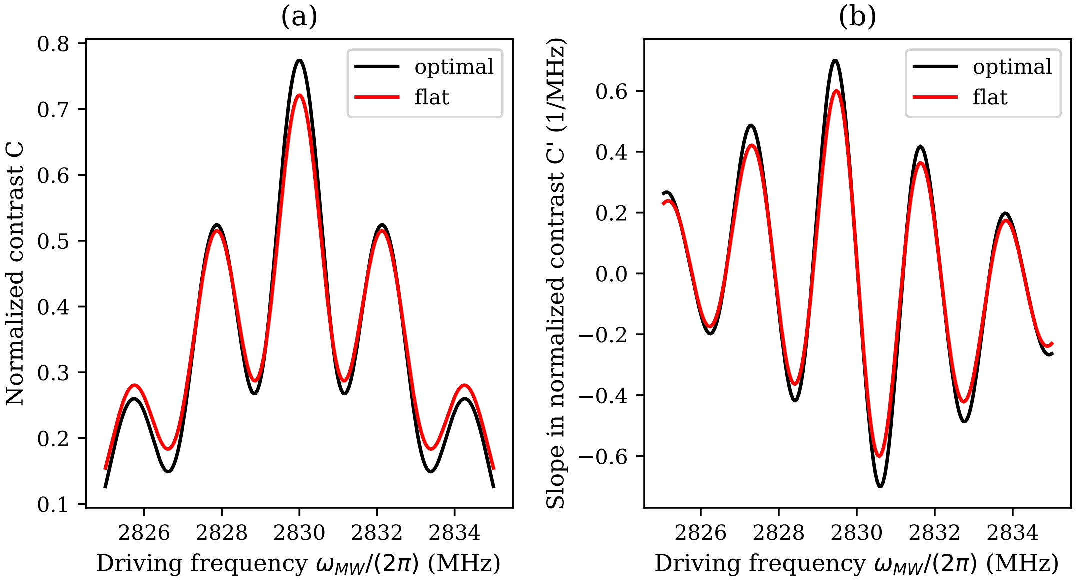

Figure 3.2: (a) The simulated π-pulse ODMR spectra for an ensemble with inhomogeneous broadening between ± 1 MHz and drive amplitude variations between $\pm 10\%$ around the intended value using either an optimal control π-pulse or a flat π-pulse. The optimal control π-pulse was optimized for inhomogeneous broadening and drive amplitude variations matching the ensemble with $t_p = 1.85\,\mu\text{s}$ and $R_{\text{lim}} = 1.9\,\text{MHz}$, while the flat π-pulse was a three-frequency drive with the Rabi frequency of the individual drives set to $\Omega_R = 2\pi \cdot 0.6\,\text{MHz}$. (b) The slopes in contrast extracted from (a).

As is illustrated in Fig. 3.2(b), the simulations indicated that one can achieve a 16% increase in the maximum π-pulse ODMR slope by using a properly designed optimal control pulse instead of an optimized three-frequency flat drive. These results motivated a collaboration with another PhD student, Joshua Clement, in order to experimentally demonstrate that such an improvement is possible. Joshua Clement was responsible for the experimental implementation, while I handled the design of the optimal control pulses. It was noted, however, that the presence of experimental imperfections and other factors that are not included in the simulations makes it possible that the improvement will not match the simulations. Similarly, the flat and optimal control π-pulses that perform best experimentally may not be the same as in the simulations. As a result, different pulses were designed and tested experimentally. The main findings are summarized in the publication in section 3.2, and the supplementary information is given in section 3.3.

3.2 Publication

Optimal control of a nitrogen-vacancy spin ensemble in diamond for sensing in the pulsed domain

Andreas F.L. Poulsen,[1, a)] Joshua D. Clement,[1, a)] James L. Webb,[1, b)] Rasmus H. Jensen,[1] Kirstine Berg-Sørensen,[2] Alexander Huck,[1, c)] and Ulrik Lund Andersen[1, d)]
[1)]*Center for Macroscopic Quantum States (bigQ), Department of Physics, Technical University of Denmark, Kgs. Lyngby, Denmark*
[2)]*Department of Health Technology, Technical University of Denmark, Kgs. Lyngby, Denmark*

Defects in solid state materials provide an ideal, robust platform for quantum sensing. To deliver maximum sensitivity, a large ensemble of non-interacting defects hosting coherent quantum states are required. Control of such an ensemble is challenging due to the spatial variation in both the defect energy levels and in any control field across a macroscopic sample. In this work we experimentally demonstrate that we can overcome these challenges using Floquet theory and optimal control optimization methods to efficiently and coherently control a large defect ensemble, suitable for sensing. We apply our methods experimentally to a spin ensemble of up to 4×10^9 nitrogen vacancy (NV) centers in diamond. By considering the physics of the system and explicitly including the hyperfine interaction in the optimization, we design shaped microwave control pulses that can outperform conventional (π-) pulses when applied to sensing of temperature or magnetic field, with a potential sensitivity improvement between 11 and 78%. Through dynamical modelling of the behaviour of the ensemble, we shed light on the physical behaviour of the ensemble system and propose new routes for further improvement.

I. INTRODUCTION

Solid state defects are a promising platform for quantum sensing, where purely quantum mechanical properties such as superposition and entanglement can be utilized to overcome classical limitations.[1,2]. Particularly in semiconductors, where they can be controllably created and manipulated, solid state defects can host quantum states that are both long-lived and sensitive to the local environment in discrete energy levels within the bandgap. A typical and extensively used defect system is the nitrogen-vacancy (NV) center in diamond. This consists of a substitutional nitrogen atom and an adjacent lattice vacancy, having discrete electronic and nuclear spin states with long coherence times up to room temperature.[3] The optical properties of the negatively-charged NV center (NV^-) are highly sensitive to a range of parameters including magnetic field[4–9], electric field[5,10], temperature[11,12] and pressure (strain).[13] Applications include sensing using a scanning diamond tip[14,15], nanoscale nuclear magnetic resonance (NMR)/ electron spin resonance (ESR)[16,17] and in biophysics,[18–21] where robustness and high biocompatibility of diamond makes it an ideal platform for sensing, even within biological samples.[22,23]

The level structure of the NV^-, illustrated schematically in Fig. 1(a) consists of spin triplet ground and excited states and metastable spin singlet states.[6,9,24–26]. When green laser light is absorbed by an NV in m_s=0, red fluorescence is emitted from decay back into the triplet ground state. However, when absorbed in the spin-split m_s=±1, decay back to m_s=0 may occur through singlet shelving states, via nonradiative and infrared emission. The populations of m_s=0 and ±1 can be controlled by applying resonant microwaves (f = 2.87 GHz in the absence of an external bias magnetic field). This results in a detectable decrease in red fluorescence output on resonance, with contrast C of 1-2 % for a large ensemble of defects and up to 30 % for a single NV[26]. The m_s=±1 states can be split in energy e.g. via the Zeeman effect by an external magnetic field, giving rise to multiple spectral features including additional sub-features due to hyperfine splitting introduced by coupling to the nuclear spin of the ^{14}N or ^{15}N impurity atom[27]. By sweeping microwave frequency, these resonances can be identified by the drop in fluorescence output, a process termed optically detected magnetic resonance (ODMR) spectroscopy. By fixing the microwave drive frequency on or close to a resonance, any frequency shift resulting from the level shift of m_s=±1 by magnetic field, electric field or local temperature can be detected.

Sensing using NV centers can be performed by a simple continuous wave (CW) method, maintaining a constant intensity of microwave and laser irradiation[25,28]. Alternatively, laser and microwave pulses can be used to control and read the ensemble[26,29]. This relies on the NV behaving as a two-level quantized system[30], with one (bright) maximally fluorescent state, $|0\rangle$, and one (dark) state with reduced fluorescence under illumination with green light, $|\pm1\rangle$. For a single NV, these correspond to the electron spin states m_s=0 and m_s=±1 respectively. Rabi oscillations can be observed in C on application of a microwave field resonant with the ground state splitting. This allows coherent control using discrete laser

---

[a)] These authors contributed equally to this work
[b)] Electronic mail: jaluwe@fysik.dtu.dk
[c)] Electronic mail: alexander.huck@fysik.dtu.dk
[d)] Electronic mail: ulrik.andersen@fysik.dtu.dk

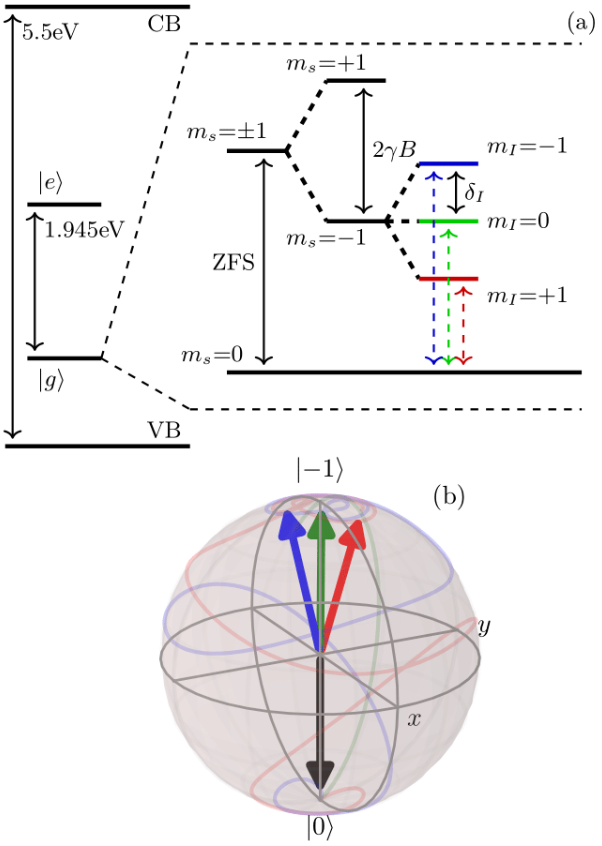

FIG. 1. Color online. (a) Simplified level diagram for a single NV$^-$ center within the diamond bandgap, with the ground state levels shown in detail. At zero magnetic field there is a splitting of 2.87 GHz (ZFS) between the m_s=0 and m_s=±1 states. At finite field B, the Zeeman effect shifts the m_s=±1 states in energy by γB. The m_s=±1 states are further split into 3 hyperfine levels (m_l=0,±1) separated by δ_l = 2.16 MHz. (b) Bloch sphere representation depicting this $m_s = \{0, -1\}$ two-level system and the time evolution and result vector for a shaped optimal microwave pulse applied to the initial ground state ($|0\rangle$, black arrow). Here we show the time evolution for each of the hyperfine resonances m_l.

and microwave pulses, offering improvement over CW methods through reduction in the power broadening of the resonance linewidths. Techniques such as Ramsey interferometry[31,32] and Hahn echo-type sequences have been demonstrated[33,34], realizing single molecule sensitivity in nanoscale diamond NMR experiments.[35–37]

Pulsed schemes are used extensively for quantum sensing measurements using single or few-NV centers often in a confocal microscopy setup.[38–40] However, as extensive nuclear magnetic- and electron spin- resonance experiments have shown, a macroscopic ensemble of many billions of electron or nuclear spins in a larger volume can also be manipulated by microwave pulse sequences in the same manner.[41] From a quantum sensing perspective, large ensembles are desirable for imaging applications,[19] for vector sensing,[42] or to maximize bulk sensitivity where spatial resolution is not required, since the shot noise-limited sensitivity scales as $1/\sqrt{N}$, with N the number of defect centers.[4] Compared to single NV readout, ensemble NV sensing with flat (fixed amplitude and phase) microwave pulses suffers from nonuniform pulse operation. Inhomogeneous broadening due to strain and bias field gradients spreads the distribution of resonance frequencies of the NV centers, detuning many from a central drive frequency. In addition, the near-field microwave drive can vary in central resonance frequency, power, and phase across the ensemble, depending on the antenna and microwave coupling to the diamond.[43] This makes control of a large ensemble challenging.

To overcome these issues, several approaches have been investigated for higher frequency AC sensing (> 10 kHz), beginning with dynamical decoupling,[7,34,44,45] and with further correction using e.g. adiabatic chirped pulses.[8]. These are however unsuitable for applications that require DC to low frequency sensing, particularly for applications in biosensing[20,46–48]. An alternative in this frequency range is to deliver shaped microwave pulses (varying phase and amplitude), in order to boost fidelity in a Ramsey or pulsed ODMR[30] scheme. Such pulses can be designed using optimal control methods.[33,49–52] Optimal pulses have been used with small ensembles of NV centers for Hahn-echo[33,49,53] or Carr-Purcell sequences,[54] to improve the robustness and temperature sensitivity of the D-Ramsey scheme,[55] to extend the coherence time of an NV,[56] and to improve the accuracy of entanglement operations[57].

In this work, we demonstrate the use of shaped microwave pulses produced by optimal control methods combined with Floquet theory that can deliver improved coherent control over a large solid state defect ensemble of diamond NV centers. We show improved ODMR contrast and therefore potentially higher sensitivity when compared to a conventional flat π-pulse sensing scheme. Our scheme is widely adaptable to a range of solid state systems where a two-level quantum system can be realized, although we specifically test our methods using an NV ensemble in diamond. We achieve our improvement through a full consideration of the physics of the system, including the hyperfine interaction with the nuclear spin of the subsitutional nitrogen in the NV center (both ^{14}N and ^{15}N). We model ensemble behaviour to further understand the physics of the system, in particular to explain the dynamics when a readout laser pulse is applied. This is also to uncover new routes for improvement for quantum sensing. We demonstrate our methods experimentally in off-the-shelf, standard grade material without significant processing or fabrication. Furthermore, we demonstrate operation at low Rabi frequencies, typical of those achievable using low-power microwave amplification e.g. in a portable sensor device.[58]

The paper is structured as follows. In Section II A we outline the basic methodology we use to construct and generate our shaped microwave pulses using optimal control theory, including our derivation for explicitly including the hyperfine interaction in the optimization algorithm. We describe a number of key control parameters, the limits of which we discuss in Section II B. In Section II C we describe in detail our experimental setup and methodology and in Sections III A and III B we demonstrate the use of optimized shaped pulses for ODMR spectroscopy, compare to a conventional π-pulse scheme using a flat microwave pulse, and analyze and discuss the optical behaviour and how this relates to the physical dynamics of the NV ensemble.

II. METHODS

A. Optimal Control

Our optimal control algorithm maximizes a functional that describes the desired transfer of one quantum state to another.[25,33,49,51,52,59]. We define our state transfer functional as:

$$F_{\mathrm{st}} = \left| \left\langle \psi_f \left| \hat{U}(t_p) \right| \psi_i \right\rangle \right|^2 , \tag{1}$$

where $\mathcal{F}_{\mathrm{st}}$ is the fidelity, of value between 0 and 1, which describes how well the pulse transfers the quantum state of a solid state defect from an initial state $|\psi_i\rangle$ to a final state $|\psi_f\rangle$. A fidelity of 1 represents a complete transfer to the desired state. The influence of the pulse is described by the unitary time evolution operator $\hat{U}(t_p)$, where t_p is the pulse duration.

To represent the state transfer of an ensemble, we calculate F_{st} for each member of a sample of defects with a specified range of frequency detuning $\hat{\Delta}$ and relative control amplitude $\hat{\alpha}$. These factors are set to be representative of the variation across a real ensemble. The relative control amplitudes α_i represent the drive field inhomogeneity across the ensemble, and each value is the ratio between the Rabi frequency at which a given single defect is driven (due to drive field inhomogeneity) and the Rabi frequency at which the pulse is designed to drive the defects. The values of α_i thus vary around unity across the representative sample. The relative control amplitude only relates to the changes in Rabi frequency caused by drive field inhomogeneity and does not include the effects of frequency detuning on the Rabi frequency. These effects are included in the optimization separately via the Δ_i values, which represent the inhomogenous broadening. We thus assign each defect in the representative sample a value of α_i and Δ_i within the specified range $\hat{\Delta}$ and $\hat{\alpha}$ and seek a pulse that maximizes the average fidelity of the entire representative ensemble. Using this model assumes that interaction between defects is minimal, such that each defect can act as as single, isolated quantum defect in the material.

We assume our detunings Δ_i follow a Gaussian distribution centered at zero. The full width at half maximum (FWHM) of this Gaussian distribution is set equal to half of the width of the considered detuning range $\hat{\Delta}$. The α_i values are assumed to follow a flat distribution. The weight of each defect in the representative ensemble is thus equal to the weight of its Δ_i value. These are normalized such that the sum of the weights of all defects in the representative ensemble is equal to 1. We therefore also use a weighted average of the fidelity. For numerical optimization, we use throughout this work a representative ensemble of size 12x12 (12 values to cover the ranges $\hat{\Delta}$ and $\hat{\alpha}$, respectively). This was based on a series of simulations of the performance of pulses transferring state $|0\rangle$ to $|-1\rangle$ (Fig. 1(b)) optimized using different representative ensembles. As shown in Fig. 2, 12x12 more than ensures convergence of the fidelity, while minimizing computational time.

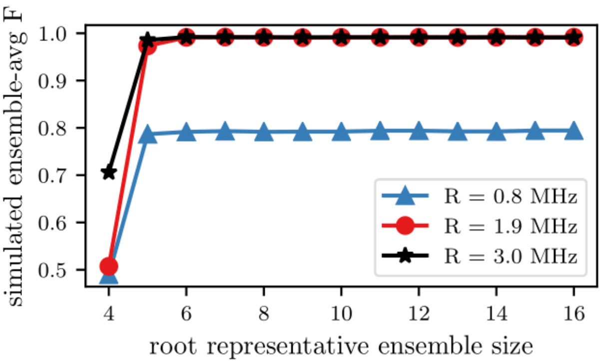

FIG. 2. Color online. The simulated weighted average fidelity of optimal control pulses optimized with different ensemble sizes as a function of representative ensemble size for three values of the maximum allowed Rabi frequency R_{lim}. The pulses were optimized for $\hat{\Delta} = \pm 1$ MHz detuning, $\hat{\alpha} = 1 \pm 10\,\%$ amplitude variations and a duration of $t_p = 1.85\,\mu\mathrm{s}$ with the indicated values of $R = R_{\mathrm{lim}}$.

For the design of our shaped microwave pulses, we use smooth optimal control. Here we choose a basis of periodic functions with the same periodicity T and discretized frequency components, resulting in the shaped pulses becoming smooth in time.[50] In this work, we use a basis of sine functions with a fundamental frequency determined by the pulse duration t_p.[33,49] Smooth optimal control has experimental advantages over alternatives such as gradient ascent pulse engineering (GRAPE)[60] in that the bandwidth and the individual frequency components are known in advance and the number of high frequency components in the pulse Fourier spectrum is reduced, making modulation in experiments less technically demanding.[50] Our smooth optimal control pulse has the general form:

$$S(t) = I(t) \cos(\omega_D t) + Q(t) \sin(\omega_D t) , \tag{2}$$

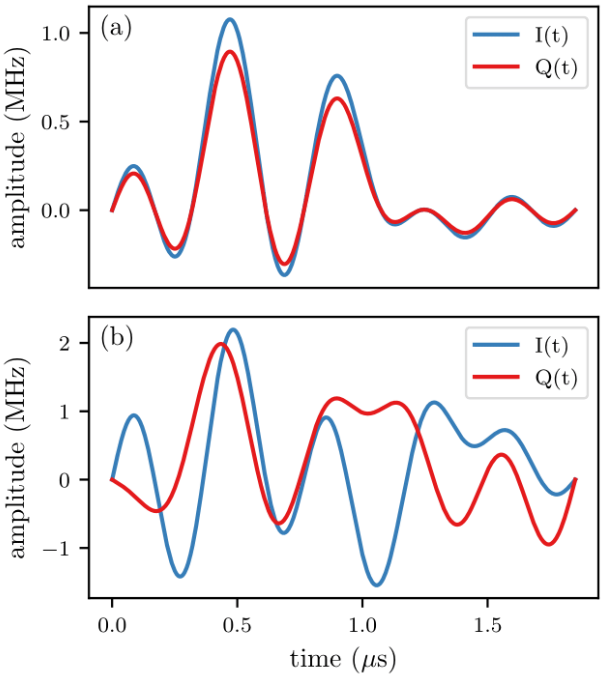

FIG. 3. Color online. Plot of $I(t)$ and $Q(t)$ in units of Rabi frequency for two optimal control pulses that were optimized by including state transfer using all three hyperfine levels. The pulses were optimized for $\hat{\Delta} = \pm 1\,\text{MHz}$ detuning and $\hat{\alpha} = 1 \pm 10\,\%$ amplitude variations with a duration of $t_p = 1.85\,\mu\text{s}$ and a maximum allowed Rabi frequency of (a) 1.4 MHz and (b) 3.0 MHz.

where

$$I(t) = \sum_{j=1}^{N_f} 2a_{jx} \sin{(j\Omega_f t)}\,,\; Q(t) = \sum_{j=1}^{N_f} 2a_{jy} \sin{(j\Omega_f t)}\,. \tag{3}$$

Here, ω_D is the central driving frequency, $\Omega_f = 2\pi/(2t_p)$ is the fundamental frequency, N_f is the number of frequency components and the real a_{jk}-values are control amplitudes. The bandwidth of such a pulse is then $N_f\Omega$. The fundamental frequency is not related to the Rabi frequency and purely serves to enforce the desired periodicity of $T = 2t_p$. The a_{jk}-values are, however, defined in units of Rabi frequency. As an example, Fig. 3 shows the in-phase and quadrature components $I(t)$ and $Q(t)$ used to modulate the microwave carrier for two of the specific pulses that we designed. In our experiments, the microwave carrier has a frequency $\omega_D \approx 2.8\,\text{GHz}$ corresponding to the splitting between the m_s=0 and m_s=-1 levels of the NV center ground state with an applied bias magnetic field.

It has been previously shown[53] that the performance of smooth optimal control pulses improves with increasing N_f until it saturates for $N_f \geq 7$. We use $N_f = 10$ for all of our pulses to ensure that we are in the saturated regime. This yields 20 different control amplitudes a_{jk} per shaped pulse, and these are the parameters that are optimized by the control algorithm. The optimization is carried out iteratively by stepping along the gradient of the fidelity with respect to the control amplitudes with a step size β. Starting with initial control amplitudes a_{jk}, we compute the resulting $\hat{U}(t_p)$, $\mathcal{F}_{\text{st}}$ and $\frac{\partial \mathcal{F}_{\text{st}}}{\partial a_{jk}}$, before updating the control amplitudes by adding $\beta\frac{\partial \mathcal{F}_{\text{st}}}{\partial a_{jk}}$. This process is then repeated until $\mathcal{F}_{\text{st}}$ converges. The choice of time-periodic basis functions yields a time-periodic Hamiltonian that can be solved using Floquet theory.[50,61,62]

In this work, we extend previous methods to include the effects of hyperfine splitting during the optimization. Although we specifically calculate for diamond NV centers here, this method is generally adaptable and applicable to any such splitting for a defect ensemble. The goal is to create a shaped pulse that performs the state transfer $|0\rangle$ to $|-1\rangle$ simultaneously and with as high fidelity as possible for each of the m_l hyperfine levels. For an NV center ensemble, this results in a higher ODMR contrast than would be otherwise achievable by acting on only one m_l. This is analogous to continuous wave methods driving multiple hyperfine lines previously described in the literature.[63] By doing this in the pulsed domain, we seek to achieve similar benefits, but without the negative effects of power broadening of the resonance linewidths. In order to explicitly account for the hyperfine splitting, it is necessary to modify the expression for the Fourier components of the Hamiltonian that make up the Floquet matrix. The Fourier components of the Hamiltonian are generally defined as

$$\hat{\mathcal{H}}_n = \frac{1}{T}\int_0^T \exp{(-in\Omega_f t)}\,\hat{\mathcal{H}}(t)\,\text{d}t, \tag{4}$$

where $T = 2t_p$ is the periodicity of the Hamiltonian and $\hat{\mathcal{H}}(t)$ is the time-domain Hamiltonian that describes the system to be optimized. The nitrogen in an NV can be either ^{14}N with $I = 1$ (highest natural abundance) or ^{15}N with $I = 1/2$, yielding either three or two hyperfine levels, respectively, as illustrated in Fig. 1(a). We assume hyperfine interaction between the ^{14}N nuclear spins and the NV electron spins in the ensemble so that three hyperfine states are possible. The nuclear spins are assumed to be in a thermal state such that all m_l hyperfine states are equally represented in the ensemble. The ODMR spectrum then contains three resonances separated by $\delta_l = 2.16\,\text{MHz}$, corresponding to the three hyperfine resonances m_l=-1,0,1. We also assume that the different NV electron spins do not interact and that the m_s=±1 states are clearly split by a static magnetic bias field. A single set of three NV centers that each correspond to one of the hyperfine transitions can then be reasonably approximated as three independent two-level systems. The drift Hamiltonian thus has the form

$$\hat{\mathcal{H}}_0 = \sum_{k=1}^{3} \frac{\omega_{0,k}}{2}\sigma_{z,k}, \tag{5}$$

where $\omega_{0,k}$ is the transition frequency of hyperfine transition k, and $\sigma_{z,k}$ is a Pauli spin-z matrix that is specific to transition k. Note that the above expression applies to any two-level defect with three equidistant hyperfine resonances that fulfills the underlying assumptions. The transition frequencies are related via $\omega_{0,1} = \omega_{0,2} - \delta_l$ and $\omega_{0,3} = \omega_{0,2} + \delta_l$. Given that the states of the three two-level systems can be completely described by a single vector of length 6, the $\sigma_{z,k}$-matrices can also be represented by 6-by-6 matrices. (See Appendix A). The same is true of the $\sigma_{x,k}$- and $\sigma_{y,k}$-matrices. The control Hamiltonian describes the interaction between the control pulse of the form given in Eq. (2) and the three allowed transitions.

Assuming the control field is linearly polarized in the x-direction, which is perpendicular to the defect axis, the control Hamiltonian can be written in the form:

$$\hat{\mathcal{H}}_c = \sum_{k=1}^{3} \sigma_{x,k}\left[I(t)\cos(\omega_D t) + Q(t)\sin(\omega_D t)\right], \tag{6}$$

and the total Hamiltonian thus has the form

$$\begin{aligned}\hat{\mathcal{H}}(t) = \sum_{k=1}^{3} \Big(&\frac{\omega_{0,k}}{2}\sigma_{z,k} \\ &+\sigma_{x,k}\left[I(t)\cos(\omega_D t) + Q(t)\sin(\omega_D t)\right]\Big).\end{aligned} \tag{7}$$

We can simplify the rest of the calculations by working in a rotating frame given by the unitary rotation operator

$$\hat{R} = \exp\left(\sum_{k=1}^{3} i\omega_D t\sigma_{z,k}/2\right), \tag{8}$$

which will commute with every term in $\hat{\mathcal{H}}_c$ except for $\sigma_{x,k}$. More precisely, $[\sigma_{z,k}, \sigma_{x,k'}] = 2i\sigma_{y,k}\delta_{k,k'}$ and $[\sigma_{z,k}, \sigma_{y,k'}] = -2i\sigma_{x,k}\delta_{k,k'}$.

The Baker-Campbell-Hausdorff lemma thus allows us to write

$$\begin{aligned}\hat{R}\hat{\mathcal{H}}_c\hat{R}^\dagger = \sum_{k=1}^{3} &\left(\sigma_{x,k}\cos(\omega_D t) + \sigma_{y,k}\sin(\omega_D t)\right) \\ &\times\left[I(t)\cos(\omega_D t) + Q(t)\sin(\omega_D t)\right].\end{aligned} \tag{9}$$

Using this expression and defining the detuning, $\Delta = \omega_{0,2} - \omega_D$, as the difference between the transition frequency of the central hyperfine transition, $\omega_{0,2}$, and the central driving frequency, ω_D, we obtain the expression

$$\begin{aligned}\hat{\mathcal{H}}' = \sum_{k=1}^{3} \Big(&\frac{\Delta + w_k\delta_l}{2}\sigma_{z,k} \\ &+ \left(\sigma_{x,k}\cos(\omega_D t) + \sigma_{y,k}\sin(\omega_D t)\right) \\ &\times\left[I(t)\cos(\omega_D t) + Q(t)\sin(\omega_D t)\right]\Big),\end{aligned} \tag{10}$$

where $w_1 = -1$, $w_2 = 0$ and $w_3 = 1$. Expanding by using trigonometric relations, the above expression can be simplified by using the rotating wave approximation to eliminate the fast-oscillating terms

$$\hat{\mathcal{H}}' = \sum_{k=1}^{3} \left(\frac{\Delta + w_k\delta_l}{2}\sigma_{z,k} + \frac{I(t)}{2}\sigma_{x,k} + \frac{Q(t)}{2}\sigma_{y,k}\right). \tag{11}$$

Combining Eq. (11) with Eq. (3) and inserted into Eq. (4), the Fourier components of the Hamiltonian become

$$\begin{aligned}\hat{\mathcal{H}}_n = \sum_{k=1}^{3} \frac{1}{T}\int_0^T \exp(in\Omega t)\Big(&\frac{\Delta + w_k\delta_l}{2}\sigma_{z,k} \\ &+\sum_{j=1}^{N_f}\left[a_{jx}\sigma_{x,k} + a_{jy}\sigma_{y,k}\right]\sin(j\Omega t)\Big).\end{aligned} \tag{12}$$

The above expression can be further simplified by using the exponential form of a sine and the integral form of a Kronecker delta. Doing so yields the final expression for the Fourier components of the Hamiltonian when the effects of hyperfine splitting are taken into account

$$\begin{aligned}\hat{\mathcal{H}}_n = \sum_{k=1}^{3} \Big(&\frac{\Delta + w_k\delta_l}{2}\sigma_{z,k}\delta_{n,0} \\ &+\sum_{j=1}^{N_f}\frac{1}{2i}\left[a_{jx}\sigma_{x,k} + a_{jy}\sigma_{y,k}\right]\cdot\left[\delta_{n,j} - \delta_{-n,j}\right]\Big)\end{aligned} \tag{13}$$

We use Eq. (13) in the construction of the Floquet matrix for the computation of $\hat{U}(t_p)$ and $\frac{\partial\mathcal{F}}{\partial a_{jk}}$ as part of the update step of the optimal control algorithm. We include the corresponding derivation for two hyperfine levels (^{15}N for NV centers) in the Supplementary Information. Control amplitude variations are included by multiplying the control amplitudes a_{jx}, a_{jy} by the α_i-value for the given defect in the representative ensemble.

In order to ensure the optimization of our control amplitudes converges while remaining within experimentally achievable limits, we include a penalty functional

$$\mathcal{F}_{\text{pen}} = -pt_p\sum_{j,k} a_{jk}^2 \tag{14}$$

in our algorithm, applied at each update step. The penalty functional includes a specified penalty constant $p > 0$ and scales with the control amplitudes. We optimize using the gradient of the sum of the penalty functional and the state transfer fidelity $\mathcal{F}_{\text{tot}}$=$\mathcal{F}_{\text{pen}}$+$\mathcal{F}_{\text{st}}$. After each update step, the maximum amplitude of the optimal control pulse is computed in units of Rabi frequency, and if it exceeds the maximum allowed Rabi frequency R_{lim}, the penalty constant is increased by a step size Δp. If the maximum amplitude of the optimal control pulse does not exceed R_{lim}, the penalty constant is reduced by Δp. R_{lim} is one of the inputs to the algorithm and is limited by the maximum achievable experimental Rabi frequency R_{max}. This method also prevents the algorithm remaining in local maxima compared to optimizing without a penalty functional.

As a demonstration of the effect of explicitly including all three hyperfine levels in the optimization, Fig. 4 shows a series of simulated fidelity maps for a single NV subject to a flat π-pulse and optimal control pulses with and without including the hyperfine components. The fidelity of a $|0\rangle$ to $|-1\rangle$ state transfer is directly proportional to the resulting ODMR contrast C since the contrast will be maximal when all NV electron spins are in the $|-1\rangle$ state and minimal in the $|0\rangle$ state. All three pulses are in the regime $R_{\mathrm{lim}} < \delta_l$. It is clear that the regular optimal control pulse has superior performance for a single hyperfine resonance. However, when considering the average of all three, the shaped pulse optimized while taking the effects of hyperfine splitting into account is significantly better, albeit within a narrower range of detuning. Fig. 4(f) indicates that the optimal control pulse including the hyperfine splitting in the optimization is capable of simultaneously performing state transfer using all three hyperfine levels with high fidelity. The narrow range of high fidelity dropping rapidly with detuning indicates that the optimal pulse will yield high contrast when applied with drive frequency ω_D close to any one of the three hyperfine resonances and low contrast when applied off-resonance. This behavior naturally translates to a high contrast and narrow resonance linewidth and thus higher sensitivity to magnetic field. As can be seen in Fig. 4(c,f), as α_1 is increased, the $|0\rangle$ to $|-1\rangle$ fidelity (i.e., ODMR contrast) further improves in the narrow range of high fidelity without significantly broadening the range of high fidelity. We therefore experimentally apply our optimal control pulses at applied microwave power equivalent to a higher maximum Rabi frequency than we use for optimization, empirically chosen to maximize the slope.

B. Optimization Details

All of our pulses were made using an initial value of the penalty constant $p = 1$ and $\Delta p = 0.05$. They were optimized to perform a state transfer from $|0\rangle$ to $|-1\rangle$. We used 150 update steps for all of the optimizations, as this was found to be sufficient to achieve convergence of $\mathcal{F}_{\mathrm{st}}$. For the first 51 steps, the step size along the gradient was kept constant at $\beta = 0.007$ and for the remaining steps, the optimal step size was determined using a line search. This was done to speed up the optimization without compromising the quality of the resulting optimal control pulses. We designed pulses using different values of R_{lim}, t_p and the ranges $\hat{\Delta}$ and $\hat{\alpha}$ and tested them experimentally. We determined the maximum achievable experimental Rabi frequency, i.e. the upper limit on the maximum allowed Rabi frequency $R_{\mathrm{lim}} \leq R_{\mathrm{max}} = 3.2\,\mathrm{MHz}$ through prior experimental measurements using flat pulses on the same diamond NV ensemble. Based on this, we defined a range of R_{lim} to generate testable optimized shaped pulses for as between $R_{\mathrm{lim}} = 0.8\,\mathrm{MHz}$ and $R_{\mathrm{lim}} = 3.2\,\mathrm{MHz}$. The minimum value of t_p necessary to achieve improvements over a comparable flat pulse was limited by the need to apply sufficient power to perform the desired state transfer. We set the lower limit of t_p to be at least twice the duration of a flat π-pulse with Rabi frequency equal to R_{lim}. The maximum value of t_p was limited by the T_2 coherence time of a single NV. Based on this, we defined a range of t_p to generate testable optimized shaped pulses for as between $t_p = 1.0\,\mu\mathrm{s}$ and $t_p = 5.0\,\mu\mathrm{s}$.

Although the possible values of detuning Δ_i are in principle not limited, higher Rabi frequencies are required to compensate for higher levels of inhomogenous broadening. Based on the considered values of R_{lim}, we therefore used $\hat{\Delta}$ up to $\pm 2\,\mathrm{MHz}$. The possible values of α_i are similarly not limited in principle, but higher Rabi frequencies are required to compensate for higher levels of drive field inhomogeneity. We therefore chose to optimize up to $\hat{\alpha} = 1 \pm 0.2$ relative control amplitude range.

Our initial a_{jk}-values were set using pseudorandom values within a range sufficient to yield a maximum Rabi frequency of the corresponding initial pulse greater than R_{lim}. This was done in order to ensure that the optimization algorithm approached the region of allowed pulses from the outside, so that pulses utilizing R_{lim} were considered. For this work, the initial Rabi frequency was 2.8 times greater than the maximum allowed Rabi frequency.

C. Experimental Setup

A schematic of our experimental setup is shown in Fig. 5(a). We used an off-the-shelf, optical-grade diamond (Element 6) with $\sim 0.5\,\mathrm{ppb}$ NV^- concentration, of dimensions $5\mathrm{x}5\mathrm{x}1.2\,\mathrm{mm}^3$. For this diamond, we measured a T_2^*-limited linewidth of 0.75 MHz and determined T_1, T_2 and T_2^* times as 7.1 ms, 7.0 µs and 0.44 µs respectively, with a maximum ensemble-averaged Rabi frequency of $R_{\mathrm{max}} = 3\,\mathrm{MHz}$ driven by our antenna (see Supplementary Information for details). A bias field of 2.9 mT aligned along the [111] crystallographic axis was applied by fixed permanent magnets, so as to split the $m_s{=}\pm1$ states. We addressed only the $m_s{=}0 \rightarrow m_s{=}{-1}$ transition to use an effective two-level system within the antenna's resonance.

The diamond was optically pumped using a 532 nm diode-pumped solid state laser (DPSS, Cobolt Samba 1500). The linearly polarized beam was focused to a waist diameter of 120 µm before Brewster-angle refraction into the diamond to optically address (with at least $1/e^2$ the center intensity) an ensemble with a minimum estimated size of $\approx 4 \times 10^9$ NV centers in a volume of

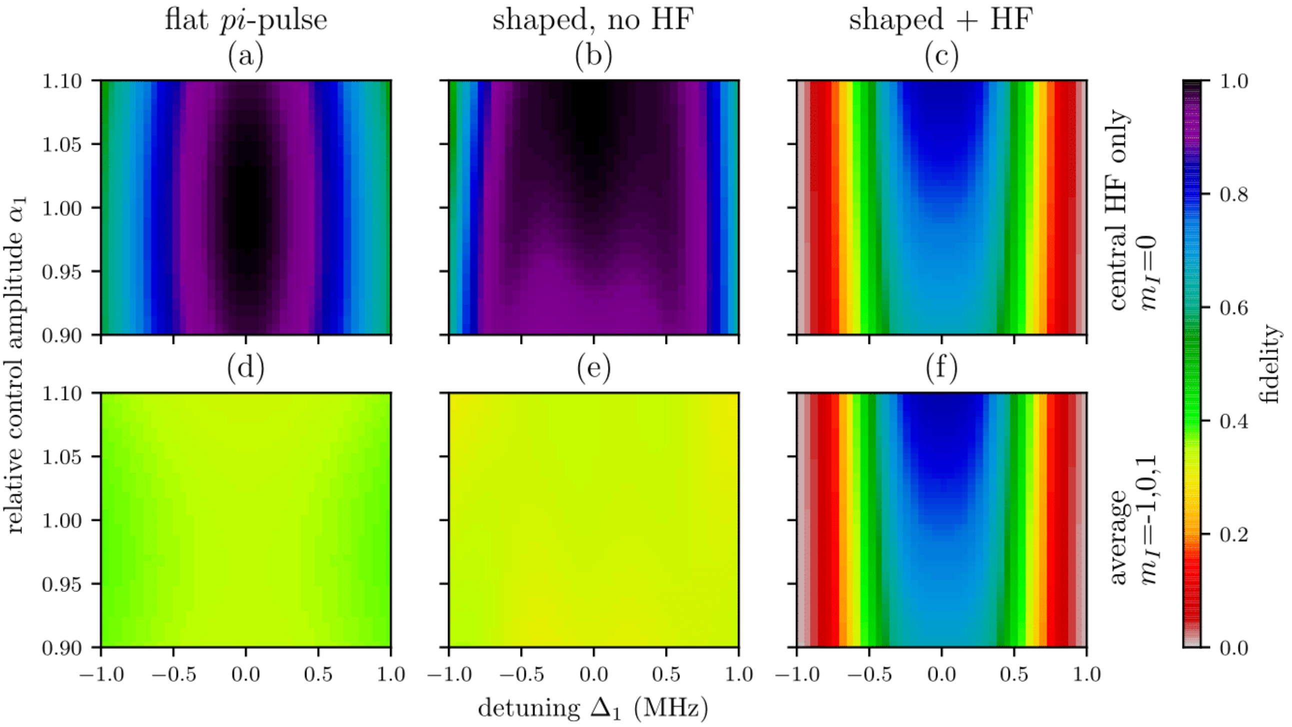

FIG. 4. Color online. Simulated maps of the state transfer fidelity (Eq. (1)) from $|0\rangle$ to $|1\rangle$ for a single NV (i=1) subject to (a,d) a flat (π)-pulse, (b, e) an optimized shaped pulse and (c, f) a shaped pulse optimized while taking the fidelity of state transfer taking all three hyperfine levels into account. The top plots (a, b, c) show the fidelity of the transfer experienced by the central hyperfine transition while the bottom plots (d, e, f) show the average of the transfer fidelities for each of the three hyperfine levels. Each point in the top plots is the fidelity for a single NV electron spin with the given values of α_1 and Δ_1. Each point in the bottom plots is the average of the fidelities for three NV electron spins with the given value of α_1 and transition frequencies detuned by Δ_1, $\Delta_1 + \delta_l$ and $\Delta_1 - \delta_l$, respectively, from the driving frequency. The flat pulse has a Rabi frequency of 1.4 MHz, and the optimal control pulses were both optimized using $\hat{\Delta} = \pm 1$ MHz detuning, $\hat{\alpha} = 1 \pm 10\,\%$ amplitude variation, R_{lim}= 1.4 MHz and a pulse duration $t_p = 1.85\,\mu$s.

$\approx 0.04\,\text{mm}^3$ based on the focused waist of the pump beam. The maximum pump laser power we delivered to the diamond was 500 mW. This resulted in 84 µW of red fluorescence escaping the front face of the diamond, of which we collected 9.1 µW by using two condenser lenses (Thorlabs ACL25416U) to first collimate to pass through a low-pass filter (FEL0550) and then focus onto an avalanche photodiode (Thorlabs APD120A), producing an amplified analog voltage output V_{fl} sampled by an analog-to-digital converter (ADC, Gage Octopus CS8300) at 50 MHz. We optically modulated our pump laser using an acousto-optic modulator (AOM, Isomet 532C-4) at $f_{\text{AOM}} = 2.6$ MHz, allowing us to perform software lock-in detection to minimize noise in the electronic readout. A fraction of the pump beam was also sampled by a second detector (Thorlabs PDA10A) to provide a reference, V_{ref}, for common-mode noise rejection.

We generated the microwave pulses necessary for implementation of the optimal control protocols using an arbitrary waveform generator (AWG, Tektronix 5000), in-phase/quadrature (IQ) modulating a Stanford SG394 RF signal generator. The microwave output was amplified (Mini-Circuits ZHL-16W-43-S+) and delivered to the diamond using a near-field antenna based on a square split-ring resonator design[64,65]. This antenna was designed for uniformity of near-field intensity in a 5x5 mm^2 region centered on the diamond with a resonance at approximately 2.8 GHz. Our AWG also controlled a switch (Minicircuits ZASWA-2-50DRA+) through which the AOM modulation drive was passed, allowing the pump beam incident on the diamond to be pulsed and modulated.

D. Pulse Sequencing and Readout

In our experimental setup, we measured contrast C, the change in fluorescence output as a result of a control pulse. We define C as the change in fluorescence output in the initial period of a pump laser readout pulse after application of a preceding microwave pulse[30,34,66]. C was measured across an ODMR resonance feature by varying microwave drive frequency ω_D. We measured

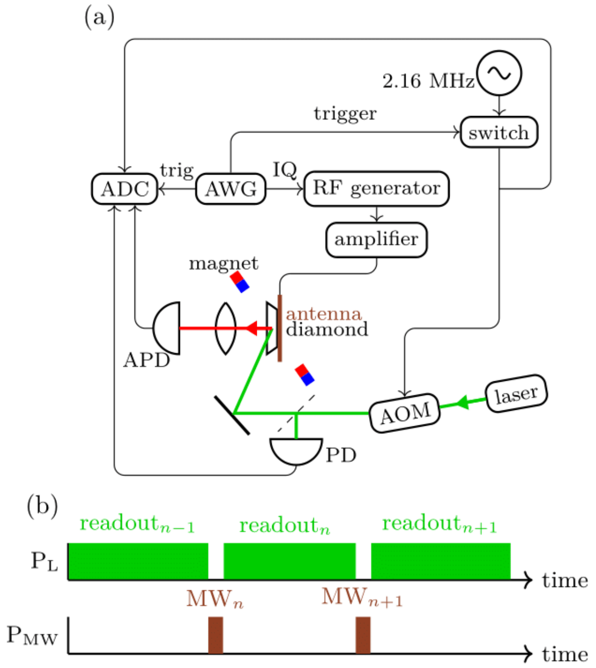

FIG. 5. Color online. (a) Schematic of our experimental setup. The pump laser is modulated by the AOM, at 2.6 MHz and controlled by the AWG. Microwave pulses are delivered to the diamond using a near-field antenna. The AWG provides IQ modulation to the signal generator to create the required control pulses. An ADC, synchronized with the AWG, digitizes the analog AOM modulation signal, the signal from the APD collecting the diamond fluorescence V_{fl} and the signal from an amplified photodetector that collects a small amount of the pump laser V_{ref}. (b) Pulsed ODMR sequence as applied in our measurements, showing the repeating sequence of pump laser pulses P_l and microwave pulses P_{MW}. This sequence is repeated continuously by the AWG.

this change in fluorescence signal V_{fl} after application of either a shaped or flat microwave pulse, relative to the laser reference signal V_{ref}. We obtained C by scaling the reference to the size of the fluorescence signal, subtracting the two, and integrating the resulting signal over a time window t_w=0.3-2.7 ms at the start of the laser pulse (see Supplementary Information for full details). This subtraction method allowed us to reject both DC and higher-frequency (>kHz) common-mode noise from the laser on the readout signal within the integration window. It also allowed us to measure a value for C from every laser pulse (rather than measuring a reference with no microwave pulse on every other fluorescence readout), maximizing the bandwidth of our readout. From C we also derived $C^{'}$ the change in contrast with microwave drive frequency. This quantity, the slope of the ODMR resonance, gives a measure of the strength of response and hence sensitivity to the local environment.

Using the pulsed protocol shown in Fig. 5(b), we first initialized the NV ensemble into the ground state using pump laser pulse $(n-1)$ of duration t_l. The pump laser was then blocked by the AOM during application of microwave control pulse n of duration t_p. A subsequent laser pulse n of the same duration t_l was then applied and the state read out via diamond fluorescence emission This pulse also acted to reinitialize the system back into the $|0\rangle$ state, allowing the next $(n+1)$ pulses to read and initialise. This method enabled measurements using only a short repeating sequence in the AWG memory. We acquired data continuously for repeated sequence sets up to the memory limit of the ADC (n=110 pulses when using t_l=3 ms). Once this limit was reached, the data was transferred to computer memory and processed, averaging over all pulse sequence sets in the acquisition to reduce noise, and then integrating to obtain C.

For direct comparison, we performed the same pulse sequence with the same readout methods for C using both shaped microwave pulses and standard fixed amplitude and phase (flat) pulses. We used the same method for calculating C throughout our measurements, to ensure accurate comparison between the different microwave pulses. In the latter case, we used pulses with a single microwave drive frequency of the form $\cos(\omega t)$ and three-frequency drive pulses of the form $\sum_{n\in\{0,\pm1\}}\cos((\omega+n\delta_l)t+\phi_n)$ to drive multiple hyperfine transitions.[67] The latter were generated using the AWG with randomized phases ϕ_n for each ADC acquisition to eliminate time-dependent artifacts.

III. RESULTS

A. Laser Pulse Duration

Our previous measurements[68] demonstrated long optical reinitialization times, requiring many milliseconds on an approximately exponential decay with laser pulse duration to fully return the ensemble to the ground state. For the comparably sized ensemble in these experiments, we observed similar exponential behavior with a time constant of of ≈1.4 ms.

Waiting tens of milliseconds per readout would severely limit the number of pulses we could read and average in a single ADC acquisition and thus our contrast resolution. We therefore first performed experiments varying laser pulse duration to determine whether we could initialize and control the ensemble using shorter laser pulses without suffering hysteresis effects, either from incomplete initialization or reionization delay across the readout laser pulses.[69–71]

Fig. 6 shows the contrast C as a function of laser readout pulse duration $t_l < 20$ ms as measured using an optimal control pulse. We observed C to be reduced for times shorter than ≈ 3 ms, indicative that an increasing number of NV centers in the sample were not fully reinitialized into the ground state. For t_l=3ms and above, we observed negligable hysteresis effects in the fluorescence readout. This is supported by Fig. 7, comparing the raw fluorescence readout and relative contrast calcu-

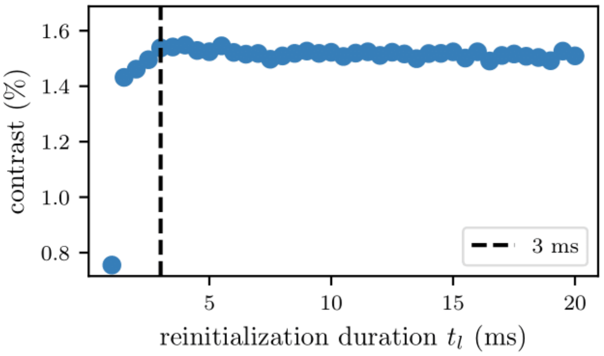

FIG. 6. Contrast as a function of laser pulse time t_l. Below 3 ms, t_l is too short to sufficiently reinitialize the ensemble, leaving to a reduction in contrast C with shorter readout/reinitilisation laser pulse length t_l.

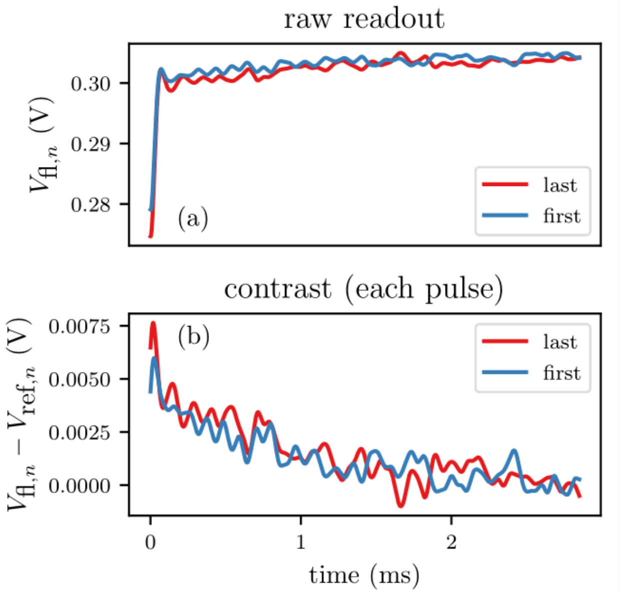

FIG. 7. Raw fluorescence readout signal $V_{\mathrm{fl},n}$ and relative contrast $C_{r,n}(t) = V_{\mathrm{fl},n} - V_{\mathrm{ref},n}$ for the first (n=1) and last (n=110) 3 ms readout laser pulse in a single ADC acquisition of 110 readout sequences. No difference within the readout noise was observed at this readout duration, as would be expected from hysteresis effects arising from insufficient reinitialization of the ensemble.

lated from the first and last individual readout pulses in a 110 pulse ADC acquisition using $t_l = 3$ ms.

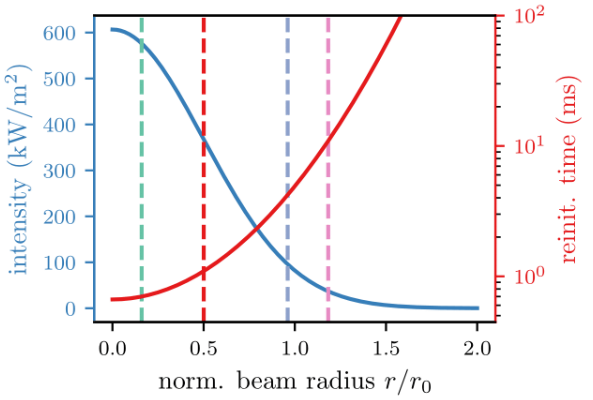

FIG. 8. Modelled variation in laser intensity and the time to reinitialize NV centers into the m_s=0 ground state level as a function of bean radius, relative to r_0 the 1/e^2 beam width. The reinitialization time increases rapidly at the lower intensity edges of the beam.

We note that the fact we can achieve the same hysteresis-free contrast for a short 3 ms laser pulse as for one much longer is somewhat surprising. We consider that this effect primarily arises due to the Gaussian intensity profile of the laser, whereby the NV centers at the low intensity edges of the beam require more time to reinitialize back into the ground state, but contribute far less to the overall fluorescence output, especially in the first few milliseconds of the readout laser pulse where contrast is measured[34]. In order to further investigate the physics of our NV ensemble and to determine the size of ensemble we address, we implemented a simple physical model of the NV population dynamics. Our model consists of a fixed NV density addressed by a radially (Gaussian-) varying laser beam intensity, with an NV at radius r receiving a pump intensity $I(r)$. We then solve a rate model for all NV centers,[72,73] from which we estimate the relative fluorescence output and ensemble contrast C. We perform our microwave pulses as an ideal π-pulse with instantaneous population transfer in the rate model between levels m_s=0 to m_s=-1. Further details of the implementation of the model are given in Supplementary Information.

In Fig. 8, we plot the relative intensity $I(r)$ and the reinitialization time, the exponential decay time required for the pump beam to return all NV centers at r into the m_s=0 ground state as a function of beam radius r/r_0. Here r_0 represents the 1/e^2 beam width as in our experiment. From this simulation, it is clear that the time period over which we integrate to derive the experimental contrast (t_w=0.3-2.7 ms) corresponds to near complete reinitialization of the NV centers within $r/r_0 \approx 0.5$, or 25 % of the ensemble. Although this does not represent the entire ensemble, this still corresponds to ≈ 1 billion NV centers, based on estimated ensemble size (4×10^9) from our experimental measurement of fluorescence emission.

The reinitilization dynamic behavior can be seen in Fig. 9(a), plotting the time evolution of the m_s=0 state population for the first 10 readout/MW pulses of length $t_l = 3$ ms for 4 increasing values of r/r_0. Below $r/r_0 = 0.5$, hysteresis-free behaviour can be achieved in our model almost immediately after the first microwave

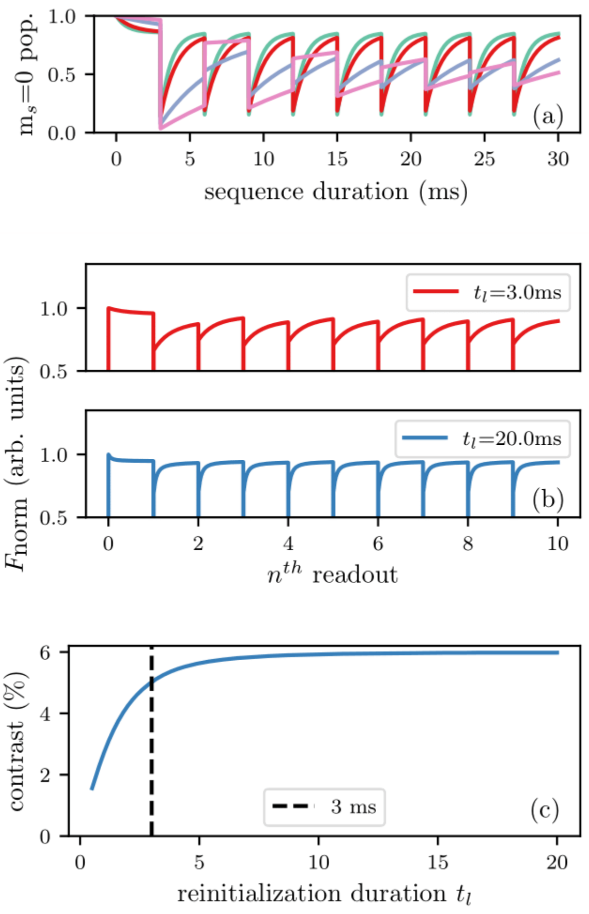

FIG. 9. (a) Modeled dynamics of the m_s=0 population for NV centers receiving pump beam intensity $I(r)$ at 4 different increasing values of r/r_0. (b) The hysteresis-free behaviour of the defects within $r/r_0 < 0.5$ dominates the fluorescence output (normalized to the initial output with all NV centers in the m_s=0 bright state). The NV centers at the beam edge that are not fully reinitialized reduce the ensemble contrast as laser pulse length is reduced, as modeled in (c).

pulse. Hysteretic behaviour is observed for NV centers further towards the edge of the beam. For these NV centers, the ground state occupancy decays to ≈ 50 % within the first 10-20 pulses. These NV centers therefore contribute by a reduced amount to the contrast (as measured in t_w) as compared to the NV centers in the beam centre, which exhibit the correct dynamics of full reinitialization by the laser and full state transfer by the microwave π-pulse. Since the outer NV centers are not fully reinitialized into the triplet ground state, they also act to produce a lower fluorescence emission as compared to the level expected with all NV centers reinitialised into the spin triplet ground state. This can be seen in Fig. 9(b), showing the total ensemble fluorescence emission as a function of time for t_l = 20 ms and t_l = 3 ms laser pulses. For the shorter pulse length, a greater number of NV centers are not fully reinitialized, reducing the the overall fluorescence emission to approximately 90% of the maximum reached for t_l=20ms. Since the NV centers on the beam edge are not properly reinitialised into the ground state, they also cannot be correctly manipulated by the microwave state transfer pulse. As laser pulse length t_l is reduced and this fraction of NV centers not fully reinitialised increases, the effect is therefore a reduction in contrast C following a microwave pulse. This modelled behaviour can be seen in Fig. 9(c) which qualitatively replicates our experimental data in Fig. 6.

The ability to rapidly read and reinitialize in this manner is an extremely useful result, since it gives a means to adequately control and read a large NV ensemble with shorter laser pulses than that required to fully reinitialize every defect center. This significantly increases the measurement bandwidth for pulsed quantum sensing schemes, while still addressing a large number of defects required to maximize sensitivity.

In order to model fluorescence behavior matching the experimental exponential decay using a Gaussian beam profile and associated volume, it was necessary to set modelled pump beam intensity a factor of 6 less than the intensity estimated experimentally. We attribute this to two factors not included in our model: reflection loss due to imperfect Brewster's angle coupling into the diamond and internal reflection within the diamond, spreading the beam across a wider volume of NV centers. The estimates of ensemble volume and number of defects addressed by the pump laser thus represents a lower bound based on the assumptions of our model. Further model development and investigations beyond the focus of this work are required to explore these aspects further, including observing changes in decay time for the fluorescence readout as a function of beam incidence angle and using a non-Gaussian laser profile.

B. ODMR Using Shaped Optimal Control Pulses

Using our optimal control algorithm including all 3 hyperfine levels for ^{14}N, we first calculated a series of shaped microwave pulses spanning the parameter space of $\hat{\Delta}$ and $\hat{\alpha}$, the Rabi frequency limit R_{lim}, and the pulse duration t_p. Their performance was then tested experimentally to explore the limits of these parameters that yield high contrast C and ODMR slope $C^{'}$. We found that extending $\hat{\Delta}$ and $\hat{\alpha}$ beyond ±1 MHz and ±10 % respectively had negligible impact, likely indicating that the real ensemble distribution in our diamond was within these ranges. Having found that pulses in the range of $1.1\,\text{MHz} < R_{\text{lim}} < 2.4\,\text{MHz}$ and $1\,\mu\text{s} < t_p < 2\,\mu\text{s}$ performed well, we experimentally searched the parameter space of these optimal control pulses applied by producing ODMR spectra using the shaped pulses and searching for the maximum slope $C^{'}$. We found the best-performing pulse optimized with $t_p = 1.85\,\mu\text{s}$ and $R_{\text{lim}} = 1.4\,\text{MHz}$, with similar performance from larger

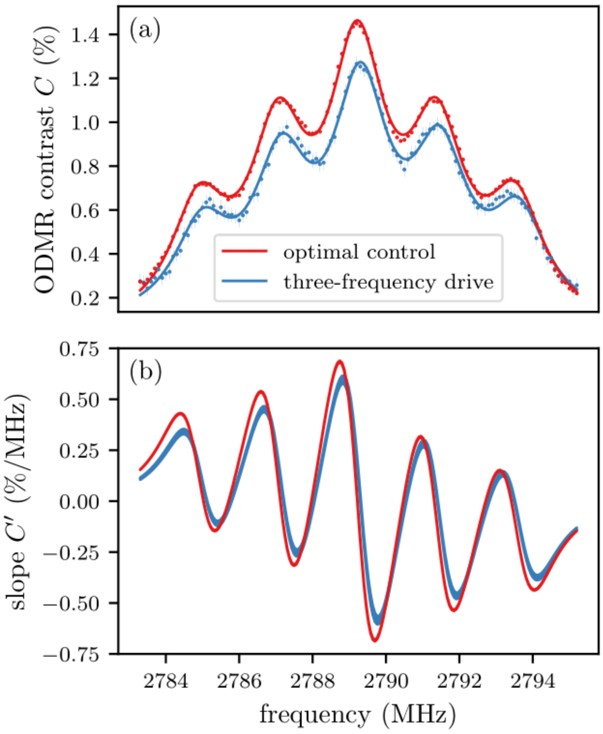

FIG. 10. Comparison of pulsed ODMR measurements using the most sensitive optimized shaped pulse and the flat pulse that delivers the highest contrast using three-frequency drive. The slope data shown in (b) is the slope of the fit to the ODMR data in (a).

R_{lim} up to 2 MHz at the same R_{exp}. The modulation components $I(t)$ and $Q(t)$ for this pulse are shown in Fig. 3(a), and the control amplitudes are given in the Supplementary Information.

The experimental ODMR spectrum from the best shaped control pulse found is shown in Fig. 10(a). By differentiating the spectrum, we also show the frequency versus contrast slope $C^{'}$ in Fig. 10(b). Here the largest possible slope is desired, since this produces the maximum response and highest sensitivity. For comparison, we plot in the same figure the ODMR spectrum using a flat three-frequency drive (π-)pulse that corresponds to the maximum slope for a conventional pulse without shaping. We found the maximum slope to be 11% higher for the shaped optimal control pulse than for this conventional flat pulse. Compared to the simplest single-frequency flat (π-)pulses most used in literature, we found significant improvement of up to 73%. This corresponds directly to the same factor of improvement in sensitivity.

We note that the length of the flat and shaped pulse that delivered maximum slope were significantly different. This could potentially lead to the longer shaped pulse achieving higher performance purely by delivering more microwave power over an extended time period. To ensure this was not the case, we compared the optimised pulse against single and three-frequency drive flat pulses over an extended parameter space of pulse lengths (up to $t_p = 1.35\,\mu\text{s}$) and applied microwave power (up to Rabi frequency $R_{max} = 3\,\text{MHz}$) . This data is shown in Fig. 11 for single frequency drive and Fig. 12 for three-frequency drive. The flat pulses performed best at the length and power that corresponded to performing a π-pulse on the largest possible subset of NV centers (maximizing contrast). However, as can be seen from these figures, the shaped microwave pulse we created using our optimal control methods always produced an ODMR slope far higher than any unshaped drive. This was the case for any pulse length or microwave power, with the optimum for the flat pulses reached well within experimental limits of R_{max} and t_p.

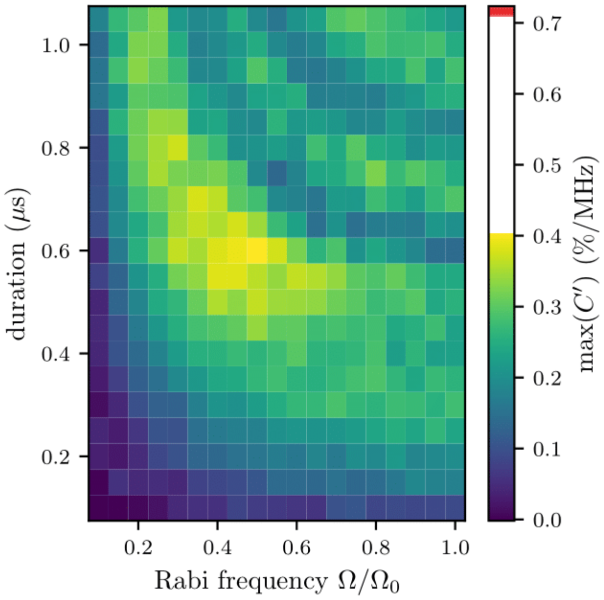

FIG. 11. The maximum contrast slope $C^{'}$ measured for flat single-frequency drive pulses over the relevant parameter space of microwave power (plotted as Rabi frequency) and duration. The red stripe in the colorbar shows the maximum contrast slope of the best optimal control pulse from Fig. 10. The equivalent plot for 3 frequency drive is given in the Supplementary Information.

For our setup, we can estimate shot-noise-limited sensitivity using the expression derived in Appendix B:

$$\eta \approx \frac{\sqrt{2t_R t_I}}{\gamma_e C' \tau_R (1 - e^{-t_R/\tau_R})\sqrt{R_0}},$$

where we take into account the times for readout and reinitialization t_R, t_I, the reinitialization decay constant τ_R, photon collection rate at max power R_0, electron gyromagnetic ratio γ_e, and measured contrast slope C'. For our setup, we estimate $\eta \approx 10\,\text{nT}/\sqrt{\text{Hz}}$. Although this is lower than state of the art figures reported elsewhere for

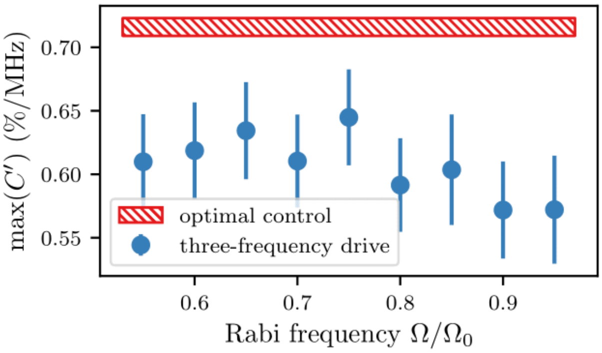

FIG. 12. ODMR spectrum frequency versus contrast slope C' for the shaped optimal control pulse and for the best flat 3-frequency drive pulses of any duration for a given microwave power (plotted as measured Rabi frequency). Error bars and the y-range of the optimal control pulse represent 1σ uncertainty. The power used for the optimal control pulse was 0.91 of the maximum Rabi frequency Ω_0. The plot covering the full parameter space in time and Rabi frequency is given in Supplementary Information.

magnetic field sensing with NV centers, we note that our setup is not optimized for sensitivity due to the standard optical grade diamond we use (rather than one materially optimized for sensing), our small APD detector area and ADC memory limitations.

IV. CONCLUSION

In this work, we demonstrate that a large ensemble of solid state defects in a macroscopic sample can be manipulated and coherently controlled in a manner beneficial for quantum sensing. We demonstrate this for an ensemble of NV centers in diamond through the use of shaped microwave pulses generated using Floquet theory and optimal control methods. Due to the scaling of sensitivity with the number of defects, such large ensembles are key for quantum sensing applications, either using NV centers or other solid state defects. Both our overall NV ensemble volume within the estimated Gaussian beam width ($\approx 4 \times 10^9$ NV centers in a $\approx 0.04\,\text{mm}^3$ volume) and our estimated NV ensemble contributing maximally to the contrast signal ($\approx 25\,\%$ of the total) was larger than NV ensembles previously studied and reported in the literature using optimal control methods largely studied using confocal microscopy.[33,49,50,53–56]

By fully considering the physics of the defect system and including the hyperfine interaction in our optimization, we demonstrate an $11\,\%$ enhancement in ODMR slope with optimized shaped pulses when compared to the best alternative 3-frequency drive flat (fixed amplitude and phase) (π-)pulses and a $78\,\%$ improvement over standard single-frequency-drive flat (π-)pulses most commonly used for coherent control in the literature. These are directly equivalent to the same factor of sensitivity improvement when used in an applied sensing scheme. This significant improvement offers potential for wider impact for DC/low-frequency sensing, for example in precision measurement of slowly varying temperature where ensemble probe bandwidth limitations imposed by the $\approx 5\,\mu\text{s}$ shaped pulse length would be less constraining.

We estimate a shot noise-limited sensitivity of $10\,\text{nT}/\sqrt{\text{Hz}}$ using our setup, while noting that neither the diamond we use nor our apparatus was optimized to maximize sensitivity at this time. Our method is not specific to the apparatus we used and could be applied equally well to a sensitivity-optimized setup, for example using an isotopically purified diamond. By measuring the ODMR contrast by referring to the signal from an additional photodetector, we were able to reject more of the laser technical noise while maximizing the number of contrast measurements we could achieve as compared to alternative time domain noise rejection methods[34].

Through modeling of the physical dynamics of the readout and initialization of the defect ensemble, we show that although many tens of milliseconds are required to fully reinitialise the whole NV ensemble, a shorter laser pulse can address and reinitialise a large proportion of the NV centers. By demonstrating reliable contrast measurements free of hysteresis, we show that these NV centers can be addressed and controlled reliably. Further work is required to fully understand the dynamics of the system and the distribution of pump light in the diamond. However, our measurements suggest the primarily limiting factor on the readout is the Gaussian shape of the laser beam, hinting at considerable future improvement using a non-Gaussian profile.

The shaped microwave pulses we generate in this work almost certainly represent local maxima of performance in a wide parameter space. We consider it very likely that advances in methods for optimization as well as experimental improvements could provide even better solutions in future. A particular flaw is the assumption of simple Gaussian distributions for detuning and other parameters, which are a poor representation of the actual properties of a real sample. A route forward may be to use experimental feedback in the optimization algorithm. This would be simplified by producing a more homogeneous microwave field through antenna improvements, increasing the ensemble Rabi frequency through better use of the microwave power, and the use of alternative laser beam profiles to improve uniformity of initialization and readout. Additionally, in this work we optimize for state transfer $|0\rangle$ to $|-1\rangle$, which aims to maximize contrast C. By instead explicitly optimizing for the change in contrast in response to the control field (the slope C' in our results above), better optimized pulses could be generated.

Our work represents an important step in the direction of using optimal control and other techniques widely used in nuclear magnetic- and electron spin- resonance experiments to explore the physics of new systems suitable for quantum sensing. These techniques, including those we outline here, can be adapted to be widely applicable, not only to diamond but to other defects in both bulk and novel quantum materials, such as those in 2D materials.[74] Using control pulses shaped by optimal control methods, which could be either microwaves, optical fields or some other means, offers the best route to reach the ultimate T_2^*-limited sensitivity for any suitable quantum system.

V. ACKNOWLEDGEMENTS

The work presented here was funded by the Novo Nordisk foundation through the synergy grant bioQ and the bigQ Center funded by the Danish National Research Foundation (DNRF).

A. SPIN MATRICES

Below are shown the 6-by-6 matrix representations of the Pauli spin matrices that are each specific to one of the three nitrogen-14 hyperfine transitions.

$$\sigma_{z,1} = \begin{pmatrix} 1 & 0 & 0 & 0 & 0 & 0 \\ 0 & -1 & 0 & 0 & 0 & 0 \\ 0 & 0 & 0 & 0 & 0 & 0 \\ 0 & 0 & 0 & 0 & 0 & 0 \\ 0 & 0 & 0 & 0 & 0 & 0 \\ 0 & 0 & 0 & 0 & 0 & 0 \end{pmatrix}, \ \sigma_{z,2} = \begin{pmatrix} 0 & 0 & 0 & 0 & 0 & 0 \\ 0 & 0 & 0 & 0 & 0 & 0 \\ 0 & 0 & 1 & 0 & 0 & 0 \\ 0 & 0 & 0 & -1 & 0 & 0 \\ 0 & 0 & 0 & 0 & 0 & 0 \\ 0 & 0 & 0 & 0 & 0 & 0 \end{pmatrix} \tag{15}$$

$$\sigma_{z,3} = \begin{pmatrix} 0 & 0 & 0 & 0 & 0 & 0 \\ 0 & 0 & 0 & 0 & 0 & 0 \\ 0 & 0 & 0 & 0 & 0 & 0 \\ 0 & 0 & 0 & 0 & 0 & 0 \\ 0 & 0 & 0 & 0 & 1 & 0 \\ 0 & 0 & 0 & 0 & 0 & -1 \end{pmatrix}, \ \sigma_{x,1} = \begin{pmatrix} 0 & 1 & 0 & 0 & 0 & 0 \\ 1 & 0 & 0 & 0 & 0 & 0 \\ 0 & 0 & 0 & 0 & 0 & 0 \\ 0 & 0 & 0 & 0 & 0 & 0 \\ 0 & 0 & 0 & 0 & 0 & 0 \\ 0 & 0 & 0 & 0 & 0 & 0 \end{pmatrix} \tag{16}$$

$$\sigma_{x,2} = \begin{pmatrix} 0 & 0 & 0 & 0 & 0 & 0 \\ 0 & 0 & 0 & 0 & 0 & 0 \\ 0 & 0 & 0 & 1 & 0 & 0 \\ 0 & 0 & 1 & 0 & 0 & 0 \\ 0 & 0 & 0 & 0 & 0 & 0 \\ 0 & 0 & 0 & 0 & 0 & 0 \end{pmatrix}, \ \sigma_{x,3} = \begin{pmatrix} 0 & 0 & 0 & 0 & 0 & 0 \\ 0 & 0 & 0 & 0 & 0 & 0 \\ 0 & 0 & 0 & 0 & 0 & 0 \\ 0 & 0 & 0 & 0 & 0 & 0 \\ 0 & 0 & 0 & 0 & 0 & 1 \\ 0 & 0 & 0 & 0 & 1 & 0 \end{pmatrix} \tag{17}$$

$$\sigma_{y,1} = \begin{pmatrix} 0 & -i & 0 & 0 & 0 & 0 \\ i & 0 & 0 & 0 & 0 & 0 \\ 0 & 0 & 0 & 0 & 0 & 0 \\ 0 & 0 & 0 & 0 & 0 & 0 \\ 0 & 0 & 0 & 0 & 0 & 0 \\ 0 & 0 & 0 & 0 & 0 & 0 \end{pmatrix}, \ \sigma_{y,2} = \begin{pmatrix} 0 & 0 & 0 & 0 & 0 & 0 \\ 0 & 0 & 0 & 0 & 0 & 0 \\ 0 & 0 & 0 & -i & 0 & 0 \\ 0 & 0 & i & 0 & 0 & 0 \\ 0 & 0 & 0 & 0 & 0 & 0 \\ 0 & 0 & 0 & 0 & 0 & 0 \end{pmatrix} \tag{18}$$

$$\sigma_{y,3} = \begin{pmatrix} 0 & 0 & 0 & 0 & 0 & 0 \\ 0 & 0 & 0 & 0 & 0 & 0 \\ 0 & 0 & 0 & 0 & 0 & 0 \\ 0 & 0 & 0 & 0 & 0 & 0 \\ 0 & 0 & 0 & 0 & 0 & -i \\ 0 & 0 & 0 & 0 & i & 0 \end{pmatrix} \tag{19}$$

B. ESTIMATION OF SHOT NOISE-LIMITED SENSITIVITY

Shot noise-limited sensitivity estimation is typically[30,67] similar to

$$\eta \approx \frac{1}{\gamma_e \sqrt{R} C'}$$

with the electron gyromagnetic ratio γ_e, the photon detection rate R and the (in this case empirically measured) ODMR slope $C' = \frac{\mathrm{d}C}{\mathrm{d}f}$. This assumes that each collected photon adds the same amonut of information, which is the case in a typical pulsed detection setup where the readout time t_R is much shorter than the total reinitialization time t_I, and the contrast barely decays during t_R. We therefore include a factor representing the mean information collected per photon

$$\frac{1}{t_R} \int_0^{t_R} e^{-t/\tau_R} \mathrm{d}t = \frac{\tau_R (1 - e^{-t_R/\tau_R})}{t_R}$$

with $\tau_R \approx 1.4\,\mathrm{ms}$ as the decay constant of the contrast, making this factor about 0.5. We additionally modify R for clarity, in terms of the maximum photon collection rate at a peak of the modulation R_0, $R = R_0 t_R / 2 t_I$, where the duration of the RF pulse is neglected, and the $1/2$ results from the modulation. In all, we obtain

$$\eta \approx \frac{\sqrt{2 t_R t_I}}{\gamma_e C' \tau_R (1 - e^{-t_R/\tau_R}) \sqrt{R_0}}.$$

[1] Tim Schröder, Sara L. Mouradian, Jiabao Zheng, Matthew E. Trusheim, Michael Walsh, Edward H. Chen, Luozhou Li, Igal Bayn, and Dirk Englund. Quantum nanophotonics in diamond [Invited]. *Journal of the Optical Society of America B*, 33(4):B65, 2016.

[2] Igor Aharonovich, Dirk Englund, and Milos Toth. Solid-state single-photon emitters. *Nature Photonics*, 10(10):631–641, 2016.

[3] J. H. N. Loubser and J. A. Van Wyk. Electron spin resonance in the study of diamond. *Reports on Progress in Physics*, 41(8):1201–1248, 1978.

[4] J M Taylor, P Cappellaro, L Childress, L Jiang, D Budker, P R Hemmer, A Yacoby, R Walsworth, and M D Lukin. High-sensitivity diamond magnetometer with nanoscale resolution. *Nature Physics*, 4(10):810–816, 2008.

[5] Zhi_Hui Wang, G. de Lange, D. Risté, R. Hanson, and V. V. Dobrovitski. Comparison of dynamical decoupling protocols for a nitrogen-vacancy center in diamond. *Physical Review B - Condensed Matter and Materials Physics*, 85(15):155204, 2012.

[6] D. Farfurnik, A. Jarmola, L. M. Pham, Z. H. Wang, V. V. Dobrovitski, R. L. Walsworth, D. Budker, and N. Bar-Gill. Improving the coherence properties of solid-state spin ensembles via optimized dynamical decoupling. In Jürgen Stuhler and Andrew J. Shields, editors, *Quantum Optics*. SPIE, April 2016.

[7] D. Farfurnik, A. Jarmola, D. Budker, and N. Bar-Gill. Spin ensemble-based AC magnetometry using concatenated dynamical decoupling at low temperatures. *Journal of Optics (United Kingdom)*, 20(2), 2018.

[8] Genko T. Genov, Yachel Ben-Shalom, Fedor Jelezko, Alex Retzker, and Nir Bar-Gill. Efficient and robust signal sensing by sequences of adiabatic chirped pulses. *Physical Review Research*, 2(3), August 2020.

[9] F Jelezko, T Gaebel, I Popa, A Gruber, and J Wrachtrup. Observation of Coherent Oscillations in a Single Electron Spin. *Physical Review Letters*, 92(7):1–4, 2004.

[10] F Dolde, H Fedder, M W Doherty, F Rempp, G Balasubramanian, F Reinhard, F Jelezko, and J Wrachtrup. Sensing electric fields using single diamond spins. *Nature Physics*, 7(6):459–463, 2011.

[11] P Neumann, I Jakobi, F Dolde, C Burk, R Reuter, G Waldherr, J Honert, T Wolf, A Brunner, J H Shim, D Suter, H Sumiya, J Isoya, and J Wrachtrup. High-Precision Nanoscale Temperature Sensing Using Single Defects in Diamond. *Nano Letters*, 13(6):2738–2742, 2013.

[12] T. Delord, L. Nicolas, M. Bodini, and G. Hétet. Diamonds levitating in a Paul trap under vacuum : Measurements of laser-induced heating via NV center thermometry. *Applied Physics Letters*, 111(1):013101, 2017.

[13] Marcus W. Doherty, Viktor V. Struzhkin, David A. Simpson, Liam P. McGuinness, Yufei Meng, Alastair Stacey, Timothy J. Karle, Russell J. Hemley, Neil B. Manson, Lloyd C. L. Hollenberg, and Steven Prawer. Electronic properties and metrology applications of the diamond nv^{-} center under pressure. *Phys. Rev. Lett.*, 112:047601, Jan 2014.

[14] I. Gross, W. Akhtar, V. Garcia, L. J. Martínez, S. Chouaieb, K. Garcia, C. Carrétéro, A. Barthélémy, P. Appel, P. Maletinsky, J.-V. Kim, J. Y. Chauleau, N. Jaouen, M. Viret, M. Bibes, S. Fusil, and V. Jacques. Real-space imaging of non-collinear antiferromagnetic order with a single-spin magnetometer. *Nature*, 549(7671):252–256, Sep 2017.

[15] L. Thiel, Z. Wang, M. A. Tschudin, D. Rohner, I. Gutiérrez-Lezama, N. Ubrig, M. Gibertini, E. Giannini, A. F. Morpurgo, and P. Maletinsky. Probing magnetism in 2d materials at the nanoscale with single-spin microscopy. *Science*, 364(6444):973–976, 2019.

[16] T Staudacher, F Shi, S Pezzagna, J Meijer, J Du, C A Meriles, F Reinhard, and J Wrachtrup. Nuclear Magnetic Resonance Spectroscopy on a (5-Nanometer)ˆ3 Sample Volume. *Science*, 339(6119):561–563, 2013.

[17] I. Lovchinsky, A. O. Sushkov, E. Urbach, N. P. de Leon, S. Choi, K. De Greve, R. Evans, R. Gertner, E. Bersin, C. Müller, L. McGuinness, F. Jelezko, R. L. Walsworth, H. Park, and M. D. Lukin. Nuclear magnetic resonance detection and spectroscopy of single proteins using quantum logic. *Science*, 351(6275):836–842, 2016.

[18] Romana Schirhagl, Kevin Chang, Michael Loretz, and Christian L. Degen. Nitrogen-Vacancy Centers in Diamond: Nanoscale Sensors for Physics and Biology. *Annual Review of Physical Chemistry*, 65(1):83–105, 2014.

[19] D. Le Sage, K. Arai, D. R. Glenn, S. J. DeVience, L. M. Pham, L. Rahn-Lee, M. D. Lukin, A. Yacoby, A. Komeili, and R. L. Walsworth. Optical magnetic imaging of living cells. *Nature*, 496(7446):486–489, Apr 2013.

[20] John F. Barry, Matthew J. Turner, Jennifer M. Schloss, David R. Glenn, Yuyu Song, Mikhail D. Lukin, Hongkun Park, and Ronald L. Walsworth. Optical magnetic detection of single-neuron action potentials using quantum defects in diamond. *Proceedings of the National Academy of Sciences of the United States of America*, 113(49):14133–14138, 2016.

[21] F Gorrini, R Giri, C E Avalos, S Tambalo, S Mannucci, L Basso, and N Bazzanella. Fast and sensitive detection of paramagnetic species using coupled charge and spin dynamics in strongly fluorescent nanodiamonds. *ACS Applied Materials and Interfaces*, 27(11):24412–24422, 2019.

[22] G. Kucsko, P. C. Maurer, N. Y. Yao, M. Kubo, H. J. Noh, P. K. Lo, H. Park, and M. D. Lukin. Nanometre-scale thermometry in a living cell. *Nature*, 500(7460):54–58, Aug 2013.

[23] Masazumi Fujiwara, Simo Sun, Alexander Dohms, Yushi Nishimura, Ken Suto, Yuka Takezawa, Keisuke Oshimi, Li Zhao, Nikola Sadzak, Yumi Umehara, Yoshio Teki, Naoki Komatsu, Oliver Benson, Yutaka Shikano, and Eriko Kage-Nakadai. Real-time nanodiamond thermometry probing in vivo thermogenic responses. *Science Advances*, 6(37), 2020.

[24] James L. Webb, Luca Troise, Nikolaj W. Hansen, Jocelyn Achard, Ovidiu Brinza, Robert Staacke, Michael Kieschnick, Jan Meijer, Jean-François Perrier, Kirstine Berg-Sørensen, Alexander Huck, and Ulrik Lund Andersen. Optimization of a diamond nitrogen vacancy centre magnetometer for sensing of biological signals. *Frontiers in Physics*, 8, October 2020.

[25] Phila Rembold, Nimba Oshnik, Matthias M. Müller, Simone Montangero, Tommaso Calarco, and Elke Neu. Introduction to quantum optimal control for quantum sensing with nitrogen-vacancy centers in diamond. *AVS Quantum Science*, 2(2):024701, 2020.

[26] F. Jelezko and J. Wrachtrup. Single defect centres in diamond: A review. *Physica Status Solidi (A) Applications and Materials Science*, 203(13):3207–3225, 2006.

[27] Adam M. Wojciechowski, Mürsel Karadas, Christian Osterkamp, Steffen Jankuhn, Jan Meijer, Fedor Jelezko, Alexander Huck, and Ulrik L. Andersen. Precision temperature sensing in the presence of magnetic field noise and vice-versa using nitrogen-vacancy centers in diamond. *Applied Physics Letters*, 113(1):013502, July 2018.

[28] Ilja Fescenko, Andrey Jarmola, Igor Savukov, Pauli Kehayias, Janis Smits, Joshua Damron, Nathaniel Ristoff, Nazanin Mosavian, and Victor M. Acosta. Diamond magnetometer enhanced by ferrite flux concentrators. *Physical Review Research*, 2(2), jun 2020.

[29] Masfer Alkahtani, Johannes Lang, Boris Naydenov, Fedor Jelezko, and Philip Hemmer. Growth of high-purity low-strain fluorescent nanodiamonds. *ACS Photonics*, 6(5):1266–1271, April 2019.

[30] A. Dréau, M. Lesik, L. Rondin, P. Spinicelli, O. Arcizet, J. F. Roch, and V. Jacques. Avoiding power broadening in optically detected magnetic resonance of single NV defects for enhanced dc magnetic field sensitivity. *Physical Review B - Condensed Matter and Materials Physics*, 84(19):1–8, 2011.

[31] John F. Barry, Jennifer M. Schloss, Erik Bauch, Matthew J. Turner, Connor A. Hart, Linh M. Pham, and Ronald L. Walsworth. Sensitivity Optimization for NV-Diamond Magnetometry. *Reviews of Modern Physics*, 92:015004, 2020.

[32] Keigo Arai, Junghyun Lee, Chinmay Belthangady, David R Glenn, Huiliang Zhang, and Ronald L. Walsworth. Geometric phase magnetometry using a solid-state spin. *Nature Communications*, 9(1):4996, 2018.

[33] Tobias Nöbauer, Andreas Angerer, Björn Bartels, Michael Trupke, Stefan Rotter, Jörg Schmiedmayer, Florian Mintert, and Johannes Majer. Smooth Optimal Quantum Control for Robust Solid-State Spin Magnetometry. *Physical Review Letters*, 115(19):190801, nov 2015.

[34] Thomas Wolf, Philipp Neumann, Kazuo Nakamura, Hitoshi Sumiya, Takeshi Ohshima, Junichi Isoya, and Jörg Wrachtrup. Subpicotesla diamond magnetometry. *Physical Review X*, 5(4):1–10, 2015.

[35] Dieter Suter and Fedor Jelezko. Single-spin magnetic resonance in the nitrogen-vacancy center of diamond. *Progress in Nuclear Magnetic Resonance Spectroscopy*, 98-99:50–62, 2017.

[36] C. Müller, X. Kong, J. M. Cai, K. Melentijevic, A. Stacey, M. Markham, D. Twitchen, J. Isoya, S. Pezzagna, J. Meijer, J. F. Du, M. B. Plenio, B. Naydenov, L. P. McGuinness, and F. Jelezko. Nuclear magnetic resonance spectroscopy with single spin sensitivity. *Nature Communications*, 5:1–2, 2014.

[37] Dmitry Budker. Extreme nuclear magnetic resonance: Zero field, single spins, dark matter. . . . *Journal of Magnetic Resonance*, 306:66–68, 2019.

[38] A Gruber, A Dräbenstedt, C Tietz, L Fleury, J Wrachtrup, and C Von Borczyskowski. Scanning Confocal Optical Microscopy and Magnetic Resonance on Single Defect Centers. *Science*, 276(5321):2012–2014, 1997.

[39] Gopalakrishnan Balasubramanian, Philipp Neumann, Daniel Twitchen, Matthew Markham, Roman Kolesov, Norikazu Mizuochi, Junichi Isoya, Jocelyn Achard, Johannes Beck, Julia Tissler, Vincent Jacques, Philip R. Hemmer, Fedor Jelezko, and Jörg Wrachtrup. Ultralong spin coherence time in isotopically engineered diamond. *Nature Materials*, 8(5):383–387, April 2009.

[40] Priyadharshini Balasubramanian, Christian Osterkamp, Yu Chen, Xiuliang Chen, Tokuyuki Teraji, E. Wu, Boris Naydenov, and Fedor Jelezko. dc magnetometry with engineered nitrogen-vacancy spin ensembles in diamond. *Nano Letters*, 19(9):6681–6686, August 2019.

[41] Forrest T. Charnock and T. A. Kennedy. Combined optical and microwave approach for performing quantum spin operations on the nitrogen-vacancy center in diamond. *Physical Review B*,

64(4), June 2001.

[42] Jennifer M Schloss, John F Barry, Matthew J Turner, and Ronald L Walsworth. Simultaneous Broadband Vector Magnetometry Using Solid-State Spins. *Physical Review Applied*, 10(3):034044, 2018.

[43] Andrew Horsley, Patrick Appel, Janik Wolters, Jocelyn Achard, Alexandre Tallaire, Patrick Maletinsky, and Philipp Treutlein. Microwave device characterization using a widefield diamond microscope. *Physical Review Applied*, 10(4), October 2018.

[44] J-M Cai, B Naydenov, R Pfeiffer, L P McGuinness, K D Jahnke, F Jelezko, M B Plenio, and A Retzker. Robust dynamical decoupling with concatenated continuous driving. *New Journal of Physics*, 14(11):113023, November 2012.

[45] G. de Lange, Z. H. Wang, D. Riste, V. V. Dobrovitski, and R. Hanson. Universal dynamical decoupling of a single solid-state spin from a spin bath. *Science*, 330(6000):60–63, September 2010.

[46] Matti J Huotari. Biosensing by insect olfactory receptor neurons. *Sensors and Actuators B-chemical*, 71(July):212–222, 2000.

[47] Heidi A Kluess, Audrey J Stone, and Kirk W Evanson. ATP overflow in skeletal muscle 1A arterioles. *Journal of Physiology*, 588(16):3089–3100, 2010.

[48] Alfredo de la Escosura-Muñiz and Arben Merkoci. Nanochannels Preparation and Application in Biosensing. *ACS Nano*, 6(9):7556–7583, 2012.

[49] Tobias Nöbauer, Andreas Angerer, Björn Bartels, Michael Trupke, Stefan Rotter, Jörg Schmiedmayer, Florian Mintert, and Johannes Majer. Smooth Optimal Quantum Control for Robust Solid-State Spin Magnetometry - Supplementary material. *Physical Review Letters*, 115(19):1–6, 2015.

[50] Björn Bartels and Florian Mintert. Smooth optimal control with Floquet theory. *Physical Review A - Atomic, Molecular, and Optical Physics*, 88(5):1–7, 2013.

[51] Navin Khaneja, Timo Reiss, Cindie Kehlet, Thomas Schulte-Herbrüggen, and Steffen J. Glaser. Optimal control of coupled spin dynamics: Design of NMR pulse sequences by gradient ascent algorithms. *Journal of Magnetic Resonance*, 172(2):296–305, 2005.

[52] R C Constantin Brif and H Rabitz. Control of quantum phenomena: past, present and future. *New Journal of Physics*, 12(7):075008, 2010.

[53] Bartels Bjorn. *Smooth Optimal Control of Coherent Quantum Dynamics*. PhD thesis, Albert-Ludwigs-Universitat Freiburg, 2015.

[54] S. Hernández-Gómez, F. Poggiali, P. Cappellaro, and Nicole Fabbri. Quantum control-enhanced sensing and spectroscopy with NV qubits in diamond. In Mario Agio, Cesare Soci, and Matthew T. Sheldon, editors, *Quantum Nanophotonic Materials, Devices, and Systems 2019*. SPIE, September 2019.

[55] Philipp Konzelmann, Torsten Rendler, Ville Bergholm, Andrea Zappe, Veronika Pfannenstill, Marwa Garsi, Florestan Ziem, Matthias Niethammer, Matthias Widmann, Sang Yun Lee, Philipp Neumann, and Jörg Wrachtrup. Robust and efficient quantum optimal control of spin probes in a complex (biological) environment. Towards sensing of fast temperature fluctuations. *New Journal of Physics*, 20(12):1–29, 2018.

[56] Lihong Dong, Hang Liang, Chang Kui Duan, Ya Wang, Zhaokai Li, Xing Rong, and Jiangfeng Du. Optimal control of a spin bath. *Physical Review A*, 99(1):1–6, 2019.

[57] Florian Dolde, Ville Bergholm, Ya Wang, Ingmar Jakobi, Boris Naydenov, Sébastien Pezzagna, Jan Meijer, Fedor Jelezko, Philipp Neumann, Thomas Schulte-Herbrüggen, Jacob Biamonte, and Jörg Wrachtrup. High-fidelity spin entanglement using optimal control. *Nature Communications*, 5(1), February 2014.

[58] James L. Webb, Joshua D. Clement, Luca Troise, Sepehr Ahmadi, Gustav Juhl Johansen, Alexander Huck, and Ulrik L. Andersen. Nanotesla sensitivity magnetic field sensing using a compact diamond nitrogen-vacancy magnetometer. *Applied Physics Letters*, 114(23):231103, 2019.

[59] F. Poggiali, P. Cappellaro, and N. Fabbri. Optimal Control for One-Qubit Quantum Sensing. *Physical Review X*, 8(2):021059, jun 2018.

[60] Thomas E Skinner, Timo O Reiss, Burkhard Luy, Navin Khaneja, and Steffen J Glaser. Application of optimal control theory to the design of broadband excitation pulses for high-resolution NMR. *Journal of Magnetic Resonance*, 163:8–15, 2003.

[61] G. Goelman, S. Vega, and D Zax. Design of broadband propagators in two-level systems. *Physical Review A*, 39(11):5725–5743, 1989.

[62] Thomas E. Skinner and Naum I. Gershenzon. Optimal control design of pulse shapes as analytic functions. *Journal of Magnetic Resonance*, 204(2):248–255, 2010.

[63] Haitham A.R. El-Ella, Sepehr Ahmadi, Adam M. Wojciechowski, Alexander Huck, and Ulrik L. Andersen. Optimised frequency modulation for continuous-wave optical magnetic resonance sensing using nitrogen-vacancy ensembles. *Opt. Express*, 25(13):14809–14821, 2017.

[64] Sepehr Ahmadi. *Continuous-Wave Magnetic Field Sensing with Nitrogen-Vacancy Centers in Diamond*. PhD thesis, Technical University of Denmark, 2018.

[65] Alper Genc and Reyhan Baktur. Tunable Microstrip Bandpass Filters Based on Planar Split Ring Resonators. *IEEE Conference Presentation*, page 4, 2008.

[66] Edlyn V. Levine, Matthew J. Turner, Pauli Kehayias, Connor A. Hart, Nicholas Langellier, Raisa Trubko, David R. Glenn, Roger R. Fu, and Ronald L. Walsworth. Principles and techniques of the quantum diamond microscope. *Nanophotonics*, 8(11):1945–1973, September 2019.

[67] Haitham A. R. El-Ella, Sepehr Ahmadi, Adam M. Wojciechowski, Alexander Huck, and Ulrik L. Andersen. Optimised frequency modulation for continuous-wave optical magnetic resonance sensing using nitrogen-vacancy ensembles. *Optics Express*, 25(13):14809, 2017.

[68] James L. Webb, Luca Troise, Nikolaj W. Hansen, Jocelyn Achard, Ovidiu Brinza, Robert Staacke, Michael Kieschnick, Jan Meijer, Jean-François Perrier, Kirstine Berg-Sørensen, Alexander Huck, and Ulrik Lund Andersen. Optimization of a diamond nitrogen vacancy centre magnetometer for sensing of biological signals. *Frontiers in Physics*, 8, October 2020.

[69] R. Giri, F. Gorrini, C. Dorigoni, C. E. Avalos, M. Cazzanelli, S. Tambalo, and A. Bifone. Coupled charge and spin dynamics in high-density ensembles of nitrogen-vacancy centers in diamond. *Physical Review B*, 98(4), July 2018.

[70] N.B. Manson and J.P. Harrison. Photo-ionization of the nitrogen-vacancy center in diamond. *Diamond and Related Materials*, 14(10):1705–1710, October 2005.

[71] N Aslam, G Waldherr, P Neumann, F Jelezko, and J Wrachtrup. Photo-induced ionization dynamics of the nitrogen vacancy defect in diamond investigated by single-shot charge state detection. *New Journal of Physics*, 2013.

[72] Lucio Robledo, Hannes Bernien, Toeno van der Sar, and Ronald Hanson. Spin dynamics in the optical cycle of single nitrogen-vacancy centres in diamond. *New Journal of Physics*, 13(2):025013, February 2011.

[73] Yannick Dumeige, Jean-Francois Roch, Fabien Bretenaker, Thierry Debuisschert, Victor Acosta, Christoph Becher, Georgios Chatzidrosos, Arne Wickenbrock, Lykourgos Bougas, Alexander Wilzewski, and Dmitry Budker. Infrared laser magnetometry with a NV doped diamond intracavity etalon. *Optics Express*, 27(2):1706, 2019.

[74] Andreas Gottscholl, Mehran Kianinia, Victor Soltamov, Sergei Orlinskii, Georgy Mamin, Carlo Bradac, Christian Kasper, Klaus Krambrock, Andreas Sperlich, Milos Toth, Igor Aharonovich, and Vladimir Dyakonov. Initialization and read-out of intrinsic spin defects in a van der Waals crystal at room temperature. *Nature Materials*, 19(May):540–545, 2020.

3.3 Supplementary information

SUPPLEMENTARY INFORMATION

A. Measurement of Readout Contrast

As shown in the main text Fig. 5, we recorded lock-in demodulated fluorescence $V_{\text{fl}}(t)$ and balanced reference $V_{\text{ref}}(t)$ signals with each readout sequence. The balancing of the reference signal was such that V_{ref} was rescaled to equal the fluorescence at the end of the laser readout pulse: $V_{\text{ref}}(t_l) = V_{\text{fl}}(t_l)$. We defined the readout contrast as $C_r \equiv \sum_{t \in t_w}(V_{\text{ref}}(t) - V_{\text{fl}}(t))$ where the difference between the curves was summed over the samples in a window of time t_w, which is bounded by the black dashed lines in Fig. 1(a). The bounds of t_w were chosen to avoid the artifacts of the AOM switching on/off combined with the lock-in demodulation.

The contrast in a pulsed NV center readout scheme is generally defined as the difference in fluorescence output $V_{\text{fl}}(t)$ with (MW on, $V_{\text{fl,on}}(t)$) or without (MW off, $V_{\text{fl,off}}(t)$) a preceding microwave pulse (for example, see main text ref [28]). It can be reported as the area between the fluorescence readout curves $\int V_{\text{fl,off}}(t) - V_{\text{fl,on}}(t)\,dt$ in units that leave unclear the fractional change in fluorescence corresponding to the spin population transferred by the MW control pulse. The contrast can be reported in absolute units as the peak fractional

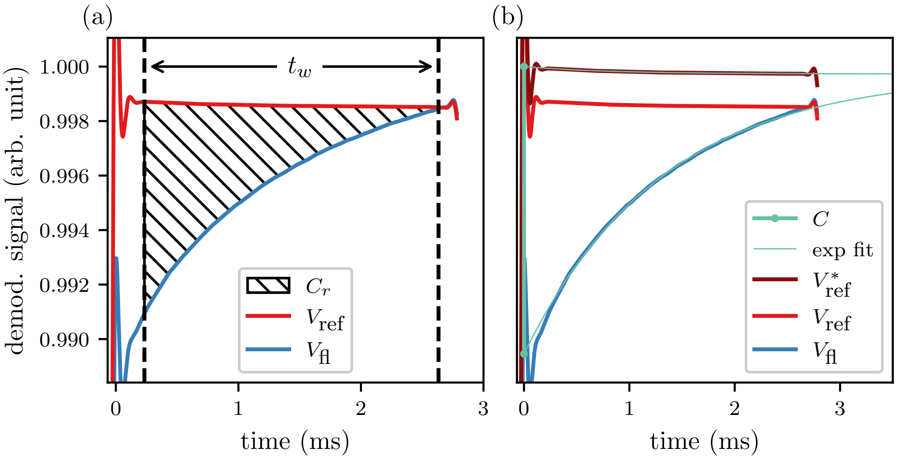

FIG. 1: Illustration of measurement protocol using ∼10000 readout sequences averaged after demodulation. We measure C_r as shown in (a) by summing over $V_{\text{ref}} - V_{\text{fl}}$ within the window t_w. The calibration procedure for converting C_r to C is shown in (b). Exponential fits of V_{ref} and V_{fl} are used first to define $V^*_{\text{ref}} = lV_{\text{ref}}$ with l such that V^*_{ref} and V_{fl} converge as $t \to \infty$. The fits are then used to evaluate C, the fractional difference at $t = 0$.

difference between the fluorescence curves $C_{\text{abs}} \equiv \max_t \left(\frac{V_{\text{fl,off}}(t)-V_{\text{fl,on}}(t)}{V_{\text{fl,off}}(t)}\right)$. We converted C_r into a quantity comparable to C_{abs} by a calibration procedure shown in Fig. 1 and justify this in the following steps.

Starting in the simpler case where t_l is long enough to completely reinitialize the ensemble, we take $V_{\text{ref}}(t) = V_{\text{fl,off}}(t)$. This is justified because the ensemble spin population is already at equilibrium at the start of the ideal $V_{\text{fl,off}}(t = 0)$ and remains so throughout the readout, so the fluorescence measured in $V_{\text{fl,off}}(t)$ is linear with the small fluctuations in pump power throughout the pulse duration: $V_{\text{ref}}(t) = kV_{\text{fl,off}}(t)$. If the pump pulse is sufficiently long, the ensemble is reinitialized into the equilibrium spin state population (see Wolf et al. 2015, citation in main text) by the time $t = t_l$ when the reference scaling is defined: $V_{\text{fl,off}}(t_l) = V_{\text{ref}}(t_l) \Rightarrow k = 1$. For complete reinitialization of the ensemble as shown in Fig. 2, we can therefore use $\frac{V_{\text{ref}}(0)-V_{\text{fl}}(0))}{V_{\text{ref}}(0)} = C_{\text{abs}}$.

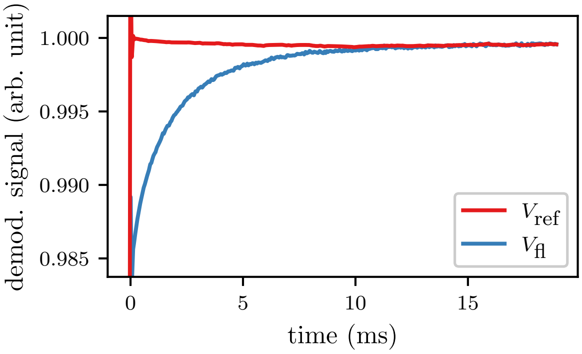

FIG. 2: Example measurement of reference and fluorescence readout with complete reinitialization of the ensemble using a long laser pulse $t_l = 20\,\text{ms}$.

With microwave pulses applied, we found our fluorescence signal V_{fl} to be dominated by a decay constant of $\tau_R = 1.4\,\text{ms}$ (see Fig. 1(a)). To fully reinitialize the weakly-pumped peripheral NV centers with slower repolarization rates, a long readout time $t_l = 20\,\text{ms}$ was necessary. These peripheral NV centers contribute a minority of the fluorescence and contrast, corresponding to a small contribution from the slower exponential decay terms present in V_{fl} in Fig. 2. With a large majority of the contrast information obtained in the first 3 ms, we used $t_l = 3\,\text{ms}$ for a substantial improvement in bandwidth and sensitivity at the expense of a small reduction in contrast. As we argue in the main text and show again in Fig. 4, the peripheral NV centers contribute much less to C than their minority share of V_{fl} for the short $t_l = 3\,\text{ms}$ and can therefore be safely neglected. Because we neglect the peripheral NV centers, we consider only those within $r < 0.5r_0$ to constitute the ensemble we address experimentally.

With the short $t_l = 3\,\text{ms}$, the strongly-pumped NV ensemble within $r < 0.5r_0$ with $\tau_R \approx 1.4\,\text{ms}$ was nearly but not fully reinitialized. In this case, our argument that $V_{\text{ref}} = kV_{\text{fl,off}}$ holds, but $k = 1$ can no longer be justified because the spin population is not at its equilibrium value at $t = t_l$. To approximate $V_{\text{fl,off}}$, we therefore fit V_{fl} and V_{ref} to single exponential decays and defined $V^*_{\text{ref}} = lV_{\text{ref}}$, with l such that the long-time limit of the fit of V^*_{ref} is equal to the long-time limit of the fit of V_{fl} as shown by the green traces in Fig. 1(b). With the reference value of V^*_{ref} set to the equilibrium value that V_{fl} decays towards, we have $lk \approx 1 \Rightarrow V^*_{\text{ref}} \approx V_{\text{fl,off}}$ for the addressed ensemble. We defined the contrast C presented for all contrast data in this work as the peak fractional difference between the exponential fits of V^*_{ref} and V_{fl}

$$C \equiv \frac{V^*_{\text{ref}}(t=0) - V_{\text{fl}}(t=0)}{V^*_{\text{ref}}(t=0)}.$$

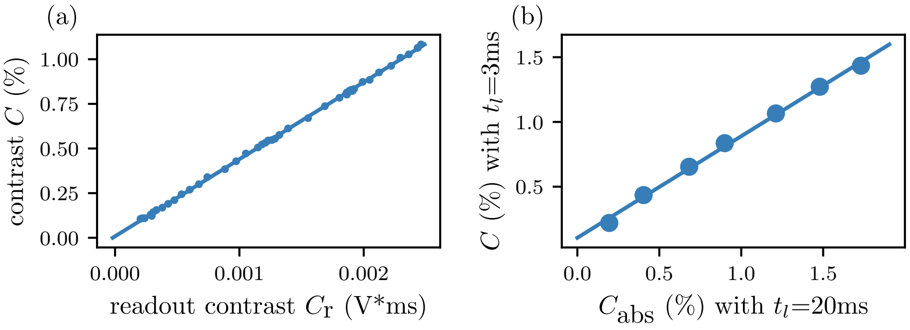

FIG. 3: (a) Calibration of scaling from C_r to C. The slope of this fit was used to scale all C_r measurements to the presented C values. (b) Demonstration of the linear relationship between the contrast C we present in all ODMR spectra measurements (using $t_l = 3\,\text{ms}$) and the absolute contrast C_{abs} obtained with a fully reinitialized ensemble ($t_l = 20\,\text{ms}$).

We measured C_r and extracted C across a broad range of experimental contrasts achieved by applying flat microwave pulses of varying power and length. All C values stated throughout this work are measurements of C_r scaled by the slope of the calibration fit in Fig. 3(a).

Finally, in Fig. 3(b), we compare the contrast C for $t_l = 3\,\text{ms}$ with the absolute contrast C_{abs} obtained by using $t_l = 20\,\text{ms}$ pulses sufficient to fully reinitialize the ensemble. We find that our method results in a small, linear decrease of the measured contrast due to the loss of contrast from the beam periphery, making C a reliable comparative estimate of the absolute total ODMR contrast C_{abs}.

B. Modelling of Readout Dynamics

Our model follows from these physically reasonable assumptions:

1. That there is a constant, fixed NV density spread throughout the diamond.
2. That our pump beam has a Gaussian lineshape and that it remains so during passage through the diamond.
3. That we can therefore model our incident beam intensity $I(r)$ as a Gaussian function, scaled to the input laser power.
4. That we can use the same incident intensity throughout the diamond, by assuming our impurity density is sufficiently low such that absorption will not significantly reduce intensity deeper into the diamond (intensity constant with thickness).
5. Because we are interested in readout properties, coherences in the spin manifold can be ignored. Therefore, the preceding MW pulse can be modelled as a population transfer between the m_s=0 and m_s=±1 states with fidelity F.
6. That this transfer occurs instantaneously, or on a timescale where the microwave pulse is significantly shorter than the laser readout pulse.
7. That the bias magnetic field is uniform, that the NV detuning varies spatially on a scale larger than the beam width, and that the MW field and therefore F does not vary significantly throughout the beam profile (it likely varies with the distance from the antenna, which is compatible with the model).

We modelled our ensemble by dividing the area of the pump beam cross section within our diamond into rings of radius r and width dr, with r=0 in the center of the pump beam profile. We then considered all NVs within the volume contained in these rings N_r to experience a laser intensity $I(r)$ with a Gaussian profile. We simulated the NV dynamics using an 8-level system (main text ref [66]), which contained the populations of the NV$^-$ m$_s \in \{0, 1\}$ optical ground (N_1 and N$_2$) and excited (N_3 and N_4) states, the singlet shelving states (N_5 and N_6), and the NV^0 optical ground (N_7) and excited (N_8) states. The level model follows the differential equations:

$$
\begin{aligned}
\frac{\mathrm{d}N_1}{\mathrm{d}t} &= -(W_g + W_{MW})N_1 + W_{MW}N_2 + k_{31}N_3 + k_{61}N_6 + W_rN_8/2 \\
\frac{\mathrm{d}N_2}{\mathrm{d}t} &= W_{MW}N_1 - (W_g + W_{MW})N_2 + k_{42}N_4 + k_{62}N_6 + W_rN_8/2 \\
\frac{\mathrm{d}N_3}{\mathrm{d}t} &= W_gN_1 - (k_{31} + k_{35} + W_i)N_3 \\
\frac{\mathrm{d}N_4}{\mathrm{d}t} &= W_gN_2 - (k_{42} + k_{45} + W_i)N_4 \\
\frac{\mathrm{d}N_5}{\mathrm{d}t} &= k_{35}N_3 + k_{45}N_4 - k_{56}N_5 \\
\frac{\mathrm{d}N_6}{\mathrm{d}t} &= k_{56}N_5 - (k_{61} + k_{62})N_6 \\
\frac{\mathrm{d}N_7}{\mathrm{d}t} &= W_iN_3 + W_iN_4 - W_{g0}N_7 + k_{87}N_8 \\
\frac{\mathrm{d}N_8}{\mathrm{d}t} &= W_{g0}N_7 - (k_{87} + W_r)N_8,
\end{aligned}
$$

where k_{ij} are the decay rates given in the cited works. The green pump intensity I_g and the cross-sections σ_j determine the rates $W_j = \sigma_j I_g \lambda_g/(hc)$ for the considered processes: W_g green excitation of the NV$^-$, W_{g0} green excitation in the neutral charge state, W_i deionization to the NV^0 state, and W_r reionization to the NV$^-$ state. To simulate the reinitialization dynamics of the ensemble, we first allowed the system to evolve under constant pump illumination $I(r)$ until population equilibrium was reached, starting from the arbitrary initial condition of $P(N_1) = 1$ which did not affect the steady state. Then, relaxation was allowed to occur ($N_3 \rightarrow N_1$, $N_4 \rightarrow N_2$, $N_5 \rightarrow N_6$, $\frac{k_{61}}{k_{61}+k_{62}}N_6 \rightarrow N_1$, $\frac{k_{62}}{k_{61}+k_{62}}N_6 \rightarrow N_2$, $N_8 \rightarrow N_7$). To implement a microwave pulse of fidelity F, we instantaneously transferred NV spins between states N_1 and N_2, with the output after the pulse $N_2' = FN_1 + (1-F)N_2, N_1' = FN_2 + (1-F)N_1$. We then continued to calculate the time evolution with the applied pump laser intensity, up to a specified laser pulse length t_l.

Here, we supplement the results of the simulation presented in the main text with two findings. First, we consider how the ensemble behaves with realistic fidelity $F < 1$, since we concluded from the main text Fig. 9(a) that the hysteresis of the beam periphery was sufficiently small to be negligible in our measurements in the $F = 1$ case. In Fig. 4, we compare the sequence behavior with ideal and sub-ideal fidelity. We find that for $F < 1$, the NV centers in the beam periphery reach their steady-state pulse response earlier. The decay of the deviation from the steady-state response is hastened by the loss of information with each imperfect π-pulse, which means the results presented in the main text are a worst-case scenario for the hysteresis.

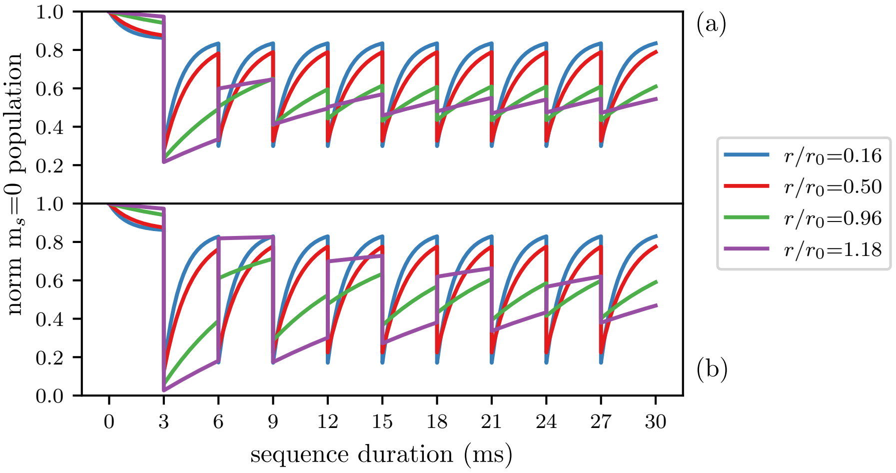

FIG. 4: Simulated time evolution showing the change in hysteresis effects with fidelity $F = 0.8$ (a) and $F = 1$ (b). Ten $t_l = 3\,\text{ms}$ laser pulses separated by relaxation and microwave pulses of the respective fidelity are simulated.

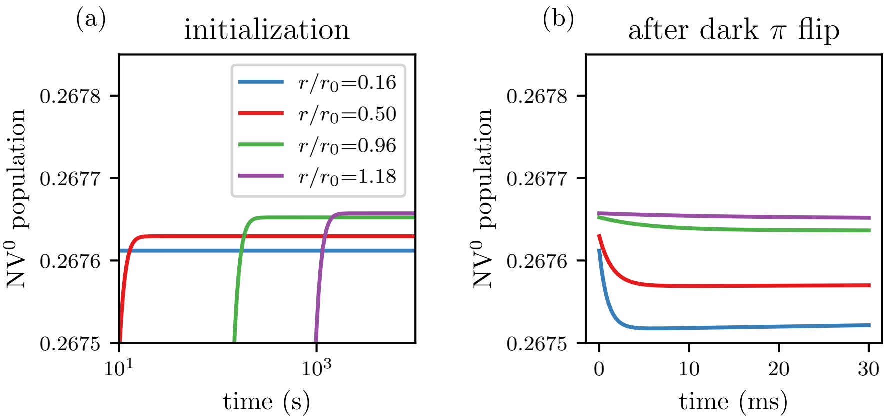

FIG. 5: Simulated charge state dynamics in intensity regime of our measurements, using the same color-matched r/r_0 values as in the main text. In (a), the charge state is initialized, and in (b), it is observed after relaxation and an electron spin flip, demonstrating that charge state dynamics are negligible.

The last consideration explored with our model was whether the NV charge state could contribute to hysteresis effects. We performed two simulations and show their result in Fig. 5. First the NV^0 state population was tracked during evolution from the N_1 state towards equilibrium. Then relaxation and a $F = 1$ π-pulse was applied to represent the largest possible change typical during the dark time in our measurements. From here, the NV^0 population was tracked under constant illumination. We found that the equilibrium NV^0 population was nearly independent of the intensity within the beam profile, and that the deviations after changes in the spin state were only of the order 0.01% in amplitude. We also note that the long timescales necessary to reach charge equilibrium under low intensity are not predictive of slow effects in our measurements, because once the charge equilibrium is reached, it remains near $P(\mathrm{NV}^0) \approx 0.2676$ under all dynamics considered.

C. NV ensemble characterization

We report the measured decay times of our NV ensemble to be $T_1 = 7.1\,\mathrm{ms}$, $T_2 = 7.0\,\mathrm{\mu s}$, and $T_2^* = 0.44\,\mathrm{\mu s}$, from measurements shown in Fig. 6 and 7. The relationship between MW power and the ensemble-averaged Rabi frequencies we obtain is shown in Fig. 8.

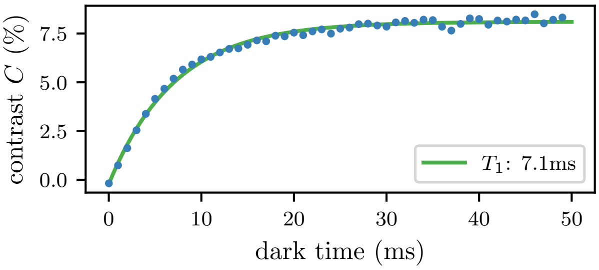

FIG. 6: T_1 decay rate measurement. Instead of the MW pulse in the readout sequence (main text Fig. 5(b)), the laser was left off for a time represented by the x-axis in (b).

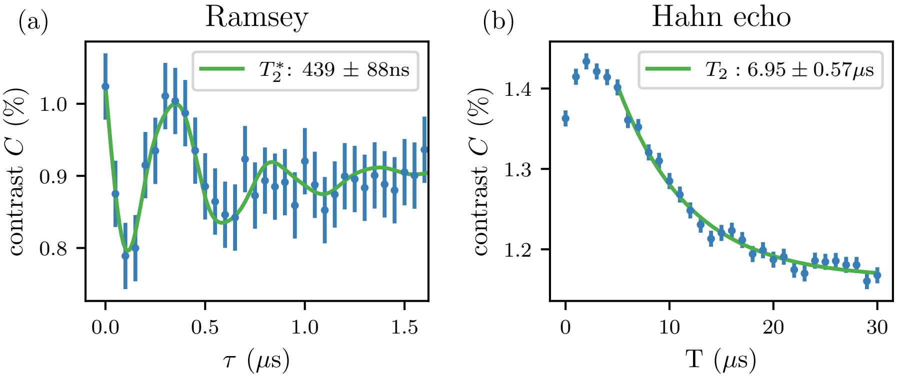

FIG. 7: Ramsey and Hahn echo measurements to retrieve the coherence times of $T_2^* = 0.44\,\mathrm{\mu s}$ and $T_2 = 7.0\,\mathrm{\mu s}$. The Ramsey measurement (a) was fit to $e^{-\tau/T_2^*}[\cos(2\pi f_1\tau + \phi_1) + \cos(2\pi f_2\tau + \phi_2) + \cos(2\pi f_3\tau + \phi_3)] + \mathrm{DC}$ to account for the possible contribution of the three hyperfine resonances. The Hahn echo measurement (b) was fit to a single exponential decay. We note that the increase in contrast for $T < 5\,\mathrm{\mu s}$ in (b) is typical of echo measurements we perform and exclude this region from the fit.

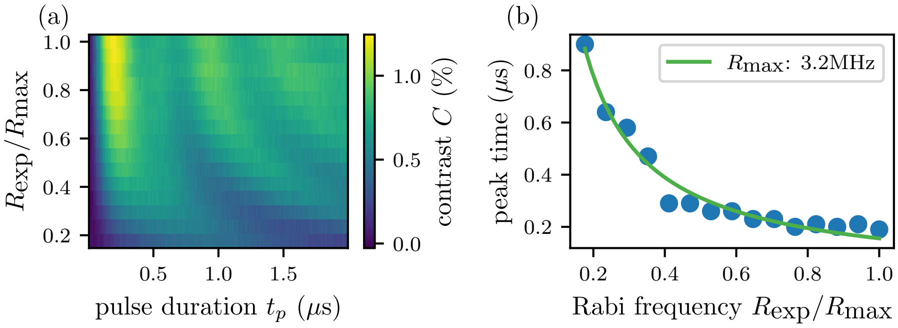

FIG. 8: (a) Rabi oscillation measurements from which we determine the scaling between the set power and ensemble average Rabi frequency. (b) Fit of the time to the initial peaks T_p for each R_{exp} in (a), used to estimate the scaling from the set MW power P_{MW} to R_{exp}, where $R_{\mathrm{exp}} = R_{\mathrm{max}}\sqrt{P_{\mathrm{MW}}/P_{\mathrm{MWmax}}}$, and $T_p = 1/2R_{\mathrm{exp}}$.

D. ODMR measurement details

In the main text, the best-performing 3fd pulse is presented for each MW power setting (in terms of the Rabi frequency Ω). The full exploration of the measured parameter space is shown here in Fig. 9. For each 3fd pulse attempted, a $2\,\mathrm{MHz}$ section of the ODMR spectrum was measured, with an example shown in Fig. 10, where the error in the slope fit was propagated from the error statistics we measured for repeated acquisitions. $2\,\mathrm{MHz}$ is sufficient because the hyperfine resonances (separated by $2.16\,\mathrm{MHz}$) are resolved, and the region of greatest slope is the $< 1\,\mathrm{MHz}$ range between the center resonance peak and the adjacent dip. We fit this data to a double-Lorentzian (ignoring the low-frequency hyperfine resonance peak outside of the measured spectral range)

$$C = \frac{a}{1 + \left(\frac{f - f_0}{\gamma/2}\right)^2} + \frac{b}{1 + \left(\frac{f - f_0 - 2.16\mathrm{MHz}}{\gamma/2}\right)^2} + \mathrm{DC}$$

and present the absolute maximum of the slope of the fit function $C' = \frac{\mathrm{d}C}{\mathrm{d}f}$. The error propagation is performed by numerically calculating the Jacobian relative to the fit parameters $\mathbf{J}(C') = \left[\frac{\partial C'}{\partial f_0}, \frac{\partial C'}{\partial \gamma}, \frac{\partial C'}{\partial a}, \frac{\partial C'}{\partial b}, \frac{\partial C'}{\partial \mathrm{DC}}\right]$ at the frequency of the greatest slope, and multiplying by the fit parameter covariance matrix $\mathbf{\Sigma_C}$, yielding

$$\sigma = \mathbf{J}\mathbf{\Sigma_C}\mathbf{J}^T.$$

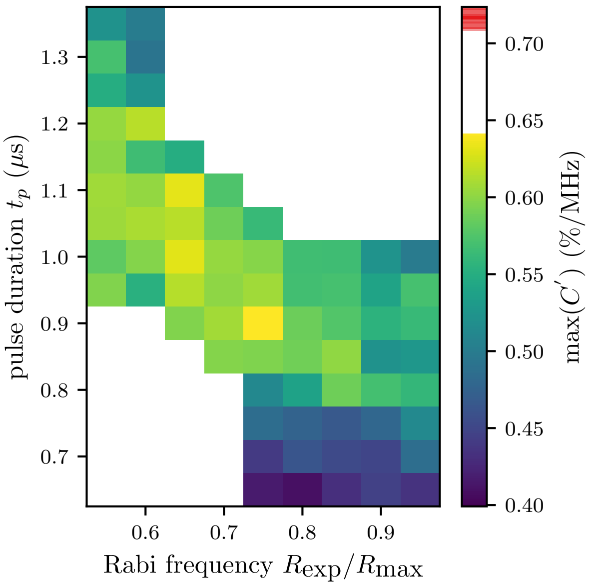

FIG. 9: Maximum ODMR slope of 3fd pulses across duration and power parameter space, determined by fitting the ODMR spectrum as described in Fig. 10. The 3fd sensitivity data shown in the main text are the most sensitive points for each column (Ω) shown here. The colorbar shows the mean value and $\pm 1\sigma$ shaded of the best optimal control pulse sensitivity for comparison.

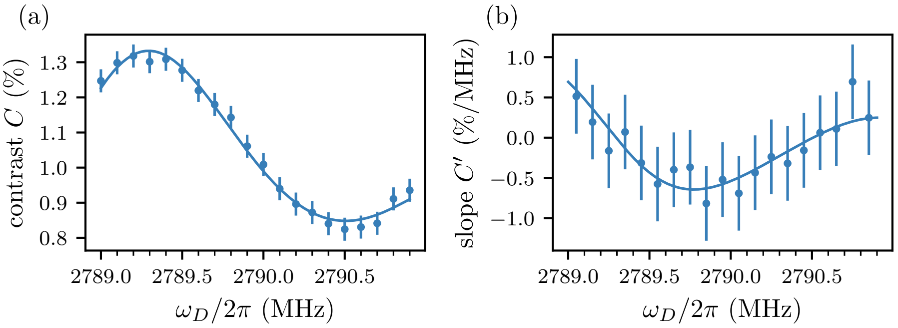

FIG. 10: Measurement and fits for the best 3fd flat pulse. The error bars on the ODMR data are the standard error of the mean for the number of acquisitions we average. The slope data are simply the discrete differential of the ODMR data with propagated error bars and are not used in fitting.

E. Including the hyperfine transitions for ^{15}N

The derivation of the Fourier components of the Hamiltonian for the two hyperfine levels of ^{15}N is similar to the one for the three hyperfine levels of ^{14}N. We assume that the m_s=±1 states are clearly split by a static magnetic bias field and no interaction between NV spins. A single set of two NV centers that each correspond to one of the hyperfine transitions can then be reasonably approximated as two independent two-level systems. The drift Hamiltonian thus has the form

$$\hat{\mathcal{H}}_0 = \sum_u \frac{\omega_{0,u}}{2}\sigma_{z,u}, \tag{1}$$

where $\omega_{0,u}$ is the transition frequency of hyperfine transition u, and $\sigma_{z,u}$ is a Pauli spin-z matrix that is specific to transition u. We choose to denote the transitions l and r to avoid confusion with the terms used for the ^{14}N hyperfine splitting. The states of the two two-level systems can be completely described by a single vector of length 4, and the $\sigma_{z,k}$-matrices can be represented by the following 4-by-4 matrices.

$$\sigma_{z,l} = \begin{pmatrix} 1 & 0 & 0 & 0 \\ 0 & -1 & 0 & 0 \\ 0 & 0 & 0 & 0 \\ 0 & 0 & 0 & 0 \end{pmatrix},\ \sigma_{z,r} = \begin{pmatrix} 0 & 0 & 0 & 0 \\ 0 & 0 & 0 & 0 \\ 0 & 0 & 1 & 0 \\ 0 & 0 & 0 & -1 \end{pmatrix} \tag{2}$$

We again assume a single-frequency control field that is linearly polarized in the x-direction, which is perpendicular to the NV axis, allowing the control Hamiltonian to be written in the form

$$\hat{\mathcal{H}}_c = \sum_j \sigma_{x,u}\left[I(t)\cos\left(\omega_D t\right) + Q(t)\sin\left(\omega_D t\right)\right], \tag{3}$$

where $\sigma_{x,u}$ is a Pauli spin-x matrix that is specific to transition u. Similarly to the $\sigma_{z,u}$-matrices, the $\sigma_{x,u}$-matrices can be represented by 4-by-4 matrices.

$$\sigma_{x,l} = \begin{pmatrix} 0 & 1 & 0 & 0 \\ 1 & 0 & 0 & 0 \\ 0 & 0 & 0 & 0 \\ 0 & 0 & 0 & 0 \end{pmatrix},\ \sigma_{x,r} = \begin{pmatrix} 0 & 0 & 0 & 0 \\ 0 & 0 & 0 & 0 \\ 0 & 0 & 0 & 1 \\ 0 & 0 & 1 & 0 \end{pmatrix} \tag{4}$$

The $\sigma_{y,u}$ matrices, which are Pauli spin-y matrices that are specific to transition j and will be used later, can also be represented by 4-by-4 matrices.

$$\sigma_{y,l} = \begin{pmatrix} 0 & -i & 0 & 0 \\ i & 0 & 0 & 0 \\ 0 & 0 & 0 & 0 \\ 0 & 0 & 0 & 0 \end{pmatrix},\ \sigma_{y,r} = \begin{pmatrix} 0 & 0 & 0 & 0 \\ 0 & 0 & 0 & 0 \\ 0 & 0 & 0 & -i \\ 0 & 0 & i & 0 \end{pmatrix} \tag{5}$$

The total Hamiltonian thus has the form

$$\hat{\mathcal{H}}(t) = \sum_u \left(\frac{\omega_{0,u}}{2}\sigma_{z,u} + \sigma_{x,u}\left[I(t)\cos\left(\omega_D t\right) + Q(t)\sin\left(\omega_D t\right)\right]\right). \tag{6}$$

We can simplify the rest of the calculations by working in a rotating frame at ω_D. This is done via the unitary rotation operator

$$\hat{R} = \exp\left(\sum_u i\omega_D t\sigma_{z,u}/2\right) \tag{7}$$

and in this frame, the Schrödinger equation can be rewritten as $i\frac{d}{dt}|\psi'\rangle = \hat{\mathcal{H}}'|\psi'\rangle$ with $|\psi'\rangle = \hat{R}|\psi\rangle$ and the Hamiltonian

$$\hat{\mathcal{H}}' = \hat{R}\hat{\mathcal{H}}\hat{R}^\dagger + i\frac{\partial\hat{R}}{\partial t}\hat{R}^\dagger,\ i\frac{\partial\hat{R}}{\partial t}\hat{R}^\dagger = -\frac{\omega_D}{2}\sum_j \sigma_{z,j}. \tag{8}$$

The drift Hamiltonian is time-independent and the $\sigma_{z,u}$ matrices all commute with each other, resulting in

$$\hat{R}\hat{\mathcal{H}}\hat{R}^\dagger = \hat{\mathcal{H}}_0 + \hat{R}\hat{\mathcal{H}}_c\hat{R}^\dagger. \tag{9}$$

The unitary rotation operator will also commute with every term in $\hat{\mathcal{H}}_c$ except for $\sigma_{x,u}$. More precisely, $[\sigma_{z,u}, \sigma_{x,u'}] = 2i\sigma_{y,u}\delta_{u,u'}$ and $[\sigma_{z,u}, \sigma_{y,u'}] = -2i\sigma_{x,u}\delta_{u,u'}$. The Baker-Campbell-Hausdorff lemma then allows us to write

$$\hat{R}\hat{\mathcal{H}}_c\hat{R}^\dagger \;=\; \sum_u \left(\sigma_{x,u}\cos\left(\omega_D t\right) + \sigma_{y,u}\sin\left(\omega_D t\right)\right) \cdot \left[I(t)\cos\left(\omega_D t\right) + Q(t)\sin\left(\omega_{MW} t\right)\right]. \tag{10}$$

If we insert the above expression in Eq. (8) and furthermore define the detuning, $\Delta = \left(\omega_{0,l} + \omega_{0,r}\right)/2 - \omega_D$, as the difference between the average of the two hyperfine transition frequencies and the central driving frequency, ω_D, we obtain the expression

$$\begin{aligned}\hat{\mathcal{H}}' = \sum_u \Bigg(\frac{\Delta + m_u\delta_I/2}{2}\sigma_{z,u} &+ \left(\sigma_{x,u}\cos\left(\omega_D t\right) + \sigma_{y,u}\sin\left(\omega_D t\right)\right) \\ &\times \left[I(t)\cos\left(\omega_D t\right) + Q(t)\sin\left(\omega_D t\right)\right]\Bigg),\end{aligned} \tag{11}$$

where $\delta_I = 3.03\,\mathrm{MHz}$ is the splitting between the hyperfine transitions, $m_l = -1$ and $m_r = 1$. Expanding by using the trigonometric relations

$$\cos\left(\omega_D t\right)^2 = \frac{1}{2}\left[1 + \cos\left(2\omega_D t\right)\right], \tag{12}$$

$$\sin\left(\omega_D t\right)^2 = \frac{1}{2}\left[1 - \cos\left(2\omega_D t\right)\right] \tag{13}$$

and

$$\cos\left(\omega_D t\right)\sin\left(\omega_D t\right) = \frac{1}{2}\sin\left(2\omega_D t\right), \tag{14}$$

one finds

$$\begin{aligned}\hat{\mathcal{H}}' = \sum_u \Big(\frac{\Delta + m_u\delta_I/2}{2}\sigma_{z,u} + I(t)\left[\sigma_{x,u}\frac{1}{2}\left[1+\cos\left(2\omega_D t\right)\right] + \sigma_{y,u}\frac{1}{2}\sin\left(2\omega_D t\right)\right] \\ + Q(t)\left[\sigma_{x,u}\frac{1}{2}\sin\left(2\omega_D t\right) + \sigma_{y,u}\frac{1}{2}\left[1-\cos\left(2\omega_D t\right)\right]\right]\Big),\end{aligned} \tag{15}$$

which can be simplified by using the rotating wave approximation to eliminate the fast oscillating terms $\cos\left(2\omega_D t\right)$ and $\sin\left(2\omega_D t\right)$.

$$\hat{\mathcal{H}}' = \sum_u \left(\frac{\Delta + m_u\delta_I/2}{2}\sigma_{z,u} + \frac{I(t)}{2}\sigma_{x,u} + \frac{Q(t)}{2}\sigma_{y,u} \right) \tag{16}$$

Combining these equations with those in the main text yields:

$$\hat{\mathcal{H}}_n = \sum_u \frac{1}{T}\int_0^T \exp\left(in\Omega t\right)\left(\frac{\Delta + m_u/2\delta_I}{2}\sigma_{z,u} + \sum_{j=1}^{N_f}\left[a_{jx}\sigma_{x,u} + a_{jy}\sigma_{y,u}\right]\sin\left(j\Omega t\right)\right). \tag{17}$$

The above expression can be further simplified by using the exponential form of a sine and the integral form of a Kronecker delta. Doing so yields the final expression for the Fourier components of the Hamiltonian when both of the ^{15}N hyperfine transitions are taken into account,

$$\hat{\mathcal{H}}_n = \sum_u \left(\frac{\Delta + m_u\delta_I/2}{2}\sigma_{z,u}\delta_{n,0} + \sum_{j=1}^{N_f}\frac{1}{2i}\left[a_{jx}\sigma_{x,u} + a_{jy}\sigma_{y,u}\right]\cdot\left[\delta_{n,j} - \delta_{-n,j}\right]\right). \tag{18}$$

F. Best Optimal Pulse Control Parameters

The control amplitudes, a_{jk}, that define our best optimal pulse are given (in MHz) in Table I. This pulse has a duration of 1.85 µs.

TABLE I: The a_{jk}-values of our best optimal pulse in MHz.

a_{1x}	a_{2x}	a_{3x}	a_{4x}	a_{5x}
0.11388948	0.09884733	-0.00809110	-0.00177604	0.00918642
a_{6x}	a_{7x}	a_{8x}	a_{9x}	a_{10x}
-0.088628	-0.11101755	0.00940646	0.11946038	0.11709449
a_{1y}	a_{2y}	a_{3y}	a_{4y}	a_{5y}
0.09465327	0.08214617	-0.00670811	-0.00148568	0.00772306
a_{6y}	a_{7y}	a_{8y}	a_{9y}	a_{10y}
-0.07368535	-0.09219246	0.00782588	0.09930594	0.09733759

4 Laser threshold magnetometry using green-light absorption by diamond nitrogen vacancies in an external cavity laser

4.1 Introduction

Conventional NV sensing involves measuring changes in the red fluorescence under green light illumination and resonant MW driving. However, this sensing approach is significantly limited by the low contrast in the signal to be measured and the high level of snot noise caused by the bright background. These limitations are particularly significant when working with ensembles of NV centers.

We proposed a way to circumvent these limitations by using the green light absorption by the NV centers in a diamond to perform laser threshold magnetometry. The diamond is placed in the external cavity of a standard external cavity laser made with a semiconductor laser diode and serves as an additional source of loss. The properties of NV centers result in the green absorption being greater when the MW drive is off-resonance than when the drive is on-resonance. By fixing the laser diode drive current at the threshold current for the situation where the MW drive is off-resonance, an external field can be used to shift the MW drive on-resonance, thereby pushing the external cavity laser across the lasing threshold. Such a setup would theoretically have 100% contrast and zero background due to the absence of lasing in the absence of external fields.

We theoretically simulated and investigated the performance of the proposed setup using realistic parameters and considered the limitations. In particular, we also considered the impact of amplified spontaneous emission near the lasing threshold, which has been neglected in previous similar works. The main findings are summarized in the publication in section 4.2, and the supplementary information is given in section 4.3.

4.2 Publication

PHYSICAL REVIEW A **103**, 062603 (2021)

Laser threshold magnetometry using green-light absorption by diamond nitrogen vacancies in an external cavity laser

James L. Webb,[1,*] Andreas F. L. Poulsen,[1] Robert Staacke,[2] Jan Meijer,[2]
Kirstine Berg-Sørensen,[3] Ulrik Lund Andersen,[1] and Alexander Huck[1]
[1]*Center for Macroscopic Quantum States (bigQ), Department of Physics, Technical University of Denmark, 2800 Kongens Lyngby, Denmark*
[2]*Division of Applied Quantum Systems, Felix Bloch Institute for Solid State Physics, Leipzig University, 04103 Leipzig, Germany*
[3]*Department of Health Technology, Technical University of Denmark, 2800 Kongens Lyngby, Denmark*

(Received 4 February 2021; revised 20 April 2021; accepted 24 May 2021; published 4 June 2021)

Nitrogen vacancy (NV) centers in diamond have attracted considerable recent interest for use in quantum sensing, promising increased sensitivity for applications ranging from geophysics to biomedicine. Conventional sensing schemes involve monitoring the change in red fluorescence from the NV center under green laser and microwave illumination. Due to the strong fluorescence background from emission in the NV triplet state and low relative contrast of any change in output, sensitivity is severely restricted by a high optical shot noise level. Here, we propose a means to avoid this issue, by using the change in green pump absorption through the diamond as part of a semiconductor external cavity laser run close to the lasing threshold. We show that theoretical sensitivity to the magnetic field on the $\mathrm{pT}/\sqrt{\mathrm{Hz}}$ level is possible using a diamond with an optimal density of NV centers. We discuss the physical requirements and limitations of the method, particularly the role of amplified spontaneous emission near threshold and explore realistic implementations using current technology.

DOI: 10.1103/PhysRevA.103.062603

I. INTRODUCTION

Optical manipulation of material defects represents an ideal method for quantum sensing, exploiting properties such as entanglement and superposition [1]. The nitrogen-vacancy (NV) center in diamond, possessing long quantum coherence times at room temperature, has in particular drawn considerable interest [2–4]. Diamond is an ideal material for sensing, being mechanically hard, chemically stable, isotopically pure, as well as biocompatible [5,6]. The negatively charged nitrogen-vacancy center (NV^-) has an energy level structure that results in optical properties that are highly sensitive to temperature [7], strain (pressure) [8], electric field [9], and, particularly, magnetic field. Sensing is conventionally performed by detecting changes in the intensity of red fluorescence (≈637–750 nm) under irradiation with green light and resonant microwaves via a process termed optically detected magnetic resonance (ODMR) spectroscopy [4,10–12]. It can be done using a continuous wave (cw) method [13] or by using short laser and microwave pulses [14,15].

However, measuring via red fluorescence suffers from two considerable physical limitations. First, the signal to be measured has a very low contrast on bright emission from decay in the NV^- triplet state. For a single NV^- or for a smaller ensemble where the NV centers are preferentially aligned through growth engineering [16], spin-dependent contrast can be up to 30% [17]. However, for bulk sensing using an ensemble of many billions of NV centers in a region encompassing a large volume of the diamond sensor (up to the whole diamond), the contrast that is realized is often, at most, a few percent [18,19]. The sensitivity is therefore limited by this low contrast and the high level of shot noise from the bright background rising from triplet state fluorescence emission. The second physical limitation is the high refractive index of diamond, which traps the majority of the fluorescence inside the diamond. Microfabrication schemes have been proposed to mitigate this issue, but have yet to deliver significant improvements [20,21].

An alternative method is to use optical absorption of the pump light by the NVs. Previous work has used the change in green absorption in an optical cavity [22,23] or by using changes in infrared (IR) absorption by the singlet state [24]. These schemes are technically demanding, requiring an optical cavity or unusual wavelength (1042 nm) laser. A promising alternative is laser threshold sensing [25], using changes in optical absorption resulting from the parameter to be sensed (e.g., magnetic field or temperature) to push a medium across the lasing threshold. This method eliminates the bright background that limits sensitivity using conventional fluorescence detection. A further attraction is the wide applicability to any material with variable optical absorption, including a wider range of defects in diamond, SiC, and two-dimensional (2D) materials [26,27].

Building on the work by Dumeige *et al.* [28] and our own previous work on diamond absorption magnetometry [22,23], here we outline a scheme to use laser threshold sensing of the magnetic field with green light in a standard external cavity laser. We show it is possible to achieve high sensitivity in the $\mathrm{pT}/\sqrt{\mathrm{Hz}}$ range with realistic assumptions for the key physical parameters. Our proposal differs from that of previous work by using simpler green pump absorption rather than IR absorption and by using an ordinary current driven laser

---

[*] jaluwe@fysik.dtu.dk

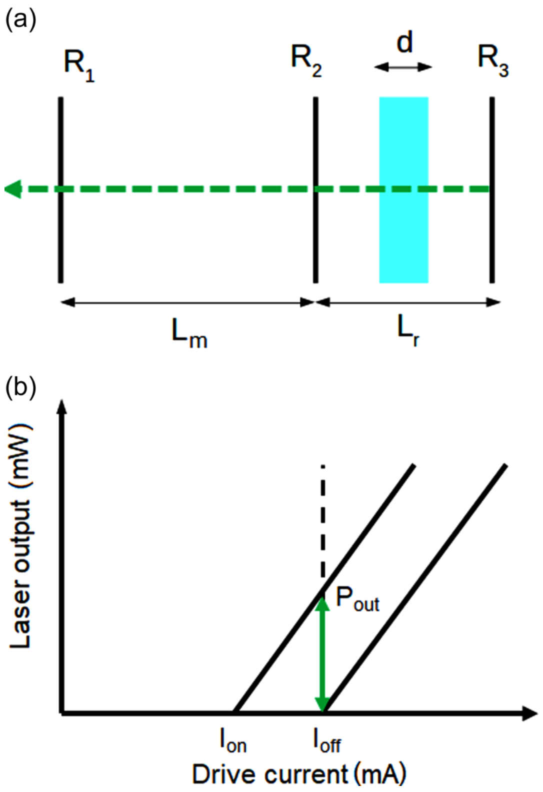

FIG. 1. (a) Schematic of the external cavity setup with a Fabry-Perot semiconductor laser diode of cavity length L_m and end facet power reflectivities R_1 and R_2 coupled to an external cavity of length L_r via mirror R_3 and diamond of thickness d. Laser emission (dashed line) is through R_1. We model our external cavity laser with the diamond as a single cavity with equivalent end reflectance R_e and the diamond absorption loss α_d included in the total cavity loss α_t. (b) Simplified schematic of the laser threshold process, where a reduction in diamond absorption through application of resonant microwaves reduces the threshold current to I_{th}^{on}, producing lasing output P_{out} when driven at I_{th}^{off}.

diode or gain chip medium without the need for an additional pump laser. We show that this configuration, which is highly suitable for miniaturization, can deliver high sensitivity, and we discuss the key physics required to reach such sensitivity levels. Finally, we discuss and calculate limiting factors that may prevent these levels from being reached in practice. This includes factors that may not have been previously considered, such as amplified spontaneous emission near to the lasing threshold.

II. METHODS

A. External cavity laser model

We place the diamond into a standard external cavity laser setup as described schematically in Fig. 1(a). This consists of a Fabry-Perot semiconductor laser diode or gain chip of length L with end facet reflectivities R_1 and R_2 coupled to an external cavity formed by mirror R_3 via an external cavity of length L_r containing the diamond of thickness d. We assume normal incidence and that transmission through the diamond is high, with minimal reflection from the diamond facets. For simplicity, we assume a single optical mode at a single wavelength. We consider the optical loss due to absorption in a diamond of thickness d. The change in laser intensity $\hat{I}$ on a pass through the diamond is given by

$$\Delta\hat{I} = \hat{I}_0 - \hat{I}_0 e^{-\alpha_d z}, \tag{1}$$

where $\hat{I}_0$ is the intensity of the laser emission with no diamond present in the external cavity, α_d is the absorption coefficient in the diamond, and z is the path length taken within the diamond. For normal incidence, $z = d$ and the absorption coefficient can be derived from the rate equation model given in the following section or can be measured experimentally. For the semiconductor lasing medium between mirrors 1 and 2, we assume a total cavity loss α_t, given by the sum of intrinsic cavity loss due to the gain medium α_c and losses from the mirrors and end facets α_m, giving a total loss α_t,

$$\alpha_t = \alpha_c + \alpha_m = \alpha_c + \frac{1}{L_m}\ln\left(\frac{1}{\sqrt{R_1R_2}}\right). \tag{2}$$

In order to simplify the analysis of the external cavity structure, we use the three mirror model [29–32] to treat the complete diode and external cavity structure as a single cavity of length $L = L_m + L_r$, with mirror R_2 replaced by an effective reflectivity R_e, with the single cavity containing the optical losses of the external cavity and diamond, the internal losses of the gain medium in the laser diode, and the loss from the cavity through the mirrors. By assuming that the losses due to the diamond are spread evenly throughout, we redefine the loss coefficient due to the diamond as $\alpha_e = (\alpha_d/L)d$, and our total cavity loss as

$$\alpha_t = \alpha_c + \alpha_e + \frac{1}{L}\ln\left(\frac{1}{\sqrt{R_1R_e}}\right), \tag{3}$$

where $R_e = |r_e|^2$ relates the power reflectivity to the complex field reflectivity r_e. We use the model for the effective reflectivity by Voumard *et al.* [33], detailed further in the Supplemental Material [34]. Neglecting phase components, at threshold, $R_1R_ee^{(\Gamma g-\alpha_t)2L} = 1$, where $g = g_{th}$ is the (threshold) gain coefficient.

For the full structure, the rate equations for photon (S) and carrier (N) density are given by the standard equations for a laser diode as

$$\frac{dN}{dt} = \frac{I}{qV} - \frac{N}{\tau_N} - GS \tag{4}$$

and

$$\frac{dS}{dt} = GS - \frac{S}{\tau_P} + \frac{\beta N}{\tau_N}. \tag{5}$$

Here, I is the drive current, V the volume of the gain region, G the gain of the lasing medium, and q the electronic charge. The term GS arises from stimulated emission in the laser diode gain medium and S/τ_P includes the cavity loss from the mirrors, gain medium, and diamond. Further, τ_P is the photon lifetime in the cavity and τ_N the carrier lifetime in the laser diode. Carriers are generated by a current I in a volume V, where $V = L \times w \times t_h$, where t_h is the thickness and w the width of the laser diode active region. The term $\beta N/\tau_N$

relates to spontaneous emission, governed by the spontaneous emission factor β.

We can define gain G phenomenologically, in the form [35]

$$G = \Gamma g = \Gamma a(N_{th} - N_{tr})(1 - \epsilon S), \tag{6}$$

where Γ is the confinement factor and ϵ is the gain compression factor that phenomenologically accounts for effects such as spectral hole burning at higher optical power. The carrier density at transparency is given by N_{tr}. The rate equations for photon and carrier density can be solved for a steady state condition ($dS/dt = 0$, $dN/dt = 0$). For carrier density $N = N_{th}$ close to N_{tr} and neglecting spontaneous emission ($\beta = 0$), the gain balances the cavity loss. The factor a is the differential gain coefficient, a material specific property defining how well the semiconductor can generate carriers for population inversion. Equation (6) is valid for heterostructure laser diodes and certain quantum well structures where the threshold is close to the transparency carrier density. Unless otherwise stated, we use the model of Eq. (6) in this work.

Using Eqs. (4)–(6) at lasing threshold, where $S = 0$, $G = 1/\tau_p$, and $\Gamma g_{th} = \alpha_t$, we can derive an equation for carrier density at threshold N_{th},

$$N_{th} = N_{tr} + \frac{\alpha_t}{\Gamma a}, \tag{7}$$

and inserting this result into the rate equation for carrier density [Eq. (4)] allows us to calculate the threshold current,

$$I_{th} = \frac{qV}{\eta_i \tau_N} N_{th} = \frac{qV}{\eta_i \tau_N}\left(N_{tr} + \frac{\alpha_t}{\Gamma a}\right). \tag{8}$$

Here we introduce the quantum efficiency of the carrier to photon conversion η_i. By using Eq. (8) in the rate equations at $I > I_{th}$, we can calculate the photon density at any current above the lasing threshold. We can then calculate the laser light power that can be emitted from the left-hand side mirror R_1 using the factor η_o, the output coupling efficiency, which is defined as the ratio of photons lost through the mirror R_1 to the total cavity loss $\alpha_t = \alpha_m + \alpha_c + \alpha_e$,

$$P_{\text{out}} = \eta_o \frac{hc}{\lambda \tau_p} \frac{V}{\Gamma} S, \tag{9}$$

where V/Γ is the effective mode volume of the cavity, λ the wavelength, and h and c Plank's constant and the speed of light, respectively. In the limit of $\epsilon S \to 0$ where there is no limiting effect on the gain, the power output can be rewritten directly in terms of the threshold current,

$$P_{\text{out}} = \eta_o \eta_i \frac{hc}{q\lambda}(I - I_{th}). \tag{10}$$

In both of these expressions,

$$\eta_o = \frac{\alpha_{m_1}}{\alpha_m + \alpha_c + \alpha_e} = \frac{\ln\frac{1}{\sqrt{R_1}}}{\ln\frac{1}{\sqrt{R_1 R_e}} + (\alpha_e + \alpha_c)L}. \tag{11}$$

For larger finite values of ϵ well above threshold or including finite spontaneous emission through nonzero β, we can numerically solve the steady state rate equations [Eqs. (4) and (5)] to calculate N, S, and the laser power output.

The total cavity absorption α_t will change when microwaves are applied to the diamond at a frequency equal to the splitting of the NV triplet ground state levels, reducing the lasing threshold current, $\Delta I_{th} = I_{th}^{\text{off}} - I_{th}^{\text{on}}$, where I_{th}^{on} is the threshold current *on* microwave resonance and I_{th}^{off} the threshold current *off* resonance. By running at drive current equal to I_{th}^{off}, the laser output is generated only while on microwave resonance. This is shown schematically in Fig. 1(b).

B. Absorption model

We use the rate equation model from [36] in order to calculate the optical absorption of green pump light by the diamond and the maximum change in absorption when on microwave resonance. The parameters we use for the transition rates are the same as those in [28], derived from [37–40]. We calculate the normalized occupancies of each energy level with microwaves supplied n_i^{on} and without microwaves n_i^{off}, where $\sum_i n_i = 1$ and index $i = 1$–8, where $i = 1$ refers to the $m_s = 0$ ground state level, $i = 2$ the $m_s = \pm 1$ ground state levels, $i = 3, 4$ the spin triplet excited states, $i = 5, 6$ the spin singlet shelving states, and $i = 7, 8$ the ground and excited state of the NV^0. We define a total NV$^-$ density N_{NV} in ppm. Off resonance, the total number density of NV$^-$ in each state N_i^{off} is given by

$$N_i^{\text{off}} = N_{NV} \frac{n_i^{\text{off}}}{\sum_i n_i^{\text{off}}}. \tag{12}$$

We define a measurement axis along one of the four possible crystallographic axes for the NV. We calculate that when microwaves are applied, we drive only the NVs aligned along one axis such that the total number density on resonance N_i^{on} is given by

$$N_i^{\text{on}} = \frac{1}{4} N_{NV} \frac{n_i^{\text{on}}}{\sum_i n_i^{\text{on}}} + \frac{3}{4} N_{NV} \frac{n_i^{\text{off}}}{\sum_i n_i^{\text{off}}}. \tag{13}$$

We calculate the change in intensity on a single pass when on and off microwave resonance as

$$\hat{I_{\text{on}}} = \hat{I}_0 e^{-\alpha_{\text{on}} d}, \quad \hat{I_{\text{off}}} = \hat{I}_0 e^{-\alpha_{\text{off}} d}, \tag{14}$$

where d is the thickness of the diamond, and the absorption coefficient α on and off resonance is given by

$$\alpha^{\text{on}} = \sigma_g\left(N_1^{\text{on}} + N_2^{\text{on}}\right) + \sigma_{g0} N_7^{\text{on}} + \sigma_e\left(N_3^{\text{on}} + N_4^{\text{on}}\right) + \sigma_r N_8^{\text{on}}, \tag{15}$$

$$\alpha^{\text{off}} = \sigma_g\left(N_1^{\text{off}} + N_2^{\text{off}}\right) + \sigma_{g0} N_7^{\text{off}} + \sigma_e\left(N_3^{\text{off}} + N_4^{\text{off}}\right) + \sigma_r N_8^{\text{off}}. \tag{16}$$

Here, σ_g and σ_{g0} are, respectively, the absorption cross sections of green light for NV$^-$ and NV^0, and σ_e and σ_r are the ionization cross sections for transfer between the charged and uncharged defect states. This allows us to calculate the change in absorption when the diamond is present without microwaves, $\hat{I_{\text{off}}}/\hat{I}_0$, the change when driven on microwave resonance, $\hat{I_{\text{on}}}/\hat{I}_0$, and the change between these, which we term the absorption contrast,

$$C = (\hat{I_{\text{off}}}/\hat{I}_0) - (\hat{I_{\text{on}}}/\hat{I}_0). \tag{17}$$

C. Key physical parameters

The key physical parameters of the model can be divided into those that are intrinsic to the semiconductor gain medium, those intrinsic to the diamond, and those defined by the setup. Examples of the latter include the mirror reflectivities R_1, R_2, R_3, the cavity length L, and any other losses, such as reflection out of the cavity or from absorption by other optical components such as lenses, included in the cavity loss factor α_c. These factors will also influence the photon lifetime in the cavity τ_P. The maximum Rabi frequency Ω_R that can be reached also depends on the microwave power and how well the microwaves can be coupled into the diamond.

The parameters which are intrinsic to the diamond are the diamond thickness d, NV^- density N_{NV}, ensemble dephasing time T_2^* defining the ODMR linewidth, and absorption contrast C arising from changes in pump absorption on or off microwave resonance. These factors define the diamond absorption factor α_d.

A number of these parameters are interrelated. The ODMR linewidth is proportional to the inverse of T_2^*, which in turn is dependent on N_{NV} concentration in the limit of high nitrogen content and the abundance of ^{13}C for low nitrogen content [41]. There is also a dependence on other material properties such as strain [42], which makes the relationship between the parameters difficult to determine. We therefore consider values in the experimental literature as a guide. Figure 2 shows a plot of T_2^* versus NV$^-$ density N_{NV} for a range of diamonds from the literature [16,38,43–47]. Typical NV$^-$ densities range from 10^{-4} ppm up to tens of ppm [48]. In general, $T_2^* < 1$ μs for samples with natural (1.1%) ^{13}C content [49,50]. Experiments typically realize Rabi frequencies Ω_R of 1–5 MHz, with up to 10 MHz using optimal antenna geometries [51].

We include only the uncharged NV^0 and negatively charged NV$^-$ nitrogen vacancy centers in our model and we do not consider the role of other types of defects in or on the diamond, including substitutional nitrogen or other materials that may be present (e.g., Si, boron). Furthermore, we assume a uniform distribution of nitrogen vacancies throughout the diamond, such that we can consider a single, fixed absorption cross section throughout. These are simplifications introduced due to the poorly known absorption cross sections of certain types of defects or dopants and the experimental difficulty in quantifying density within (or on) diamonds. We highlight that this implies that the sensitivities estimated by our model represent a best-case scenario, with no optical loss from the NV$^-$ system used for sensing due to the presence of other defects, dopants, or adsorbents in or on the diamond.

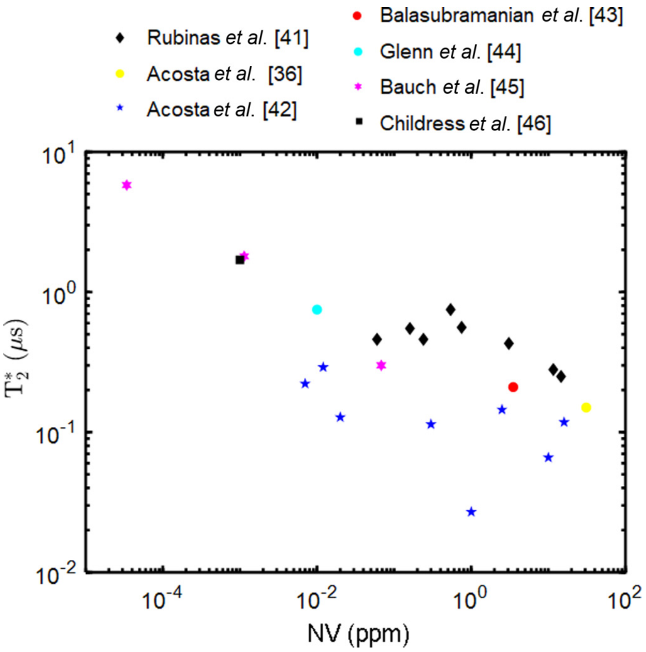

FIG. 2. Dephasing time T_2^* vs NV$^-$ density N_{NV}, where both values are given in other works (citations given in the main text). T_2^* in those with low NV concentration are limited by interaction with ^{13}C spin, with the highest values given by diamonds isotropically purified with ^{12}C spin during growth. T_2^* in those with high NV concentration are limited by dipolar interaction between defects, including other substitutional nitrogen defects such as P1 centers. Note that the NV$^-$ density for the work by Childress *et al.* is an upper estimate made here assuming a 10% NV$^-$ fraction; total substitutional nitrogen content for this diamond was given as $\leqslant 0.1$ ppm. (Both axes use a $\log_{10}$ scale.)

Those parameters, intrinsic to the laser diode or gain chip that is used, are the carrier density at transparency N_{tr}, the gain compression factor ϵ that arises from effects that limit the gain well above threshold, the differential gain coefficient a that relates the gain and carrier density, the threshold carrier lifetime τ_N, the confinement factor Γ, the volume of the gain medium V, and the spontaneous emission factor β. For our gain medium, we take a III-V semiconductor heterostructure device, such as the nitride compounds capable of emission at green wavelengths (e.g., InGaN) [66]. Table I shows a typical range of values for each of these parameters. We take the typical ranges shown based on experimental results from different structures (quantum well, vertical cavity) and from calculations based on bulk material properties such as effective mass. N_{tr} effectively defines the size of the lasing threshold current I_{th}. The desired change in threshold current on change in absorption factor α_t is defined, in particular, by Γ and the gain coefficient a in Eqs. (3) and (7).

TABLE I. Typical ranges for the key semiconductor gain medium parameters. Here, N_{tr}, τ_N, and a are taken for typical III-nitride semiconductors. The range for Γ is given for laser diodes with a thin (sub-μm) active layer and is typically no more than a few percent. The range of β is given for the literature values for a range of laser diodes where confinement is not deliberately sought, e.g., microcavities, and where values several orders of magnitude higher than the given range are possible [65].

Parameter	Range	Ref.
Transp. carrier density, N_{tr}	3×10^{18}–2×10^{19} cm^{-3}	[52–56]
Carrier lifetime, τ_N	1–5 ns	[57,58]
Differential gain factor, a	10^{-17}–10^{-22} m^2	[59,60]
Confinement factor, Γ	0.01–0.1	[61,62]
Spont. emission factor, β	10^{-5}–10^{-2}	[63,64]

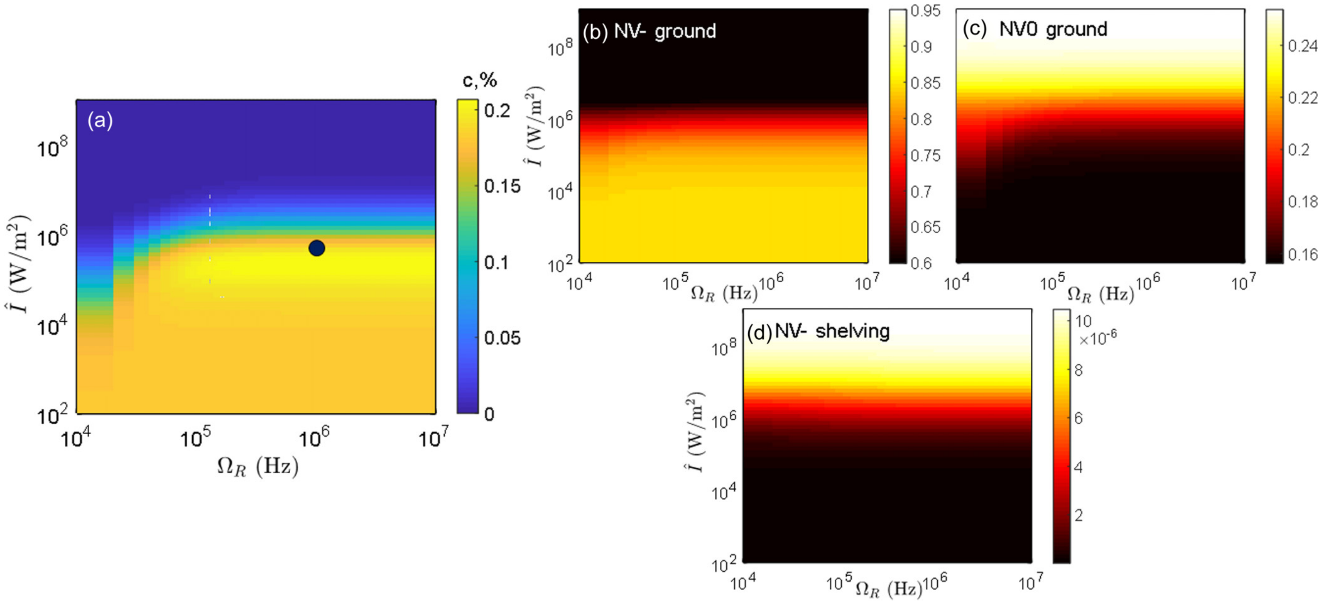

FIG. 3. (a) Absorption contrast percentage calculated from the rate model for diamond D3. This is the maximum change in absorption between on microwave resonance and off microwave resonance as a function of Rabi frequency Ω_R and laser intensity $\hat{I}$ in W/m^2. (b)–(d) Normalized level occupancy for the NV$^-$ triplet ground state, responsible for green absorption, the uncharged NV^0 defect state, and the NV$^-$ singlet state. At high laser intensities, population transfer to NV^0 limits the achievable absorption contrast. For reference, 10 mW of laser power with a 1-mm-diameter circular beam on the diamond gives an intensity $\hat{I} = 10^4$ W/m^2. The black spot indicates the Rabi frequency and power for calculations later in this work. (All x and y axes use a $\log_{10}$ scale.)

III. RESULTS

A. Absorption contrast

We first calculate, from the rate model, the fraction of incident pump light which is absorbed by the diamond and the change in this absorption (C) when on microwave resonance. We choose to model three different diamonds covering different regimes: D1, D2, and D3 with parameters (NV density and T_2^*) representative of the values seen in the literature (Fig. 2). For diamond D1, we choose a low NV$^-$ concentration $N_{NV} = 0.001$ ppm and high $T_2^* = 5$ μs, representative of ^{12}C enriched diamonds. For diamond D2, we choose a medium NV$^-$ concentration $N_{NV} = 0.1$ ppm and $T_2^* = 0.75$ μs, representative of chemical vapor deposition (CVD)-grown diamond with natural ^{13}C abundance. For diamond D3, we choose $N_{NV} = 10$ ppm and $T_2^* = 0.1$ μs, characteristic of high nitrogen content high-pressure high-temperature (HPHT) diamond. We use a diamond thickness $d = 500$ μm for all, representative of commercially available single-crystal plates.

Using the rate model, we can calculate the absorption of light incident on the diamond D1: $\hat{I_{\rm off}}/\hat{I}_0$, where $\hat{I}_0$ is the intensity of the incident light and $\hat{I_{\rm off}}$ is the intensity of the light after the diamond (without supplying microwaves). The calculated absorption for diamonds D1–D3 is 0.015%, 1.498%, and 77%, respectively, as expected from increasing NV density. We can also calculate the change in absorption when on and off microwave resonance. This is shown in Fig. 3 as absorption contrast C for D3 as a function of microwave drive power (as Rabi frequency Ω_R) and laser output (as intensity). The equivalent plots for D1 and D2 are given in the Supplemental Material [34]. The maximum $C = 0.22\%$ for D3 and lowest for D1 with the lowest NV density with $C = 10^{-4}\%$. This contrast is comparable to our previous absorption experiments using a diamond with equivalent ppb-level NV$^-$ density [22]. We note that at Rabi frequencies above 100 kHz and laser outputs above 10^6 W/m^2, the absorption contrast begins to drop. This results from depopulation of the triplet ground state ^{3}A$_2$ [normalized occupancy in Fig. 3(b)] in favor of the NV^0 [Fig. 3(c)] and the singlet shelving state [Fig. 3(d)]. However, since we aim to operate near the lasing threshold, laser intensity will be low in our scheme, avoiding this issue and ensuring that we remain in the region of highest contrast.

To further validate the absorption modeling, we have also measured diamond absorption on a high-density sample consisting of a 1-mm-thick HPHT diamond with 200 ppm nitrogen content, irradiated with 10 MeV electrons and annealed at 900 °C. The estimated NV content for this sample was 10–20 ppm. The absorption contrast for this sample is shown in Fig. 4. The sample was found to be moderately polycrystalline and was therefore measured without an offset field to produce a single central dip in fluorescence, with a number of satellite features resulting from the polycrystallinity and residual magnetic field in the laboratory. Here, total off-resonance diamond absorption was 90% of incident pump light and maximum absorption contrast $C = 0.13\%$. For comparison to experiment, we model absorption contrast with our model with NV density of 15 ppm and $T_2^* = 100$ ns, derived from an estimate of the resonance linewidth, an estimated Rabi frequency of 1 MHz, and the same 100 mW laser power as used experimentally. This gives a total off-resonance absorption of 89% of the pump light and absorption contrast of $C = 0.14\%$, in good agreement with our measurements.

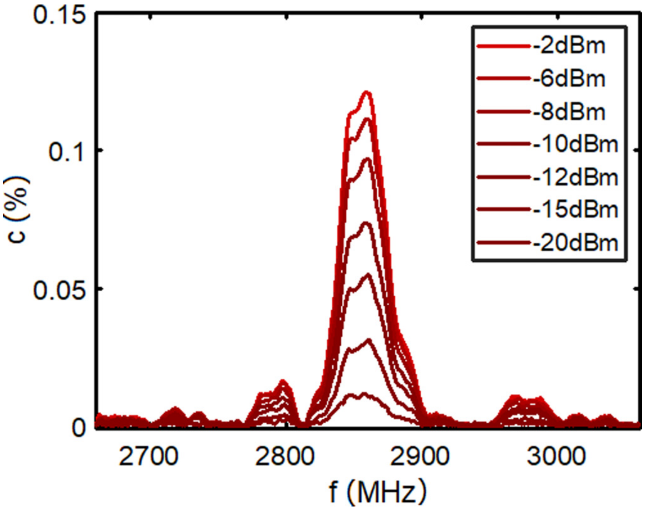

FIG. 4. Experimental absorption contrast percentage as a function of microwave drive frequency and microwave power before the amplifier (Minicircuits ZHL-16W), measuring through the diamond with 100 mW of laser light ($\hat{I} = 2.5 \times 10^4$ W/m^2). The sample was used to test the absorption model using estimates of NV density and T_2^* from the observed linewidth (values in the main text). Note that due to input loss, we remain below the maximum gain threshold of the amplifier for all microwave powers shown, which is exceeded at +3 dBm.

B. Change in threshold current

We first calculate the lasing threshold current I_{th} with the diamond absent from the cavity. To do this, we fixed some of the parameters of the semiconductor gain medium. We choose a transparency carrier density of $N_{tr} = 1 \times 10^{25}$ m^{-3} in the range typical for InGaN laser structures [52], a gain region volume of $V = 1.25 \times 10^{-16}$ m^3 (25 μm × 100 nm × 100 μm), zero total cavity absorption $\alpha_t = 0$, a typical differential gain factor $a = 5 \times 10^{-20}$ m^2, a confinement factor Γ of 2%, and a carrier lifetime $\tau_N = 4$ ns, giving a reasonable lasing threshold current of 50 mA [66]. We take the relation between the gain and the carrier density to be linear, with the carrier density close to transparency. We make the simplifying assumption that due to the low power, running close to lasing threshold we do not encounter gain compression effects, such that the factor $\epsilon \rightarrow 0$. We also initially make the simplifying assumption that the spontaneous emission rate is low, with $\beta \rightarrow 0$ (the importance of this second assumption will be tested in the final section of this work). These assumptions allow the threshold current I_{th} to be calculated easily from Eq. (8). We define $L_r = 10$ mm, which is sufficient to include the diamond and any necessary optics in a practical implementation. We set mirror reflectivity $R_3 = 0.99$ and collect laser output from transmission through mirror R_1. We calculate reflectivity R_2 from the Fresnel equations assuming an In$_x$Ga$_{1-x}$N-air interface with refractive index $n \approx 2.6$–2.9 for In$_x$Ga$_{1-x}$N [67].

We impose two feasibility limits on the threshold current I_{th}. The first is that it should not exceed 300 mA, based on the limits discussed in the technical documentation, in order to maintain thermal stability and for practical heat sinking for a miniaturized diode or gain chip medium. The second is that the change in the threshold caused by the diamond absorption must exceed the shot noise of the drive current. From Fig. 5, we can see that these are mutually exclusive objectives. Setting an absorption contrast $C = 0.2\%$ (diamond D3) and output mirror reflectivity $R_1 = 0.9$ in order to achieve laser output while keeping the threshold current reasonably low, a low confinement factor Γ and high differential gain coefficient a result in the highest change in the threshold current ΔI_{th} and thus the strongest effect for sensing, but for very high I_{th}. Conversely, a higher value of Γ or lower a gives lower I_{th}, but ΔI_{th} shifts which are too small to be resolved.

Although N_{tr} is a factor usually defined by the semiconductor material, we note that the other parameters here which define I_{th}, Γ, a, and total cavity loss α_t including the mirror reflectivity and cavity output through R_1, are all factors which are well understood and can be controlled and optimized at either the semiconductor growth stage or in the external cavity design.

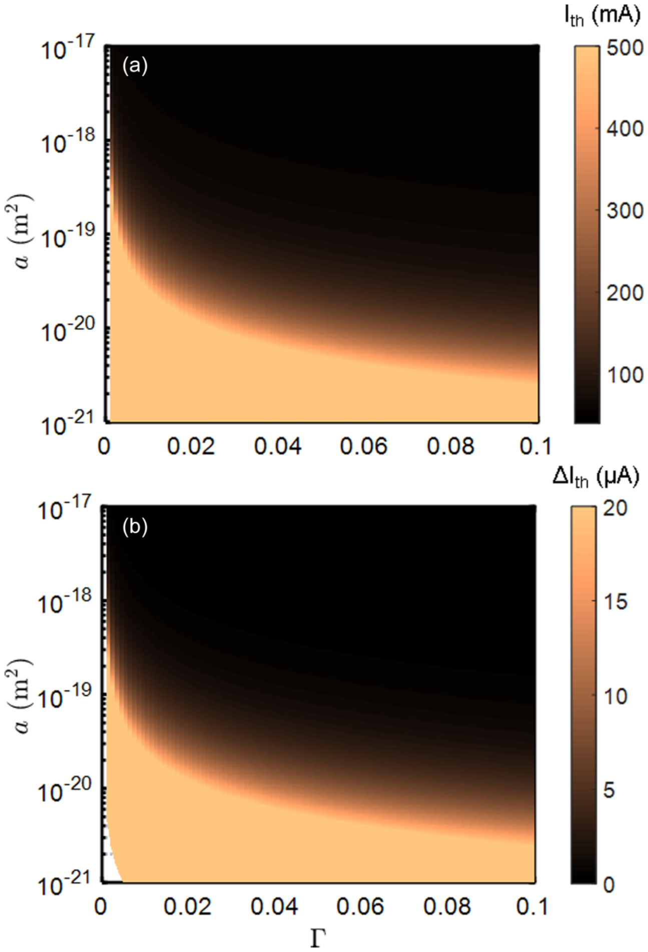

FIG. 5. (a) Threshold current as a function of differential gain factor a and confinement factor Γ for diamond D3. (b) Change in threshold current due to the diamond absorption contrast $C = 0.02\%$ for diamond D3. Here, external cavity length L_r was 10 mm and output mirror reflectivity $R_1 = 0.9$. (Both the x and y axes use a $\log_{10}$ scale.)

C. Simulated ODMR

Here we calculate the ODMR spectrum that would be produced from the external cavity laser. We model a single microwave resonance from a single $m_s = 0 \rightarrow m_s = \pm 1$ transition using a Lorentzian line shape typical of ODMR for diamond [18]. We center our resonance at 2.82 GHz, replicating an ODMR resonance feature associated with a single NV axis, split from resonance features from other axes by an arbitrary weak DC offset magnetic field. The maximum amplitude is defined by the maximum change in threshold current between on and off microwave resonance and full width half maximum linewidth f_l. For simplicity, we assume that we can reach the pulsed readout linewidth defined by T_2^*. We calculate the external cavity laser output power using Eq. (10). Figure 6(a) shows the simulated ODMR for diamond D3, with a laser power output in the mW range for reasonable values of $\Gamma < 0.1$ and $a = 10^{-17}$–10^{-21} m^2. The equivalent plots for diamonds D1 and D2 are given in the Supplemental Material [34], with maximum power outputs in the range of nW and μW, respectively. Unlike for conventional red fluorescence ODMR, the spectrum using this method is a peak at microwave resonance with zero background, rather than a small percentage change on a bright background.

D. Magnetic field sensitivity

We calculate the sensitivity to a magnetic field by taking the background noise level, dividing by the maximum ODMR slope, and by assuming a maximum frequency shift of ≈ 28 Hz–1 nT [13]. In our model, the primary sources of noise are readout from the photodetector and the noise on the drive current. The ultimate limit on both of these is shot noise of the output laser light and the drive current shot noise. We make no account for other direct sources of noise which are difficult to quantify, such as vibration or temperature fluctuations. Figure 7 shows a plot of the sensitivity for diamond D3 versus laser diode parameters for (a) the optical shot noise and (b) drive current shot noise limited regimes. We highlight that these calculated values neglect any effects from amplified spontaneous emission near threshold, which we explicitly include in Sec. III E. We note that in practice, the shot noise limited operation may be experimentally difficult to realize and we include an estimate based on a commercial current source with ppm-level noise in the Supplemental Material [34].

The noise limitations as a function of diode parameters are highlighted in Fig. 8 for diamond D3. Here, regions A and C represent where the operation is noise limited, and region B represents the region in which the system can operate. In region A, the change in the threshold current is less than the shot noise of the laser drive current ($\Delta I_{th} < I_{sh}$). In region C, the threshold current $I_{th} > 300$ mA exceeds a reasonable maximum drive current in order to maintain thermal stability. The limitations we impose mean that diamonds D1 or D2 have no viable operating region. For completeness, their sensitivity plots are included in the Supplemental Material [34].

By solving the rate model and calculating for laser diode output, we can calculate the sensitivity to a magnetic field for any valid physical parameters of the system, regardless of whether a diamond can be created with the requisite properties. This includes whether a value of T_2^* can be realized for a corresponding N_{NV}, making no assumption regarding the relation between these parameters or whether N_{NV} can be realized experimentally. Here we choose parameters R_1, Γ, T_2^*, a, and NV$^-$ density N_{NV} as the optimization variables, while fixing the diamond thickness ($d = 500$ μm), Rabi frequency ($\Omega_R = 1$ MHz), laser beam width (0.5 mm), power (200 mW), and mirror reflectivities. We limit our laser power to 200 mW based on our rate model calculations to ensure that the majority of light is absorbed by the NV$^-$ defects. We optimize using standard gradient descent methods. Figure 9 shows a plot of optical shot noise limited field sensitivity as a function of T_2^* and NV density. Sensitivity increased with higher T_2^* as would be expected, with maximum sensitivity at NV density of 10 ppm, above which high overall absorption by the diamond

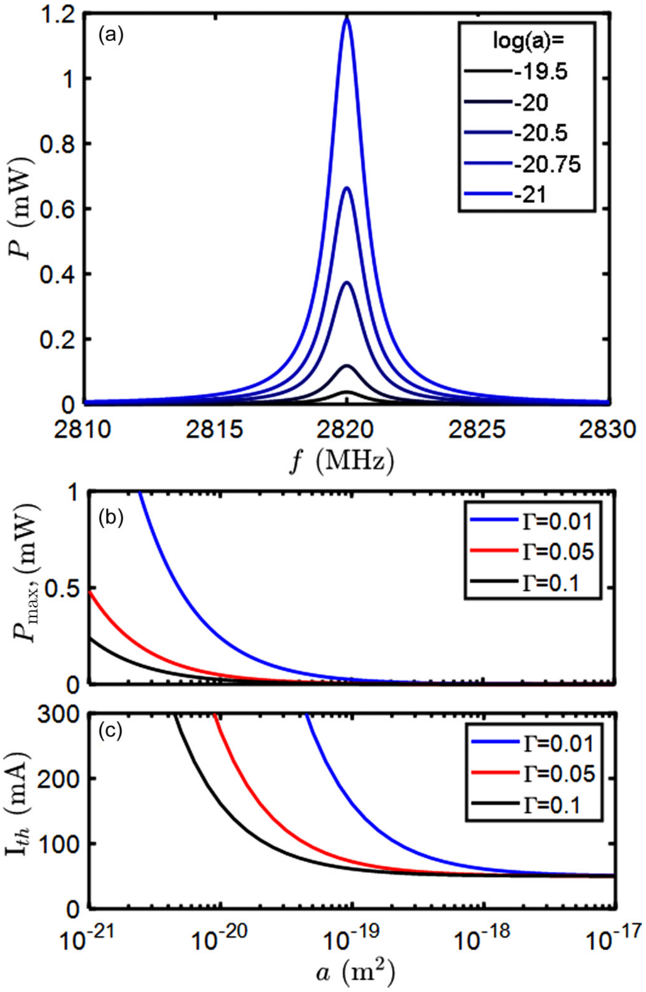

FIG. 6. (a) Simulated ODMR for diamond D3 at a range of differential gain factors $a = 10^{-21} \rightarrow 10^{-19.5}$ m^2 (exponents given in legend) measured by calculating the external cavity laser output power P as a function of microwave frequency for a Lorentzian line shape transition centered at 2.83 GHz and of linewidth defined by $f_l = \frac{1}{\pi T_2^*} = 3.2$ MHz. (b) Maximum laser power output $P_{\max}$ on resonance as a function of gain coefficient a for confinement factor $\Gamma = 0.01, 0.05, 0.1$. (c) The lasing threshold current for $I_{th} < 300$ mA, for the same three values of Γ. [The x axis in (b) and (c) uses a $\log_{10}$ scale.]

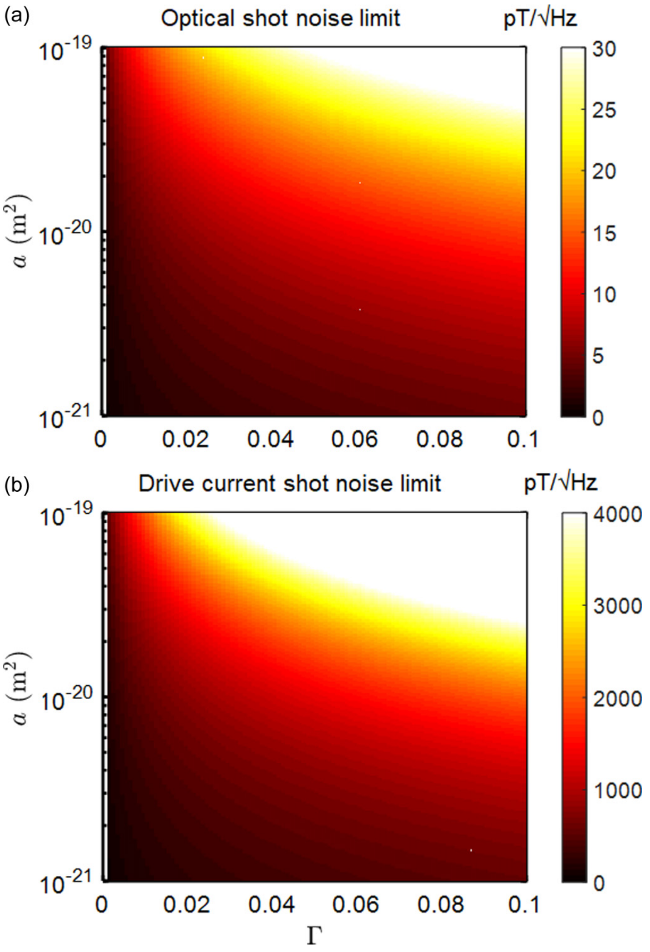

FIG. 7. (a) Optical shot noise limited sensitivity for diamond D3 within a viable range for diode parameters a and Γ. Sensitivity is in the picotesla range, enabled by the elimination of the high noise from the background in the conventional fluorescence detection scheme. (b) The ultimate sensitivity limit imposed by shot noise on the laser drive current, worse by up to two orders of magnitude. These plots do not consider practical viability, with threshold currents > 4 A at low Γ. Zoomed-in plots in the low-Γ, low-a range are included in the Supplemental Material [34] for clarity. (Both the x and y axes use a $\log_{10}$ scale.)

acted to excessively reduce laser output. Subpicotesla level sensitivity is predicted for $T_2^* > 1\ \mu$s (0.3–0.02 pT/$\sqrt{\text{Hz}}$ for $T_2^* = 1$–10 μs). Here the optimal parameters were $a = 1.6 \times 10^{-20}$ m^2, $R_1 = 0.154$, and $\Gamma = 0.025$. These are parameters within the achievable range for a semiconductor gain medium (see Table I). We note that current demonstrations show that achieving long T_2^* times (e.g., 10 μs) becomes impractical for high NV densities (e.g., 10 ppm), as detailed by Fig. 2, due to the impact of *N*-*N* interaction.

We note that in general, the highest sensitivity is realized for the lowest differential gain factor a. A standard laser diode demands a large a, maximizing gain vs carrier density (steeper output power vs drive current slope). Our scheme requires the reverse: that a small change in gain produced by the diamond on-off microwave resonance results in a large change in N_{th} and I_{th}. In this respect, a quantum well structure with a flatter logarithmic relation between gain and carrier density would seem preferable. However, as we demonstrate in Fig. 10, using our model, with modifications to the phenomenological

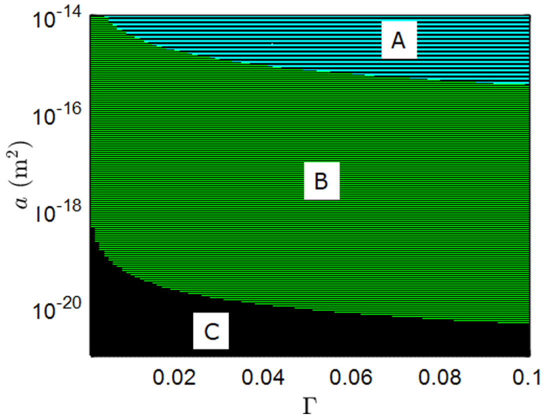

FIG. 8. Regions where the sensor can and cannot operate due to imposed limitations. In regions A and C, operation is constrained by having a change in threshold that is less than the shot noise of the drive current and $I_{th} > 300$ mA, respectively. In region B, operation is possible. (Both the x and y axes use a $\log_{10}$ scale.)

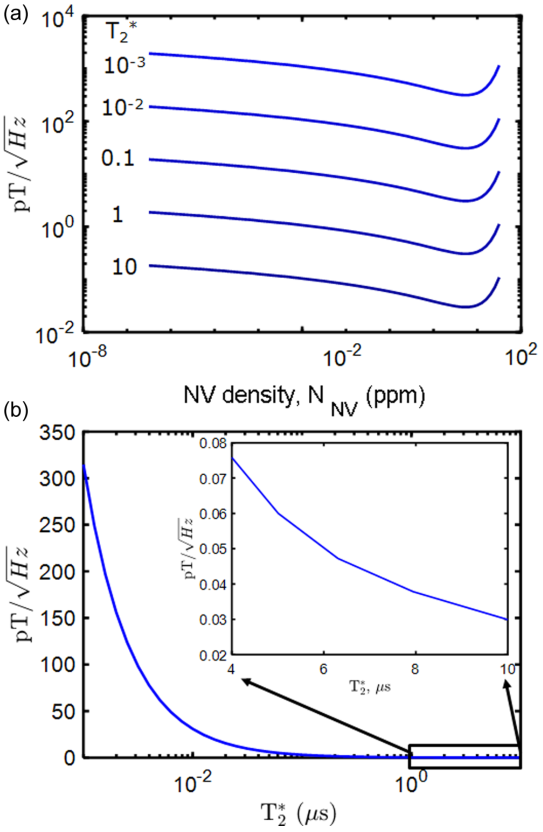

FIG. 9. Best field sensitivity optimizing variables listed in the main text as a function of (a) NV$^-$ density and (b) T_2^* in μs, with the inset showing a zoomed plot at the highest simulated values of T_2^*. The best sensitivity was observed at the highest T_2^*, for NV$^-$ density of 10 ppm. Above this, the total absorption for the diamond was too high, limiting laser output and sensitivity. [The x and y axes in (a) and x axis in (b) use a $\log_{10}$ scale.]

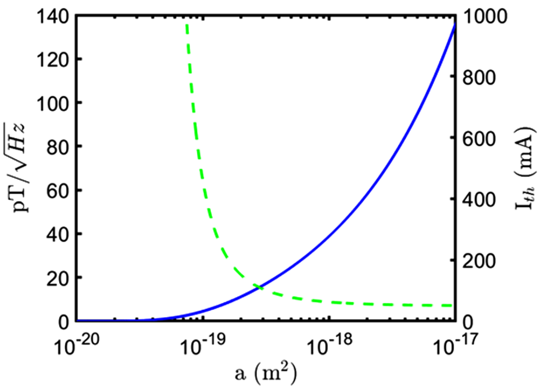

FIG. 10. Calculated magnetic field sensitivity (left y axis) and laser diode threshold current (right y axis, dashed) as a function of differential gain factor a using an empirical model for a quantum well laser diode. The lasing threshold current increases such that subpicotesla sensitivity is not reached at a feasible threshold current ($<$ 300 mA). Here we take confinement factor $\Gamma = 0.01$ as an example of the low values that are typical of a quantum well laser diode. (The x and y axes use a $\log_{10}$ scale.)

description of the medium gain (detailed in the Supplemental Material [34]) and with the same optimization methodology as above results in the threshold current exponentially exceeding drive current feasibility limits before subpicotesla/$\sqrt{\text{Hz}}$ sensitivity is reached, for any typical value for Γ in the low percentage range.

E. Effect of spontaneous emission

In the previous sections and past literature, the physical role of spontaneous emission in the semiconductor gain medium that was used was not considered. In order to maximize sensitivity, it is necessary to operate at or close to the off-resonance lasing threshold. Without spontaneous emission, this can be treated as a step cut-on, with zero or near-zero emission before lasing begins at I_{th}. With spontaneous emission included, modeled by finite β in Eqs. (4) and (5) above, the power-current relationship close to threshold instead follows a shallow curve, resulting from weak amplification of spontaneous emission near threshold producing light emission below I_{th}. Figure 11(a) shows this effect for varying β. This acts to severely limit sensitivity [Fig. 11(b)] by reducing the contrast and adding background shot noise. Typical values of β range from 10^{-3} to 10^{-5}, depending on the laser diode structure. We estimate approximately an order of magnitude worse sensitivity at the low end of this range than with $\beta = 0$.

IV. CONCLUSION

In this work, we propose a scheme for laser threshold sensing using an external cavity laser configuration with a current driven semiconductor lasing medium. Using the change in lasing threshold, light emission only occurs on microwave resonance. This eliminates the bright background that limits sensitivity using conventional red fluorescence emission. Predicted sensitivities (summarized in Table II) for magnetometry with realistic cavity parameters and intrinsic material parameters are in the pT/$\sqrt{\text{Hz}}$ range, offering a route to improvement over existing methods. We find that these sensitivities may be reachable at far lower laser power ($<$ 200 mW) than realized in equivalent fluorescence-based diamond bulk sensing schemes, including our recent experimental work which utilized up to 2 W of green pump laser to obtain equivalent sensitivities in the tens of pT range [68]. This significant decrease of laser power may facilitate sensor miniaturization and thus the implementation of portable sensing schemes.

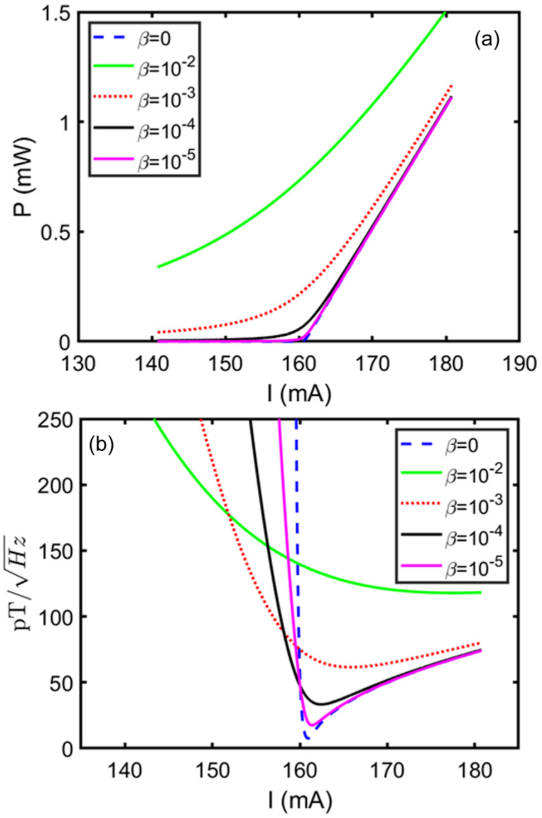

FIG. 11. (a) External cavity laser output P as a function of semiconductor laser medium drive current I, varying spontaneous emission factor β. The result of increasing β is that there is no longer a sharp lasing cut-on at the threshold. (b) The effect on the achievable sensitivity of this effect, with sensitivity considerably reduced by up to two orders of magnitude for $\beta = 10^{-2}$.

Our model has limitations: we base our calculations on emission into a single laser mode and do not calculate the dynamics of the system, such as rapid switching in a pulsed operation scheme. Although beyond the focus of this work, we note that the latter may be a promising route for future investigation. A scheme where the laser medium could be initially pumped and then the pump shut off while retaining population inversion during sensing, typical of a Q-switched setup, would only be limited by the optical shot noise of any emitted laser light. This is, however, challenging to achieve for a semiconductor laser due to the short excited state (carrier) lifetime.

A key physical limitation of any laser threshold scheme is the role of amplified spontaneous emission. This blurs the sharp lasing transition, giving nonzero light emission even below threshold and compromising sensitivity. A broad transition can be avoided by minimizing gain factor β, although

TABLE II. Summary of key values from our calculations for modeled diamonds D1–D3 and an optimal (ideal) diamond, including the assumed NV density, T_2^*, maximum shift in threshold current, and best calculated sensitivities within the modeled parameter ranges of a, Γ, with and without spontaneous emission (SE) taken into account. We present the best sensitivity within the modeled range limited by either the optical shot noise (SN) of the laser emission or limited by the shot noise of the drive current (brackets). For D1 and D2, * denotes not viable, as the drive current shot noise exceeds the change in threshold ΔI_{th}.

Diamond	NV density (ppm)	T_2^* (μs)	Maximum threshold shift (μA)	Best sensitivity, without SE, optical (current) SN limit pT/$\sqrt{\text{Hz}}$	Best sensitivity, including SE, optical SN limit, $\beta = 10^{-5} \rightarrow 10^{-3}$ pT/$\sqrt{\text{Hz}}$
D1	10^{-3}	5	0.00122	4.6 (1834*)	
D2	0.1	0.75	41.4	3.1 (124*)	
D3	10	0.1	6.2×10^3	4.3 (53)	22–73
Ideal	10	1–10	7.3×10^3–8.4×10^3	0.3–0.02 (-)	

this is difficult for a semiconductor laser, particularly since β can scale inversely with the size of the gain medium [69]. Obtaining a gain chip or antireflective coated laser diode with the right parameters is challenging, especially for green wavelengths. This problem also exists for infrared absorption since the laser emission must match the 1042 nm gap in the singlet state. In our scheme, running in the infrared could be achieved by extending the external cavity design proposed here using a diffraction grating in a Littrow and Littman-Metcalf configuration to create a tunable system.

We consider, in this work, a normal incidence beam path through a fixed diamond thickness $d = 500$ μm. We note that a higher sensitivity within feasible limits of threshold current could potentially be reached with a thinner diamond with a very high NV density. However, in the limit of $d \rightarrow 0$, other effects not considered in our model may act to limit performance, such as variation in NV density and the role of other types of defects. Measurements of absorption and T_2^* as a function of diamond thickness would be extremely useful in determining behavior in this regime. We also consider that it may be possible to reach higher sensitivity in the low NV density regime using an extended beam path achieved through internal reflection in a thicker diamond. This again requires new experimental measurements to precisely quantify the losses (due to reflection or absorption) in such a geometry.

We note that the fundamental limit for the scheme is the level of contrast C generated between the on-off microwave resonance states, which is very low for a large diamond ensemble. However, the scheme is not specifically limited to diamond and is broadly applicable for any material where a large enough, controllable difference in optical absorption could be generated. The advantage of using diamond is the ability to coherently manipulate the desired states in a quantum sensing scheme. Our calculations indicate the scheme will likely only work for diamonds with a high (> 1 ppm) NV$^-$ density. Such diamonds have a worse ensemble T_2^* time, limited by nitrogen spin interaction. A developing solution here may be to use optimal control methods in order to better control the ensemble. Such methods are widely implemented for nuclear magnetic resonance and electron spin resonance on bulk samples, but have yet to be fully developed for sensing using diamond defects [70].

ACKNOWLEDGMENTS

The work presented here was funded by the Novo Nordisk Foundation through the Synergy Grant bioQ (NNF17OC0028086) and the bigQ (bigQDNRF142) Center funded by the Danish National Research Foundation (DNRF).

---

[1] W. P. Schleich, K. S. Ranade, C. Anton, M. Arndt, M. Aspelmeyer, M. Bayer, G. Berg, T. Calarco, H. Fuchs, E. Giacobino *et al.*, Appl. Phys. B **122**, 130 (2016).

[2] A. Gruber, Science **276**, 2012 (1997).

[3] M. W. Doherty, N. B. Manson, P. Delaney, F. Jelezko, J. Wrachtrup, and L. C. Hollenberg, Phys. Rep. **528**, 1 (2013).

[4] J. M. Taylor, P. Cappellaro, L. Childress, L. Jiang, D. Budker, P. R. Hemmer, A. Yacoby, R. Walsworth, and M. D. Lukin, Nat. Phys. **4**, 810 (2008).

[5] R. Schirhagl, K. Chang, M. Loretz, and C. L. Degen, Annu. Rev. Phys. Chem. **65**, 83 (2014).

[6] J. L. Webb, L. Troise, N. W. Hansen, J. Achard, O. Brinza, R. Staacke, M. Kieschnick, J. Meijer, J.-F. Perrier, K. Berg-Sørensen *et al.*, Front. Phys. **8**, 430 (2020).

[7] G. Kucsko, P. C. Maurer, N. Y. Yao, M. Kubo, H. J. Noh, P. K. Lo, H. Park, and M. D. Lukin, Nature (London) **500**, 54 (2013).

[8] S. Knauer, J. P. Hadden, and J. G. Rarity, npj Quantum Inf. **6**, 50 (2020).

[9] F. Dolde, H. Fedder, M. W. Doherty, T. Nöbauer, F. Rempp, G. Balasubramanian, T. Wolf, F. Reinhard, L. C. L. Hollenberg, F. Jelezko *et al.*, Nat. Phys. **7**, 459 (2011).

[10] S. Hong, M. S. Grinolds, L. M. Pham, D. L. Sage, L. Luan, R. L. Walsworth, and A. Yacoby, MRS Bull. **38**, 155 (2013).

[11] L. Rondin, J.-P. Tetienne, T. Hingant, J.-F. Roch, P. Maletinsky, and V. Jacques, Rep. Prog. Phys. **77**, 056503 (2014).

[12] J. F. Barry, J. M. Schloss, E. Bauch, M. J. Turner, C. A. Hart, L. M. Pham, and R. L. Walsworth, Rev. Mod. Phys. **92**, 015004 (2020).

[13] J. L. Webb, J. D. Clement, L. Troise, S. Ahmadi, G. J. Johansen, A. Huck, and U. L. Andersen, Appl. Phys. Lett. **114**, 231103 (2019).

[14] T. Wolf, P. Neumann, K. Nakamura, H. Sumiya, T. Ohshima, J. Isoya, and J. Wrachtrup, Phys. Rev. X **5**, 041001 (2015).

[15] D. B. Bucher, D. P. L. A. Craik, M. P. Backlund, M. J. Turner, O. B. Dor, D. R. Glenn, and R. L. Walsworth, Nat. Protoc. **14**, 2707 (2019).

[16] P. Balasubramanian, C. Osterkamp, Y. Chen, X. Chen, T. Teraji, E. Wu, B. Naydenov, and F. Jelezko, Nano Lett. **19**, 6681 (2019).

[17] C. Osterkamp, M. Mangold, J. Lang, P. Balasubramanian, T. Teraji, B. Naydenov, and F. Jelezko, Sci. Rep. **9**, 5786 (2019).

[18] A. O. Levchenko, V. V. Vasil'ev, S. A. Zibrov, A. S. Zibrov, A. V. Sivak, and I. V. Fedotov, Appl. Phys. Lett. **106**, 102402 (2015).

[19] A. M. Wojciechowski, M. Karadas, C. Osterkamp, S. Jankuhn, J. Meijer, F. Jelezko, A. Huck, and U. L. Andersen, Appl. Phys. Lett. **113**, 013502 (2018).

[20] Z. Liu, H. N. Abbasi, T.-F. Zhu, Y.-F. Wang, J. Fu, F. Wen, W. Wang, S. Fan, K. Wang, and H.-X. Wang, AIP Adv. **9**, 125218 (2019).

[21] T.-Y. Huang, R. R. Grote, S. A. Mann, D. A. Hopper, A. L. Exarhos, G. G. Lopez, G. R. Kaighn, E. C. Garnett, and L. C. Bassett, Nat. Commun. **10**, 2392 (2019).

[22] S. Ahmadi, H. A. R. El-Ella, A. M. Wojciechowski, T. Gehring, J. O. B. Hansen, A. Huck, and U. L. Andersen, Phys. Rev. B **97**, 024105 (2018).

[23] S. Ahmadi, H. A. El-Ella, J. O. Hansen, A. Huck, and U. L. Andersen, Phys. Rev. Appl. **8**, 034001 (2017).

[24] K. Jensen, N. Leefer, A. Jarmola, Y. Dumeige, V. Acosta, P. Kehayias, B. Patton, and D. Budker, Phys. Rev. Lett. **112**, 160802 (2014).

[25] J. Jeske, J. H. Cole, and A. D. Greentree, New J. Phys. **18**, 013015 (2016).

[26] T. Y. Jeong, H. Kim, S.-J. Choi, K. Watanabe, T. Taniguchi, K. J. Yee, Y.-S. Kim, and S. Jung, Nat. Commun. **10**, 3825 (2019).

[27] S. Castelletto and A. Boretti, J. Phys.: Photon. **2**, 022001 (2020).

[28] Y. Dumeige, J.-F. Roch, F. Bretenaker, T. Debuisschert, V. Acosta, C. Becher, G. Chatzidrosos, A. Wickenbrock, L. Bougas, A. Wilzewski *et al.*, Opt. Express **27**, 1706 (2019).

[29] Y. Cunyun, *Tunable External Cavity Diode Lasers* (World Scientific, Singapore, 2004).

[30] K. Petermann, *Laser Diode Modulation and Noise* (Springer, Netherlands, 1988).

[31] P. J. de Groot, G. M. Gallatin, and S. H. Macomber, Appl. Opt. **27**, 4475 (1988).

[32] J. Li, H. Niu, and Y. Niu, Opt. Eng. **56**, 050901 (2017).

[33] C. Voumard, R. Salathé, and H. Weber, Appl. Phys. **12**, 369 (1977).

[34] See Supplemental Material at http://link.aps.org/supplemental/10.1103/PhysRevA.103.062603 for additional figures and data referred to above.

[35] J. W. Allen, Adv. Mater. Opt. Electron. **4**, 51 (1994).

[36] L. Robledo, H. Bernien, T. van der Sar, and R. Hanson, New J. Phys. **13**, 025013 (2011).

[37] J.-P. Tetienne, L. Rondin, P. Spinicelli, M. Chipaux, T. Debuisschert, J.-F. Roch, and V. Jacques, New J. Phys. **14**, 103033 (2012).

[38] V. M. Acosta, E. Bauch, A. Jarmola, L. J. Zipp, M. P. Ledbetter, and D. Budker, Appl. Phys. Lett. **97**, 174104 (2010).

[39] I. Meirzada, Y. Hovav, S. A. Wolf, and N. Bar-Gill, Phys. Rev. B **98**, 245411 (2018).

[40] T.-L. Wee, Y.-K. Tzeng, C.-C. Han, H.-C. Chang, W. Fann, J.-H. Hsu, K.-M. Chen, and Y.-C. Yu, J. Phys. Chem. A **111**, 9379 (2007).

[41] K. D. Jahnke, B. Naydenov, T. Teraji, S. Koizumi, T. Umeda, J. Isoya, and F. Jelezko, Appl. Phys. Lett. **101**, 012405 (2012).

[42] P. Kehayias, M. J. Turner, R. Trubko, J. M. Schloss, C. A. Hart, M. Wesson, D. R. Glenn, and R. L. Walsworth, Phys. Rev. B **100**, 174103 (2019).

[43] R. Rubinas, V. V. Vorobyov, V. V. Soshenko, S. V. Bolshedvorskii, V. N. Sorokin, A. N. Smolyaninov, V. G. Vins, A. P. Yelisseyev, and A. V. Akimov, J. Phys. Commun. **2**, 115003 (2018).

[44] V. M. Acosta, E. Bauch, M. P. Ledbetter, C. Santori, K.-M. C. Fu, P. E. Barclay, R. G. Beausoleil, H. Linget, J. F. Roch, F. Treussart *et al.*, Phys. Rev. B **80**, 115202 (2009).

[45] D. R. Glenn, D. B. Bucher, J. Lee, M. D. Lukin, H. Park, and R. L. Walsworth, Nature (London) **555**, 351 (2018).

[46] E. Bauch, C. A. Hart, J. M. Schloss, M. J. Turner, J. F. Barry, P. Kehayias, S. Singh, and R. L. Walsworth, Phys. Rev. X **8**, 031025 (2018).

[47] L. Childress, M. V. G. Dutt, J. M. Taylor, A. S. Zibrov, F. Jelezko, J. Wrachtrup, P. R. Hemmer, and M. D. Lukin, Science **314**, 281 (2006).

[48] L.-J. Su, C.-Y. Fang, Y.-T. Chang, K.-M. Chen, Y.-C. Yu, J.-H. Hsu, and H.-C. Chang, Nanotechnology **24**, 315702 (2013).

[49] E. Bauch, S. Singh, J. Lee, C. A. Hart, J. M. Schloss, M. J. Turner, J. F. Barry, L. Pham, N. Bar-Gill, S. F. Yelin *et al.*, Phys. Rev. B **102**, 134210 (2020).

[50] J. R. Maze, P. L. Stanwix, J. S. Hodges, S. Hong, J. M. Taylor, P. Cappellaro, L. Jiang, M. V. Gurudev Dutt, E. Togan, A. S. Zibrov *et al.*, Nature **455**, 644 (2008).

[51] V. Yaroshenko, V. Soshenko, V. Vorobyov, S. Bolshedvorskii, E. Nenasheva, I. Kotel'nikov, A. Akimov, and P. Kapitanova, Rev. Sci. Instrum. **91**, 035003 (2020).

[52] H. Fu, W. Sun, O. Ogidi-Ekoko, J. C. Goodrich, and N. Tansu, AIP Adv. **9**, 045013 (2019).

[53] S. Nakamura, Semicond. Sci. Technol. **14**, R27 (1999).

[54] L. A. M. Sulmoni, Static and dynamic characteristics of InGaN-based laser diodes, Ph.D. thesis, Lausanne, EPFL, 2014, https://doi.org/10.5075/epfl-thesis-6083.

[55] F. Tabataba-Vakili, C. Brimont, B. Alloing, B. Damilano, L. Doyennette, T. Guillet, M. E. Kurdi, S. Chenot, V. Brändli, E. Frayssinet *et al.*, Appl. Phys. Lett. **117**, 121103 (2020).

[56] R. M. Farrell, D. A. Haeger, P. S. Hsu, K. Fujito, D. F. Feezell, S. P. DenBaars, J. S. Speck, and S. Nakamura, Appl. Phys. Lett. **99**, 171115 (2011).

[57] S. Lutgen, A. Avramescu, T. Lermer, D. Queren, J. Müller, G. Bruederl, and U. Strauss, Phys. Status Solidi (a) **207**, 1318 (2010).

[58] S. Nakamura, IEEE J. Sel. Top. Quantum Electron. **3**, 435 (1997).

[59] M. S. Al-Ghamdi, A. Bakry, and M. Ahmed, J. Eur. Opt. Soc.-Rapid Publ. **15**, 22 (2019).

[60] T. Frost, A. Banerjee, and P. Bhattacharya, Appl. Phys. Lett. **103**, 211111 (2013).

[61] S. Stańczyk, T. Czyszanowski, A. Kafar, J. Goss, S. Grzanka, E. Grzanka, R. Czernecki, A. Bojarska, G. Targowski, M. Leszczyński *et al.*, Appl. Phys. Lett. **103**, 261107 (2013).

[62] L. Q. Zhang, D. S. Jiang, J. J. Zhu, D. G. Zhao, Z. S. Liu, S. M. Zhang, and H. Yang, J. Appl. Phys. **105**, 023104 (2009).

[63] D. T. Cassidy, J. Opt. Soc. Am. B **8**, 747 (1991).

[64] W. G. Scheibenzuber, U. T. Schwarz, L. Sulmoni, J. Dorsaz, J.-F. Carlin, and N. Grandjean, J. Appl. Phys. **109**, 093106 (2011).

[65] S. Kreinberg, W. W. Chow, J. Wolters, C. Schneider, C. Gies, F. Jahnke, S. Höfling, M. Kamp, and S. Reitzenstein, Light: Sci. Appl. **6**, e17030 (2017).

[66] J. Yang, D. G. Zhao, D. S. Jiang, X. Li, F. Liang, P. Chen, J. J. Zhu, Z. S. Liu, S. T. Liu, L. Q. Zhang *et al.*, Opt. Express **25**, 9595 (2017).

[67] M. Anani, H. Abid, Z. Chama, C. Mathieu, A. Sayede, and B. Khelifa, Microelectron. J. **38**, 262 (2007).

[68] J. L. Webb, L. Troise, N. W. Hansen, C. Olsson, A. M. Wojciechowski, J. Achard, O. Brinza, R. Staacke, M. Kieschnick, J. Meijer *et al.*, Sci. Rep. **11**, 2412 (2021).

[69] R.-M. Ma and R. F. Oulton, Nat. Nanotechnol. **14**, 12 (2018).

[70] T. Nöbauer, A. Angerer, B. Bartels, M. Trupke, S. Rotter, J. Schmiedmayer, F. Mintert, and J. Majer, Phys. Rev. Lett. **115**, 190801 (2015).

4.3 Supplementary information

Supplementary Information: Laser threshold magnetometry using green light absorption by diamond nitrogen vacancies in an external cavity laser

James L. Webb,[1,*] Andreas F. L. Poulsen,[1] Robert Staacke,[2] Jan Meijer,[3]
Kirstine Berg-Sørensen,[4] Ulrik Lund Andersen,[1] and Alexander Huck[1]

[1]*Center for Macroscopic Quantum States (bigQ), Department of Physics, Technical University of Denmark, Kgs. Lyngby, Denmark*

[2]*Division of Applied Quantum System,*
Felix Bloch Institute for Solid State Physics,
Leipzig University, 04103, Leipzig, Germany

[3]*Division Applied Quantum System,*
Felix Bloch Institute for Solid State Physics,
Leipzig University, 04103, Leipzig, Germany

[4]*Department of Health Technology, Technical University of Denmark, Kgs. Lyngby, Denmark*

(Dated: April 16, 2021)

---

[*] jaluwe@fysik.dtu.dk

I. MODEL FOR EFFECTIVE REFLECTIVITY

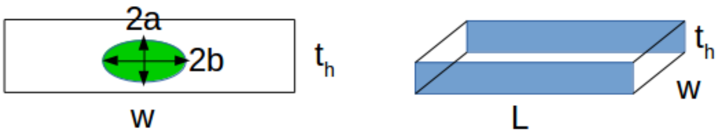

FIG. 1. We assume a rectangular laser diode with active volume V=WxLxt$_{\mathrm{h}}$, with a near field emission spot at the end facet of size $2a$x$2b$,

We calculate the effective reflectivity using the equation:

$$r_e = r_2 - \frac{1-R_2}{r_2}\sum_n \epsilon_n(-r_2 r_3 e^{2i\theta})^n \tag{1}$$

where r_i are the mirror complex reflectivities derived from the Fresnel equations where $R_i = |r_i|^2$. We assume that the diamond is not in contact with the diode or the reflector mirror (interface is always to air). The phase angle $\theta = 2\pi L_r/\lambda$ is the phase component arising from the external cavity and ϵ_n are the individual coupling factors from the nth reflection in the cavity. We assume that we can adjust our external cavity length such that the phase term $e^{2i\theta}$=1. An approximate expression for ϵ_n is given in the work by Voumard et al. (citation in main text) using the dimensions a and b of the radii of the near field spot size of the laser emission from the diode. (See Supplementary Figure 1)

II. QUANTUM WELL GAIN

We can also modify this model for quantum well structures to follow a logarithmic relation, such that:

$$G = \Gamma a N_{tr} \ln{(N_{th}/N_{tr})}(1 - \epsilon S) \tag{2}$$

We use the above expression in calculating the estimated sensitivity and threshold currents for a quantum well structure in the main text.

III. ABSORPTION CONTRAST FOR DIAMOND D1 AND D2

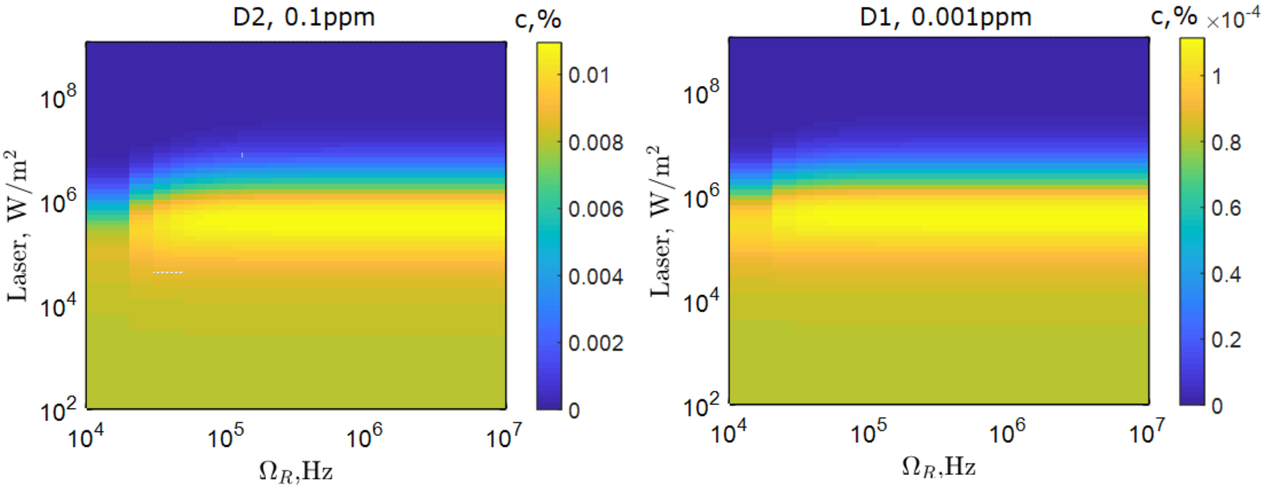

FIG. 2. Absorption contrast percentage calculated from the rate model for Diamond D1 and D2. The 1x10^{-4} level percentage absorption contrast matches the level observed experimentally in our previous work for a diamond with ppb-level NV density (Ahmadi et al., citation in the main text)

IV. CALCULATED ODMR FOR DIAMOND D1 AND D2

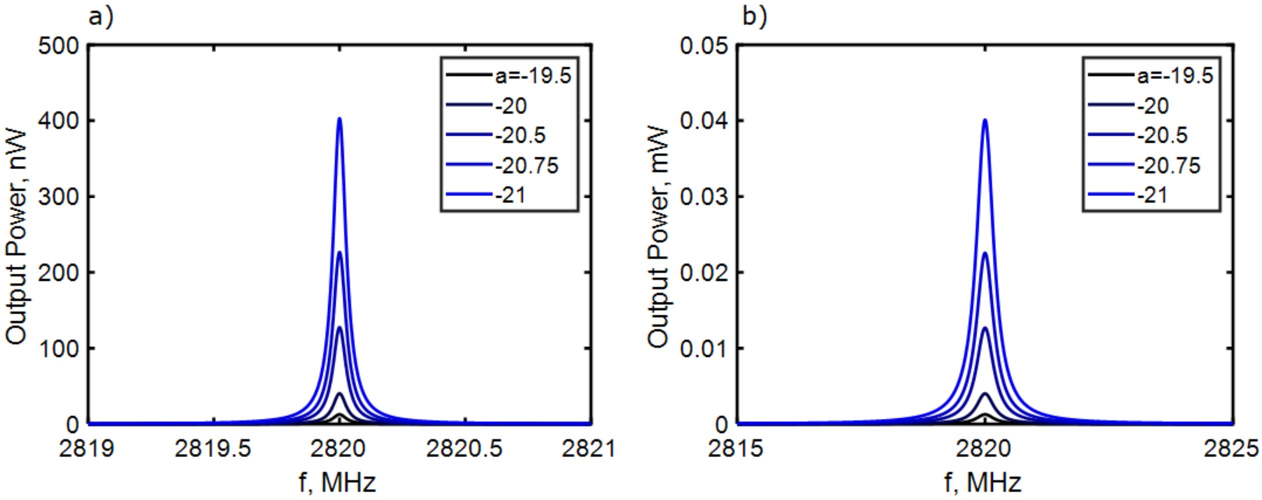

FIG. 3. Calculated ODMR from laser emission on resonance for a) Diamond D1 and b) Diamond D2

Supplementary Figure 3 gives the calculated ODMR for Diamond D1 and Diamond D2. Despite the reduced linewidth for both D1 and D2 as compared to D3, the small change in threshold current and the low output power makes best possible sensitivity worse than for D3 (see below).

V. MAGNETIC FIELD SENSITIVITY FOR DIAMOND D1 AND D2

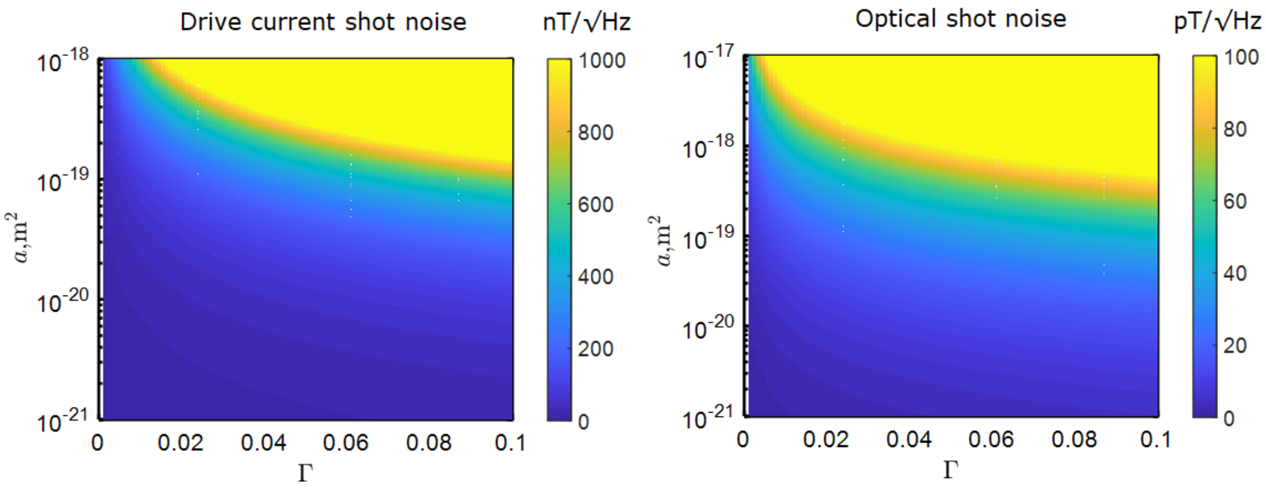

FIG. 4. Calculated magnetic field sensitivity in the optical (right) and gain medium drive current (left) shot noise limited regimes for Diamond D1, as a function of a and Γ

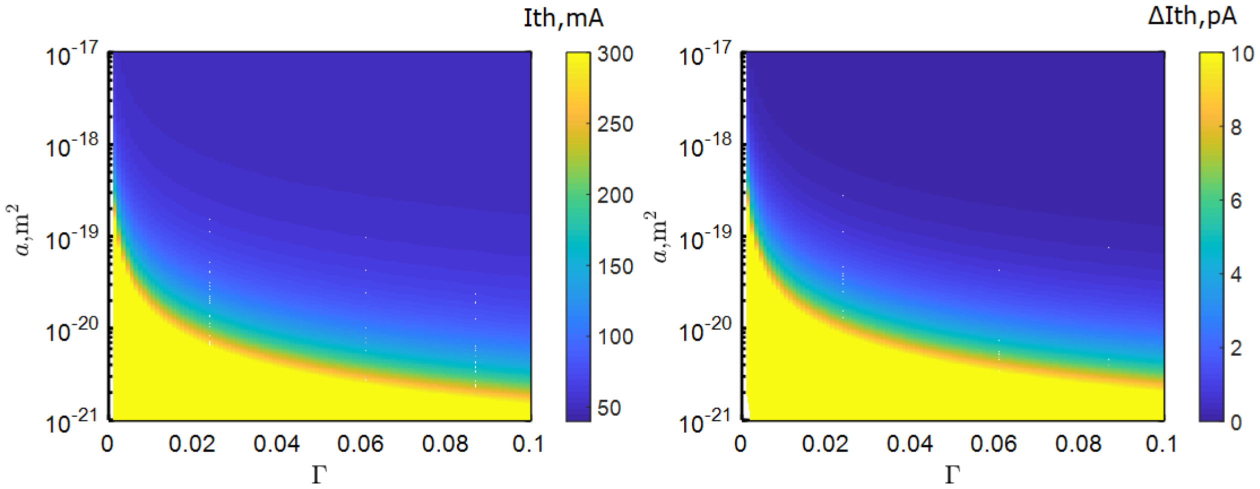

FIG. 5. Threshold current I_{th} and change in threshold current ΔI_{th} for Diamond D1

Supplementary Figure 5, left gives the calculated threshold current I_{th} for Diamond D1. These are not significantly different from D2 and D3 as they are primarily defined by the semiconductor laser gain medium and associated parameters. However, the change in threshold (Supplementary Figure 5, right) is significantly smaller (pA) due to the lower absorption contrast of D1. This makes the drive current limited sensitivity much worse than

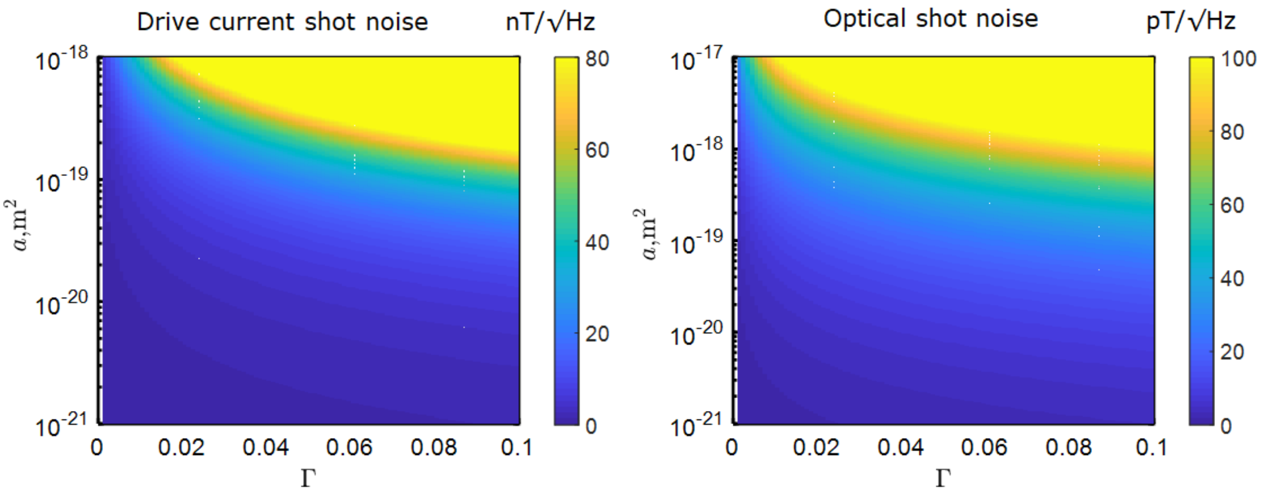

FIG. 6. Calculated magnetic field sensitivity in the optical (right) and gain medium drive current (left) shot noise limited regimes for Diamond D2, as a function of a and Γ

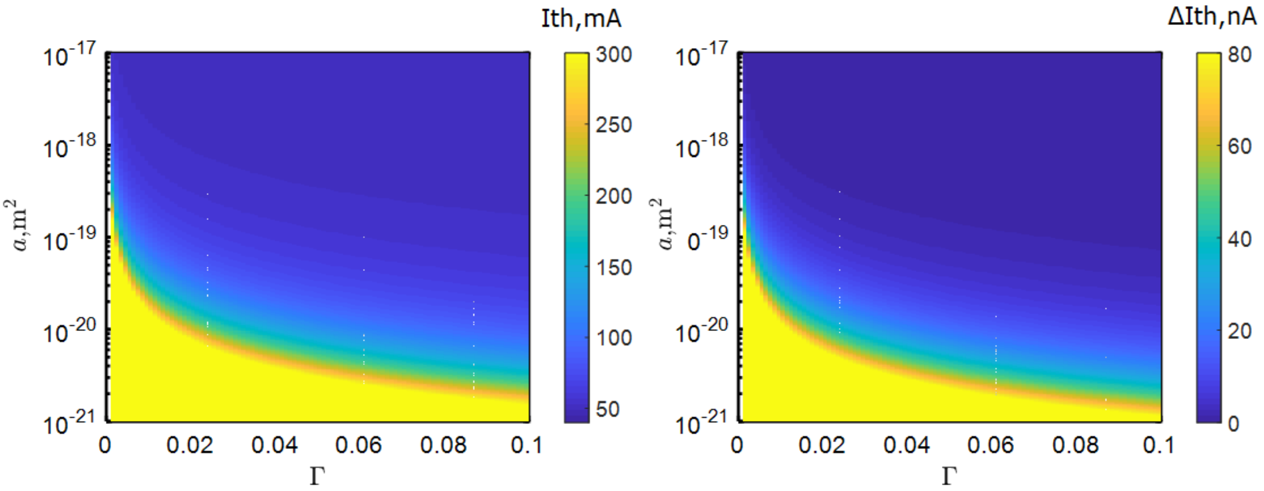

FIG. 7. Threshold current I_{th} and change in threshold current ΔI_{th} for Diamond D2

for D3 (nT/$\sqrt{\text{Hz}}$, see Supplementary Figure 4). D2 represents the middle case between D1 and D3, with a higher ΔI_{th}, but still severely limited by drive current shot noise.

VI. ESTIMATED LIMITATIONS DUE TO CURRENT SOURCE NOISE

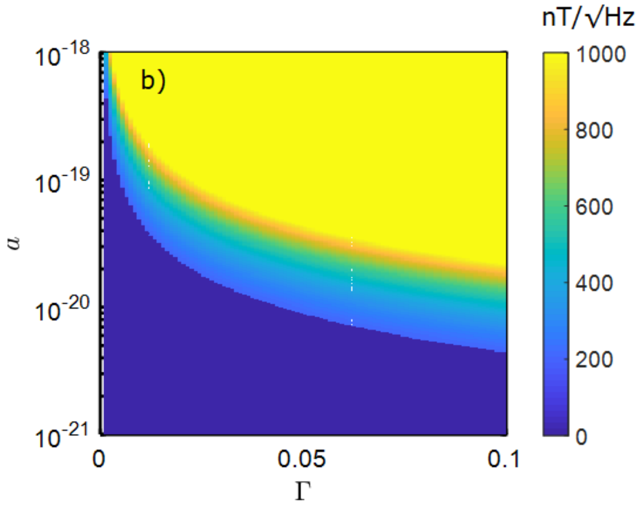

FIG. 8. Estimated sensitivity limit for Diamond D3 assuming a realistic 30nA/$\sqrt{\text{Hz}}$ noise current source. The dark blue area covers the region where the change in threshold current is below the noise floor and therefore sensitivity is set to be zero. Best achievable sensitivity within this region is approximately 235nT/$\sqrt{\text{Hz}}$

Where operation is not intrinsically limited in region B, we must also consider what level of noise can be reached by a realistic current source. From examples in literature, we consider drive current stability of 1ppm of full range as achievable. This is ≈1μA on a 500mA max output range with 1kHz bandwidth (30nA/$\sqrt{\text{Hz}}$). We assume this limit can be reached through feedback control from the laser output. Imposing such a limit on the sensor gives a sensitivity in the nT/$\sqrt{\text{Hz}}$ range (Figure 8). We note that the limit on drive current stability and maximum threshold current is purely technical, rather than a limit imposed by the physics of the system.

VII. EXPERIMENTAL CONTRAST VERSUS MICROWAVE POWER

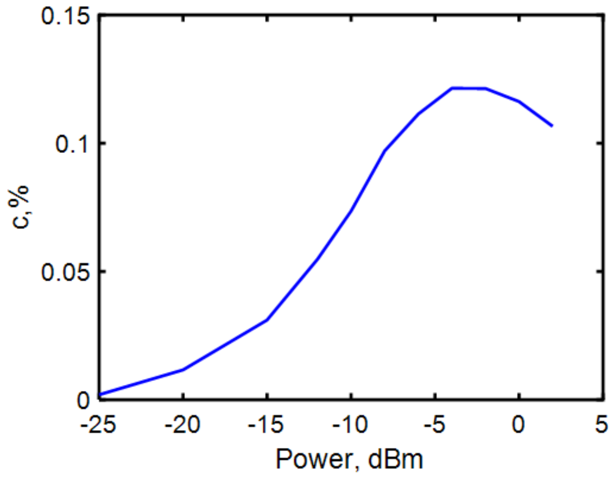

FIG. 9. Maximum experimentally measured absorption contrast as a fuction of microwave power before amplification in dBm

Supplementary Figure 9 showing the variation in absorption contrast versus microwave power for the experimentally measured diamond. Contrast peaks at an input power before the amplifier of -5dBm (amplifier gain 45dB).

VIII. ZOOMED PLOTS FOR LOW-Γ AND a

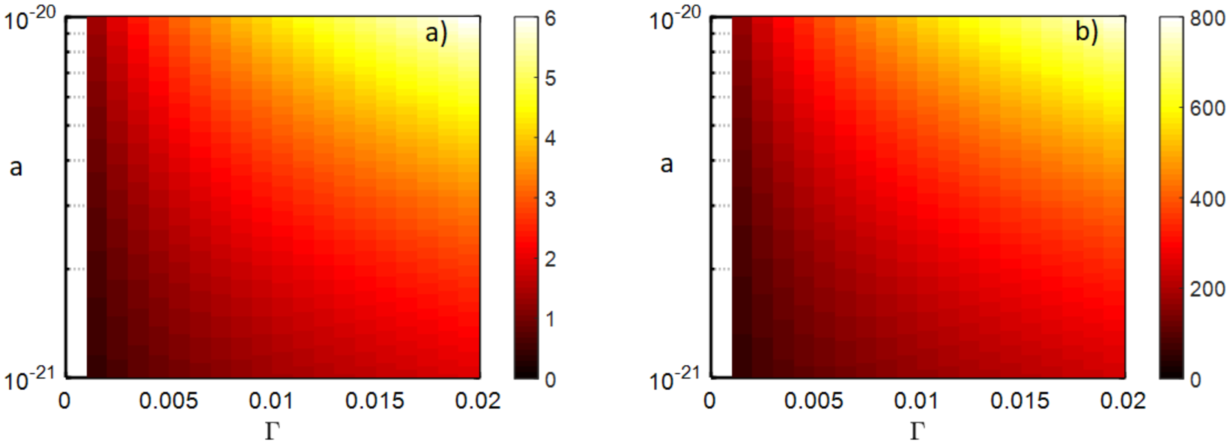

FIG. 10. Zoomed in plots for Figure 7 in the main text, showing the region for low Γ and a.

5 Investigation and comparison of measurement schemes in the low frequency biosensing regime using solid-state defect centers

5.1 Introduction

The low-frequency sensing regime is of particular importance to studies of biology, as many signals of interest are found in this regime. Several different NV sensing schemes can be applied to perform sensing in the low-frequency regime. However, choosing the optimal sensing scheme for a given task is made challenging by the differing properties of the various schemes. In particular, the impact of inhomogeneous broadening and drive amplitude variations on the achievable sensitivity differs from scheme to scheme.

In order to address this issue, we theoretically investigated and compared the achievable sensitivity of the three most commonly used low-frequency sensing schemes for varying levels of inhomogeneous broadening and drive amplitude variations. The considered schemes were CW ODMR, π-pulse ODMR and Ramsey interferometry. The schemes were compared in terms of the maximum achievable slope in contrast, which is directly linked to the sensitivity.

The maximum achievable contrast slope for each scheme was simulated for varying levels of inhomogeneous broadening and drive amplitude variations. The resulting values were compared in order to determine the region(s) where each scheme was preferable. Simultaneously, we extracted information about the impact of inhomogeneous broadening and drive amplitude variations on each of the three considered schemes. The main findings are summarized in the publication in section 5.2, and the supplementary information is given in section 5.3.

5.2 Publication

Investigation and comparison of measurement schemes in the low frequency biosensing regime using solid-state defect centers

Andreas F.L. Poulsen,[1] James L. Webb,[1, *] Kirstine Berg-Sørensen,[2] Ulrik Lund Andersen,[1, †] and Alexander Huck[1, ‡]
[1] *Center for Macroscopic Quantum States (bigQ), Department of Physics, Technical University of Denmark, 2800 Kongens Lyngby, Denmark*
[2] *Department of Health Technology, Technical University of Denmark, 2800 Kongens Lyngby, Denmark*

Ensembles of solid state defects in diamond make promising quantum sensors with high sensitivity and spatiotemporal resolution. The inhomogeneous broadening and drive amplitude variations across such ensembles have differing impacts on the sensitivity depending on the sensing scheme used, adding to the challenge of choosing the optimal sensing scheme for a particular sensing regime. In this work, we numerically investigate and compare the predicted sensitivity of schemes based on continuous-wave (CW) optically detected magnetic resonance (ODMR) spectroscopy, π-pulse ODMR and Ramsey interferometry for sensing using nitrogen-vacancy centers in the low-frequency (< 10 kHz) range typical for signals from biological sources. We show that inhomogeneous broadening has the strongest impact on the sensitivity of Ramsey interferometry, and drive amplitude variations least impact the sensitivity of CW ODMR, with all methods constrained by the Rabi frequency. Based on our results, we can identify three different regions of interest. For inhomogeneous broadening less than 0.3 MHz, typical of diamonds used in state of the art sensing experiments, Ramsey interferometry yields the highest sensitivity. In the regime where inhomogeneous broadening is greater than 0.3 MHz, such as for standard optical grade diamonds or in minaturized integrated devices, drive amplitude variations determine the optimal protocol to use. For low to medium drive amplitude variations, the highest sensitivity is reached using π-pulse ODMR. For high drive amplitude variations, relevant for widefield microscopic imaging, CW ODMR can yield the best sensing performance.

I. INTRODUCTION

Defect centers in diamond are promising candidates for applications in quantum sensing due to high attainable sensitivity, their atomic scale dimensions, the chemical stability of diamond and compatibility with biological samples [1–4]. In particular, the negatively charged nitrogen-vacancy center (NV) in diamond possesses several properties advantageous for sensing including long coherence times of the associated electron spin even at room temperature, optical initialization and readout of the spin state [5, 6] and the ability to coherently manipulate the spin with resonant microwaves (MW) [7]. The level structure and spin-state dependent transitions of the NV center, illustrated in Fig. 1, render the system sensitive to temperature [8, 9], pressure [10], electric fields [11, 12] and magnetic fields [7], but it has received the most focus for its potential as a magnetometer [7, 13–16].

NV center based sensing most commonly involves applying a static magnetic field to lift the degeneracy of the $m_S = \pm 1$ spin states and addressing either the $m_S = 0 \leftrightarrow m_S = 1$ or $m_S = 0 \leftrightarrow m_S = -1$ transition as an effective two-level system [17]. This two-level system is then either driven continuously with constant amplitude microwave and pump laser illumination or in a pulsed manner according to the sensing scheme applied for the specific task. Due to the spin-state dependent fluorescence properties of the NV center, when microwaves are supplied at a resonance frequency matching the triplet ground state spin transition, fluorescence emission is reduced due to nonradiative and infrared decay via a singlet shelving state. Sensing can be performed by recording this environmental-dependent change in fluorescence while probing the spin resonance. This can be practically achieved by many different sensing schemes, including continuous-wave optically detected magnetic resonance spectroscopy (CW ODMR) [18], π-pulse ODMR [19, 20], Ramsey interferometry [21], Hahn Echo [22] and many others[17, 23, 24].

Choosing the right scheme for the specific sensing task is essential to achieving the best possible sensitivity. To maximize bulk sensitivity, it is necessary to use a large ensemble of NV centers as in the shot-noise limited regime [13] the sensitivity is proportional to $\sqrt{N}$, where N is the number of NV centers. It is also necessary to use a large ensemble for other applications, in particular wide field of view microscopy with high spatial resolution. The use of an NV center ensemble introduces challenges of its own. Variations in the local environment of NV centers, e.g. related to varying crystal strain across the ensemble, lead to inhomogeneous broadening (IHB) of their spin triplet transition frequencies, making it challenging for a single-frequency MW drive to be on-resonance with the entire ensemble. Depending on the physical extent of the ensemble and the used MW antenna geometry, it is also possible for the MW drive amplitude to vary across the ensemble. Both of these effects can have a negative impact on the performance of sensing schemes. The impact

---

[*] jaluwe@fysik.dtu.dk
[†] ulrik.andersen@fysik.dtu.dk
[‡] alexander.huck@fysik.dtu.dk

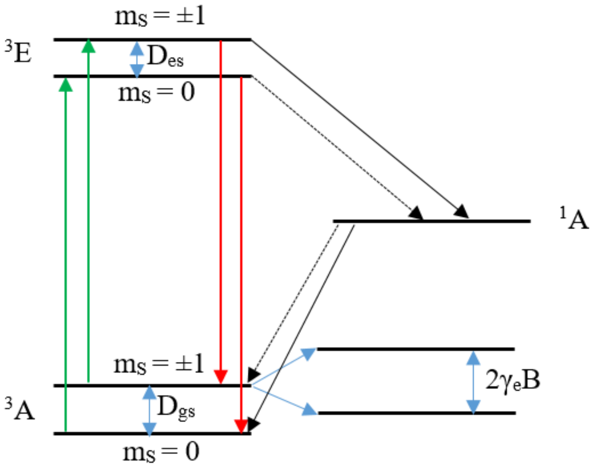

FIG. 1. Simplified energy-level diagram of the negatively charged nitrogen-vacancy center (NV). The diagram illustrates the spin-conserving excitation from ground state triplet ^{3}A to excited state triplet ^{3}E caused by green illumination, the radiative (red fluorescence) decay back to the ground state triplet and the non-radiative decay paths to and from the metastable singlet state ^{1}A. Dashed arrows indicate relatively weaker decay rates. The diagram also exemplifies the splitting induced by the Zeeman effect when a magnetic field B is applied. We show the zero-field splitting in the ground state, $D_{gs} = 2.87$ GHz, and excited state, $D_{es} = 1.42$ GHz, and the splitting of the $m_S = \pm 1$ states due to a magnetic field B given by the gyromagnetic ratio $\gamma_e = 28$ MHz/mT.

of sample or drive scheme inhomogeneity can also vary between different sensing schemes, which further complicates the choice of the optimal sensing scheme for a given task.

In this article, we numerically investigate and compare the sensitivity of different sensing schemes for different levels of inhomogeneous broadening and drive amplitude variations. We note that for high frequency AC field sensing, such as sensing nuclear spins using single NV centres [25, 26], spin-echo techniques offer by far the best sensitivity achievable. In this work, we instead focus on the DC to low frequency (< 10 kHz) sensing regime. This frequency range is of particular importance for biosensing, including sensing of action potentials on the millisecond timescale [27] and seconds to hours temperature sensing using nanodiamonds within cells [3, 28]. This is a primary application for NV centers due to the high degree of biocompatibility of diamond. We consider three sensing schemes: Ramsey interferometry, π-pulse ODMR and CW ODMR. These are the most commonly used schemes for this frequency range using the NV center platform [21]. We theoretically investigate and compare the predicted relative sensitivities for these three schemes in varying sensing regimes and discuss how these simulations can relate to potential applications, including widefield microscopy and microfabricated sensors.

II. METHODS

We model an ensemble of N nitrogen-vacancy centers as the sum of independent single NV, denoted i, following the level structure in Fig. 1 and following the state dynamics of N independent quantum systems. This assumption is valid due to the relatively low density of NV centers in a typical sensing sample (up to parts per million range), meaning the sum total of interaction between NV centers in the ensemble is low. We assume zero noise, such that our sensitivity is only dependent on the response of the ensemble, excluding difficult to quantify noise sources such as time varying background magnetic fields from laboratory equipment or laser technical noise. The time varying application of microwave and laser fields to the ensemble for each of the three sensing schemes considered in this article are illustrated in Fig. 2.The exact theoretical approach of the simulations differs between the three considered sensing schemes, but we include the effects of inhomogeneous broadening and MW drive amplitude variations across the ensemble in the same way in all three protocols.

We simulate inhomogeneous broadening across our ensemble via a distribution of transition frequencies, which can be modelled as varying detuning, δ_i, from a central transition with frequency $\omega_0 = 2\pi \cdot f_0$. This detuning contributes to the total detuning $\Delta_i = 2\pi \cdot \delta_i - (\omega_{MW} - \omega_0)$ between the transition frequency and the driving frequency $\omega_{MW} = 2\pi \cdot f_{MW}$. We define the term drive detuning to correspond to the difference $f_{MW} - f_0$ between the driving frequency f_{MW} and the central transition frequency f_0. The drive detuning can be altered without changing f_0 by varying f_{MW}. We simulate microwave drive amplitude variations as an effective Rabi frequency $\alpha_i \Omega_R$ varying across the ensemble. Here, α_i is defined as the ratio between the effective Rabi frequency and the intended Rabi frequency in the non-detuned case Ω_R, which is kept fixed [29].

The ensemble is modelled as consisting of NV centers, each with a particular value of δ_i and α_i, while all other parameters are assumed to be constant across the entire ensemble. A pump laser pulse is assumed to return every NV center to the $m_S = 0$ ground state $|0\rangle$ and the readout is assumed to reflect the exact state distribution. For simplicity, we consider only NV centers aligned along one crystallographic axis of diamond and assume that the magnetic field is aligned along that axis. The δ_i-values are considered to follow a Gaussian distribution centered at zero with a full width at half maximum (Γ). The values of δ_i are taken in the range $\pm\Gamma$. In our results and discussion below, the upper limit of this range is used to indicate the level of inhomogeneous broadening L_{IHB} for a given simulation, i.e. a Γ of 0.5 MHz equals $L_{IHB} = 0.5$ MHz. The α_i-values follow a flat distribution between 0 and 1 to approximate a decaying MW drive field. The range below 1 spanned by the α_i-values is used to indicate the level of MW drive amplitude variations, termed L_{DAV} below, i.e. if α_i varies between 0.9

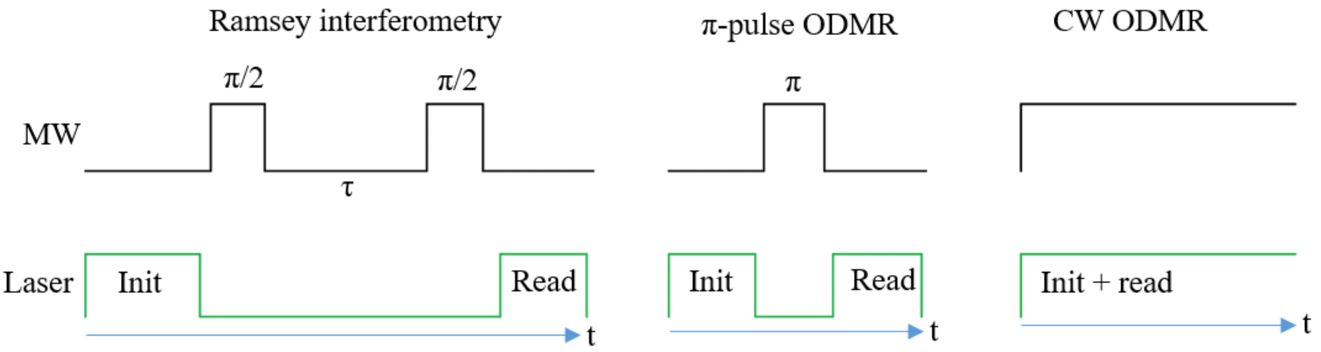

FIG. 2. Simple sketch illustrating the application of each of the three considered sensing schemes. Ramsey interferometry and π-pulse ODMR are pulsed sequences while CW ODMR involves constant application of both laser power and microwaves.

and 1, $L_{DAV} = 0.1$. MW drive amplitude variations can be neglected by setting $\alpha_i = 1$ in all cases.

A. Ramsey interferometry

Simulations of Ramsey interferometry were performed using a Hamiltonian representing a coherently driven single NV two-level spin system in a rotating frame

$$\hat{H} = \frac{\Delta_i}{2}\hat{\sigma}_z + \frac{\alpha_i \Omega_R}{2}\hat{\sigma}_x, \tag{1}$$

where $\hat{\sigma}_x$ and $\hat{\sigma}_z$ are Pauli spin-matrices, and $\hbar$ is equal to one. The simulations are performed in three steps. First, an input state representing an NV center initialized in state $m_s = 0$, $|\psi_i\rangle = |0\rangle = (1\,0)^T$, is allowed to evolve under the influence of Ω_R for a duration $T_p = \pi/(2\Omega_R)$ corresponding to and simulating the effect of a $\pi/2$-pulse. In the second step, the resulting state is then used as the input state for an evolution where $\Omega_R = 0$ for a duration equal to the considered free precession time τ. In the final and third step, the resulting output state after free precession is used as the input state for an evolution where Ω_R is again non-zero for a duration of $T_p = \pi/(2\Omega_R)$, accounting for the effect of the final $\pi/2$-pulse. For the output of our simulation, we define a normalized contrast C_i, obtained for the resulting final output state $|\psi_f\rangle$ by determining its overlap with state $|1\rangle = (0\,1)^T$ corresponding to either $m_s = 1$ or $m_s = -1$,

$$C_i = |\langle 1|\psi_f\rangle|^2. \tag{2}$$

The obtained value of C_i represents normalized fluorescence contrast between on and off microwave resonance, calculated for a single NV center in the ensemble with parameters Δ_i and α_i. The parameter C_i is a valid measure of the normalized contrast, given that the contrast will be minimal when the NV center is in state $|0\rangle$ and maximal when the NV center is in state $|1\rangle$. We assume that a normalized contrast of $C_i = 1$ corresponds to a fluorescence contrast of 30%, the maximum typically measured in an optically detected magnetic resonance experiment using a single NV center in bulk diamond [17]. We define a total normalized contrast for the ensemble C as the mean normalized contrast taken by averaging across all C_i values.

We can also include pure dephasing in the simulation by using a quantum master equation for a two-level system

$$\frac{d\rho}{dt} = -i\left[\hat{H},\rho\right] + \Gamma_{pure}\left(\hat{\sigma}_z\rho\hat{\sigma}_z - \frac{1}{8}\hat{\sigma}_z\hat{\sigma}_z\rho - \frac{1}{8}\rho\hat{\sigma}_z\hat{\sigma}_z\right), \tag{3}$$

where $\rho = |\psi\rangle\langle\psi|$ for a pure state and the rate of pure dephasing is given by $\Gamma_{pure} \approx 1/T_2^*$. Otherwise, the simulations are performed using the exact same three-step approach that was previously described for the case without pure dephasing. In density matrix notation, the input state corresponding to an NV initialized in state $m_s = 0$ is $\rho_i = \begin{bmatrix} 1 & 0 \\ 0 & 0 \end{bmatrix}$, and the normalized contrast C_i is directly obtained from the second diagonal element of ρ_f, which is the output density matrix obtained from the third and final step of the simulation.

As a demonstration of the effect of inhomogeneous broadening, we present in Fig. 3 the ensemble-average normalized contrast C as a function of free precession time simulated for the Ramsey protocol for a $N = 41$ ensemble with $\Omega_R = 2\pi \cdot 5$ MHz, no pure dephasing, a drive detuning equal to 1.2 MHz, no drive amplitude variations and three different values of L_{IHB}. As expected, we observe Ramsey fringes where the contrast is seen to oscillate at a frequency equal to the detuning between the drive and the central transition frequency. The Ramsey interference fringes seen in Fig. 3, are observed to decay within a time constant that roughly corresponds to $1/L_{IHB}$. The observed decay caused by inhomogeneous broadening is thus similar in effect to a decay of the contrast value caused by pure dephasing.

In order to provide a quantitative measure of the presence of Ramsey fringes and their relative strength, we define a figure of merit q that is equal to the difference in normalized contrast between the second-highest fringe maximum and the second-lowest minimum, as indicated in Fig. 3. This ensures the presence of at least two clear

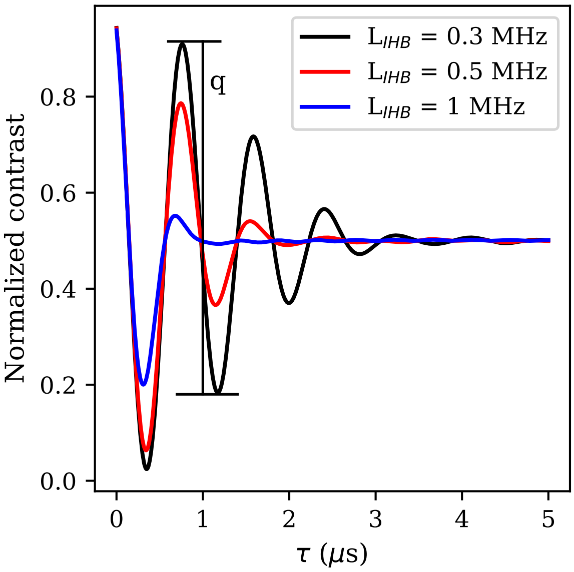

FIG. 3. Color online. Simulated Ramsey measurement for $\Omega_R = 2\pi \cdot 5$ MHz, no pure dephasing, a drive detuning equal to 1.2 MHz and three different values of L_{IHB}. The quantity q indicated on the plot for $L_{IHB} = 0.3$ MHz is a self-defined figure of merit used to judge the relative strength of the Ramsey fringes.

fringes for large q, separating a genuine Ramsey interference measurement from relaxation or ensemble π-pulse rotation effects that might resemble a single fringe. For each value of Ω_R that we consider in the simulations, we then determine q for different values of the drive detuning and L_{IHB}. For each set of L_{IHB}, we then extract the drive detuning that yields the maximum value q_{max} and hence the most pronounced Ramsey fringes. The extracted drive detuning value is used for the estimation of the maximum achievable slope in normalized contrast for the set values of Ω_R and L_{IHB}.

For direct comparison with CW and π-pulse ODMR, it was necessary to convert the change in normalized contrast as a function of the target sensing parameter into the equivalent normalized contrast change (slope) as a function of variation in microwave drive frequency f_{MW}, $C^{'} = dC/df_{MW}$. Unlike CW or π-pulse ODMR, where sensing is simply dependent on the change in microwave resonance frequency of the ODMR features caused by a change in the parameter to be sensed, e.g. magnetic field or temperature, the sensitivity of the Ramsey scheme approach is not directly related to the maximum slope of the Ramsey fringes. Instead, a change in the parameter to be sensed will change the resonance frequency, thereby changing the total detuning Δ_i and thus the oscillation frequency of the Ramsey fringes. This causes the Ramsey fringes to be compressed or stretched in free precession time τ and leads to a measurable oscillation in the contrast for a fixed $\tau \neq 0$ as a function of the sensing parameter. This is exemplified in Fig. 4 for the case of magnetic field sensing. Here, the addition of a magnetic field B shifts the resonance frequency and thus the total detuning by $m_s \gamma_e B$, with $\gamma_e = 28\,\mathrm{MHz/mT}$ the gyromagnetic ratio of an electron spin. Figure 4(a) shows how the Ramsey fringes are shifted by a change in the magnetic field B while Fig. 4(b) illustrates how the contrast at a fixed τ oscillates as a function of the

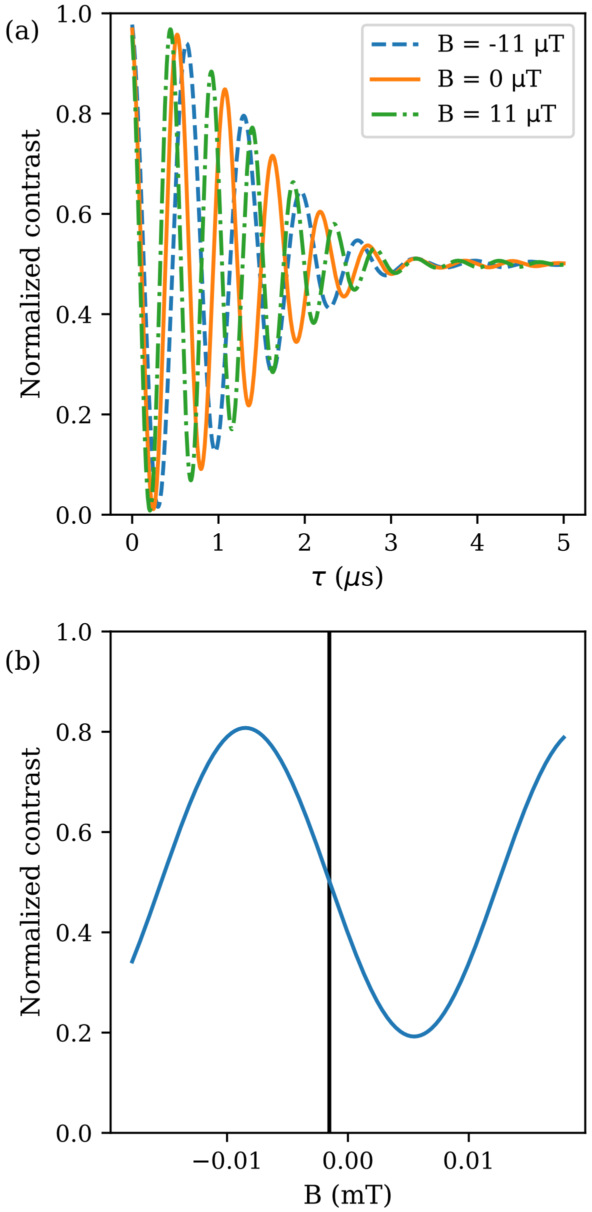

FIG. 4. (a) Ramsey interferometry contrast versus τ for $L_{IHB} = 0.3$ MHz, $\Omega_R = 2\pi \cdot 10$ MHz, no pure dephasing and a drive detuning of 1.8 MHz with three different values of B. (b) Ramsey interferometry contrast versus B for $\tau = 1.25\,\mu\mathrm{s}$ and otherwise identical parameters to (a). Position of maximum slope dC/dB indicated by vertical line.

magnetic field B. The maximum slope of this oscillation dC/dB, shown in Fig. 4(b) for $\tau = 1.25\,\mu\mathrm{s}$, is the point of maximum attainable sensitivity η_B of Ramsey sensing of magnetic fields. The maximum achievable slope is dependent on the fixed value of τ due to the effects of inhomogeneous broadening and/or pure dephasing.

In order to determine the maximum sensitivity of the Ramsey scheme, it was therefore necessary to simulate the normalized contrast as a function of the sensing parameter (e.g. magnetic field B) for different fixed τ, obtaining a τ_{opt} that maximises η_B. The maximum achievable slope as a function of the sensing parameter can then be converted to $C'{=}dC/df_{MW}$ using a conversion factor for the known change in transition frequency as a function of a given sensing parameter for a single NV axis (e.g. $\gamma_e = 28$ MHz/mT for magnetic field or -74.2 kHz/K for temperature).

In this work, we performed this conversion by determining the change in ensemble average normalized contrast in a simulated applied magnetic field between $-3.6\,\mu\mathrm{T}$ and $3.6\,\mu\mathrm{T}$ with varying τ up to $5\,\mu\mathrm{s}$. In each case considered in the simulation, the driving frequency ω_{MW} was chosen such that the total drive detuning Δ_i without field ($B = 0$) maximizes the figure of merit q to ensure clear Ramsey fringes. From these simulations we determined the maximum dC/dB and converted this to $C'{=}dC/df_{MW}$ using the above conversion factor. This permitted direct comparison of the Ramsey interferometery scheme with CW and π-pulse ODMR sensing.

B. π-pulse ODMR

For the case of simulating the π-pulse ODMR scheme, simulations were performed using the same methods as for simulating the Ramsey protocol, but by replacing the three-step sequence with a single step where an input state $|\psi_i\rangle = |0\rangle$ was allowed to evolve under the influence of a drive field with strength Ω_R for a duration $T_p = \pi/\Omega_R$ equal to a π-pulse. The normalized contrast C obtained for the resulting output state $|\psi_f\rangle$ was then calculated using Eq. 2. This approach was repeated for varying values of the drive frequency f_{MW}, from which a normalized contrast spectrum and the measurable maximum slope was extracted.

C. CW ODMR

We performed the simulation of the CW ODMR protocol using a five-level model of the NV center [30], including spin, optical and non-radiative transitions. The decay rates typical for an NV center in bulk diamond are listed in [31], and the optical excitation rate is Γ_p.

The steady-state solutions for the ground state populations for a single NV can be obtained directly via the expressions [30]

$$\rho_{11}^{ss} = \left[1 + \Xi + \frac{\Gamma_p}{K_3} + \frac{\Gamma_p \Xi}{K_4} + \frac{k_{35}\Gamma_p}{K_3 K_5} + \frac{k_{45}\Gamma_p \Xi}{K_4 K_5}\right]^{-1}, \quad (4)$$

and

$$\rho_{22}^{ss} = \left[1 + \frac{1}{\Xi} + \frac{\Gamma_p}{K_4} + \frac{\Gamma_p}{K_3 \Xi} + \frac{k_{45}\Gamma_p}{K_4 K_5} + \frac{k_{35}\Gamma_p}{K_3 K_5 \Xi}\right]^{-1}, \quad (5)$$

where

$$\Xi = \frac{\left[\frac{k_{21}}{2} + \frac{\Gamma_p(k_{32}K_5 + k_{52}k_{35})}{K_3 K_5} + \frac{(\alpha_i \Omega_R)^2 \gamma_2'}{2(\gamma_2'^2 + \Delta_i^2)}\right]}{\left[\Gamma_p + \frac{k_{21}}{2} - \frac{\Gamma_p(k_{42}K_5 + k_{52}k_{45})}{K_4 K_5} + \frac{(\alpha_i \Omega_R)^2 \gamma_2'}{2(\gamma_2'^2 + \Delta_i^2)}\right]} \quad (6)$$

and

$$\begin{aligned} K_3 &= k_{35} + k_{31} + k_{32}, \\ K_4 &= k_{41} + k_{42} + k_{45}, \\ K_5 &= k_{51} + k_{52}, \end{aligned} \quad (7)$$

where Γ_p is the optical pumping rate, k_{nm} is the decay rate from level n to level m, K_n is the total decay rate from level n, $\gamma_2' = \gamma_2 + \Gamma_p/2$ is the optical dephasing rate, and $\gamma_2 = 2\pi/T_2^* + k_{21}/2$ is the spin dephasing rate. The steady-state solutions for the ground state populations can be used to obtain the CW ODMR spectrum as

$$\mathcal{I}_{CW} = \beta_3 \rho_{33}^{ss} + \beta_4 \rho_{44}^{ss} = \beta_3 \frac{\Gamma_p}{K_3} \rho_{11}^{ss} + \beta_4 \frac{\Gamma_p}{K_4} \rho_{22}^{ss} \quad (8)$$

where

$$\beta_3 = \frac{k_{31} + k_{32}}{K_3}, \; \beta_4 = \frac{k_{41} + k_{42}}{K_4}. \quad (9)$$

We include pure dephasing via $2\pi/T_2^*$ in the term $\gamma_2' = 2\pi/T_2^* {+} k_{21}/2 {+} \Gamma_p/2$ and can neglect the influence of pure dephasing by setting $2\pi/T_2^* = 0$. Eqs. (4-9) can thus be used to obtain the CW ODMR spectrum for a single NV center as a function of microwave drive frequency.

The spectrum values $\mathcal{I}_{CW}$ were converted to contrast relative to the value obtained when the microwave drive is far off-resonance. These values are divided by the maximum contrast obtained in the asymptotic limit where Ω_R is very large in order to obtain a normalized contrast value C_i. By repeated simulation for all values of Δ_i and α_i, we then calculate the ensemble average normalized contrast C as the mean of all C_i values in the ensemble. By varying the simulated microwave drive frequency f_{MW}, we can then derive the maximum slope as a function of drive frequency $C' {=} dC/df_{MW}$. This can be directly compared to the equivalent values obtained from the simulation of a Ramsey or π-pulse scheme, representing a measure of the maximum achievable sensitivity for CW ODMR sensing.

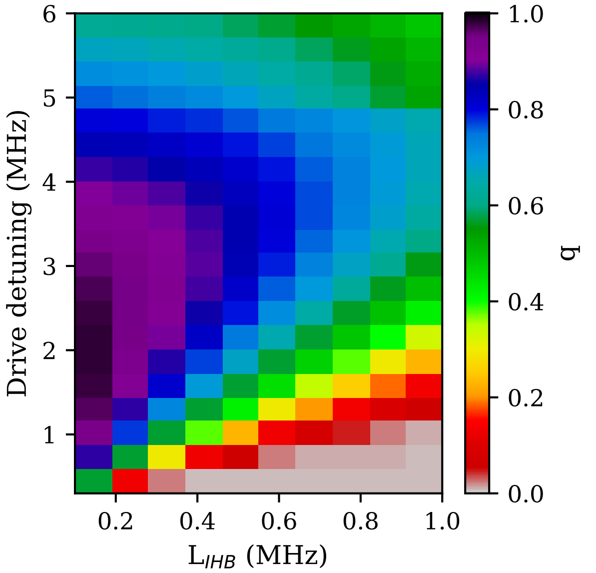

FIG. 5. Plot of the self-defined figure of merit q as a function of drive detuning and L_{IHB} for $\Omega_R = 2\pi \cdot 3$ MHz and no pure dephasing or drive amplitude variations.

III. RESULTS AND DISCUSSION

A. Ramsey interferometry

We first calculated how the visibility of the Ramsey fringes depended on the degree of drive detuning and the inhomogenous broadening (L_{IHB}). This was done in terms of the figure of merit q, to give a clear picture of how well the interferometry performs as a function of these parameters. Figure 5 shows a plot of q as a function of drive detuning and inhomogenous broadening at a fixed overall Rabi frequency $\Omega_R = 2\pi \cdot 3$ MHz with no pure dephasing or drive amplitude variations included. In the Supplementary information, we include examples of the individual Ramsey interferometry simulations that were used to obtain this plot. It is clear that the optimal drive detuning to maximize the figure of merit q and thus the quality of the Ramsey fringes increases with increasing inhomogeneous broadening. Moreover, we see that the fringes worsen with increasing inhomogeneous broadening. This is as expected, with an increase in L_{IHB} leading to a faster decay of the Ramsey fringes and thus requiring a larger oscillation frequency (drive detuning) in order to obtain sufficient Ramsey fringes to perform Ramsey interferometry. Also as expected, as L_{IHB} reaches its upper range (> 1 MHz), it becomes increasingly difficult to obtain interference fringes, as the broadening means the fixed microwave pulse length is no longer $\pi/2$ for an increasingly larger number of NV center spins in the ensemble.

By the procedure outlined in Methods, we calculate the maximum fluorescence contrast slope C' for Ramsey interferometry. We initially focus on a particular scenario for an ideal high sensitivity measurement with a strong, uniform microwave field across the diamond resulting in no ensemble drive amplitude variations and a high Rabi frequency ($\Omega_R > 2\pi \cdot 2$ MHz). We then simulate the influence of Rabi frequency and inhomogeneous broadening on the predicted maximum slope C'.

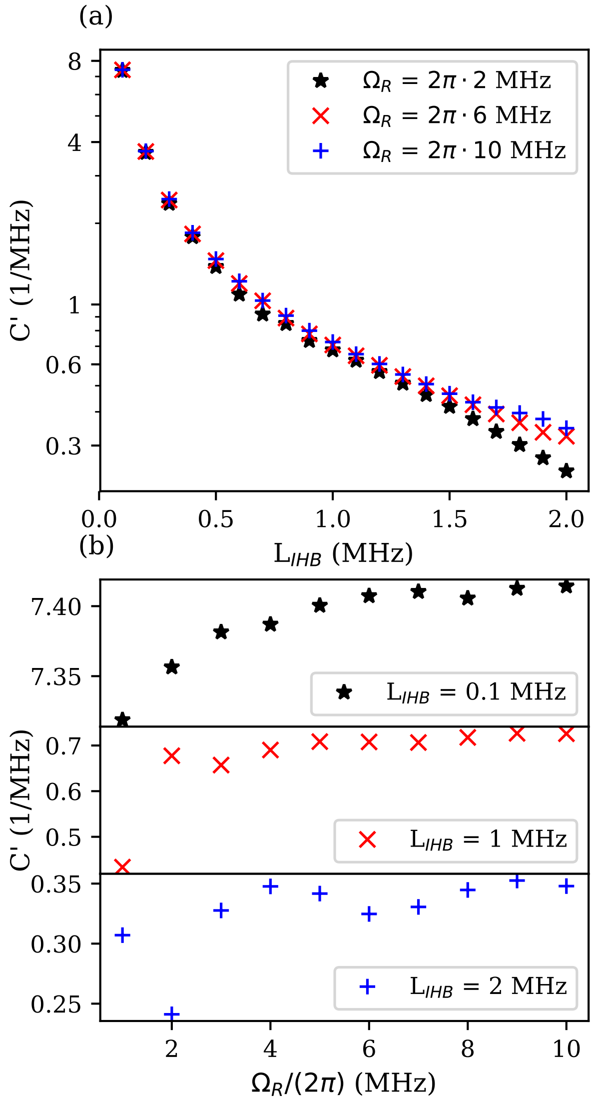

FIG. 6. Maximum achievable slope in normalized contrast for Ramsey interferometry with no drive amplitude variations or pure dephasing as a function of (a) inhomogeneous broadening with various Rabi frequencies and (b) Rabi frequency with various levels of inhomogeneous broadening.

Figure 6(a) shows the simulated C' as a function of inhomogeneous broadening for three different Rabi frequencies and Fig. 6(b) shows the simulated C' as a function of Rabi frequency for three different L_{IHB}-values, with L_{DAV}=0 (no drive amplitude variations) and no pure dephasing. The plots in Fig. 6(b) also include anomalous features where the slope decreases with increasing Rabi frequency. This arises because for each value of Ω_R and L_{IHB}, we calculate the drive detuning that yields the maximum q, rather than maximizing C' directly. As outlined in *Methods*, this is to maximize fringe visibility to remain in the regime where we are performing genuine Ramsey interferometry. If this were not the case, the optimization routine might, for example, find the maximum C' for zero or near-zero precession time τ, which would be indistinguishable from the π-pulse scheme. The result of the method we choose is that the optimized drive detuning between values of Ω_R or L_{IHB} may reach different local maxima in q, leading to a step change in C' between adjacent points. This can lead to the anomalies we observe.

Two aspects are clear from the data shown in Fig. 6(a). First, the achievable slope C' in the Ramsey scheme decreases in a pseudo-exponential fashion with increasing inhomogeneous broadening. This indicates a lower sensitivity for all schemes with higher inhomogeneous broadening. As discussed above, this is what would be expected based on the observed effect of inhomogeneous broadening, acting to reduce the fringe visibility and number as illustrated in Fig. 3. Secondly, the achievable slope increases only slightly with increasing Rabi frequency, particularly at low inhomogeneous broadening. This result is somewhat surprising, as it would be expected that by increasing the microwave power supplied using a pulsed scheme resistant to power broadening, the microwave resonance should be better defined, increasing contrast C and C'.

The slight increase can be attributed to the relationship between Rabi frequency and $\pi/2$-pulse performance. As Rabi frequency is increased, the $\pi/2$-pulses will be able to perform well for NV center spins with larger detuning from the driving frequency. However, once the pulses are able to perform well for most or all of the target ensemble, increasing the Rabi frequency further does not significantly improve the overall pulse performance and thus does not significantly improve the achievable slope. The point where the $\pi/2$-pulses are able to affect most of the ensemble correctly naturally occurs at a lower Rabi frequency for ensembles with lower levels of inhomogeneous broadening.

This result implies that for sensing experiments using the Ramsey scheme, increasing microwave amplification or enhancing antenna design to achieve a higher Rabi frequency will not necessarily lead to significant enhancement in sensitivity. This is an important result for both benchtop systems aiming for state of the art sensitivity and for systems with low Rabi frequency, such as microfabricated NV sensors with low available microwave power [32, 33]. For a high quality diamond with low $L_{IHB} = 0.1$ MHz, an increase in Rabi frequency from 1 MHz to 10 MHz only increases the slope C' by a factor of $\approx 1.3\%$, see Fig. 6. In our zero noise model, this corresponds to the same factor of enhancement in sensitivity to any target parameter using this scheme.

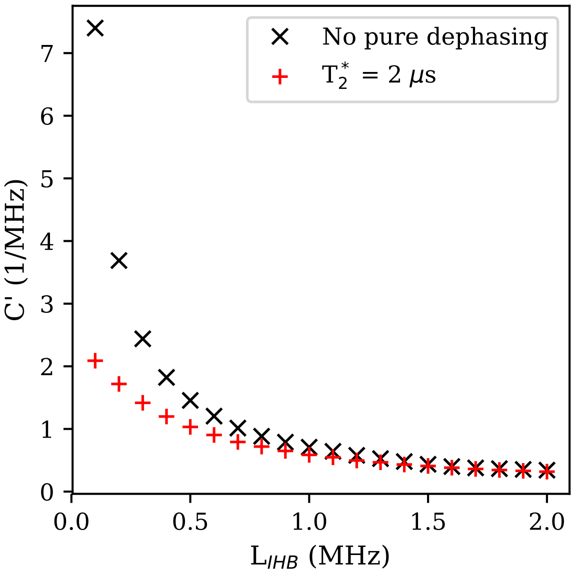

FIG. 7. Maximum achievable slope in normalized contrast as a function of inhomogeneous broadening for Ramsey measurements with $\Omega_R = 2\pi \cdot 5$ MHz with and without pure dephasing. The indicated T_2^*-value is the one induced by pure dephasing alone.

We also simulate the introduction of pure dephasing, which additionally acts to reduce the Ramsey fringe visibility. This has an effect very similar to that of inhomogeneous broadening (Fig. 4), with a decay in normalized contrast. The limit on interferometry performance will therefore depend on both pure dephasing and inhomogeneous broadening and their relative strengths defined by T_2^* and L_{IHB}, respectively. We illustrate this in Fig. 7 where the simulated C' as a function of inhomogeneous broadening is plotted with and without pure dephasing.

The difference between the slopes obtained decreases with higher inhomogeneous broadening. In the regime of large values of L_{IHB}, the maximum achievable slope is limited by the inhomogeneous broadening. For low values of L_{IHB}, the maximum C' is constrained by pure dephasing. This implies that even if long T_2^* times are achieved, as is often sought in sensing experiments through well designed pulsed protocols, the inhomogeneous broadening will still act to ultimately constrain the maximum sensitivity of the Ramsey scheme, and that increasing the Rabi frequency (through increasing the MW power) of the MW pulses will not necessarily overcome this issue. This highlights the critical importance of material (diamond) design to minimize IHB (e.g. by minimizing inhomogeneous non-NV diamond nitrogen content or minimizing material strain).

B. CW and π-pulse ODMR

Fig. 8 shows example simulated ODMR spectra in terms of normalized ensemble contrast C as a function of microwave drive frequency ω_{MW} for CW and π-pulsed schemes. We show a single resonance feature corresponding to a single NV axis, split by 40 MHz by a simulated static magnetic field with a 1.4 mT amplitude along the NV axis. The parameters we use are $\Gamma_p = 2\pi \cdot 1$ MHz, $\Omega_R = 2\pi \cdot 2$ MHz for the CW simulation and $\Omega_R = 2\pi \cdot 2$ MHz for the π-pulse simulation. We plot the ideal spectra, with zero pure dephasing, inhomogeneous broadening and no MW drive amplitude variations. The π-pulse ODMR spectrum was obtained using a fixed π-pulse duration chosen to match the on-resonance frequency. This leads to oscillations in contrast as this fixed duration periodically matches different Rabi frequencies obtained at different driving frequencies. Examples of simulated spectra varying the above parameters are shown in the Supplementary Information.

We note that for CW and π-pulse ODMR, the relationship between slope C' and Rabi frequency is not straightforward and larger Rabi frequency can result in lower slope. This is due to the fact that while larger Rabi frequency will result in larger achievable ODMR contrast, which serves to increase the slope, the additional microwave power necessary to achieve it will broaden the NV resonance linewidths, which acts to decrease the slope C'. The inverse is also true for green laser intensity/pumping rate, where resonance linewidth can narrow with higher laser intensity [23, 34]. For the ODMR simulations, we thus individually optimize the Rabi frequency and the green pumping rate to yield the maximum slope for each L_{IHB} and L_{DAV}.

C. Scheme comparison

We compare the maximum sensitivity for the Ramsey interferometry, CW and π-pulse ODMR sensing schemes. Again, we assume zero noise such that the sensitivity is directly proportional to the ensemble response via slope C'. For simplicity of comparison, we compare the best possible Ramsey interferometry simulations using $\Omega_R = 2\pi \cdot 10$ MHz with the other two schemes. We consider that $\Omega_R = 2\pi \cdot 10$ MHz is a reasonable upper limit that can be achieved experimentally [35, 36].

We first consider only the effects of inhomogenous broadening, while neglecting drive amplitude variations and pure dephasing. Figure 9(a) shows the resulting simulated maximum slope as a function of L_{IHB} for Ramsey interferometry, CW ODMR and π-pulse ODMR while neglecting drive amplitude variations and pure dephasing. The obtained optimal Rabi frequencies for CW and π-pulse ODMR were below $2\pi \cdot 3$ MHz in all cases. For ease of comparison, the ratios between the obtained ODMR slopes and the obtained Ramsey interferometry slopes are shown in Fig. 9(b) with a horizontal line at unity, i.e. equal performance.

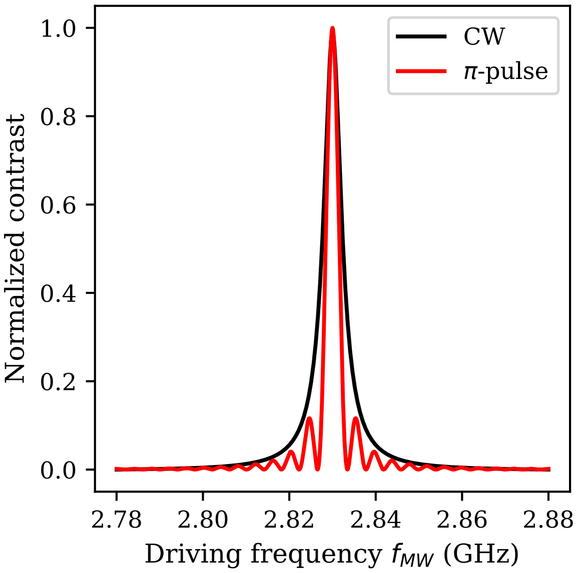

FIG. 8. Normalized contrast values for a simulated CW ODMR spectrum for $\Gamma_p = 2\pi \cdot 1$ MHz, $\Omega_R = 2\pi \cdot 2$ MHz and a simulated π-pulse ODMR spectrum for $\Omega_R = 2\pi \cdot 2$ MHz with zero inhomogeneous broadening, no pure dephasing and no MW drive amplitude variations using the five-level model.

The plots in Fig. 9 illustrate how the achievable slope decreases with increasing inhomogeneous broadening for all three techniques, but the decrease is most significant in the low IHB regime (< 0.2 MHz) for Ramsey interferometry. As can be seen in Fig. 9(b), the simulations predict a larger C' and hence greater achievable sensitivity for $\pi-$pulse ODMR than Ramsey interferometry when $L_{IHB} \geq 0.3$ MHz. Given that π-pulse ODMR is no more complicated to implement than Ramsey interferometry, this indicates that π-pulse ODMR should be the preferred protocol when the inhomogeneous broadening is in this regime. For $L_{IHB} < 0.3$ MHz, the simulations predict the largest slope for Ramsey interferometry, indicating that one can gain sensitivity by implementing Ramsey interferometry in this regime. The CW ODMR simulations at best predict a slope that is close to 80% of the Ramsey interferometry slope predicted for the same L_{IHB}.

The plots in Fig. 9(b) also include several anomalous features such as the ratio decreasing with increasing L_{IHB} at several points and oscillations in the data for increasing L_{IHB}. As previously detailed, these arise due to the chosen method of optimizing the drive detuning. We can also perform this optimization directly in terms of C' only, from which the same overall trends can be observed. This data can be seen in the Supplementary information.

Having investigated the behavior of the three sensing

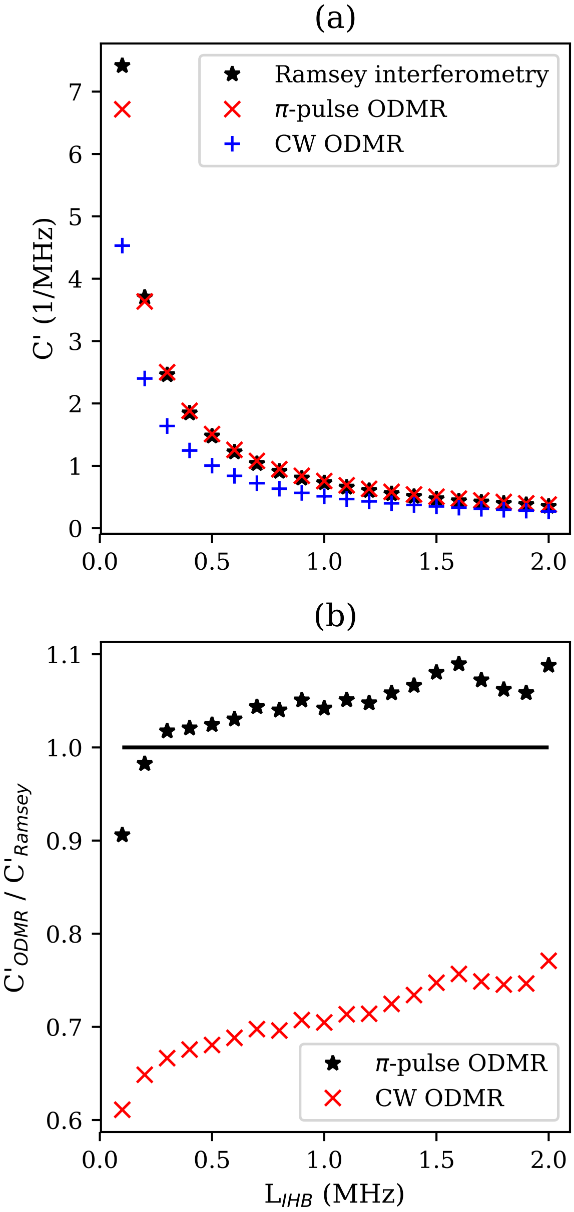

FIG. 9. a) Maximum achievable slope in normalized contrast as a function of inhomogeneous broadening for Ramsey measurements with $\Omega_R = 2\pi \cdot 10$ MHz, optimized CW ODMR and optimized π-pulse ODMR. All values were obtained while neglecting drive amplitude variations and pure dephasing. b) Ratios between the ODMR and Ramsey interferometry slopes shown in a).

schemes in the absence of variations in microwave drive across the ensemble, we then perform the same comparison with finite drive amplitude variation L_{DAV}. Figure 10 shows plots of the ratio between the simulated maximum achievable slope for (a) CW ODMR and (b) π-pulse ODMR and Ramsey interferometry as a function of L_{IHB} for MW drive amplitude variations between 10% and 90% (L_{DAV} = 0.1-0.). Here we see that increasing the level of MW drive amplitude variation increases the performance (higher C') of CW and π-pulse ODMR relative to Ramsey interferometry. For π-pulse ODMR, this effect is relatively small, with the same distinction in performance above and below L_{IHB} = 0.3 MHz as simulated in Fig. 9. However, the effect is far more pronounced for CW. When the MW drive amplitude variations exceed 50%, CW starts to outperform Ramsey measurements at large levels of inhomogeneous broadening. As the MW drive amplitude variations increase further, CW will outperform Ramsey at smaller and smaller levels of inhomogeneous broadening, eventually becoming preferable for nearly all levels of inhomogeneous broadening. For MW drive amplitude variations of around 80% or larger, CW ODMR also outperforms π-pulse ODMR, as evidenced by achieving a larger ratio to the Ramsey measurement slopes. This is a surprising result, as pulsed readout schemes are usually assumed to offer better sensitivity (which is true in the limit of pure dephasing) [19]. Here we instead show there can be regimes where sensitivity is greater for a continuous wave scheme than for the pulsed alternatives when other factors are considered.

We account for this result as arising due to the pulsed schemes being more adversely affected by MW drive amplitude variations. These schemes rely on the precise application of π and $\pi/2$ pulses of the correct length for the maximum number of NV center spins in an ensemble. By increasing the variation in drive amplitude across the sample, this condition is no longer met for an increasingly large fraction of NV center spins. This leads to a reduction in both contrast and slope through broadening effects associated with incorrect length pulse application [12]. For CW, this problem is less apparent as the states of the defect centers are continuously driven between the $m_S = 0$ to $m_S = \pm 1$ levels, maintaining contrast as long as there is sufficient pump laser power to maintain spin polarization in the system.

We consider this result to be particularly relevant for sensing schemes where such a wide variation in drive amplitude may occur. This includes two particular scenarios: 1) where the diamond is relatively large with respect to an antenna and the field of view of fluorescence collection is large and 2) where the microwaves are particularly localized to maximize contrast in a particular region. The first such scenario describes widefield imaging with NV centres, where there can be considerable variation in drive frequency across a diamond [37, 38]. The second may describe a confocal experiment, using lithographically patterned microwave antennas.

Elements of both scenarios cover sensing experiments looking at nanodiamonds, for example for temperature sensing in biological tissue [39]. Here both L_{DAV} and L_{IHB} can be high due to variations in microwave drive if looking at multiple diamonds across a large single field of view and due to large differences in IHB between very few NV centers within each diamond, with considerable effects of crystal strain and surface interaction due to

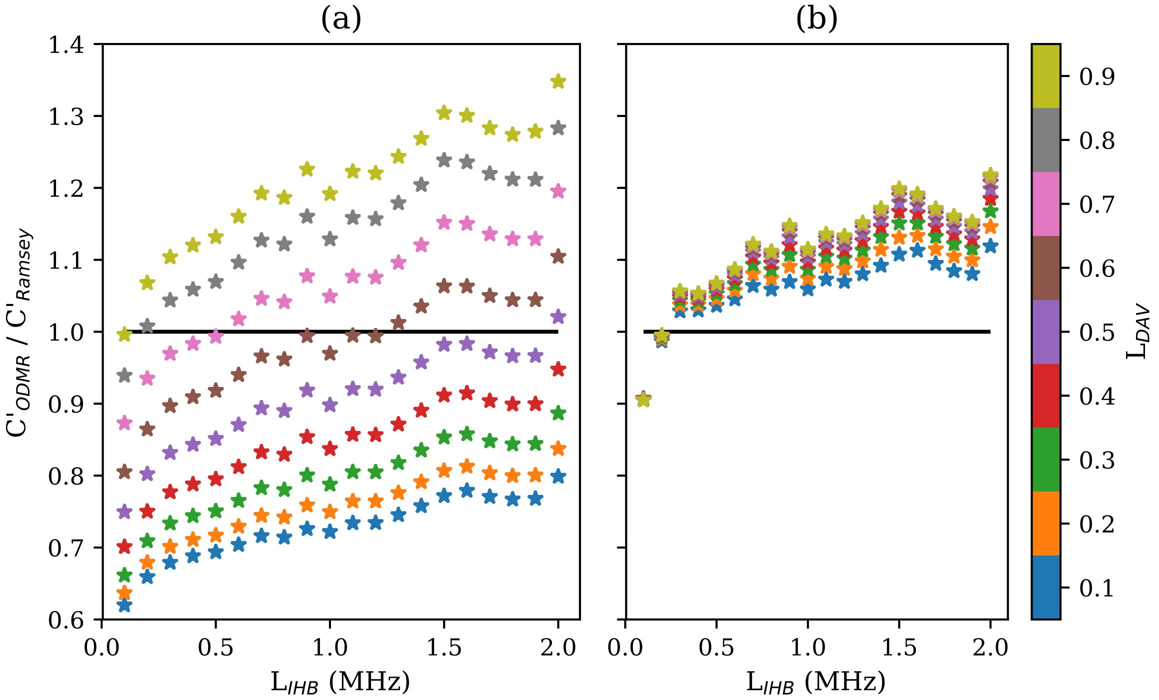

FIG. 10. Ratio between the maximum achievable slope in normalized contrast for (a) optimized CW ODMR or (b) optimized π-pulse ODMR and Ramsey measurements with $\Omega_R = 2\pi \cdot 10$ MHz as a function of inhomogeneous broadening for varying levels of MW drive amplitude variations.

their small form factor [40].

Finally, we seek to perform our simulations using experimental data from a real diamond sample, to estimate the optimal sensing scheme for a real diamond. We achieve this through widefield CW ODMR imaging to extract the variation in zero offset magnetic field microwave resonance frequency across a $10{\times}10$ μm^2 region of a diamond. We use a chemical vapor deposition (CVD) diamond overgrown with ^{15}N with ^{12}C purification. The procedures and diamond details we use for the measurement are the same as given in [41]. As this region is significantly smaller than our nearfield antenna, we assume that across the field of view we image there is a homogeneous microwave field, with minimal variation in microwave drive amplitude. We therefore assume that all of the variation we observe is due to inhomogenous broadening as our input δ_i-distribution. This experimental distribution can be seen in Appendix A. Figure 11 shows the simulated ratios between the maximum achievable slope in normalized contrast for optimized CW or π-pulse ODMR and Ramsey interferometry as a function of the Rabi frequency Ω_R used for Ramsey interferometry with three different values of L_{DAV}. We calculate π-pulse ODMR to be the best possible scheme for all values of microwave drive variation, particularly in the low microwave power (low Rabi frequency) regime. Our simulations also suggest that in this regime, CW ODMR is close to outperforming the sensitivity of the Ramsey

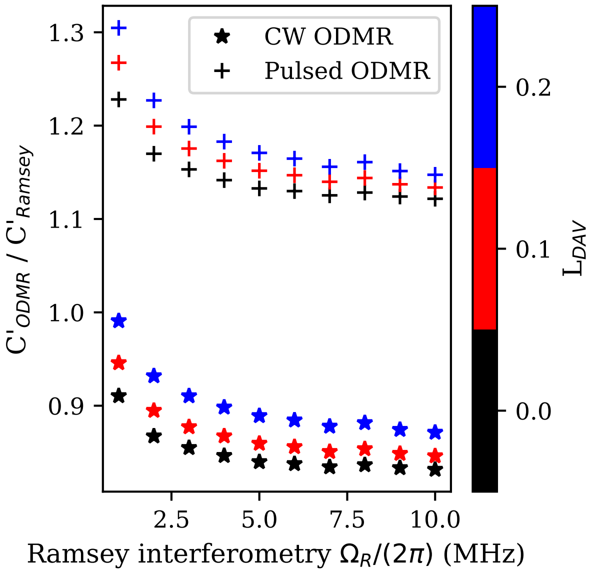

FIG. 11. Ratio between the maximum achievable slope in normalized contrast for optimized CW or π-pulse ODMR and Ramsey measurements as a function of the Ramsey interferometry Ω_R for a measured δ_i-distribution with varying levels of MW drive amplitude variations.

scheme. This diamond has recently been used for CW ODMR sensing of electrical current [41], but we do not presently have the capability to perform pulsed sensing using it. We also note that other factors such as readout noise and measurement time can play a role in a real experiment. Here we aim only to maximize the response of the sensing medium (the NV ensemble) in terms of maximizing the change in fluorescence output (slope C') in response to a target factor (e.g. magnetic field or temperature).

IV. CONCLUSION

In this work, we compared Ramsey interferometry, π-pulse ODMR and CW ODMR sensing schemes using nitrogen-vacancy centers and investigated the impact of inhomogeneous broadening and MW drive amplitude variations. We demonstrate that the achievable response of the sensing ensemble in terms of the contrast slope C', which is directly proportional to sensitivity, plateaus with increasing Rabi frequency for Ramsey interferometry. The performance of Ramsey interferometry can therefore not necessarily be improved simply by increasing the MW power. This is of considerable interest for realization of devices with low available power, such as microfabricated sensors with integrated semiconductor amplification, where significant MW amplification is not easy to realize due to e.g. heat dissipation concerns.

We demonstrate that when the inhomogeneous broadening exceeds 0.3 MHz, π-pulse ODMR yields a larger C' than Ramsey interferometry, indicating that π-pulse ODMR gives higher sensitivity in this regime. This indicates that Ramsey interferometry should only be considered when using a high-quality diamond with low inhomogeneous broadening, such as in low impurity samples with a relatively low nitrogen content [20, 42].

The influence of MW drive amplitude variations is demonstrated to significantly improve the relative performance of CW ODMR compared to pulsed sensing schemes and π-pulse ODMR. For MW drive amplitude variations of around 80% or larger, CW ODMR can outperform both Ramsey interferometry and pulsed ODMR for even a low level of inhomogeneous broadening. These results are of particular significance to applications that naturally have high levels of drive field variation, such as wide field of view NV center imaging [37, 38] or imaging of microwave frequency microcircuitry [41].

Finally, we apply our simulation to measurements from a real diamond, recently used for CW imaging [41]. Our calculations predict that sensitivity could be improved by switching to a π-pulse sensing scheme. We however note that other factors beyond the scope of this work may limit sensitivity and these may vary between the schemes considered. In particular, in this work we only consider the maximal response of the sensing medium. We do not consider noise, arising from electronic or optical sources, or errors in pulse application. Further investigation beyond the scope of this work is required to fully examine these aspects before confirmation of our prediction.

Our results represent an important step towards a greater understanding of the relation between sensor material properties, sensing regime and the ideal sensing scheme. We consider our results of particular interest to groups working with DC to low-frequency magnetometry and temperature sensing, particularly from biosamples, using diamonds both off-the-shelf or irradiated where low inhomogeneous broadening cannot be guaranteed.

A. MEASURED δ_i-DISTRIBUTION

Plot of the experimentally measured δ_i-distribution used for the simulations in Fig. 11. The distribution was measured on a CVD diamond overgrown with ^{15}N without isotopic purification.

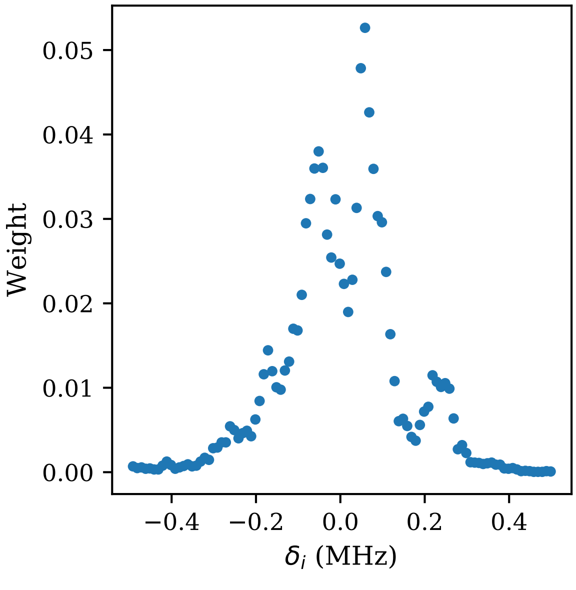

FIG. 12. Experimentally measured δ_i-distribution from a CVD diamond overgrown with ^{15}N without isotopic purification. The distribution was used for the simulations in Fig. 11.

---

[1] T. Schröder, S. L. Mouradian, J. Zheng, M. E. Trusheim, M. Walsh, E. H. Chen, L. Li, I. Bayn, and D. Englund. Quantum nanophotonics in diamond. *J. Opt. Soc. Am. B*, 33(4):B65–B83, 2016.

[2] I. Aharonovich, D. Englund, and M. Toth. Solid-state single-photon emitters. *Nat. Phot.*, 10(10):631–641, 2016.

[3] G. Kucsko, P. C. Maurer, N. Y. Yao, M. Kubo, H. J. Noh, P. K. Lo, H. Park, and M. D. Lukin. Nanometre-scale thermometry in a living cell. *Nature*, 500(7460):54–58, 2013.

[4] R. Schirhagl, K. Chang, M. Loretz, and C. L. Degen. Nitrogen-Vacancy Centers in Diamond: Nanoscale Sensors for Physics and Biology. *Annu. Rev. Phys. Chem.*, 65(1):83–105, 2014.

[5] J. H. N. Loubser and J. A. Van Wyk. Electron spin resonance in the study of diamond. *Rep. Prog. Phys.*, 41(8):1201–1248, 1978.

[6] A. Gruber, A. Dräbenstedt, C. Tietz, L. Fleury, J. Wrachtrup, and C. von Borczyskowski. Scanning Confocal Optical Microscopy and Magnetic Resonance on Single Defect Centers. *Science*, 276(5321):2012–2014, 1997.

[7] F. Jelezko, T. Gaebel, I. Popa, A. Gruber, and J. Wrachtrup. Observation of Coherent Oscillations in a Single Electron Spin. *Phys. Rev. Lett.*, 92(7):1–4, 2004.

[8] P. Neumann et al. High-Precision Nanoscale Temperature Sensing Using Single Defects in Diamond. *Nano Lett.*, 13(6):2738–2742, 2013.

[9] T. Delord, L. Nicolas, M. Bodini, and G. Hétet. Diamonds levitating in a Paul trap under vacuum : Measurements of laser-induced heating via NV center thermometry. *Appl. Phys. Lett.*, 111(1):013101, 2017.

[10] M. W. Doherty et al. Electronic properties and metrology applications of the diamond nv$^-$ center under pressure. *Phys. Rev. Lett.*, 112(4):047601, 2014.

[11] F. Dolde, H. Fedder, M. W. Doherty, F. Rempp, G. Balasubramanian, F. Reinhard, F. Jelezko, and J. Wrachtrup. Sensing electric fields using single diamond spins. *Nat. Phys.*, 7(6):459–463, 2011.

[12] Z.-H. Wang, G. de Lange, D. Ristè, R. Hanson, and V. V. Dobrovitski. Comparison of dynamical decoupling protocols for a nitrogen-vacancy center in diamond. *Phys. Rev. B*, 85(15):155204, 2012.

[13] J. M. Taylor, P. Cappellaro, L. Childress, L. Jiang, D. Budker, P. R. Hemmer, A. Yacoby, R. Walsworth, and M. D. Lukin. High-sensitivity diamond magnetometer with nanoscale resolution. *Nat. Phys.*, 4(10):810–816, 2008.

[14] D. Farfurnik, A. Jarmola, L. M. Pham, Z. H. Wang, V. V. Dobrovitski, R. L. Walsworth, D. Budker, and N. Bar-Gill. Improving the coherence properties of solid-state spin ensembles via optimized dynamical decoupling. *Proc. SPIE*, 9900:99000N, 2016.

[15] D. Farfurnik, A. Jarmola, D. Budker, and N. Bar-Gill. Spin ensemble-based AC magnetometry using concatenated dynamical decoupling at low temperatures. *J. Opt. (United Kingdom)*, 20(2):024008, 2018.

[16] G. T. Genov, Y. Ben-Shalom, F. Jelezko, A. Retzker, and N. Bar-Gill. Efficient and robust signal sensing by sequences of adiabatic chirped pulses. *Phys. Rev. Res.*, 2(3):033216, aug 2020.

[17] F. Jelezko and J. Wrachtrup. Single defect centres in diamond: A review. *Physica Status Solidi A*, 203(13):3207–3225, 2006.

[18] Y. Zhang, Z. Li, Y. Feng, H. Guo, H. Wen, J. Tang, and J. Liu. High-sensitivity DC magnetic field detection with ensemble NV centers by pulsed quantum filtering technology. *Opt. Express*, 28(11):16191, 2020.

[19] A. Dréau, M. Lesik, L. Rondin, P. Spinicelli, O. Arcizet, J. F. Roch, and V. Jacques. Avoiding power broadening in optically detected magnetic resonance of single NV defects for enhanced dc magnetic field sensitivity. *Phys. Rev. B*, 84(19):1–8, 2011.

[20] T. Wolf, P. Neumann, K. Nakamura, H. Sumiya, T. Ohshima, J. Isoya, and J. Wrachtrup. Subpicotesla diamond magnetometry. *Phys. Rev. X*, 5(4):1–10, 2015.

[21] L. Rondin, J.-P. Tetienne, T. Hingant, J.-F. Roch, P. Maletinsky, and V. Jacques. Magnetometry with nitrogen-vacancy defects in diamond. *Rep. Prog. Phys.*, 77(5):056503, 2014.

[22] S. Hong, M. Grinolds, L. Pham, D. Sage, L. Luan, R. Walsworth, and A. Yacoby. Nanoscale magnetometry with nv centers in diamond. *MRS Bulletin*, 38:155–161, 2013.

[23] J. F. Barry, J. M. Schloss, E. Bauch, M. J. Turner, C. A. Hart, L. M. Pham, and R. L. Walsworth. Sensitivity Optimization for NV-Diamond Magnetometry. *Rev. Mod. Phys.*, 92(1):015004, 2020.

[24] I. Fescenko, A. Jarmola, I. Savukov, P. Kehayias, J. Smits, J. Damron, N. Ristoff, N. Mosavian, and V. M. Acosta. Diamond magnetometer enhanced by ferrite flux concentrators. *Phys. Rev. Res.*, 2(2):023394, 2020.

[25] A. Laraoui, J. S. Hodges, and C. A. Meriles. Magnetometry of random ac magnetic fields using a single nitrogen-vacancy center. *Appl. Phys. Lett.*, 97(14):143104, 2010.

[26] A. Laraoui, J. S. Hodges, C. A. Ryan, and C. A. Meriles. Diamond nitrogen-vacancy center as a probe of random fluctuations in a nuclear spin ensemble. *Phys. Rev. B*, 84(10):104301, 2011.

[27] J. F. Barry, M. J. Turner, J. M. Schloss, D. R. Glenn, Y. Song, M. D. Lukin, H. Park, and R. L. Walsworth. Optical magnetic detection of single-neuron action potentials using quantum defects in diamond. *Proc. Nat. Acad. Sci. USA*, 113(49):14133–14138, 2016.

[28] M. Fujiwara et al. Real-time nanodiamond thermometry probing in vivo thermogenic responses. *Sci. Adv.*, 6(37):9636, 2020.

[29] A. F. L. Poulsen, J. D. Clement, J. L. Webb, R. H. Jensen, K. Berg-Sørensen, A. Huck, and U. L. Andersen. Optimal control of a nitrogen-vacancy spin ensemble in diamond for sensing in the pulsed domain. *arXiv:2101.10049*, 2021.

[30] S. Ahmadi, H. A. R. El-Ella, J. O. B. Hansen, A. Huck, and U. L. Andersen. Pump-Enhanced Continuous-Wave Magnetometry using Nitrogen-Vacancy Ensembles. *Phys. Rev. Applied*, 8(3):034001, 2017.

[31] S. Ahmadi, H. A. R. El-Ella, J. O. B. Hansen, A. Huck, and U. L. Andersen. Supplementary for "Pump-Enhanced Continuous-Wave Magnetometry using Nitrogen-Vacancy Ensembles". *Phys. Rev. Applied*, 8(3):034001, 2017.

[32] M. Zhu, J. Li, M. Toda, and T. Ono. Microfabrication of a scanning probe with nv centers in a selectively grown diamond thin film through a xenon difluoride etching process. *J. Micromech. Microeng.*, 27:125007, 2017.

[33] S. Mi, M. Kiss, T. Graziosi, and N. Quack. Integrated photonic devices in single crystal diamond. *J. Phys. Photonics*, 2(4):042001, 2020.

[34] Z. Rui, Z. Binbin, W. Lei, G. Hao, T. Jun, and L. Jun. Optimization method of the limit sensitivity for the diamond nv color center magnetometer. *Micronanoelectronic Technology*, 55(9):683–699, 2018.

[35] T. Nöbauer, A. Angerer, B. Bartels, M. Trupke, S. Rotter, J. Schmiedmayer, F. Mintert, and J. Majer. Smooth Optimal Quantum Control for Robust Solid-State Spin Magnetometry. *Phys. Rev. Lett.*, 115(19):190801, 2015.

[36] P. Rembold, N. Oshnik, M. M. Müller, S. Montangero, T. Calarco, and E. Neu. Introduction to quantum optimal control for quantum sensing with nitrogen-vacancy centers in diamond. *AVS Quant. Sci.*, 2(2):024701, 2020.

[37] K. Mizuno, M. Nakajima, H. Ishiwata, Y. Masuyama, T. Iwasaki, and M. Hatano. Wide-field diamond magnetometry with millihertz frequency resolution and nanotesla sensitivity. *Aip Advances*, 8(12):125316, 2018.

[38] D. J. McCloskey, N. Dontschuk, D. A. Broadway, A. Nadarajah, A. Stacey, J.-P. Tetienne, L. C. L. Hollenberg, S. Prawer, and D. A. Simpson. Enhanced widefield quantum sensing with nitrogen-vacancy ensembles using diamond nanopillar arrays. *arXiv:1902.02464*, 2019.

[39] D. A. Simpson, E. Morrisroe, J. M. McCoey, A. H. Lombard, D. C. Mendis, F. Treussart, L. T. Hall, S. Petrou, and L. C. L. Hollenberg. Non-neurotoxic nanodiamond probes for intraneuronal temperature mapping. *Acs Nano*, 11(12):12077–12086, 2017.

[40] A. I. Shames, V. Y. Osipov, J. P. Boudou, A. M. Panich, H. J. Von Bardeleben, F. Treussart, and A. Y. Vul'. Magnetic resonance tracking of fluorescent nanodiamond fabrication. *J. Phys. D: Appl. Phys.*, 48(15):155302, 2015.

[41] J. L. Webb, L. Troise, N. W. hansen, L. F. Frellsen, C. Osterkamp, F. Jelezko, S. Jankuhn, J. Meijer, K. Berg-Sørensen, J.-F. Perrier, A. Huck, and U. L. Andersen. High-speed microcircuit and synthetic biosignal widefield imaging using nitrogen vacancies in diamond. *arXiv:2107.14156*, 2021.

[42] C. Zhang, M. Shagieva, F. Widmann, M. Kuebler, V. Vorobyov, P. Kapitanova, E. Nenasheva, R. Corkill, O. Rohrle, K. Nakamura, H. Sumiya, S. Onoda, J. Isoya, and J. Wrachtrup. Diamond magnetometry and gradiometrty towards subpicotesla dc field measurement. *Phys. Rev. Appl.*, 15(6):20, 2021.

5.3 Supplementary information

Supplementary Information: Investigation and comparison of measurement schemes in the low frequency biosensing regime using solid-state defect centers

Andreas F.L. Poulsen,[1] James L. Webb,[1, a)] Kirstine Berg-Sørensen,[2] Ulrik Lund Andersen,[1, b)] and Alexander Huck[1, c)]

[1)] *Center for Macroscopic Quantum States (bigQ), Department of Physics, Technical University of Denmark, 2800 Kongens Lyngby, Denmark*

[2)] *Department of Health Technology, Technical University of Denmark, 2800 Kongens Lyngby, Denmark*

[a)] Electronic mail: jaluwe@fysik.dtu.dk

[b)] Electronic mail: ulrik.andersen@fysik.dtu.dk

[c)] Electronic mail: alexander.huck@fysik.dtu.dk

I. EXAMPLE RAMSEY SIMULATIONS

Shown here are four of the individual Ramsey simulations used to obtain the q-values plotted in Fig. 5 in the main article. All of the simulations were performed without pure dephasing or drive amplitude variations. The individual simulations were made using (a) drive detuning (DD) equal to 0.3 MHz and $L_{IHB} = 0.1$ MHz, (b) DD $= 1.8$ MHz and $L_{IHB} = 0.1$ MHz, (c) DD $= 1.8$ MHz and $L_{IHB} = 1$ MHz and (d) DD $= 3.9$ MHz and $L_{IHB} = 0.6$ MHz.

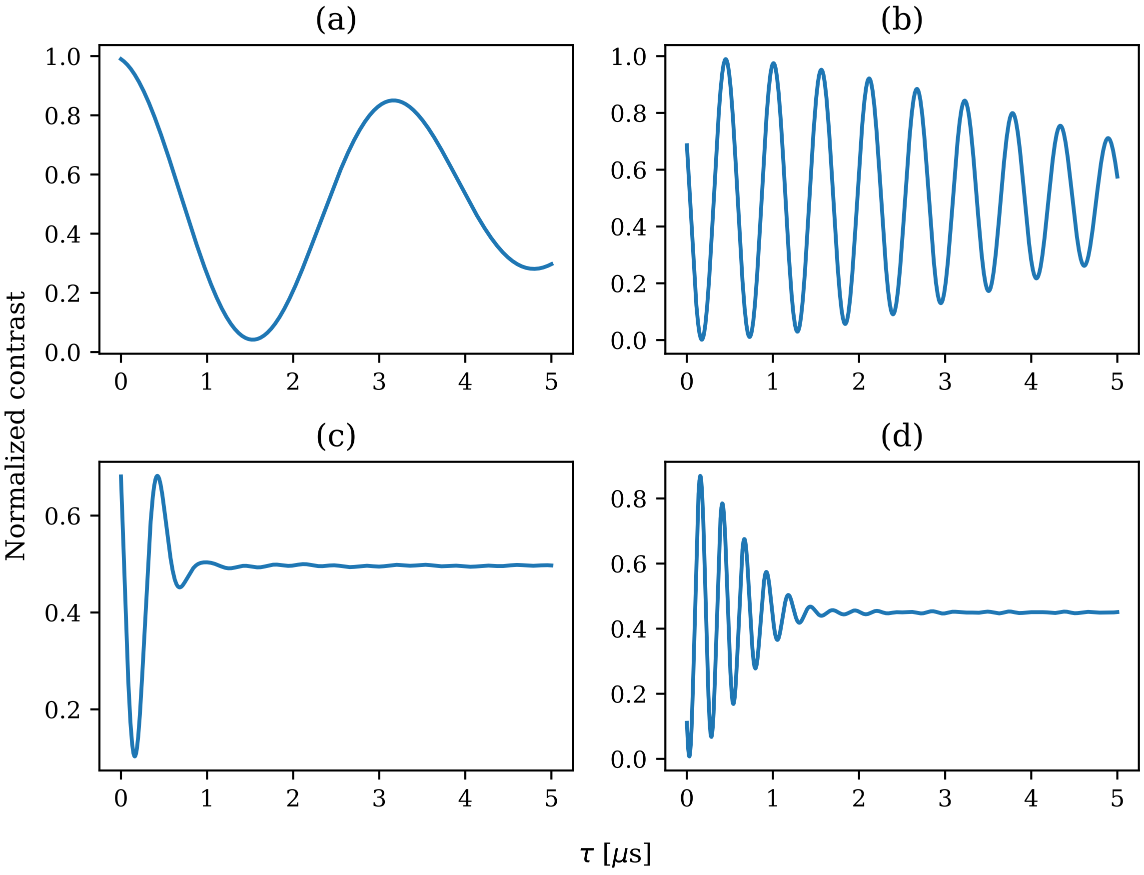

FIG. 1: Simulations of the Ramsey interferometry contrast C as a function of the free precession time τ with no pure dephasing or drive amplitude variations. The parameters were (a) DD $= 0.3$ MHz and $L_{IHB} = 0.1$ MHz, (b) DD $= 1.8$ MHz and $L_{IHB} = 0.1$ MHz, (c) DD $= 1.8$ MHz and $L_{IHB} = 1$ MHz and (d) DD $= 3.9$ MHz and $L_{IHB} = 0.6$ MHz.

II. CW AND π-PULSE ODMR WITH VARYING PARAMETERS

Below are shown three plots illustrating the effect of varying the optical pumping rate Γ_p and the Rabi frequency Ω_R for the CW and π-pulse ODMR simulations. All simulations show a single resonance feature corresponding to a single NV axis, split by 40 MHz by a simulated static magnetic field with a 1.4 mT amplitude along the NV axis. The plotted spectra are ideal, with zero pure dephasing, inhomogeneous broadening and no MW drive amplitude variations. Figure 2 shows CW ODMR spectra for $\Gamma_p = 2\pi \cdot 1\,\text{MHz}$ and three values of Ω_R. As expected, increasing Ω_R increases the maximum contrast, but also power broadens the resonance feature. Conversely, decreasing Ω_R reduces the maximum contrast, but also narrows the resonance feature by reducing the effect of power broadening.

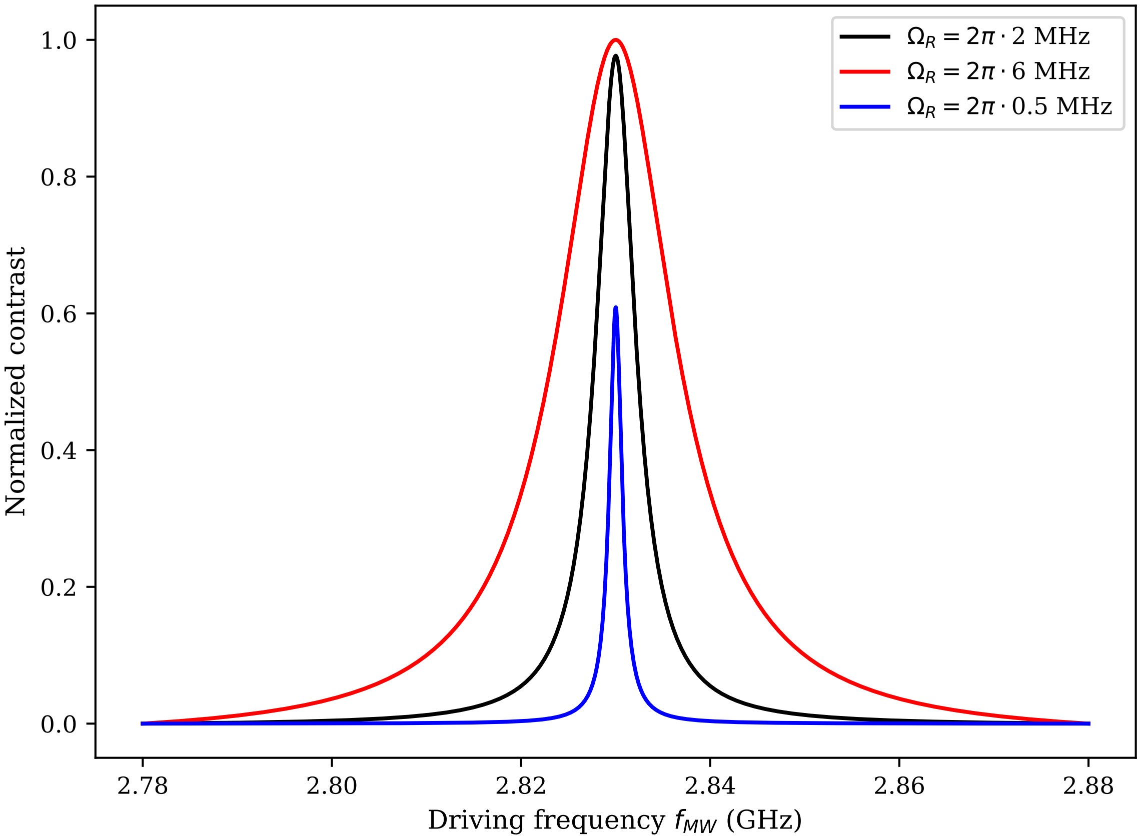

FIG. 2: Normalized contrast values for simulated CW ODMR spectra for $\Gamma_p = 2\pi \cdot 1\,\text{MHz}$ and the three indicated values of Ω_R with zero inhomogeneous broadening, no pure dephasing and no MW drive amplitude variations.

Figure 3 shows CW ODMR spectra for $\Omega_R = 2\,\text{MHz}$ and three different values of Γ_p. The behavior is as expected. Increasing the optical pumping rate Γ_p can lead to an increase in the absolute change in fluorescence at the resonance, but it also increases the background fluorescence such that the contrast might decrease. Conversely, decreasing the optical pumping rate Γ_p will decrease the background fluorescence, but it also decreases the rate of reinitialization, which leads to a lower absolute change in fluorescence at the resonance and potentially lower contrast.

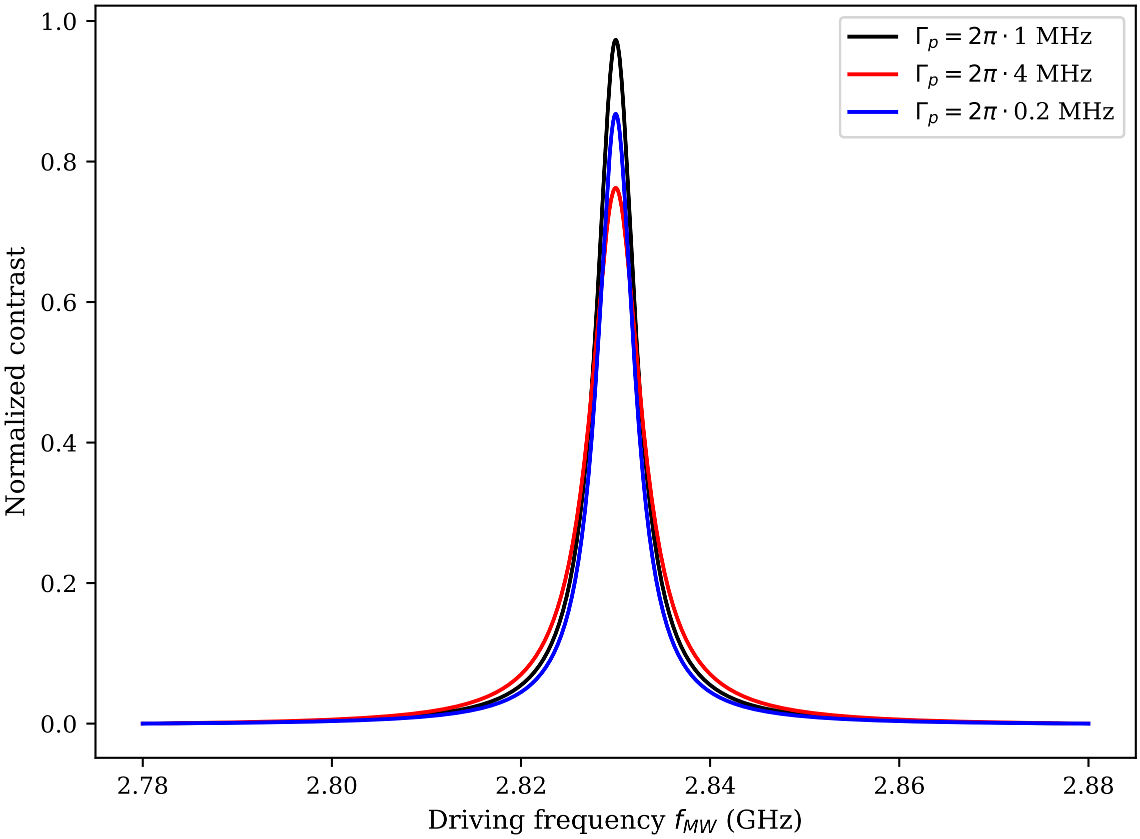

FIG. 3: Normalized contrast values for simulated CW ODMR spectra for $\Omega_R = 2\pi \cdot 2\,\text{MHz}$ and the three indicated values of Γ_p with zero inhomogeneous broadening, no pure dephasing and no MW drive amplitude variations.

Figure 4 shows π-pulsed ODMR spectra for three different values of Ω_R. As expected, these spectra also show a form of power broadening due to π-pulses with larger Rabi frequency being more robust against detuning, but the broadening is noticeably less significant than for CW ODMR. The decrease in maximum contrast with decreasing Ω_R is much less significant than for CW ODMR due to π-pulses being able to implement a π-flip for a single resonant NV very well, even at low Rabi frequencies. The duration of a π-pulse is, however, inversely proportional to the Rabi frequency.

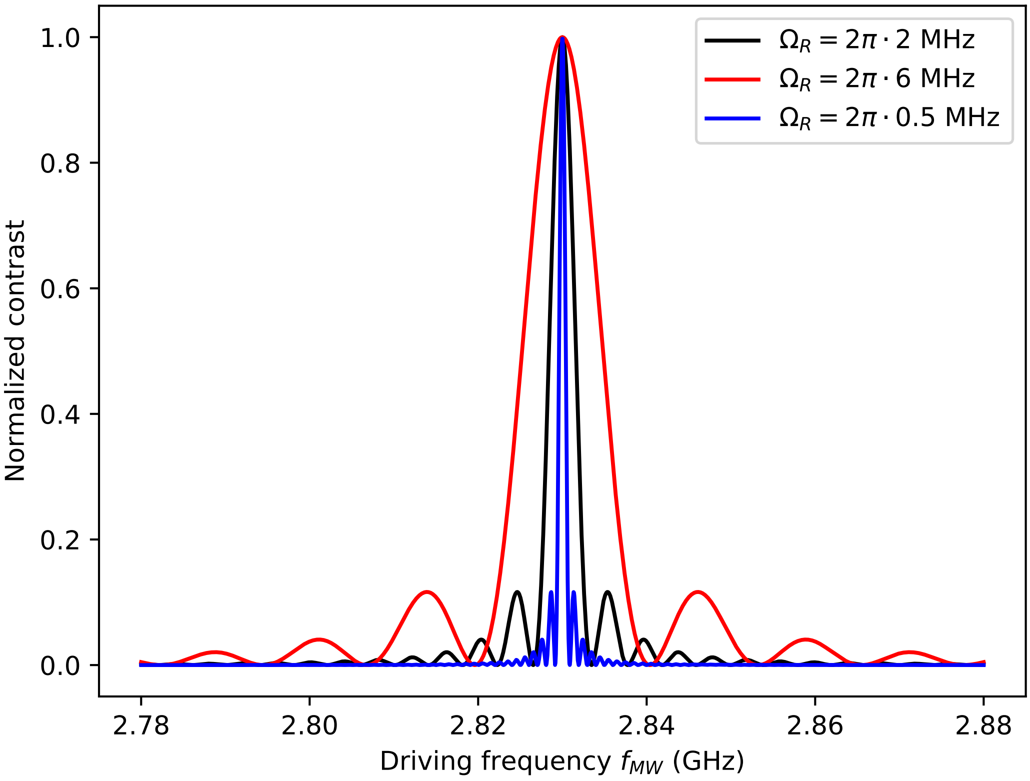

FIG. 4: Normalized contrast values for simulated π-pulse ODMR spectra for the three indicated values of Ω_R with zero inhomogeneous broadening, no pure dephasing and no MW drive amplitude variations.

III. SLOPE COMPARISON WITH SLOPE-OPTIMIZED RAMSEY DRIVE DETUNING

Here we show the version of Fig. 9 from the main article obtained when optimizing the Ramsey interferometry drive detuning directly for C'. The anomalous features observed in Fig. 9(b) in the main article are almost entirely gone and the ratios increase almost completely smoothly as a function of L_{IHB}. We observe the same overall trends as in Fig. 9 in the main article.

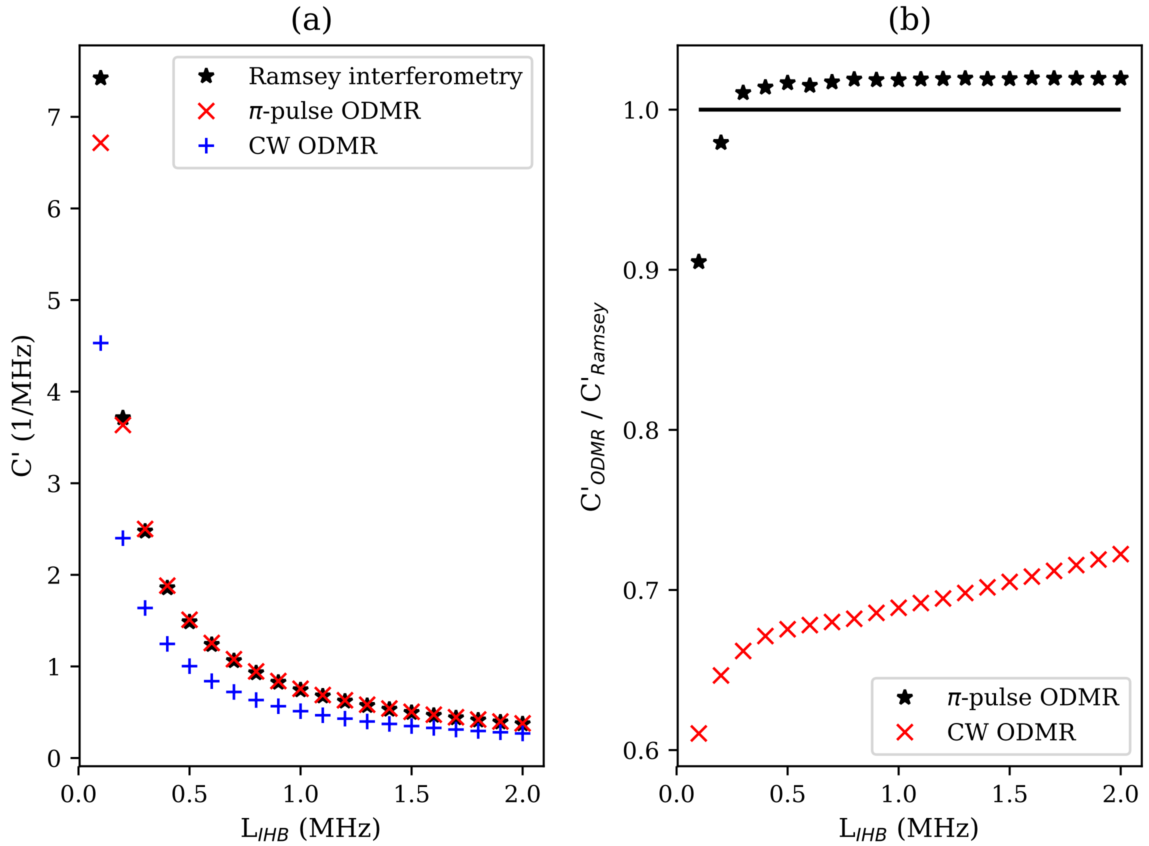

FIG. 5: a) Maximum achievable slope in normalized contrast as a function of inhomogeneous broadening for Ramsey measurements with $\Omega_R = 2\pi \cdot 10\,\text{MHz}$, optimized CW ODMR and optimized π-pulse ODMR. All values were obtained while neglecting drive amplitude variations and pure dephasing. The Ramsey measurement drive detuning values were obtained by optimizing directly for C'. b) Ratios between the ODMR and Ramsey interferometry slopes shown in a).

6 Conclusion and outlook

This thesis covers three projects, which are all devoted to the goal of improving the sensitivity of nitrogen-vacancy (NV) magnetometry. The ultimate goal of such improvements is to realize the many potential applications of the mechanically stable and chemically inert NV sensor, which can function under ambient conditions, but is limited by the currently achievable sensitivity. Said potential applications include and exceed those of other high-sensitivity quantum magnetometers like superconducting quantum interference devices (SQUID) and atomic-vapor magnetometers, which both suffer from limitations that do not affect NV magnetometers. The approach taken in the projects mainly involves attempts to optimize the utilization of the quantum properties of the NV center in order to boost the achievable sensitivity.

The first project focuses on the use of optimal control theory to design shaped microwave (MW) control pulses that are robust against the influence of inhomogeneous broadening and drive amplitude variations. The optimal control approach using smooth optimal control was expanded to include the effects of hyperfine splitting, such that shaped MW pulses capable of simultaneously driving all of the hyperfine transitions could be designed. Simulations of π-pulse ODMR with either a smooth optimal control pulse optimized for all of the hyperfine transitions or flat MW pulses were performed. The simulations predicted that a properly designed smooth optimal control pulse would yield major improvements in the ODMR slope compared to an equivalent flat single-frequency pulse and significant improvements compared to an equivalent flat three-frequency pulse. Experiments were performed in collaboration with another PhD student in order to verify the predictions. The experimental results yielded the same general trends as the simulations, although the exact numbers differed. An 11% increase in the maximum ODMR slope compared to the best equivalent flat three-frequency pulse was demonstrated experimentally. These results represent an important step in the direction of utilizing optimal control theory to improve the sensitivity of NV magnetometry schemes.

The experiments were performed using a setup that was not optimized for maximum sensitivity and thus serve mainly as a proof-of-principle. A relevant future step would then be to implement the smooth optimal control pulses in a top-of-the-line setup in order to push the limits of NV magnetic field sensing.

The second project focuses on the use of the green absorption by NV centers for laser threshold magnetometry as an alternative to the standard measuring of changes in the red fluorescence. A proposed setup where an NV diamond is included in an external cavity laser, and the change in green absorption caused by a shift from off- to on-resonance MW driving is used to push the setup across the lasing threshold was theoretically investigated. The investigation also considered the effect of spontaneous emission, which is typically neglected in similar proposals. The predicted sensitivities for optimal but realistic cavity and material parameters were found to be in the $\mathrm{pT}/\sqrt{\mathrm{Hz}}$ range. The approach thus represents a potential route to improved sensitivity compared to existing methods. However, the effect of amplified spontaneous emission near the lasing threshold, which reduces the sharp lasing cut-on to a gradual transition, significantly limits the achievable sensitivity. For large values of the spontaneous emission factor, the sensitivity can be reduced by up to two orders of magnitude compared to the situation without spontaneous emission. The suppression of spontaneous emission is thus an important consideration for laser threshold magnetometers.

The third project focuses on the theoretical investigation and comparison of CW ODMR, π-pulse ODMR and Ramsey interferometry for low-frequency sensing. The maximum achievable contrast slope (sensitivity) for each scheme was simulated and compared for different levels of inhomogeneous broadening and MW drive amplitude variations, with the goal of determining the optimal sensing scheme for different conditions. It was found that Ramsey interferometry was the most strongly impacted by inhomogeneous broadening and only yielded the largest contrast slope for low inhomogeneous broadening. CW ODMR was the least strongly impacted by drive amplitude variations and yielded the largest contrast slope for large drive amplitude variations. In the intermediate region where the inhomogeneous broadening is not low and the drive amplitude variations are not large, π-pulse ODMR was found to yield the largest contrast slope. The knowledge of which sensing scheme provides the best sensitivity for a given set of conditions can be used to more efficiently design and optimize setups and experiments, thereby paving the way for further sensitivity improvements.

Going forward, one could attempt to achieve further improvements of the sensitivity by combining aspects of the different projects. Optimal control theory could potentially be used to improve the sensitivity of the pulsed measurement schemes in the regimes where they are preferable. The laser threshold magnetometry setup could be considered for a π-pulse ODMR sensing scheme, which could be combined with optimal control theory to improve the performance. It would also be interesting to consider the potential of experimental optimization of the control pulses. This could be done by starting with an appropriate optimal control pulse and then making adjustments to the pulse parameters based on the experimental response to minor changes in said parameters, repeating the process until optimal experimental performance is achieved.

References

[1] R. Schirhagl, K. Chang, M. Loretz, and C. L. Degen. Nitrogen-Vacancy Centers in Diamond: Nanoscale Sensors for Physics and Biology. *Annu. Rev. Phys. Chem.*, 65(1):83–105, 2014.

[2] D. Le Sage, K. Arai, D. R. Glenn, S. J. DeVience, L. M. Pham, L. Rahn-Lee, M. D. Lukin, A. Yacoby, A. Komeili, and R. L. Walsworth. Optical magnetic imaging of living cells. *Nature*, 496(7446):486–489, 2013.

[3] J. F. Barry, M. J. Turner, J. M. Schloss, D. R. Glenn, Y. Song, M. D. Lukin, H. Park, and R. L. Walsworth. Optical magnetic detection of single-neuron action potentials using quantum defects in diamond. *Proc. Nat. Acad. Sci. USA*, 113(49):14133–14138, 2016.

[4] F. Gorrini, R. Giri, C. E. Avalos, S. Tambalo, S. Mannucci, L. Basso, and N. Bazzanella. Fast and sensitive detection of paramagnetic species using coupled charge and spin dynamics in strongly fluorescent nanodiamonds. *ACS Appl. Mat. & Interfaces*, 11(27):24412–24422, 2019.

[5] J. P. Wikswo, J. P. Barach, and J. A. Freeman. Magnetic field of a nerve impulse: first measurements. *Science*, 208(4439):53–55, 1980.

[6] M. Hamalainen, R. Hari, R. J. Ilmoniemi, J. Knuutila, and O. J. Lounasmaa. Magnetoencephalography - theory, instrumentation, and applications to non-invasive studies of the working human brain. *Rev. Mod. Phys.*, 65(2):413–497, 1993.

[7] S. Baillet. Magnetoencephalography for brain electrophysiology and imaging. *Nature Neuroscience*, 20(3):327–339, 2017.

[8] A. Irimia, W. O. Richards, and L. A. Bradshaw. Magnetogastrographic detection of gastric electrical response activity in humans. *Phys. Med. Biol.*, 51(5):1347–1360, 2006.

[9] C. E. Eichler, L. K. Cheng, N. Paskaranandavadivel, P. Du, L. A. Bradshaw, and R. Avci. Effects of magnetogastrography sensor configurations in tracking slow wave propagation. *Comput. Biol.*, 129:104169, 2021.

[10] D. B. Sneag, S. C. Lee, J. H. Feinberg, D. P. Melisaratus, and I. Amber. Magnetic resonance imaging patterns of mononeuropathic denervation in muscles with dual innervation. *Skeletal Radiology*, 46(12):1657–1665, 2017.

[11] D. Q. Liu, Z. Jia, M. Jin, Q. Liu, Z. L. Liao, J. Y. Zhong, H. W. Ye, and G. Chen. Cardiac magnetic resonance image segmentation based on convolutional neural network. *Computer methods and programs in biomedicine*, 197, 2020.

[12] H. Kobayashi, R. Nakayama, A. Hizukuri, M. Ishida, K. Kitagawa, and H. Sakuma. Improving image resolution of whole-heart coronary mra using convolutional neural network. *Journal of Digital Imaging*, 33(2):497–503, 2020.

[13] R. Kleiner, D. Koelle, F. Ludwig, and J. Clarke. Superconducting quantum interference devices: State of the art and application's. *Proceedings of the IEEE*, 92(10):1534–1548, 2004.

[14] J. F. Schneiderman. Information content with low- vs. high-t-c squid arrays in meg recordings: The case for high-t(c)squid-based megs. *Journal of Neuroscience Methods*, 222:42–46, 2014.

[15] B. I. Oladapo, S. A. Zahedi, S. C. Chaluvadi, S. S. Bollapalli, and M. Ismail. Model design of a superconducting quantum interference device of magnetic field sensors for magnetocardiography. *Biomedical signal processing and control*, 46:116–120, 2018.

[16] S. Woetzel, V. Schultze, R. IJsselsteijn, T. Schulz, S. Anders, R. Stolz, and H. G. Meyer. Microfabricated atomic vapor cell arrays for magnetic field measurements. *Review of Scientific Instruments*, 82(3), 2011.

[17] A. Horsley and P. Treutlein. Microfabricated atomic vapor cell arrays for magnetic field measurements. *Appl. Phys. Lett.*, 108(21), 2016.

[18] M. T. Hummon, S. Kang, D. G. Bopp, Q. Li, D. A. Westly, S. Kim, C. Fredrick, S. A. Diddams, K. Srinivasan, V. Aksyuk, and J. E. Kitching. Photonic chip for laser stabilization to an atomic vapor with 10(-11) instability. *Optica*, 5(4):443–449, 2018.

[19] T. Schröder, S. L. Mouradian, J. Zheng, M. E. Trusheim, M. Walsh, E. H. Chen, L. Li, I. Bayn, and D. Englund. Quantum nanophotonics in diamond. *J. Opt. Soc. Am. B*, 33(4):B65–B83, 2016.

[20] G. Kucsko, P. C. Maurer, N. Y. Yao, M. Kubo, H. J. Noh, P. K. Lo, H. Park, and M. D. Lukin. Nanometre-scale thermometry in a living cell. *Nature*, 500(7460):54–58, 2013.

[21] I. Aharonovich, D. Englund, and M. Toth. Solid-state single-photon emitters. *Nat. Phot.*, 10(10):631–641, 2016.

[22] F. Jelezko, T. Gaebel, I. Popa, A. Gruber, and J. Wrachtrup. Observation of Coherent Oscillations in a Single Electron Spin. *Phys. Rev. Lett.*, 92(7):1–4, 2004.

[23] L. Rondin, J.-P. Tetienne, T. Hingant, J.-F. Roch, P. Maletinsky, and V. Jacques. Magnetometry with nitrogen-vacancy defects in diamond. *Rep. Prog. Phys.*, 77(5):056503, 2014.

[24] J. H. N. Loubser and J. A. Van Wyk. Electron spin resonance in the study of diamond. *Rep. Prog. Phys.*, 41(8):1201–1248, 1978.

[25] A. Gruber, A. Dräbenstedt, C. Tietz, L. Fleury, J. Wrachtrup, and C. von Borczyskowski. Scanning Confocal Optical Microscopy and Magnetic Resonance on Single Defect Centers. *Science*, 276(5321):2012–2014, 1997.

[26] T. Wolf, P. Neumann, K. Nakamura, H. Sumiya, T. Ohshima, J. Isoya, and J. Wrachtrup. Subpicotesla diamond magnetometry. *Phys. Rev. X*, 5(4):1–10, 2015.

[27] J. F. Barry, J. M. Schloss, E. Bauch, M. J. Turner, C. A. Hart, L. M. Pham, and R. L. Walsworth. Sensitivity Optimization for NV-Diamond Magnetometry. *Rev. Mod. Phys.*, 92(1):015004, 2020.

[28] J. M. Taylor, P. Cappellaro, L. Childress, L. Jiang, D. Budker, P. R. Hemmer, A. Yacoby, R. Walsworth, and M. D. Lukin. High-sensitivity diamond magnetometer with nanoscale resolution. *Nat. Phys.*, 4(10):810–816, 2008.

[29] M. W. Doherty, N. B. Manson, P. Delaney, F. Jelezko, and L. C. Wrachtrup, J. Hollenberg. The nitrogen-vacancy colour centre in diamond. *Phys. Rep.*, 528(1):1–45, 2013.

[30] J. L. Webb, L. Troise, N. W. Hansen, J. Achard, O. Brinza, R. Staacke, M. Kieschink, J. Meijer, J.-F. Perrier, K. Berg-Sørensen, A. Huck, and U. L. Andersen. Optimization of a diamond nitrogen vacancy centre magnetometer for sensing of biological signals. *Frontiers Phys.*, 8:522536, 2020.

[31] J. R. Maze, A. Gali, E. Togan, Y. Chu, A. Trifonov, E. Kaxiras, and M. D. Lukin. Properties of nitrogen-vacancy centers in diamond: The group theoretic approach. *New J. Phys.*, 13(2):025025, 2011.

[32] G. Balasubramian, I. Y. Chan, R. Kolesov, M. Al-Hmoud, J. Tisler, C. Shin, C. Kim, A. Wojcik, P. R. Hemmer, A. Krueger, T. Hanke, A. Leitenstorfer, R. Bratschitsch, F. Jelezko, and J. Wrachtrup. Nanoscale imaging magnetometry with diamond spins under ambient conditions. *Nature*, 455(7213):648–651, 2008.

[33] G. D. Fuchs, V. V. Dobrovitski, R. Hanson, A. Batra, C. D. Weis, T. Schenkel, and D. D. Awschalom. Excited-state spectroscopy using single spin manipulation in diamond. *Phys. Rev. Lett.*, 101(11):117601, 2008.

[34] A. T. Collins, M. F. Thomaz, and M. I. B. Jorge. Luminescence decay time of the 1.945 ev centre in type ib diamond. *J. Phys. C: Solid State Phys.*, 16(11):2177–2181, 1983.

[35] A. Batalov, C. Zierl, T. Gaebel, P. Neumann, I. Y. Chan, G. Balasubramian, P. R. Hemmer, F. Jelezko, and J. Wrachtrup. Temporal coherence of photons emitted by single nitrogen-vacancy defect centers in diamond using optical rabi- oscillations. *Phys. Rev. Lett.*, 100(7):077401, 2008.

[36] L. Robledo, H. Bernien, T. van der Sar, and R. Hanson. Spin dynamics in the optical cycle of single nitrogen-vacancy centres in diamond. *New J. Phys.*, 13(2):025013, 2011.

[37] N. Aslam, G. Waldherr, P. Neumann, F. Jelezko, and J. Wrachtrup. Photo-induced ionization dynamics of the nitrogen vacancy defect in diamond investigated by single-shot charge state detection. *New J. Phys.*, 15(1):013064, 2013.

[38] L. J. Rogers, S. Armstrong, M. J. Sellars, and N. B. Manson. Infrared emission of the nv centre in diamond: Zeeman and uniaxial stress studies. *New J. Phys.*, 10(10):103024, 2008.

[39] F. Jelezko and J. Wrachtrup. Single defect centres in diamond: A review. *Physica Status Solidi A*, 203(13):3207–3225, 2006.

[40] M. W. Doherty et al. Electronic properties and metrology applications of the diamond nv$^-$ center under pressure. *Phys. Rev. Lett.*, 112(4):047601, 2014.

[41] J. P. Tetienne, L. Rondin, P. Spinicelli, M. Chipaux, T. Debuisschert, J. F. Roch, and V. Jacques. Magnetic-field-dependent photodynamics of single nv defects in diamond: an application to qualitative all-optical magnetic imaging. *New J. Phys.*, 14(10):103033, 2012.

[42] Y. Zhang, Z. Li, Y. Feng, H. Guo, H. Wen, J. Tang, and J. Liu. High-sensitivity dc magnetic field detection with ensemble nv centers by pulsed quantum filtering technology. *Opt. Express*, 28(11):16191, 2020.

[43] C. Zhang, M. Shagieva, F. Widmann, M. Kuebler, V. Vorobyov, P. Kapitanova, E. Nenasheva, R. Corkill, O. Rohrle, K. Nakamura, H. Sumiya, S. Onoda, J. Isoya, and J. Wrachtrup. Diamond magnetometry and gradiometry towards subpicotesla dc field measurement. *Phys. Rev. Appl.*, 15(6):20, 2021.

[44] S. Hong, M. Grinolds, L. Pham, D. Sage, L. Luan, R. Walsworth, and A. Yacoby. Nanoscale magnetometry with nv centers in diamond. *MRS Bulletin*, 38:155–161, 2013.

[45] A. Dréau, M. Lesik, L. Rondin, P. Spinicelli, O. Arcizet, J. F. Roch, and V. Jacques. Avoiding power broadening in optically detected magnetic resonance of single NV defects for enhanced dc magnetic field sensitivity. *Phys. Rev. B*, 84(19):1–8, 2011.

[46] D. B. Bucher, D. P. L. Aude Craik, M. P. Backlund, M. J. Turner, O. Ben Dor, D. R. Glenn, and R. L. Walsworth. Quantum diamond spectrometer for nanoscale nmr and esr spectroscopy. *Nat. Prot.*, 14(9):2707–2747, 2019.

[47] V. Jacques, P. Neumann, J. Beck, M. Markham, D. Twitchen, J. Meijer, F. Kaiser, G. Balasubramian, F. Jelezko, and J. Wrachtrup. Dynamic polarization of single nuclear spins by optical pumping of nitrogen-vacancy color centers in diamond at room temperature. *Phys. Rev. Lett.*, 102(5):057403, 2009.

[48] V. V. Soshenko, O. R. Rubinas, V. V. Vorobyov, S. V. Bolshedvorskii, V. N. Kapitanova, P. V.and Sorokin, and A. V. Akimov. Microwave antenna for exciting optically detected magnetic resonance in diamond nv centers. *Lebedev Physics Institute Bulletin*, 45(8):237–240, 2018.

[49] O. R. Opaluch, N. Oshnik, R. Nelz, and E. Neu. Optimized planar microwave antenna for nitrogen vacancy center based sensing applications. *Nanomaterials*, 11(8):2108, 2021.

[50] N. Khaneja, T. Reiss, C. Kehlet, T. Schulte-Herbrüggen, and S. J. Glaser. Optimal control of coupled spin dynamics: Design of NMR pulse sequences by gradient ascent algorithms. *J. Magnetic Resonance*, 172(2):296–305, 2005.

[51] C. Brif, R. Chakrabarti, and H. Rabitz. Control of quantum phenomena: past, present and future. *New J. Phys.*, 12(7):075008, 2010.

[52] B. Bartels and F. Mintert. Smooth optimal control with Floquet theory. *Phys. Rev. A*, 88(5):1–7, 2013.

[53] B. Bartels. *Smooth Optimal Control of Coherent Quantum Dynamics*. PhD thesis, Albert-Ludwigs-Universität Freiburg, 2015.

[54] T. Nöbauer, A. Angerer, B. Bartels, M. Trupke, S. Rotter, J. Schmiedmayer, F. Mintert, and J. Majer. Smooth Optimal Quantum Control for Robust Solid-State Spin Magnetometry. *Phys. Rev. Lett.*, 115(19):190801, 2015.

[55] F. Poggiali, P. Cappellaro, and N. Fabbri. Optimal Control for One-Qubit Quantum Sensing. *Phys. Rev. X*, 8(2):021059, 2018.

[56] P. Rembold, N. Oshnik, M. M. Müller, S. Montangero, T. Calarco, and E. Neu. Introduction to quantum optimal control for quantum sensing with nitrogen-vacancy centers in diamond. *AVS Quant. Sci.*, 2(2):024701, 2020.

[57] T. E. Skinner, T. O. Reiss, B. Luy, N. Khaneja, and S. J. Glaser. Application of optimal control theory to the design of broadband excitation pulses for high-resolution NMR. *J. Magnetic Resonance*, 163(1):8–15, 2003.

[58] T. W. Borneman, M. D. Hurlimann, and D. G. Cory. Application of optimal control to cpmg refocusing pulse design. *J. Magn. Reson.*, 207(2):220–233, 2010.

[59] J. Tian, T. Du, Y. Liu, H. Liu, F. Jin, R. S. Said, and J. Cai. Optimal quantum optical control of spin in diamond. *Phys. Rev. A*, 100(1):012110, 2019.

[60] J. H. Shirley. Solution of the schrödinger equation with a hamiltonian periodic in time. *Phys. Rev.*, 138(4B):B979–B987, 1965.

[61] G. Agarwal. *Quantum Optics.* Cambridge University Press, United Kingdom, 2012.

[62] S. Ahmadi, H. A. R. El-Ella, J. O. B. Hansen, A. Huck, and U. L. Andersen. Pump-Enhanced Continuous-Wave Magnetometry using Nitrogen-Vacancy Ensembles. *Phys. Rev. Applied*, 8(3):034001, 2017.

[63] S. Ahmadi, H. A. R. El-Ella, J. O. B. Hansen, A. Huck, and U. L. Andersen. Supplementary for "Pump-Enhanced Continuous-Wave Magnetometry using Nitrogen-Vacancy Ensembles". *Phys. Rev. Applied*, 8(3):034001, 2017.

[64] C. Osterkamp, M. Mangold, J. Lang, P. Balasubramanian, T. Teraji, B. Naydenov, and F. Jelezko. Engineering preferentially-aligned nitrogen-vacancy centre ensembles in cvd grown diamond. *Sci. Reports*, 9(1):1–7, 2019.

[65] A. M. Wojciechowski, M. Karadas, C. Osterkamp, S. Jankuhn, J. Meijer, F. Jelezko, A. Huck, and U. L. Andersen. Precision temperature sensing in the presence of magnetic field noise and vice-versa using nitrogen-vacancy centers in diamond. *Appl. Phys. Lett.*, 113(1):013502, 2018.

[66] T. Y. Huang, R. R. Grote, S. A. Mann, A. L. Hopper, D. A. Exarhos, G. G. Lopez, G. R. Kaighn, E. C. Garnett, and L. C. Bassett. A monolithic immersion metalens for imaging solid-state quantum emitters. *Nat. Commun.*, 10(1):2392, 2019.

[67] J. Jeske, J. H. Cole, and A. D. Greentree. Laser threshold magnetometry. *New J. Phys.*, 18(1):013015, 2016.

[68] Y. Cunyun. *Tunable External Cavity Diode Lasers.* World Scientific, Singapore, 2004.

[69] K. Petermann. *Laser Diode Modulation and Noise.* Springer, Netherlands, 1988.

[70] P. J. de Groot, G. M. Gallatin, and S. H. Macomber. Ranging and velocimetry signal generation in a backscatter-modulated laser diode. *Appl. Phys.*, 27(21):4475–4480, 1988.

[71] J. Li, H. Niu, and Y. Niu. Laser feedback interferometry and applications: A review. *Opt. Eng.*, 56(5):050901, 2017.

[72] A. Petrova-Major and S. Gimbal. Advanced lab on fresnel equations. *Amer. J. Phys.*, 83(11):935–941, 2015.

[73] C. Voumard, R. Salathe, and H. Weber. Resonance amplifier model describing diode lasers coupled to short external resonators. *Appl. Phys.*, 12(4):369–378, 1977.

[74] J. W. Allen. Semiconductor lasers, g. p. agrawal and n. k. dutta. 2nd edn. van nostrand reinhold, new york, 1993. isbn 0 442 01102 4, £66.00. no. of pages 616. *Adv. Mater. Opt. Electron.*, 4(1):51, 1994.

[75] Y. Dumeige, J. F. Roch, F. Bretenaker, T. Debuisschert, V. Acosta, C. Becher, G. Chatzidrosos, A. Wickenbrock, L. Bougas, A. Wilzewski, and D. Budker. Infrared laser threshold magnetometry with a nv doped diamond intracavity etalon. *Opt. Exp.*, 27(2):1706–1717, 2019.